

Dissertation
submitted to the
Combined Faculties of the Natural Sciences and
Mathematics
of the Ruperto-Carola-University of Heidelberg,
Germany
for the degree of
Doctor of Natural Sciences

Put forward by
Thomas Malte Spieker
born in Bad Nauheim

Oral examination on July 16th, 2019

Detector Corrected Search for Dark Matter in Monojet and Vector Boson Fusion Topologies with the ATLAS Detector

Referees: Prof. Dr. Hans-Christian Schultz-Coulon
Prof. Dr. Klaus Reygers

Zusammenfassung

Eine von Detektoreffekten bereinigte Suche nach Dunkler Materie wird präsentiert, unter der Verwendung von 36.2 fb^{-1} von Proton-Proton Kollisionen bei $\sqrt{s} = 13 \text{ TeV}$, die vom Large Hadron Collider produziert und vom ATLAS Detektor aufgezeichnet wurden. Die Suche zielt auf die Produktion von Dunkler Materie zusammen mit mindestens einem hadronischen Jet und deren Produktion in einer Vektor-Boson-Fusion Topologie. Das Verhältnis zwischen der Signalregion und der Kombination zweier Kontrollregionen wird differenziell als Funktion von vier Observablen gemessen. Letztere messen die Produktion leptonisch zerfallender Z Bosonen, in ähnlichen Topologien wie das erwartete Dunkle Materie Signal. Die Daten werden durch eine Entfaltungsmethode von Detektoreffekten bereinigt, um den Vergleich mit Modellen jenseits des Standardmodells zu vereinfachen, da dann keine Detektorsimulation mehr von Nöten ist. Es werden Strategien für das Entfalten der Daten mit und ohne Hintergrundsubtraktion untersucht, wobei sich zeigt, dass letztere verzerrte Ergebnisse produziert. Folglich wird die erste der beiden Strategien verwendet und es zeigt sich, dass die Daten mit den Erwartungen übereinstimmen. Ausschlussgrenzen bei einem Konfidenzniveau von 95% werden daher für ein vereinfachtes Dunkle Materie Modell abgeleitet. Außerdem werden Ausschlussgrenzen auf das unsichtbare Verzweigungsverhältnis des Higgs Bosons aus dem Standardmodell bestimmt.

Abstract

A detector-corrected dark matter search is presented using 36.2 fb^{-1} of proton-proton collisions at $\sqrt{s} = 13 \text{ TeV}$, delivered by the Large Hadron Collider and recorded by the ATLAS detector. The search targets dark matter production in association with at least one jet as well as dark matter produced in a vector boson fusion topology. The ratio of cross sections between the signal region and two combined control regions is measured differentially as a function of four observables. The control regions target the leptonic decay of Z bosons, in similar topologies like the expected dark matter signal. The data is corrected for detector effects via an unfolding technique to facilitate the comparison to new physics models without the need for a detector simulation. Unfolding strategies with and without background subtraction are investigated, where the latter has been shown to introduce biases on the results. The former strategy is consequently used and the data is found to be in agreement with its predictions. Exclusion limits at 95% confidence level are derived on a simplified dark matter model and the invisible branching fraction of the Standard Model Higgs boson.

Contents

	Page
1 Introduction	1
2 Experimental Setup	5
2.1 The Large Hadron Collider	5
2.2 The ATLAS Experiment	9
2.3 Physics Object Reconstruction and Calibration	16
3 Theoretical Background	23
3.1 The Standard Model of Particle Physics	23
3.2 Physics Beyond the Standard Model	28
3.3 The Search for Dark Matter	33
3.4 Previous Collider Searches	34
3.5 Limitations in Current Interpretations	38
4 Unfolding in Searches	39
4.1 Mathematical Formulation	40
4.2 Iterative Dynamically Stabilized Unfolding	43
5 MET + Jet Reconstruction-level Analysis	53
5.1 Search Strategy	53
5.2 Datasets and Frameworks	56
5.3 Particle-level Object and Event Selection	60
5.4 Reconstruction-level Object and Event Selection	62
5.5 Backgrounds	70
5.6 Uncertainties	71
5.7 Reconstruction-level Results	76
6 Correcting for Detector Effects	83
6.1 Binning Optimization for Observables	83
6.2 Unfolding Strategies	86
6.3 Detector Corrected Measurement	97

7	Interpretation	105
7.1	Simplified S-Channel Mediator Model	109
7.2	Invisible Higgs Decays	112
8	Conclusion and Outlook	115
	Appendix	117
A	Equivalence of IDS and Bayesian Unfolding	117
B	Parameter Estimation for the IDS Method	118
C	Choice of Lepton p_T Cut	119
D	Monte Carlo Simulation Samples used for the Analysis	120
E	Bootstrapped Uncertainties in Systematic Variations	127
F	Trigger Efficiency for $Z \rightarrow ee$ and $Z \rightarrow \mu\mu$ Selection	128
G	Non-Collision Background in the Signal Region	131
H	Binning Optimization for Observables	132
I	Variations of Process versus Topology Detector Responses	137
J	Covariances and Correlations after Unfolding	140
K	Likelihood Combination of $Z \rightarrow ee$ and $Z \rightarrow \mu\mu$ for 2016 Paper	142
	Bibliography	145
	Acknowledgements	161

Chapter 1

Introduction

The search for dark matter has become one of the biggest challenges in particle physics today. A multitude of astrophysical observations show additional gravitational force being exerted on stars and galaxies in the universe, which can not be explained by the visible baryonic matter alone. While there is a broad range of possible explanations, the most widely accepted one is the existence of additional gravitating matter, which does not interact electromagnetically. This form of matter is invisible to common telescopes and, thus, it was named *dark matter*. Recent measurements have estimated dark matter to contribute about 27% to the energy content in today's universe, while baryonic matter makes up only about 5% [1].

If dark matter is of particle nature and interacts with the known Standard Model particles via any of the other fundamental forces, it is expected to manifest itself in the particle collisions produced by the Large Hadron Collider (LHC) at CERN. The experiments designed to measure these collisions, therefore, try to find deviations from the Standard Model predictions due to dark matter contributions. Dark matter is not expected to interact with the detector material and leaves no detectable signal. A common strategy at the LHC is therefore to search for dark matter in association with a Standard Model particle. The dark matter recoils against this particle and leaves an imbalance of the deposited energy in the transverse plane of the detector, which is why these signatures are often referred to as MET¹ + X searches. Many of these searches have been performed in the past [2, 3], but so far none of them have found significant deviation from the Standard Model predictions.

In conventional dark matter searches the Standard Model predictions are simulated and subsequently propagated through a detector simulation, in order to be comparable to the measured data. Deviations between data and simulation would hint to contributions from physics *beyond the Standard Model* (BSM). In the absence thereof, limits are derived on potential new physics models. Events of the tested models are simulated using Monte Carlo techniques and the compatibility with the measured data is determined. The BSM predictions are also propagated through a detector simulation in order to account for the finite detector resolution, reconstruction efficiencies and the limited acceptance of the detector. The detector simulation is computationally expensive and only a limited amount of models are simulated and constrained in this way. Setting limits on additional models

¹ Other common abbreviations are Missing E_T , or E_T^{miss} .

after the data is published is disadvantageous, since the detailed detector simulation of the collaborations is not publicly available and inferior parametrized detector simulations have to be used.

A new search strategy was investigated and published by the ATLAS collaboration in 2016 [4], in which the data was corrected for detector effects. This uses the detailed detector simulation available within the collaboration and allows to compare the measured data to new physics models without the need of a detector simulation for the generated models. The latter allows for an efficient limit setting procedure in the absence of significant deviations and many models can be constrained. Furthermore, it enhances the longevity of the results, as limits can be derived for new models directly when they arise.

In this work a search for dark matter is performed using 36.2 fb^{-1} of proton-proton collisions at $\sqrt{s} = 13 \text{ TeV}$, delivered by the LHC and recorded by the ATLAS detector. The analysis extends the approach taken in [4] using a more sophisticated method to correct the data for detector effects. This method consistently treats unknown structures in the data caused by potential new physics contributions, which was not the case in the first iteration of the analysis. Furthermore, the amount of data which is analyzed increased by more than one order of magnitude. Additionally, two unfolding strategies are investigated. The first approach requires no background subtraction, but corrects the entire topological selection for detector effects. The second strategy subtracts all but the leading Standard Model contributions in the selection and, subsequently, unfolds the remaining data.

The analysis targets the production of dark matter in association with at least one jet as well as a second signature with an increased sensitivity to the electroweak production of dark matter. To this end the latter selects a vector boson fusion topology. The Standard Model process in which a Z boson decays to two neutrinos is indistinguishable from the signal and is, thus, added to the signal definition. The cross section of this signal is measured differentially as a function of four observables. In addition, two control regions aiming for Z bosons decaying to two leptons are defined. The final results are presented as a ratio of cross sections between the signal and the combined control regions.

This thesis is structured as follows: In chapter 2 the experimental setup is presented, which includes an introduction to the Large Hadron Collider and the ATLAS experiment as well as reconstruction algorithms and calibrations of the measured objects. Chapter 3 discusses the theoretical models required for this work. This includes an introduction to the Standard Model of particle physics as well as possible beyond the Standard Model theories predicting dark matter. Furthermore, common search strategies are presented together with possible limitations and proposals on how to improve them. In chapter 4 the concept of unfolding is introduced theoretically and challenges arising in searches are highlighted. In addition, the algorithm used in this work, the Iterative Dynamically Stabilized unfolding, is explained. Chapter 5 introduces the search strategy, along with the data and simulated datasets used in the analysis. The particle and event selections at reconstruction-level and at particle-level are introduced and backgrounds and uncertainties are discussed. Finally, the reconstruction-level results are presented. In chapter 6 the data is unfolded to particle-level. An optimized binning for the observables of interest is introduced, before two possible

unfolding strategies are investigated. Lastly, the unfolded distributions are presented. In chapter 7 a limit setting procedure is introduced which is used to constrain two possible BSM models. The conclusion of this thesis is provided in chapter 8.

Authors Contribution

The presented analysis would not have been possible without the help of many people. As a member of the ATLAS collaboration I profited from the hundreds of people who contributed to the design, construction and successful operation of the experiment. Furthermore, I used software frameworks, algorithms, calibrations and many other helpful tools and support which aided the work I present in this thesis.

Personally, I contributed to the efforts within the ATLAS collaboration when working on a hadronic calibration for the Level-1 trigger system. The details of this work are not discussed in the presented analysis and are thus summarized here. During the first long shutdown in 2013 and 2014 the Multi-Chip-Modules (MCM) of the Level-1 Calorimeter Trigger were replaced by new Multi-Chip-Modules (nMCM). The MCMs are the central components of the L1Calo PreProcessor performing major signal processing tasks. The upgraded chips allow, amongst various other improvements, the introduction of a second look-up table in order to provide separate calibrations for the Jet Energy Processor (JEP) and the Cluster Processor (CP). A better energy calibration for the jets identified by the JEP system targets a steeper turn-on curve for the L1 jet trigger efficiencies. This results in a smaller rate of L1-accepted events, which are subsequently rejected by the High-Level-Trigger algorithms. The Level-1 bandwidth can thus be reduced allowing to trigger more interesting events. While a non-linear calibration scheme showed very promising results, it also turned out to be very sensitive to the changing operation conditions of the LHC. The increased complexity, thus, outweighed the improvements and the new calibration was not implemented, but important information about the system was gained.

I then started working on the detector-corrected search for dark matter within the ATLAS collaboration. The first iteration of this search was close to publication. I contributed to this work with a cross check of the statistical combination of two control regions, which was performed within this analysis. The details of this combination are not discussed within the context of this thesis, but a short introduction is added in appendix K.

After publication an improved iteration of the analysis started. Improvements envisioned a larger dataset, increasing the analyzed data by almost a factor of 50, a more sophisticated unfolding method, as well as additional signal and control regions. The additional regions are sought to overcome statistical limitations in the first publication and extend the sensitivity of the analysis. I contributed to various aspects of the analysis. I was the author of the skimming framework, which was developed to implement baseline event selections, as well as apply the most recent calibrations to all physics objects. Furthermore, I was one of the main contributors in unifying the analysis selections between the different analysis groups and, thus, authored the full analysis chain. Additionally, I derived trigger scale factors, which are applied in the analysis and I defined an optimized binning for the observables of interest. The latter is necessary to make optimal use of the

shape information, which needs to balance restrictions from the unfolding procedure.

Most importantly, I was responsible for the studies and the implementation of the unfolding procedure, which is expected to be one of the main improvements to the analysis strategy. This includes the study of the optimal parameters of the unfolding method, as well as the investigation of different unfolding strategies considered for the analysis. In the course of this work I analyzed a subset of about one fourth of the data envisioned for the full analysis and measured the final distributions and uncertainties thereof. Furthermore, I developed a limit setting procedure to constrain possible beyond the Standard Model theories. Limits on two different models are derived in this work. I generated the events for both of these models within the ATLAS simulation framework. Furthermore, I modified an existing Rivet routine to analyze the simulated events at the particle-level, allowing to use the resulting distributions in the limit setting procedure.

Chapter 2

Experimental Setup

The experimental efforts to expand on the knowledge about the constituents of the universe have reached new heights, when the Large Hadron Collider (LHC) and its four experiments¹ started full operation after construction completed in 2009. The experimental facilities are designed to measure proton-proton and heavy-ion collisions at the highest man-made energies and, thus, provide the unique possibility to study rare particle interactions in a controlled laboratory environment. The collisions analyzed in this work were delivered by the LHC and recorded by the ATLAS detector. The setup of these two experimental facilities is introduced in sections 2.1 and 2.2. For further details the reader is referenced to [5] and [6].

After the data is recorded, reconstruction algorithms are applied to the digitized detector output in order to determine which particles were produced in the collisions. The particle types and multiplicities, as well as their energy and location are thus inferred. The reconstruction algorithms and calibration procedures are introduced in section 2.3.

2.1 The Large Hadron Collider

The Large Hadron Collider (LHC) is a machine of superlatives. With a circumference of 26.658 km [7] it is the largest particle accelerator in the world² [8]. Furthermore, it collides particles at unprecedented energies, with a design center of mass collision energy of 14 TeV. Together with peak instantaneous luminosities of 10^{34} cm⁻²s⁻¹ [7] the LHC poses an ideal environment for scientists to explore the production of rare events and provides great discovery potential for physics beyond established theoretical models (see section 3.1). One of the most prominent goals of the LHC was to allow for the discovery of the Higgs Boson, which was finally achieved by the ATLAS and CMS collaboration in 2012 [9, 10].

The LHC is located north of the main site of the European Organization for Nuclear Research (CERN)³, about 10 km northwest of the city of Geneva. It is installed in the

¹ **ATLAS** (own name, formerly A Toroidal LHC ApparatuS), **Compact Muon Solenoid** (CMS), **Large Hadron Collider beauty** (LHCb), **A Large Ion Collider Experiment** (ALICE)

² This award was handed out by Guinness World Records Ltd. Among other records it is also the longest vacuum system and the largest fridge.

³ The name is derived from the French name Conseil Européen pour la Recherche Nucléaire

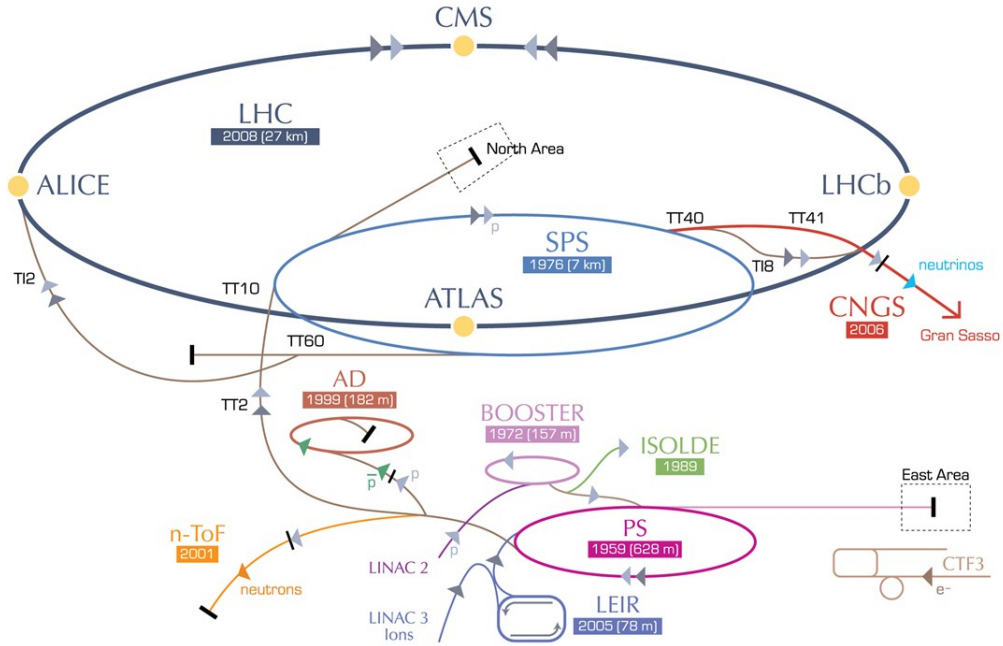


Figure 2.1: *The LHC ring included into the accelerator complex at CERN. Linac2 + Booster as well as Linac3 + LEIR both lead into PS and SPS as pre-accelerators for LHC [12].*

tunnel of its predecessor, the Large Electron-Positron Collider (LEP), which is situated between 45 m and 170 m below the surface. This upgrade was already envisioned at the first official mention of the LHC at the *Large Hadron Collider in the LEP Tunnel Workshop* [11] in 1984, when LEP was still being built. LHC was supposed to be and became the natural extension of the CERN accelerator complex, when LEP approached its limits in terms of energy reach.

Since starting operation in 2011 the LHC has delivered proton-proton collisions at center of mass energies of 7 TeV, 8 TeV and 13 TeV. It will reach its design energy of 14 TeV in 2021. Accelerating particles to these energies is done in several stages. For proton-proton operation, hydrogen atoms are extracted from a hydrogen bottle and the electrons are stripped off their nucleus in an electric field. The resulting protons are accelerated to 50 MeV in Linac2, providing beam intensities of 180 mA [13]. This initial beam then traverses the Proton Synchrotron Booster (PSB) and the Proton Synchrotron (PS), which increase the beam energy to 1.4 GeV and 25 GeV respectively. The PS is also where the beam gets its bunch structure, meaning that just before ejection dedicated radio frequency (RF) cavities compress the beam into a train of bunches, which are all separated in time by 25 ns. By design each bunch contains 1.15×10^{11} protons in order to reach the design peak luminosity. The bunches then enter the Super Proton Synchrotron (SPS), where they are ramped up to an energy of 450 GeV before finally being injected into the LHC ring. In order to fill all bunches of the LHC ring, the pre-accelerators have to go through this cycle

several times, resulting in an ideal filling time of about 16 minutes, with this standard filling scheme [5].

The LHC can furthermore collide lead ions, providing more complex collisions with very high energy densities, in which phenomena like the quark-gluon plasma can be studied. Operations for lead-lead collisions are very similar to proton-proton collisions. The lead atoms are delivered from an electron cyclotron resonance (ECR) source before being pre-accelerated to 4.2 MeV per nucleon (MeV/n) in Linac3. In the low energy ion ring (LEIR) the long ion beam is transformed into bunches and accumulated before being accelerated to 72.2 MeV/n. Like the proton bunches, the ions are then accelerated to 5.9 GeV/n and 177 GeV/n in PS and SPS, before being injected into LHC. Along this path the ions traverse electron strippers after the ECR, Linac3 and PS to strip all 82 electrons off their cores [14].

With the particles of higher mass, compared to electrons and positrons, which were collided at LEP, synchrotron radiation at the LHC no longer limits the collision energy⁴. Instead it was necessary to develop superconducting magnets with unprecedented magnetic fields, to keep the particles on their circular orbit. In 2007, 23 years after the first workshop, the LHC was finally equipped with 1 232 superconducting Nb-Ti bending magnets, each providing a magnetic field of up to 8.4 T at temperatures of 1.9 K [15]. This allows for peak energies of 7 TeV per charge, resulting in the maximal center of mass energies of 14 TeV in proton-proton collisions and 5.52 TeV/n in lead-lead collisions⁵.

Additional quadrupole magnets control the beam size, which is crucial to avoid losses along the LHC ring. Furthermore, they provide for a high precision beam control at the interaction points. The beams are squeezed at these interaction points in order to increase the proton density within the colliding bunches, hence increasing the rate of proton-proton interactions. The beam is compressed to diameters of 16.7 μm at the interaction points of ATLAS and CMS [7], while being kept at larger radii during the remaining orbit.

Luminosity

The figure of merit to quantify the amount of collisions delivered to the experiments is called *luminosity*

$$L = \frac{N_1 N_2 f N_b}{4\pi\sigma_x\sigma_y} \cdot W \cdot e^{\frac{B^2}{A}} \cdot S, \quad (2.1)$$

where N_i are the number of particles in the colliding bunches, N_b is the number of bunches per beam and f the revolution frequency. σ_x and σ_y are the beam sizes in x and y direction, perpendicular to the beam direction. This assumes identical beam parameters for the two colliding beams and Gaussian bunch profiles. The correction factors W , S and $\exp^{\frac{B^2}{A}}$ are

⁴ The power loss due to synchrotron radiation $P_{sync} \propto \frac{E^4}{r^2 m^4}$ made it inefficient at LEP to increase the energy further. By using protons instead of electrons this effect is $(m_p/m_e)^4 \sim 1800^4$ times weaker, thus negligible at the LHC.

⁵ Lead ($^{208}\text{Pb}^{82+}$) fully stripped, i.e. charged 82+, results in $\sqrt{s} = 82 \times 7 \text{ TeV} \times 2 = 1148 \text{ TeV}$, distributed among all 208 nucleons.

introduced to take into account that the beams might collide at a crossing angle (S) or might have an offset (W) or both (W , S and $\exp\frac{B^2}{A}$) [16]. While some of the parameters, like the revolution frequency f are fixed by design, others are optimized by the LHC collaboration to maximize the luminosity delivered to the experiments.

The *integrated luminosity* is defined as:

$$L_{int} = \int_0^T L(t') dt'. \quad (2.2)$$

This number directly relates the cross section σ_{event} of a given process to the expected number of events N_{event} produced in the collisions:

$$N_{event} = L_{int} \cdot \sigma_{event}. \quad (2.3)$$

Pileup

The high density of protons within the bunches and the large revolution frequency, and hence collision frequency of 40 MHz, introduce an additional challenge at the LHC, known as *pileup*. Pileup refers to several overlapping signals, originating from multiple collisions inside the detector. Two cases are differentiated: *in-time* pileup and *out-of-time* pileup.

In-time pileup refers to multiple interactions in the same bunch crossing. The probability for this to happen is very high at the LHC, due to the large proton density inside the bunches, when they are squeezed at the collision points. Typically up to ~ 60 proton-proton interactions occur per bunch crossing (peak interactions per bunch crossing in 2018 [17]), which will further increase to ~ 140 in the coming years. The most energetic interaction is usually selected as the primary interaction and is referred to as the hard interaction, while the others are disregarded. However, the additional signals in the detector distort the main interaction and the origins of the signals need to be differentiated.

Similarly, out-of-time pileup refers to additional signals originating from bunch crossings before or after the interaction of interest. The additional signals from these bunch crossings deteriorate the measurement, since some detector signals take the time of several bunch crossings to be read out. Increasing the collision frequency from 20 MHz to 40 MHz between Run-1 in 2011 and 2012 and Run-2 starting in 2015 further increased the effect of out-of-time pileup [18].

Pileup is a challenge in analyses, since it alters the momentum resolution at which particles are reconstructed. Furthermore, particles may falsely be assigned to the main collision and thus modify the particle content of a collision event. To mitigate the effect of pileup the reconstruction algorithms introduced in the following section 2.3 are designed to suppress signals from pileup interactions. Additionally, averaged pileup corrections depending on the average interaction per bunch crossing μ , which is used as a figure of merit for the pileup environment, are applied in the object calibrations [18].

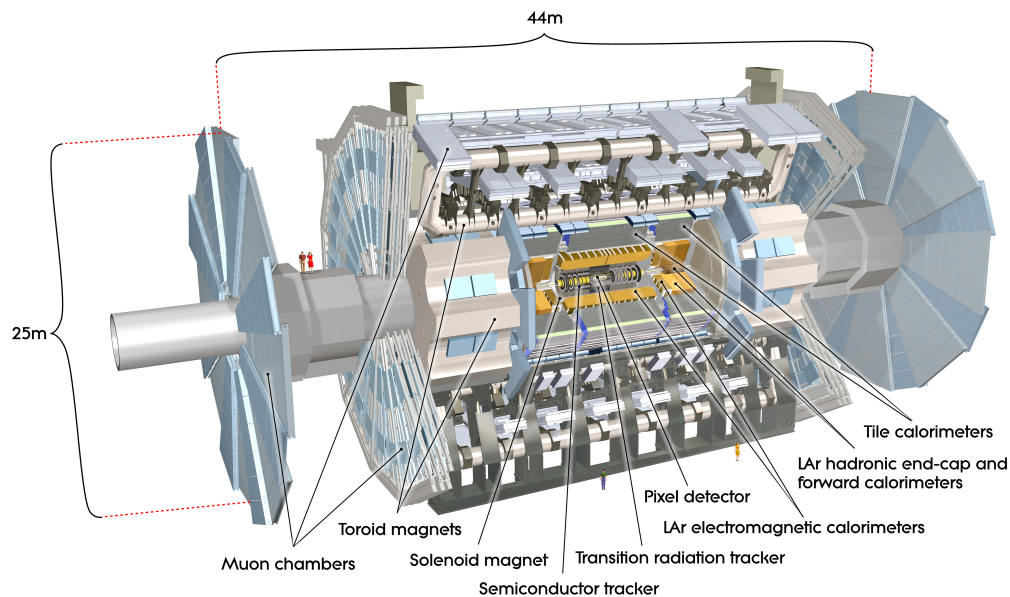


Figure 2.2: *The ATLAS detector with its onion-like structure around the interaction point. The sub-detectors going outwards from the interaction point are the tracking system, followed by the calorimeters and the muon system [19].*

2.2 The ATLAS Experiment

The ATLAS experiment is located in a cavern at the interaction point 1 (IP1) of the LHC ring. The detector is 25 m high, 44 m long and weighs about 7000 tons. Its design is that of a general purpose detector, meaning that it is instrumented in almost 4π solid angle around the interaction point and is layered like an onion with different sub-detectors. Inside out it consists of the inner detector, followed by the calorimeters and the muon system. This chapter follows largely the information given in [6]. The full layout of the ATLAS detector is depicted in figure 2.3.

The detector is symmetric around the interaction point with the inner detector (ID) surrounded by a thin superconducting solenoid magnet. This magnet immerses the inner detector in a 2 T magnetic field, thus bending the trajectories of charged particles. The inner detector then provides precise position information about the trajectories, which are used to determine charge, momentum, type and origin of the traversing particle. In order to minimize the deflection and absorption of particles, the material budget is kept to a minimum. After the solenoid magnet there is the calorimeter system. The first layer, the electromagnetic calorimeter (ECAL), is designed to absorb electrons and photons and measures their position and deposited energy. Hadrons, which can not be stopped by the ECAL alone, are then absorbed and measured in the hadronic calorimeter (HCAL).

The last layer, the muon system, consists of an eight-fold azimuthal symmetric toroid magnet which bends the muon trajectories. Like in the inner detector, the trajectories of

the muons are measured to reconstruct their momentum and charge.

In order to benchmark the performance goals of each sub-detector, the search for the Standard Model Higgs boson was used (see section 3.1), as it posed many decay and production mechanisms which depended on the Higgs mass, each of which needed to be detectable [6]. Additionally, the detectors were designed for a rich physics program including the search for physics beyond the Standard Model. This can be the search for dark matter, which would evade the detector without any trace, leaving a p_T imbalance in the transverse plane of the detector. But also the production of new heavy gauge bosons, decaying to high p_T leptons or hints for quark compositeness in jet production cross sections are targeted. And finally there are high precision measurements of known Standard Model processes to be performed, as well as the discovery of yet unobserved final states which are predicted by the Standard Model [6].

Each of these measurements pose challenging requirements to the detector systems. Among others it needs a good charged particle momentum resolution, excellent vertex reconstruction, very good electromagnetic calorimetry and a good muon system. Furthermore, excellent event selection is required to record only the most interesting collisions, while keeping the background events to a minimum.

Coordinate System

The interaction point at the center of the ATLAS detector serves as the origin of its right-handed coordinate system. The z-axis points into the direction of the beam-line, which traverses the detector. The x- and y-axis therefore span the plane transverse to the beam-line. While the positive x-axis points into the center of the LHC ring, the positive y-axis points upwards. Additionally, the azimuthal-angle ϕ around the z-axis and the polar-angle θ from the beam-line are defined. The latter is used to define the pseudorapidity $\eta = -\ln[\tan \theta/2]$. The rapidity $y = 1/2 \ln[(E + p_z)/(E - p_z)]$ is equivalent to the pseudorapidity, except that it respects particle masses⁶. Furthermore, the distance $\Delta R = \sqrt{\Delta\eta^2 + \Delta\phi^2}$ in the pseudorapidity-azimuthal space is defined. Transverse variables like the transverse momentum p_T or the missing transverse energy E_T^{miss} are defined in the x-y plane of the ATLAS detector.

Inner Detector

The inner detector records detailed position information about traversing charged particles. This is accomplished by several concentric layers of detectors in each of which the particles deposit energy by ionizing the material. According to the Bethe-Bloch formula the deposited energy depends on the type and amount of material a particle traverses [20]. In order to obtain only the position information and altering the momentum of the particle as little as possible, the layers are designed with a minimal material budget. From

⁶ It is also invariant under boosts along the z-axis.

the individual hits in the detector layers, reconstruction algorithms calculate continuous tracks.

The inner detector is furthermore immersed in a 2 T magnetic field parallel to the beam-line, provided by a superconducting solenoid, which surrounds the inner detectors. This way the charged particle tracks are bent in the transverse plane by the Lorentz force and a positive and negative charge can be distinguished. Assuming that the particle mass is negligible for high energy particles, the magnetic field and the bending radius allow to infer the momentum of the particle.

The inner detector is installed at pseudorapidities of $|\eta| < 2.5$ with cylindrical layers covering the small $|\eta|$ (barrel) region and several disks (end cap) covering the highest $|\eta|$ region. Details on the exact geometrical layout are found in [6]. Closest to the interaction point the particle density is largest. Hence a high-granularity pixel detector with 4 layers of silicon pixel sensors of $R - \phi \times z = 50 \times 400 \mu\text{m}^2$ is installed. This provides position information of $10 \mu\text{m}$ in the $R - \phi$ and $115 \mu\text{m}$ in the z -direction, with about 80 million channels installed. The radial distance of the pixel detector from the interaction point ranges from 3-15 cm.

At larger radii the particle density decreases, reducing the need for such high granularities. The following silicon microstrip (SCT) trackers installed at 25-56 cm therefore only needs 8 layers with about 6 million channels. The position resolution here is designed to be $17 \mu\text{m}$ in $R - \phi$ and $580 \mu\text{m}$ in the z -direction.

The last layer consists of a transition radiation tracker (TRT) covering the region of $|\eta| < 2.0$ at radii of 56-106 cm. It consists of straw tubes, parallel to the beam-line (in the barrel) and has no segmentation in η . Thus it only provides $R - \phi$ information at a resolution of $130 \mu\text{m}$ per straw tube. The amount of measurements due to the many straw layers provides significant additional information for the inner detector. Furthermore, the amount of measured transition radiation allows to aid particle identification.

Overall a relative momentum resolution of

$$\sigma_p/p = (4.83 \pm 0.16) \times 10^{-4} \text{GeV}^{-1} \times p_T \quad (2.4)$$

and a transverse impact parameter resolution of $22.1 \pm 0.9 \mu\text{m}$ are achieved [21].

Calorimeter

The inner detector and the superconducting solenoid are followed by the calorimeter system. It is designed to absorb and measure the energy of charged and neutral particles, as well as their direction. Furthermore, the shape of the signal deposited in the detector allows to assist particle identification, as some characteristics of this shape can be exploited. Most importantly for this work, particles invisible to the detector can be identified with the help of the calorimeter. This is because all known particles (except for muons and neutrinos) will be stopped by the calorimeter and deposit their energy there. From the energy depositions, the energy balance in the transverse plane can be calculated (adding in muons via a separate measurement). As the energies of all particles should sum up to zero

due to momentum conservation (there is no initial momentum in the transverse direction), missing transverse energy hints to invisible particles (neutrinos or yet unknown particles).

The calorimeter system is split into two layers: the *electromagnetic calorimeter* and the *hadronic calorimeter*. Both calorimeter systems are sampling calorimeters, consisting of dense absorption layers alternating with active detector layers. In the absorption layers, the traversing particles interact with the detector material and a combination of strong interactions, bremsstrahlung, multiple scattering, as well as pair production of electrons and positrons produce a particle shower. This way a high energy particle cascades down to many low energy particles, which are then measured with the active material. The full ATLAS calorimeter system covers the region of $|\eta| < 4.9$.

The electromagnetic calorimeter (ECAL) consists of an electromagnetic barrel at $|\eta| < 1.475$ and two end-caps at $1.375 < |\eta| < 3.2$. The overlap of the two systems ensures full coverage, however, service lines to the inner detector add to the inactive material in this region, which deteriorates the performance. Both the electromagnetic barrel and end-caps consist of accordion-shaped kapton electrodes with a regular spacing of 2.1 mm filled with liquid argon. Lead absorber plates provide the absorption layers. The total thickness of the ECAL corresponds to 22 radiation lengths X_0 in the barrel and 24 X_0 in the end-caps⁷ [20].

The granularity of the detector decreases with the radius. The first layer is designed to differentiate between π^0 particles decaying to two photons and isolated photons. Hence slices of $0.025/8 \times 0.1$ in $\eta \times \phi$ are read out, with a total thickness of $4.3 X_0$. The following slice is the largest with about 16 X_0 sliced in blocks of 0.025×0.025 . Most of the particle energy is deposited in this layer. The third layer where only a small fraction of the particle energy is recorded has 0.05×0.025 slices and has a thickness of $2.0 X_0$. The slicing changes slightly, especially in the overlap regions of barrel and end-cap, as well as the forward region, where larger slices are sufficient [6]. An additional layer, referred to as the presampler, is placed before the first sampling layer without any absorber material in order to correct for energy losses in the inner detector and the solenoid magnet. The total material budget before the calorimeter varies with η and lies between 1.0 and $3.0 X_0$, 0.6 of which are due to the magnet system [6].

In a test beam measurement a total energy resolution of

$$\sigma_E/E = \frac{10\%}{\sqrt{E(\text{GeV})}} \oplus 0.17\% \quad (2.5)$$

was achieved [22] in the barrel with similar performance in the end-cap region [23].

The hadronic calorimeter (HCAL) consists of scintillating tiles as active material and steel absorbers for the absorption layer at $|\eta| < 1.7$. It is subdivided into a barrel and extended barrel with equal granularity of 0.1×0.1 in η and ϕ . The total thickness of the hadronic barrel calorimeter is about $\lambda = 7.4$ interaction lengths⁸. The hadronic end-

⁷ A radiation length X_0 is defined as the distance, after which the energy of an electron is reduced by a factor $1/e$.

⁸ An interaction length λ is defined as the distance, after which the energy of a high energy hadron is reduced by a factor $1/e$.

caps are equipped with the accordion-shaped liquid argon calorimeter, here with copper absorber plates at $1.5 < |\eta| < 3.2$.

The energy resolution is required to be within

$$\sigma_E/E = \frac{50\%}{\sqrt{E(\text{GeV})}} \oplus 3\%, \quad (2.6)$$

according to [6]. Test beam measurements have shown reasonable agreement with this prediction [24, 25].

Finally, the liquid argon *forward calorimeter* (FCal) covers the region at $3.1 < |\eta| < 4.9$. It has a thickness of approximately 10λ and combines a electromagnetic calorimeter first layer and hadronic calorimeter in the second and third layer into one. The first layer is equipped with copper absorbers, while the second and third layer use tungsten. The latter is a highly dense material necessary to retain a large total thickness of $\lambda = 10$.

According to [6] the energy resolution for hadrons is required to be within

$$\sigma_E/E = \frac{100\%}{\sqrt{E(\text{GeV})}} \oplus 10\%. \quad (2.7)$$

Test beam measurements have shown that this was well achievable [26].

Muon Spectrometer

The last detector layer is the muon spectrometer. Muons are minimally ionizing particles (MIPs), meaning their energy deposition per path-length lies at the minimum of the Bethe-Bloch formula. Hence they do not interact enough with the material of the calorimeter to be stopped and measured efficiently. The muon spectrometer is another tracking system for charged particles, which solves this challenge. Like the inner detector, the muon system is built of concentric layers of detectors, tracking the positional information of the traversing particle and thus allowing for a precise track reconstruction. It is constructed of Monitored Drift Tubes (MDT) and Cathode Strip Chambers (CSC) for precision tracking, and Resistive Plate Chambers (RPC) and Thin Gap Chambers (TGC) for fast triggering.

The MDTs span the entire range of $|\eta| < 2.7$ in three concentric layers. They consist of multiple drift tubes of ~ 30 mm diameter, with a gold-plated tungsten-rhenium anode wire in the center. They are filled with a gas mixture of argon and carbon-dioxide, which is ionized when a charged particle traverses the tube. The drift time of the produced electrons to the anode is measured to estimate the exact position of the traversing particle, resulting in an overall positional resolution of 30-35 μm depending on the number of drift tubes per MDT.

The CSCs are multi-wire proportional chambers installed in the high rate region of the detector, which is the first layer at $2.0 < |\eta| < 2.7$. Like the MDT, it is made of several planes to allow for a combined position measurement and to mitigate failure of single components. It is also operated with a gas mixture of argon and carbon-dioxide

at slightly different concentration and due to its layout provides a bi-directional position measurement. Its resolution in the bending direction of the particle is $40 \mu\text{m}$.

The bending of the particles is facilitated by an eight-fold symmetric air-cooled toroid magnet, arranged around the barrel of the detector. It provides a magnetic field of 0.5 T in $|\eta| < 1.4$ bending the particles in the $R - \phi$ plane. The end-caps are supplemented with additional toroid magnets, rotated by 22.5° with respect to the barrel magnets. They provide magnetic fields of 1 T at $1.6 < |\eta| < 2.7$. The overlap region is a superposition of both magnets.

The RPCs and TGCs are installed in the barrel and end-caps, respectively. They serve a three-fold purpose, providing bunch crossing identification (BCID) and a reliable p_T threshold for triggering, as well as the second coordinate of the traversing particle, complementing those measured by the precision chambers introduced above. The RPC consists of two resistive plates, placed at a distance of 2 mm from each other. An electric field of 4.9 kV/mm is applied, such that traversing particles ionize the filled gas to produce a measurable avalanche of particles. The time resolution of this detector is at 10 ns, allowing for precise bunch crossing identification and triggering. The TGCs are multi-wire proportional chambers with wire-to-cathode distances of 1.4 mm. This distance being smaller than the wire-to-wire distance and the chambers are filled with a highly quenching gas, allowing to operate the TGC in a quasi-saturated mode. It was shown that the TPC signal will arrive within 25 ns in the desired 99% of the time, allowing for accurate BCID and triggering [6].

Trigger System

The trigger system is a crucial component in the successful operation of the ATLAS detector. The high rates of 40 MHz and an event size of ~ 1.6 MB produce a data-stream, which is too large to handle for present-day readout and storage system. The trigger system is thus used to select only the most interesting events in two stages, reducing the recording rate first to ~ 100 kHz and finally to ~ 1 kHz [27]. The two reductions are performed through a hardware-based decision by the the Level-1 (L1) trigger and a software-based decision by the High-Level-Trigger (HLT).

The decisions are taken based on predefined selection criteria. The selections are formulated as trigger items in the so-called trigger menu, which includes thresholds for objects at L1 and HLT, as well as *prescales*. Prescales are reduction factors, which reduce the bandwidth of certain trigger items, by only reading out every n^{th} event.

The Level-1 trigger decision uses a coarse, partial readout of the detector to take a decision within a latency of $2.5 \mu\text{s}$. Two subsystems: the Level-1 Calorimeter (L1Calo) and the Level-1 Muon (L1Muon) trigger send measurements to the Central Trigger Processor (CTP), which takes the final Level-1 decision. The Level-1 calorimeter system consists of a PreProcessor (PPr), the Cluster Processor (CP) and the Jet/Energy-sum Processor (JEP). The PPr digitizes the incoming analog pulses of coarse segments of the calorimeter (~ 7200 trigger towers), determines their transverse energy and applies a peak finder algorithm to determine the correct bunch crossing. Furthermore, it applies a bunch-by-

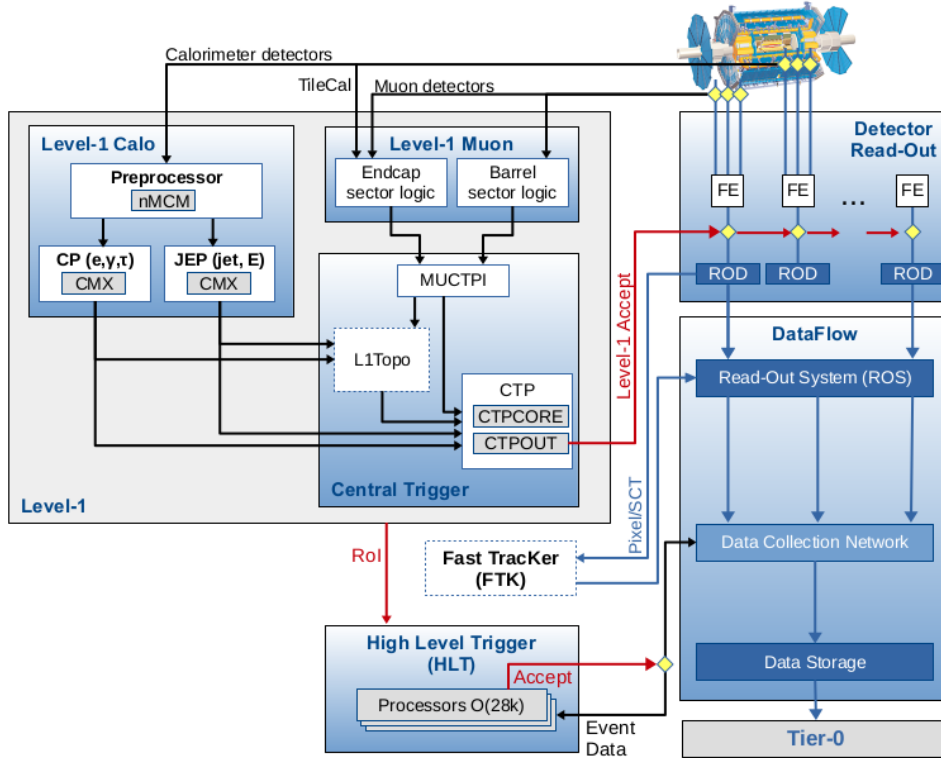


Figure 2.3: *The ATLAS trigger and data acquisition system in Run-2 [27].*

bunch pedestal (pileup) correction, which is especially important to linearize the missing energy trigger rates as a function of the instantaneous luminosity [27]. The resulting digitized trigger towers are calibrated using two dedicated lookup tables, one for the trigger towers sent to the CP and another one for the trigger towers sent to the JEP. Using the algorithms specified in [28] the JEP (CP) identifies regions of interest (RoI), in which jets (electrons/photons/taus) are reconstructed. Their energy is determined by the sum of the trigger towers corresponding to the RoI. Furthermore, the JEP calculates the missing transverse energy at Level-1. It is calculated by summing up the E_x and E_y components of all trigger towers which were passed to the JEP.

The Level-1 muon system requires coinciding signals, in space and time, in 2 (3) layers of their fast RPCs and TGCs for low (high) p_T muons. The energy is then determined by checking against certain *roads*. These roads are defined as the area filled by all possible trajectories between the interaction point and the measured hit, given muons of a certain p_T or higher [29]. If the muons trajectory lies within such a road, it thus satisfies the p_T requirement.

The Fast Tracker (FTK) which will provide tracking information at Level-1 in the future is still being commissioned at this point [30]. In the long shutdown between Run-

1 and Run-2 (LS1: 2013-2014) a topological trigger (L1Topo) was added to the system, which performs selections based on the kinematic and geometric input coming from L1Calo and L1Muon.

The decisions (i.e. multiplicities of passes thresholds) from L1Calo, L1Muon and L1Topo are then passed on to the CTP, which compares this input with the trigger menu. A logical **OR** of all trigger items determines the Level-1 decision. If an event is accepted the full detector is read-out into the Read-Out System (ROS), where the event is buffered while the HLT decision is taken.

The High-Level-Trigger is seeded with the RoIs of the accepted event and partially or fully reconstructs the event depending on its input. This is done by running the necessary algorithms on a dedicated computing cluster. The HLT has access to the full granularity of the calorimeter, as well as all muon chambers and the inner detector, which is not available at Level-1 due to the latency constraint. Interesting events can thus be selected more precisely and tighter selection criteria are applied resulting in a reduction of the recording rate to ~ 1 kHz. The events passing both, the Level-1 and HLT selection are written to disk at CERNs Tier-0 data center for the offline reconstruction and storage, ready to be analyzed.

2.3 Physics Object Reconstruction and Calibration

Physics object reconstruction refers to the task of converting the digital information recorded by the ATLAS sub-detectors into information about the type, multiplicity, energy and location of the particles produced in the proton-proton collisions. However, the reconstruction algorithms, which are developed to perform this task in most cases do not operate on the raw detector output, but rather work with derived meta-information like reconstructed *tracks* and *calorimeter clusters*. This information itself is subject to reconstruction algorithms, which feed into the higher-level algorithms.

After the particle information is derived from the detector output, the particles are furthermore calibrated to the correct energy scale. The calorimeter segments only measure the energy, which was deposited inside the active material and apply corrections for the absorber layers. These corrections, however, are different depending on the type of interacting particle. Once a shower is classified as a specific physics object, it can thus be calibrated to a more precise energy estimate.

As illustrated in figure 2.4, the different physics objects leave very distinct signatures in the detector, given by combinations of the track-information in the inner detector, the electromagnetic- and hadronic-calorimeter as well as the muon spectrometer. Additional challenges arise from the detector itself in the form of missed signals and noise. Furthermore, in-flight decays and radiation of the primary particles⁹ as well as pileup and the underlying event, which is the interaction of the colliding proton excluding the hard interaction, increase the complexity of this task. Pileup and the underlying event add to

⁹ Primary here refers to the particles produced in the hard interaction.

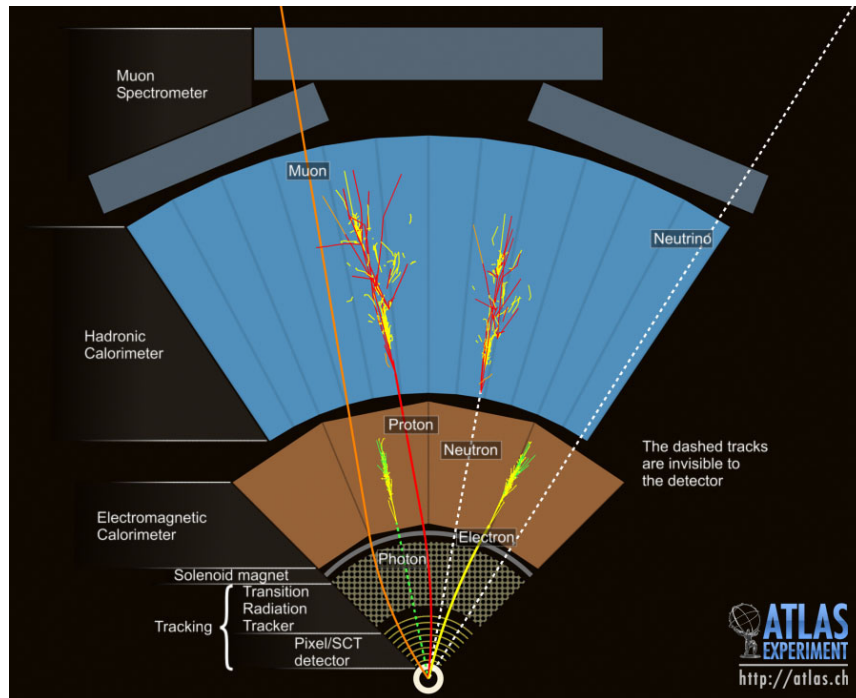


Figure 2.4: Particle identification with the ATLAS detector. Different patterns in the sub-detectors identify the Standard Model particles [31].

the signals measured by the detector and hence make a clean detection of the individual particles more challenging.

Tracks

The track reconstruction, also referred to as *track-finding*, identifies continuous charged tracks in the inner detector, as well as the muon spectrometer. It operates on the information of the tracking systems, which deliver *space-points* of a traversing particle [32].

The track-finding is seeded by sets of three space-points, which are ranked by the sub-detectors, in which the three seeds are measured, to increase purity. Seeds from SCT-only result in the largest fraction of high quality tracks and are thus considered first, followed by pixel-only and mixed-detector seeds. Once a set compatible with the interaction point is found, a Kalman filter [33] is employed to create a continuous track including all tracking layers. An initial momentum estimate is inferred from the curvature of the track.

The tracks are further cleaned by solving ambiguities of shared hits (clusters) between multiple tracks. This is done with the help of a so-called track-score, ranking the tracks according to their quality. A set of selection requirements are applied, based on the track kinematics, their distance to the interaction point as well as the number of hits and holes¹⁰ [32]. Finally, a high precision fit is performed on the final track candidates, yielding

¹⁰ Holes are space-points where there should have been a hit, even though none was found.

continuous tracks. A detailed description of the track finding can be found in [34].

Additional algorithms identify non-prompt tracks, not originating from the primary interaction vertex. They utilize an outside-in approach starting at the TRT and adding non-assigned space-points at smaller radii. These are helpful to identify secondary vertices from interacting primary particles [35].

Clusters

The calorimeter clusters are reconstructed in two different ways depending on their use case [36]. Electron and photon reconstruction use clusters from a sliding window algorithm, which uses rectangles of fixed size (depending on the particle type) to scan the electromagnetic calorimeter cells. In each of the 200×256 possible positions the total transverse energy of the cells within this window is determined and excesses above a noise threshold are recorded.

The jet reconstruction employs a topological algorithm, which adds neighboring cells together as long as they contain significant amounts of energy. For hadrons, which are not expected to leave a very collimated signal in the calorimeter, this is of advantage, as the window size and shape are not fixed. These topological clusters are seeded by so-called proto-clusters, which are cells with a high signal-to-noise ratio. Neighboring cells are added as long as a second signal-to-noise threshold is satisfied. In a third and final step, cells adjacent to the cluster are added, if they satisfy a third signal-to-noise threshold. The optimization of the three thresholds is explained in [36].

Electrons

Electrons are seeded by the sliding window algorithm detailed above with a window size of 0.075×0.125 in $\Delta\eta \times \Delta\phi$ and a E_T threshold of 2.5 GeV [37]. An overlap removal is employed keeping only the higher E_T seed in cases of two nearby overlapping seeds. Nearby tracks are then fitted using an electron hypothesis for the radiative losses due to bremsstrahlung. If the fit, extended to the 2nd layer of the electromagnetic calorimeter, is compatible with the barycenter of the cluster, the two are matched. Afterwards, an improved fit for the electron energy losses is performed, which enhances the precision on the trajectory. Converted photons are rejected by rejecting tracks, which can be matched to secondary vertices. Finally, the clusters are extended to a size of 0.075×0.175 in the barrel and 0.125×0.125 in the end-caps to calculate the electron energy. The η and ϕ direction are taken from the track, which has a better position resolution.

The final energy calibration is obtained from multivariate techniques, described in [38], which optimizes the energy resolution based on Monte Carlo simulation. Furthermore, known disagreements between recorded data and the Monte Carlo simulation are corrected for. Finally, the electrons are adjusted to the correct energy scale measured in data, using measurements of Z bosons decaying to electron-positron pairs. The full procedure is validated using J/Ψ decays to electron-positron pairs and radiative Z boson decays [38].

Muons

Muons are reconstructed primarily as tracks in the inner detector and the muon spectrometer (MS). This is done independently in both systems before being merged into a combined muon reconstruction. The reconstruction in the inner detector is detailed above. The track reconstruction in the MS starts by forming segments in each of the muon chambers, which are hit patterns in the different layers of the chambers. The segments of different layers are then fitted together to find possible track candidates. The fit is primarily seeded by segments from the middle layer, before seeds from the outer and inner layers are considered. For a track to be accepted it has to contain at least 2 matching segments (except for the overlap region where one high quality segment suffices) and the corresponding χ^2 fit has to satisfy certain quality criteria [39].

The information from ID and MS is supplemented by calorimeter information to obtain the muon candidates. Four different types of muons are distinguished. Combined muons (CB) use a combined fit in which tracks from the MS are matched to the ID, by using the hits of all sub-detectors. The matching is mostly performed outside-in, where MS hits are matched with ID hits, however, an inside-out approach is used complementarily. Segment-tagged muons (ST) are muons where a track in the ID is only matched to a single segment in the MDT or CSC chambers. This happens mostly for low p_T muons or in regions of low MS acceptance. Calorimeter tagged (CT) muons need to match an energy deposit compatible with a minimally ionizing particle to an ID track. This is mainly to recover low acceptances in less instrumented regions like the $|\eta| < 0.1$ region. In the extended acceptance region of $2.5 < |\eta| < 2.7$ extrapolated (ME) muons are defined, which match a MS track with the primary vertex where the ID is no longer available [39].

The large lever arms of the muon spectrometer allows for a very accurate muon momentum resolution from the track fitting. Regardless, known disagreements between data and Monte Carlo simulation in the momentum scale and resolution are corrected to obtain a precision at the permil and percent level, respectively. This is done using measurements of Z bosons and the J/Ψ resonance decaying to opposite charged muons, as detailed in [39].

Jets

Quarks and gluons, which are produced in the hard interaction, are not detected as free particles, but rather start to hadronize immediately (at the time and distance scale accessible with today's technology) after their production. This is due to the phenomenon called confinement detailed in section 3.1 and results in numerous hadronic particles being produced. These hadrons all originate from the same initial quark (or gluon) and are hence clustered into a jet, whose four-momentum reconstructs that of the initial quark (or gluon).

The jet clustering algorithm uses topological (topo-) clusters as input, which represent the many hadrons, produced in the hadronization process. The topological clusters are reconstructed as detailed above, following a “420”-scheme, indicating the signal-to-noise threshold utilized in the clustering algorithm (“4” meaning four standard deviations above

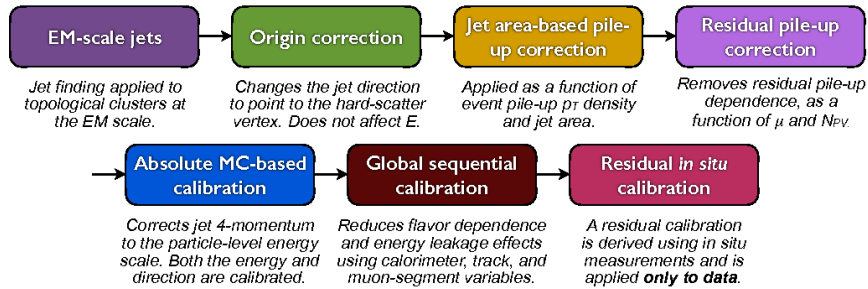


Figure 2.5: Jet Calibration applied in several stages. All corrections except for the origin correction are applied to the four-momenta of the jets [45].

the noise energy). The last value being zero means that in the last step any cell, neighboring the proto-cluster, are included into the topo-cluster. This is optimized to efficiently find low energy clusters [40]. The combined energies of all cells clustered into the topo-cluster represent the cluster energy, while the location is the three dimensional center of gravity, using the cell energies as weights and the cell center for their location [40].

The topo-clusters are then combined using the anti- k_T algorithm [41], which is an infrared and collinear safe jet-clustering algorithm. It is a modification of the sequential recombination algorithms k_T [42] and Cambridge/Aachen [43, 44], with a distance measure defined as

$$d_{ij} = \min(k_{Ti}^{-2}, k_{Tj}^{-2}) \frac{\Delta_{ij}^2}{R^2}, \quad (2.8)$$

$$d_{iB} = k_{Ti}^{-2}, \quad (2.9)$$

where $\Delta_{ij}^2 = (y_i - y_j)^2 + (\phi_i - \phi_j)^2$ and k_{Ti} , y_i and ϕ_i are the transverse momentum, the rapidity and the azimuthal angle of cluster i , respectively. The Standard radius parameter used at ATLAS is $R = 0.4$. The algorithm uses all reconstructed topo-clusters as input and iteratively adds the two clusters with the smallest distance measure, according to equation 2.8. It terminates when the closest distance is larger than d_{iB} for all remaining clusters. It is to be noted, that the algorithm works equivalently with particles as input, as only directions and momenta are required.

The jets used throughout this work use topo-clusters calibrated at the electromagnetic (EM) scale. This means that no additional calibrations, which take shower shapes and cluster moments into account, are applied to the clusters. The jet calibration is applied solely after the jets are clustered using the anti- k_T algorithm. Figure 2.5 illustrates the different corrections applied in the jet energy scale calibration and the following description thereof is based on information provided in [45].

First, an origin correction is applied, which recalculates the four-momentum of the jet to point to the primary vertex, rather than the center of the detector. During this recalculation the jet energy is kept at its previous value. This correction improves the η resolution of the jet. Two pileup corrections adjust the jet energy for contributions coming from in-time and out-of-time pileup. The first correction is based on the averaged

p_T -density in the $\eta - \phi$ plane due to pileup jets in the event, multiplied by the jet area. To derive the pileup p_T -density the topo-clusters are reclustered using the k_T algorithm, without a minimal energy requirement. The resulting jets are divided by their jet-area and the median of this distribution is taken as the pileup p_T -density. The second correction employs a residual correction as a function of μ and N_{PV} , which is derived from simulation.

Another correction referred to as the absolute MC-based calibration is applied. This correction is entirely based on simulation and corrects the jet energy scale and residual biases in the η reconstruction. This is done by matching particle-level jets to reconstructed jets and taking the ratio of their energies $E^{\text{reco}}/E^{\text{particle-level}}$ binned in $E^{\text{particle-level}}$ and η . A Gaussian fit to the core of the distribution and a numerical inversion to E^{reco} provides the necessary correction factors [46]. A residual dependence of the jet energy scale on η in the transition regions between barrel and end-cap, as well as end-cap and forward calorimeters is observed. Therefore, an additional η calibration is derived to correct the η and p_T values of the jet four momenta.

Following this procedure comes the global sequential calibration (GSC), which improves the jet energy resolution, by taking into account variables sensitive to the flavor dependent shower shapes. Gluon initiated jets have been shown to contain more, but softer particles per jet, resulting in a wide shower profile. Quark initiated jets on the other hand contain less, but harder particles, which penetrate the calorimeter deeper, with a narrower shower profile. The variables used in the GSC are thus the energy fraction in the first layer of the tile calorimeter f_{Tile0} , the energy fraction in the third electromagnetic calorimeter layer f_{LAR3} , the number of tracks associated to a jet n_{Trk} , the track width defined as the p_T weighted sum of track distances to the jet center: $W_{\text{Trk}} = \sum_i^{N_{\text{Trk}}} p_T^i \Delta R(i, \text{jet}) / \sum_i^{N_{\text{Trk}}} p_T^i$ and the number of muon segments associated to the jet n_{segments} . A correction based on the jet response is thus sequentially derived as a function of every variable and applied to the jet.

To mitigate the dependence on the Monte Carlo simulation a residual in-situ correction is applied, correcting for data-Monte Carlo simulation differences. In a first η -intercalibration, forward jets of $0.8 < |\eta| < 4.5$ are balanced in dijet events against central jets of $|\eta| < 0.8$. The well measured central jets serve as reference objects, as in dijet events the transverse momenta of the two jets should be equal. A response $R = p_T^{\text{jet}}/p_T^{\text{ref}}$ in data and the simulation is defined and the double ratio serves as a correction factor applied to data. The same principle is applied again afterwards, when jets are measured against well calibrated objects like Z bosons, photons and finally in multijet events. Again here the p_T of the two measured objects should balance at leading order and the response R is measured in data and simulation. A correction factor is again derived from the double ratio.

The many corrections applied in the jet energy calibration lead to 80 sources of uncertainties, most of which are coming from the in-situ calibrations, detailed in the last paragraph. The uncertainties are treated as uncorrelated among each other, but fully correlated in bins of p_T and η . Only the electron and photon energy scales are treated as fully correlated. The combined uncertainty is illustrated in figure 2.6 and shows a total uncertainty of between 4.5% and 1.5% at $\eta = 0$.

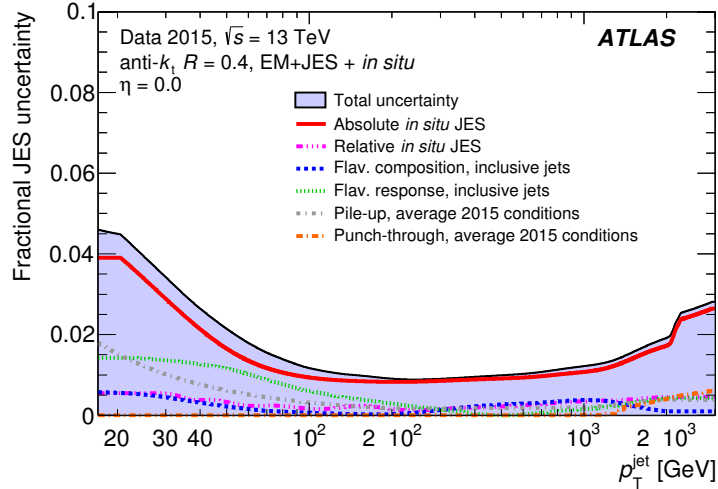


Figure 2.6: Combined jet energy scale uncertainty on calibrated jets as a function of p_T at $\eta = 0$ [45].

Taus

Taus have a mean lifetime of only $290.3 \pm 0.5 \times 10^{-15}$ s [47] and thus decay within a short distance from the interaction point. They decay into a W boson and a neutrino, where the boson can either decay into a charged lepton and another neutrino, or into hadrons. In this work only hadronically decaying tau leptons are considered, since leptonically decaying taus are identified as electrons and muons, which is sufficient for the lepton veto employed in this work. Hadronically decaying taus are seeded by jets, reconstructed by the anti- k_T algorithm with a radius parameter of 0.4. The tau-jets are required to satisfy $p_T > 10$ GeV and $|\eta| < 2.5$. The topo-clusters within these jets are calibrated using the *local hadronic cell weighting* (LCW) calibration, which aims at calibrating jets to the hadronic scale at cluster level as described in [40]. The total energy of cells within a radius of $\Delta R = 0.2$ defines the visible energy of a hadronically decaying tau $\tau_{\text{had-vis}}$.

The tau vertex (TV), which might be displaced from the primary vertex, is reconstructed using all tracks associated to the seed jet in order to improve the reconstruction efficiency and reduce the effect of pile-up. Furthermore, all tracks are selected which are within $\Delta R = 0.2$ of the seed jet direction and have a $p_T > 1$ GeV as well as several track quality criteria [48]. Taus decay primarily in so called 1-prong and 3-prong modes, meaning into one or three charged hadrons plus neutral particles. The charged track multiplicity associated to the tau candidate is therefore a prime selection criterion for hadronically decaying taus.

In addition to the LCW calibration of the topo-clusters, the tau calibration corrects for pileup contributions using an energy offset. The offset is parametrized as a function of the number of primary vertices N_{PV} and η for 1-prong and multi-prong tau candidates. Final the response $(E_{\text{LC}} - E_{\text{pileup}})/E_{\text{vis}}^{\text{true}}$ is computed for 1-prong and multi-prong candidates as function of η and $E_{\text{vis}}^{\text{true}}$ and applied as a correction.

Chapter 3

Theoretical Background

The complex and precise measurements performed at the Large Hadron Collider are driven by the success of the theoretical model describing the interactions of fundamental particles. The *Standard Model of Particle Physics* mainly developed in the 1960s when S.L. Glashow, A. Salam and S. Weinberg combined the electromagnetic and weak interactions into a single quantum field theory. However, many other scientists contributed until the Standard Model, as introduced in section 3.1, reached its current form. Many predictions of the Standard Model, including top and bottom quarks, as well as the Higgs boson, were later confirmed by experimental observations. However, there are phenomena, like neutrino oscillations, dark matter or dark energy, which can not be explained by it. Great effort in theoretical physics is made to incorporate these new phenomena into the Standard Model and several examples are given in section 3.2.

The search for dark matter has become one of the most prominent challenges in particle physics today. There is convincing experimental evidence from astrophysical observations for the existence of dark matter. With the possibilities provided by modern experimental facilities, a proof for the existence of dark matter is sought in a laboratory environment. Possible experimental strategies as well as previous collider searches are introduced in section 3.3 and 3.4. Finally, in section 3.5 some shortcomings of the current collider searches are addressed and possible improvements, as suggested in this work, are outlined.

3.1 The Standard Model of Particle Physics

The Standard Model of particle physics is a *relativistic quantum field theory*, which describes the interactions of what today are believed to be the most elementary particles of our universe. It is built upon the assumption that any interaction between these particles should be invariant under space-time translations, rotations in space, as well as the Lorentz boosts of special relativity. Requiring these symmetries, which are summarized in the Poincaré group [49], make the Standard Model a relativistic theory and results in conserved Noether currents [50], like the conservation of energy and momentum, as well as angular momentum. Furthermore, it is formulated using quantized fields, which are defined at all points in space-time. Particles appear as excitations of these fields.

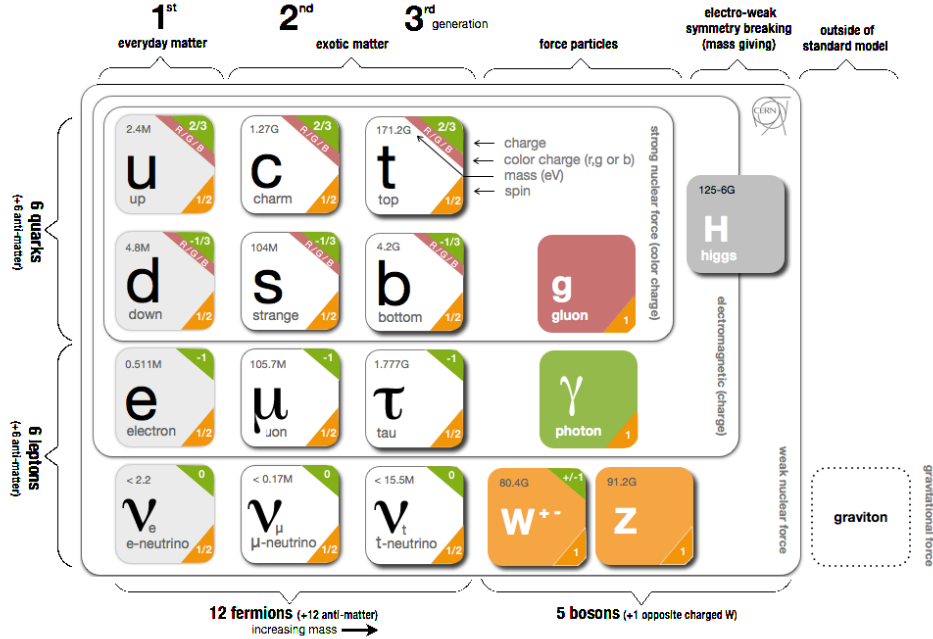


Figure 3.1: Particle content of the Standard Model, categorized by spin, color and electric charge [51].

The interactions between the particles are described by additional local gauge symmetries, which make the Standard Model a *gauge theory*. The symmetries are formulated as a $SU(3)_C \times SU(2)_L \times U(1)_Y$ gauge group, in which the generators of each of the three Lie groups give rise to transformations, under which the current of the respective group is conserved. To ensure this invariance additional fields need to be introduced. This can be understood as a gauge boson mediating a force between two charged particles, while conserving the overall charge. In the case of the $SU(3)_C$ group, this gives rise to eight gauge fields G , mediating between particles with a color charge C . The $SU(2)_L$ introduces three gauge fields W , which conserve the weak isospin T , while the $U(1)_Y$ group results in a gauge field B , conserving the weak hypercharge Y . The subscript L of the $SU(2)$ group indicates that only left-handed particles carry a non-zero weak isospin. The charges are also referred to as quantum numbers.

The particle content of the Standard Model can be categorized in several ways as depicted in figure 3.1. First, they are categorized by their spin-state: the Higgs boson is the only spin zero particle, while fermions have half-integer spin and the gauge bosons introduced above are of spin one. The fermions are further categorized into quarks and leptons, where only the former carry a color charge. Furthermore, quarks carry a fractional electric-charge of $2/3$ or $-1/3$, while leptons carry an integer electric-charge of -1 or 0 . Each of the leptons has a corresponding anti-particle, which is identical in mass, but has inverted above-mentioned charges. Finally, the fermions are ordered in three generation, where the higher-generation particles are heavier than their lower-generation partners, but

carry the same quantum numbers.

The graviton is a hypothetical particle mediating the gravitational force. However, the Standard Model does not include the gravitational force, but only describes the remaining three fundamental forces: electromagnetic, weak- and strong-nuclear force. Gravity is described by the separate theory of general relativity [52].

Electroweak Sector

Historically, the $SU(2)_L \times U(1)_Y$ gauge group represents the beginning of the Standard Model, as it first united the weak-nuclear force and the electromagnetic force into a combined gauge theory. Together with the mechanism of *spontaneous symmetry breaking*, which breaks the $SU(2)_L \times U(1)_Y$ into a $U(1)_{EM}$ gauge group, the gauge bosons W^a ($a = 1, 2, 3$) and B can be combined into the photon γ , as well as two massive, W^\pm bosons carrying an electric charge of ± 1 and a massive Z^0 boson carrying no electric charge:

$$\begin{pmatrix} \gamma \\ Z^0 \end{pmatrix} = \begin{pmatrix} \cos \theta_W & \sin \theta_W \\ -\sin \theta_W & \cos \theta_W \end{pmatrix} \begin{pmatrix} B \\ W_3 \end{pmatrix}, \quad (3.1)$$

$$W^\pm = \frac{1}{\sqrt{2}}(W_1 \mp iW_2), \quad (3.2)$$

where θ_W is defined as the weak mixing angle which is also used to parametrize the mass difference between the Z^0 boson and the W^\pm bosons:

$$M_Z = \frac{M_W}{\cos \theta_W}. \quad (3.3)$$

The $SU(2)_L \times U(1)_Y$ symmetry is broken by introducing a complex scalar field ϕ , which is a complex isospin doublet with a potential following¹

$$V = -\frac{1}{2}\mu^2(\phi^*\phi) + \frac{1}{4}\lambda^2(\phi^*\phi)^2, \quad (3.4)$$

with $\mu^2 > 0$ and $\lambda^2 > 0$. This potential has degenerate non-zero vacuum expectation values, where one has to be chosen. This spontaneously breaks the symmetry and results in a Higgs field h and three Goldstone bosons, which are absorbed into the a-priori massless gauge bosons and grants masses to the W^\pm and Z^0 bosons.

Because of the symmetry breaking, the third component of the weak isospin T_3 is combined with the weak hypercharge Y into the new conserved charge of $U(1)_{EM}$: the electromagnetic charge $Q = T_3 + Y/2$.

Extensive introductions to the topic of gauge theories, as well as the Higgs mechanism can be found in [20, 53].

¹ Notation taken from [53].

Quantum Chromodynamics

The electroweak sector was extended by the $SU(3)_C$ group, to describe the strong interaction. This extension is referred to as *quantum chromodynamics* (QCD). The coupling strength of the strong interaction is stronger than the weak- and electromagnetic forces. While the weak and electromagnetic theory can be calculated using perturbation theory, in QCD this is only true for a limited regime. This is because of a phenomenon called the *running coupling*, which means that the coupling α_S significantly changes its strength as a function of energy. The coupling strength α_S is described by the renormalization group equation (RGE) or β -function [47]:

$$\mu_R^2 \frac{d\alpha_S}{d\mu_R^2} = \beta(\alpha_S) = -(b_0\alpha_S^2 + b_1\alpha_S^3 + b_2\alpha_S^4 + \dots), \quad (3.5)$$

with μ_R a (unphysical) renormalization scale, which is usually set to the value of the energy transfer in the process of interest Q and

$$\beta_0 = 11 - \frac{33 - 2n_f}{12\pi}, \quad (3.6)$$

$$\beta_1 = \frac{153 - 19n_f}{24\pi^2}, \quad (3.7)$$

$$\beta_2 = \frac{2857 - 5033/9 \cdot n_f + 325/27 \cdot n_f^2}{128\pi^3}. \quad (3.8)$$

The RGE is obtained in the renormalization procedure of the theory and is calculated only up to a certain order in the perturbative expansion. The solution of this equation allows to extrapolate α_S from a given interaction energy Q_0^2 to a different energy Q^2 .

For QCD β_0 is larger than zero (in QED $\beta_0 = -4/3$), which leads to *asymptotic freedom*. It predicts a smaller coupling strength at larger values of Q^2 , meaning that at high energies/short distances the interaction between quarks and gluons is decreased and they are thus asymptotically free. Conversely, at low energies/large distances, the interaction strength is very large, which is often referred to as *confinement*. Confinement is the reason why free colored particles are never observed in nature, since the interactive forces become strong at large distances, forcing quarks and gluons to form bound state immediately after they are produced.

The phenomenon of forming many bound states is also referred to as *hadronization* and, since it is a low energy phenomenon, can only be described using effective theories. When two quarks move apart due to their initial momentum (like in a collision) their interactive force becomes stronger. This can be viewed as additional gluon lines connecting the two, which become more and more dense. The energy stored in these field lines increases with distance, until it becomes energetically more favorable to produce a new quark anti-quark pair from the vacuum, each of which are then bound to one of the initial quarks. In simulation, models like the Lund string model [54] or the cluster model [55] are employed to produce large quantities of hadrons from the initial quarks to form hadronic jets.

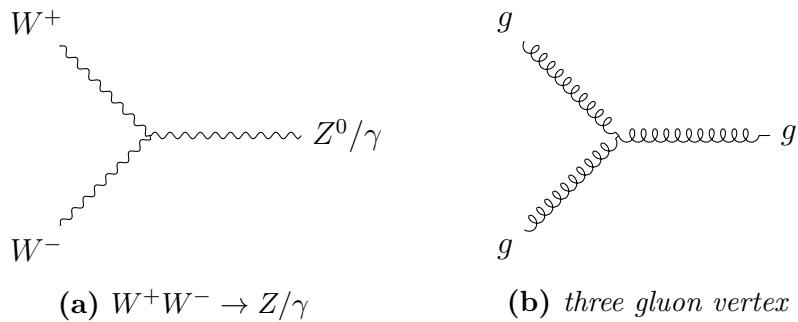


Figure 3.2: Selection of possible Feynman diagrams due to the non-abelian structure of the $SU(2)_L$ and $SU(3)_C$ gauge groups. The self interaction of the W and G bosons result in (a) vector boson fusion and (b) gluon self interaction.

Another feature of QCD is that the quarks are not eigenstates of mass and flavor at the same time. That means when calculating the cross section of a weakly interacting up quark (mass eigenstate), this requires to take into account contributions from all up-type quarks, since the flavor eigenstates, which interact weakly, are mixtures of the mass eigenstates and vice versa. The rotation matrix connecting the two is called Cabibbo-Kobayashi-Maskawa-Matrix (CKM) [56, 57].

Self-Interaction

The $SU(2)_L$ and $SU(3)_C$ groups are non-abelian, which means that the matrices, which are the generators of these groups, do not commute. As a consequence, the kinetic terms of the vector-bosons W and G include self-interaction terms. Two examples of possible three-particle interactions are illustrated in figure 3.2 showing examples for (a) vector boson fusion in the electroweak sector and (b) gluon self-interaction in QCD. The interacting particles in (a) are those obtained after spontaneous symmetry breaking, however, the self-interaction is explained by the original W bosons of the $SU(2)_L$ group which are rotations thereof. Also note that the diagrams can be rotated to illustrate different production and fusion diagrams.

Free Parameters

The Standard Model has a total of 19 free parameters (excluding neutrino masses and mixing angles), which are not predicted theoretically, but have to be determined experimentally. The parameters include nine fermion masses, three mixing angles and a CP violating phase of the CKM matrix, as well as the gauge couplings of the three gauge groups $SU(3)_C \times SU(2)_L \times U(1)_Y$. Finally, there is the CP violating angle of QCD, the Higgs vacuum expectation angle and the Higgs mass.

Factorization and Parton Density Functions

The features of QCD are especially important at the LHC as it produces proton-proton collisions. Protons are composite particles consisting of two up- and a down-quark (*valence quarks*). This means that the colliding particles at LHC are in fact the constituents of the proton. In the hard interaction a large energy transfer Q^2 is expected. This allows to calculate the cross section of this interaction using perturbative techniques. The constituents of the proton, however, are a matter of low energy-, confined quarks and gluons (partons), since vacuum fluctuations add *sea quarks* and gluons to the proton constituents. This has to be treated using effective theories. According to the *factorization theorem*, the two effects can be separated and the total cross section to produce particles X and Y can be calculated as:

$$\begin{aligned} \sigma(p_1 p_2 \rightarrow XY) &= \sum_{n=0}^{\infty} \alpha_S^n(\mu_R^2) \sum_{i,j} \int dx_1 dx_2 f_{i/h_1}(x_1, \mu_F^2) f_{j/h_2}(x_2, \mu_F^2) \\ &\times \hat{\sigma}_{ij \rightarrow XY}^n(x_1 x_2 s, \mu_R^2, \mu_F^2), \end{aligned} \quad (3.9)$$

where s is the center of mass energy, $n = 0$ is the leading order prediction, while $n \geq 1$ are the higher orders, μ_R and μ_F are the renormalization and factorization scale, respectively. The *parton density functions* $f_{i/p}(x, \mu_F^2)$ are the probability densities for a parton i to carry the momentum fraction x of the colliding proton p and $\hat{\sigma}_{ij \rightarrow XY}$ is the cross section for partons i and j to produce particles X and Y . Furthermore, s is the center-of-mass energy of the colliding protons.

The factorization scale μ_F can be understood as a cutoff scale which defines in which part of the calculation the collinear emissions of the partons are treated. At low transverse momenta they are treated via the parton density function, while at high momenta they are treated in the QCD corrections to the process cross section. The former is treated by the so-called Dokshitzer-Gribov-Lipatov-Altarelli-Parisi (DGLAP) equations [58, 59, 60, 61], which modify the existing parton density by the use of splitting functions.

3.2 Physics Beyond the Standard Model

Despite its success there are observed phenomena the Standard Model does not address. Some are more of aesthetic nature, like the hierarchy problem which addresses large differences in the particle masses and the strengths of the fundamental forces. Furthermore, the Higgs mass is fine tuned, as it receives large higher order corrections, yet it is measured at a comparably small mass [62]. The question why this is the case is not addressed by the theory itself, but arises from the observed, experimentally measured free parameters of the Standard Model. Also gravity is not included in the theory and there is a desire to develop a generalized theory, which would include all four fundamental forces. Other open questions are neutrino oscillations, which can only be explained by neutrinos having mass and thus mixing flavor and mass eigenstates. This is incorporated using the Pontecorvo-Maki-Nakagawa-Sakata-Matrix (PMNS) [63, 64], which adds three additional parameters to the Standard Model.

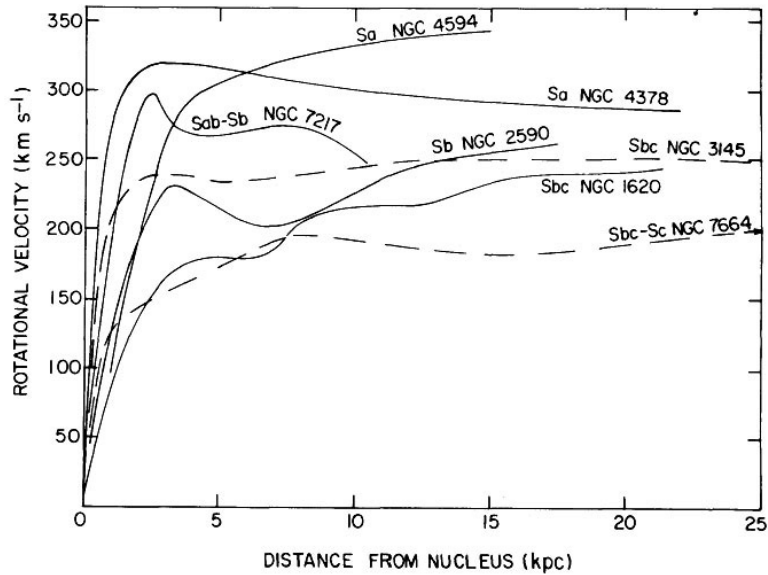


Figure 3.3: Rotation curves of seven different types of galaxies. Plotted are the rotational velocities as a function of distance from the galactic center [66].

One of the most pressing issues today is the lack of a viable dark matter candidate. Evidence of dark matter has been found in a multitude of astrophysical observations, including the rotational velocity of galaxies, gravitational lensing and the measurement of the cosmic microwave background. But also latest simulations on galaxy formation require additional (dark) matter to explain today's observation of the universe. In all above examples dark matter has only been observed via its gravitational force. As it does not appear to interact strongly via the electromagnetic force, photons can not reveal its existence (hence the name *dark* matter) and common telescopes detecting light of various wavelengths are unable to observe it. While particle dark matter is regarded as the most likely scenario, the Standard Model does not provide a candidate which fits this profile, except for the neutrinos. However, observations of cosmic structure and the low neutrino masses introduce additional constraints, which largely exclude it as a possible candidate [65].

Evidence for Dark Matter

The most prominent evidence for dark matter is the *rotational velocity of galaxies*. Since the 1930s J. Oort, F. Zwicky and others have found that the speed at which stars orbit galaxies does not correspond to the velocity profile expected from the visible matter [67, 68]. As the gravitational force decreases with distance from the center of gravity, stars orbiting a galaxy at large radii r are expected to move slower than at small radii, given the spatial distribution of the visible matter. Their speed would have to follow a distribution proportional to $\sim 1/\sqrt{r}$, such that the centrifugal force and the gravitational force balance. It was observed, however, that the velocities of stars at growing radii remains almost constant, as illustrated in figure 3.3 for several galaxies [66].

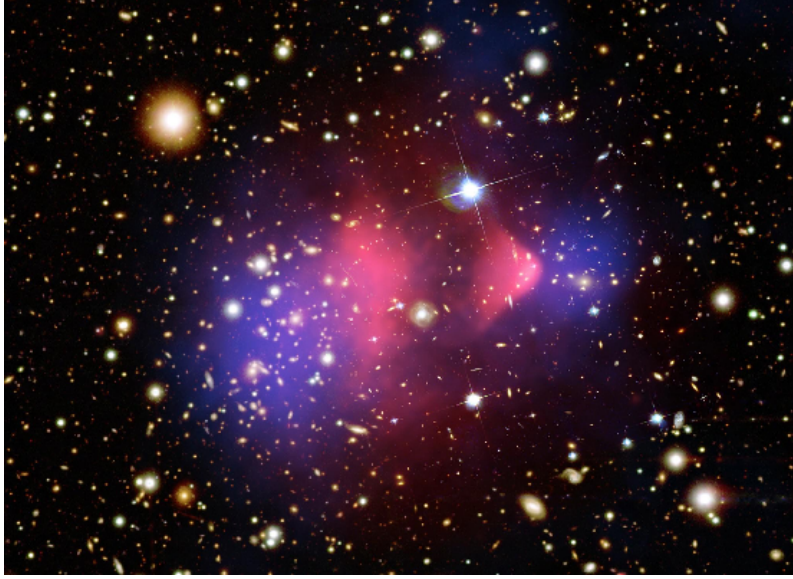


Figure 3.4: *Image of the bullet cluster 1E 0657-558. (Figure credit: X-ray: NASA/CXC/CfA/ M.Markevitch et al.; Lensing Map: NASA/STScI;ESO WFI; Magellan/U.Arizona/ D.Clowe et al. Optical image:NASA/STScI;Magellan/U.Arizona/D.Clowe et al.)*

This behavior can be explained by additional gravitating matter, which is invisible to common telescopes. Another explanation would be to alter the theories of gravity, so to either modify or replace Newtonian gravity and general relativity. However, so-called MOND theories [69, 70, 71, 72, 73] have shown more difficulties at explaining the wealth of measured observations and are not compatible with the observations of the so-called bullet cluster [74].

The term bullet cluster usually refers to an observed collision of two galaxies called 1E 0657-558, as depicted in figure 3.4. Two clusters have passed through each other and the gas, which is expected to constitute most of the gravitating mass, has interacted and separated from the rest of the galaxy, forming its own field of visible matter in the collision region. The stars of the galaxies have moved away from this region again, such that a smaller gravitational lensing effect would be expected away from the collision center. The observation of gravitational lensing due to the bending of space-time is predicted by general relativity around massive objects [75, 76] and thus allows to infer the amount of gravitating matter. Instead of the expected lensing effect, a larger gravitational lensing signal is observed in the region away from the collision center, indicating that weakly interacting dark matter could be co-moving with the galactic centers. Since this dark matter only interacted weakly with the other matter, the bullet cluster thus allows to estimate the interaction cross section of dark matter [74, 77].

Furthermore, the measurement of the cosmic microwave background (CMB) allows to fit the parameters of the Lambda-CDM model to great precision [1]. The latter is often referred to as the Standard Model of cosmology and predicts *cold dark matter* (i.e. non-

relativistic dark matter particles which could be realized for example by *weakly interacting massive particles* (WIMPs)) together with a cosmological constant Λ , which is associated to dark energy. It predicts the evolution of the universe since the big bang and according to the CMB fit, only about 5% of the total energy in the universe is baryonic (visible) matter. About 27% on the other hand is predicted to be dark matter and about 68% is associated to dark energy.

The presented evidence leads to many experimental and theoretical efforts to detect dark matter in a laboratory environment and to include dark matter into particle physics theories. Some of the latter efforts are presented below. The presented models are most relevant to this work, since limits on these models are set in section 7, however, many more models exist, like supersymmetry or effective-field-theories [78, 79].

Simplified S-Channel Mediator Model

Simplified models lie somewhere in between a full new physics model (like the Minimal Supersymmetric Standard Model (MSSM) [80]), which usual adds a whole wealth of new particles in order to be fully self-consistent, and an effective theory, which combines complex interactions into single operators. In a simplified model usually the particle of interest is added to the Standard Model, together with a mediator which connects the two. Additional particles are assumed to play a negligible role in the searches the model is designed for and the model typically adds only a few parameters which can be constrained by measurements.

To construct a simplified model, an additional symmetry, for example in the form of a U(1) group, is added to the Standard Model and is spontaneously broken. Like for the Standard Model this generates an additional massive boson. Furthermore, additional particles, like in this case fermionic dark matter, are added. The Lagrangian is thus extended by mass and kinetic terms, as well as interaction terms for the mediator boson and the dark matter candidate. In this work the mediator is assumed to carry a spin of one, however, similar models can be constructed for scalar mediators. Additionally, it is assumed to couple to both the Standard Model particles as well as the dark matter particle:

$$\mathcal{L}_{\text{BSM}} \supset A_\mu \bar{\chi} \gamma^\mu (g_\chi^V - g_\chi^A \gamma^5) \chi + \sum_{f=q,l,\nu} A_\mu \bar{f} \gamma^\mu (g_f^V - g_f^A \gamma^5) f, \quad (3.10)$$

where q, l, ν are the Standard Model fermions, A_μ is the new massive boson, χ is the fermionic dark matter and $g_\chi^{A/V}, g_f^{A/V}$ are the (axial-)vector couplings of the new boson to dark matter and fermions, respectively [81].

The total decay width of the mediator is described by

$$\Gamma_A = \frac{m_A}{12\pi} \sum_{i=f,\chi} N_C^i \left(1 - \frac{4m_i^2}{m_A^2}\right)^{1/2} \left[(g_i^V)^2 + (g_i^A)^2 + \frac{m_i^2}{m_A^2} (2(g_i^V)^2 - 4(g_i^A)^2) \right], \quad (3.11)$$

where $N_C^i = 1$ for leptons and dark matter and $N_C^i = 3$ for quarks and i sums over all fermions above the production threshold [81]. Assuming identical couplings $g_i^{V/A}$, equation

3.11 shows a reduced decay width for purely axial-vector mediator models compared to purely vector mediator models, when $m_i \approx m_A$. When constraining these models typically stronger limits can thus be derived in vector mediator models in the $m_A - m_\chi$ mass plane near the threshold where $m_A = 2m_\chi$ [82]. This is especially true when m_A is small, since Standard Model particles then contribute significantly to the last term in the total decay width as well.

In this work a pure axial-vector mediator is considered, coupling equally to up-type and down-type quarks. To ensure comparability with other searches, the ATLAS CMS Dark Matter Forum recommends to set the coupling $g_\chi^A = 1$ and the coupling $g_q^A = 0.25$ [83]. The remaining parameters are the dark matter mass m_χ and the mediator mass m_A , which span a mass plane in which limits are derived. Fixing two of the four parameters is convention to allow for well readable and comparable plots, as well as to limit the computational effort to set reasonable limits on any such models.

Invisible Higgs Decays

The mediator coupling the dark sector to the Standard Model might be the Standard Model Higgs boson. Since it couples to the Standard Model particles, with a strength depending on their mass, it might as well couple to dark matter in a similar way. In that case the Higgs boson would possess an additional invisible decay channel. In the Standard Model the only invisible Higgs decay is via two Z bosons, which then decay to two neutrinos, each ($H \rightarrow ZZ \rightarrow \nu\bar{\nu}\nu\bar{\nu}$). The branching fraction for this process is $\sim 0.1\%$, which no current search is sensitive to [84, 85]. Any detection of an invisible Higgs would thus point to new physics.

Using the Higgs boson as a mediator to the dark sector only requires to add a mass term for the dark matter particle S , as well as a coupling to the Higgs boson [86]. In this example the dark matter particle is assumed to be a scalar particle S :

$$\mathcal{L}_{\text{BSM}} = \frac{1}{2}\mu_S^2 S^2 + \frac{1}{2}\lambda_{h,S} S^2 |H|^2, \quad (3.12)$$

where S is the scalar dark matter particle and H the Standard Model Higgs boson. Such a model predicts a branching fraction of

$$\Gamma_{\text{inv}} = \frac{\lambda_{h,S}^2 v_0^2}{32\pi m_h} (1 - 4m_S^2/m_h^2)^{1/2}, \quad (3.13)$$

additional to the invisible branching fraction of the Higgs boson predicted by the Standard Model. There are many other models predicting additional contributions to the invisible branching fraction of the Higgs [87, 88, 89, 90, 91], thus, setting upper limits on this invisible branching fraction further narrows down the size of possible additional contributions.

3.3 The Search for Dark Matter

In addition to the numerous astrophysical observations, particle dark matter is sought to be measured in a laboratory environment. Not only would this prove its existence in a complementary way, it would also allow to inspect dark matter in a controlled environment, which allows to understand its properties. Generally, approaches to search for dark matter are classified in three categories: indirect, direct and collider searches.

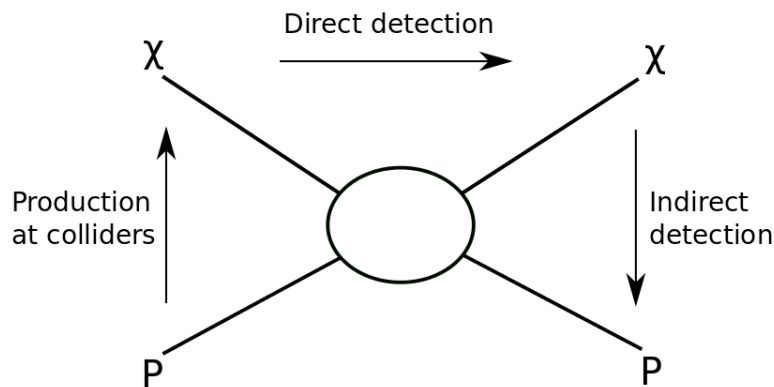


Figure 3.5: Feynman diagram with an unknown interaction between dark matter and the Standard Model. Depending on the direction of the diagram it illustrates the three different detection strategies: collider searches, direct- and indirect detection [92].

Indirect searches rely on the assumption, that dark matter particles annihilate with each other, thereby producing Standard Model particles. This is assumed to occur in areas of the universe where a large abundance of dark matter is expected. Searches are thus performed with satellites to avoid the earth's atmosphere or with larger ground-based telescopes. In the annihilation it is assumed that photons and other cosmic rays are produced, which can be detected by the experiments. Furthermore, ground based experimental facilities search for enhanced neutrino fluxes, which may also be produced in dark matter annihilation [93].

In direct searches, dark matter is expected to scatter off Standard Model particles, thus transferring some of its energy onto the Standard Model particle. The nucleus, the dark matter interacted with recoils and the recoil energy can be measured. Different experiments have different approaches and depending on the active material the recoil energy is measured via ionization, heat, light, or the combinations thereof. The experimental facilities are usually deep underground to provide proper shielding from other cosmic particles entering the detector. These backgrounds, however, as well as the remaining radioactive material in the detector, must be well understood in order to distinguish additional contributions from dark matter interactions from the expected signals [94].

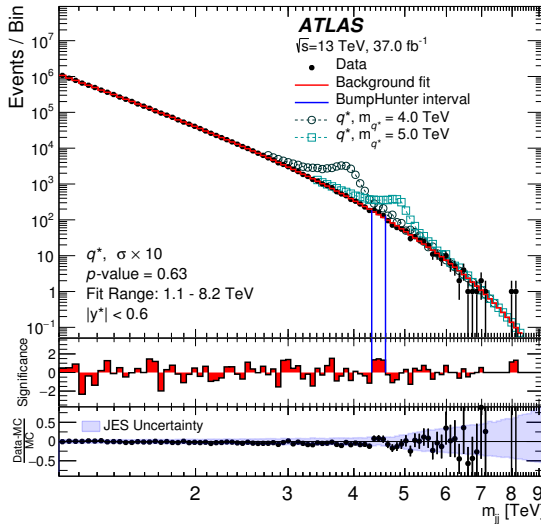
At collider searches Standard Model particles are accelerated and either fired onto a fixed target, or two beams in opposite directions are collided. In both cases it is assumed that dark matter particles can be produced in the collision. Searching for new particles

means that many particle collisions need to be recorded, since most of the collisions will produce known Standard Model particles. Dark matter particles would manifest themselves as additional contributions to the expected observations. At colliders the initial state of the collision is well studied, allowing for a very accurate estimation of the expected Standard Model contributions [95].

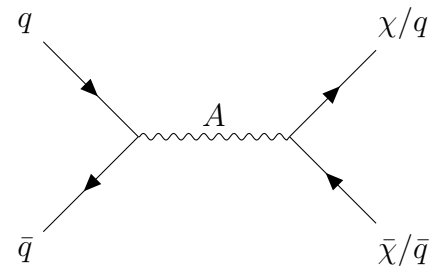
All three approaches, illustrated in figure 3.5, have their strengths and weaknesses, making their combinations a powerful tool to further narrow down the properties of dark matter. This work focuses on collider searches performed with the ATLAS detector at the LHC, which is particularly powerful, if the dark matter mediator (and the dark matter particle) is within the energy reach of the collider. In this case the mediator can be produced on-shell, meaning that it does not only contribute via virtual loop corrections, and the production cross section for dark matter particles increases significantly.

3.4 Previous Collider Searches

Many searches for dark matter have been performed at colliders, however, so far dark matter has evaded detection. Generally, there are two main strategies at ATLAS how to search for dark matter [97]. The first one assumes a mediator coupling to dark matter as well as to the Standard Model. This mediator can be detected if instead of decaying to dark matter particles, it decays back to two quarks or gluons as shown in figure 3.6b. This way it would manifest itself as a *bump* in the otherwise smoothly falling dijet mass



(a) bump hunt in m_{jj} spectrum



(b) Feynman diagram leading to dijet resonance

Figure 3.6: (a) Dijet search looking for a resonant signal in the invariant mass m_{jj} distribution of the dijet final state [96]. (b) A new mediator A coupling to Standard Model quarks (and/or gluons) as well as the dark matter particle χ could yield such a resonance.

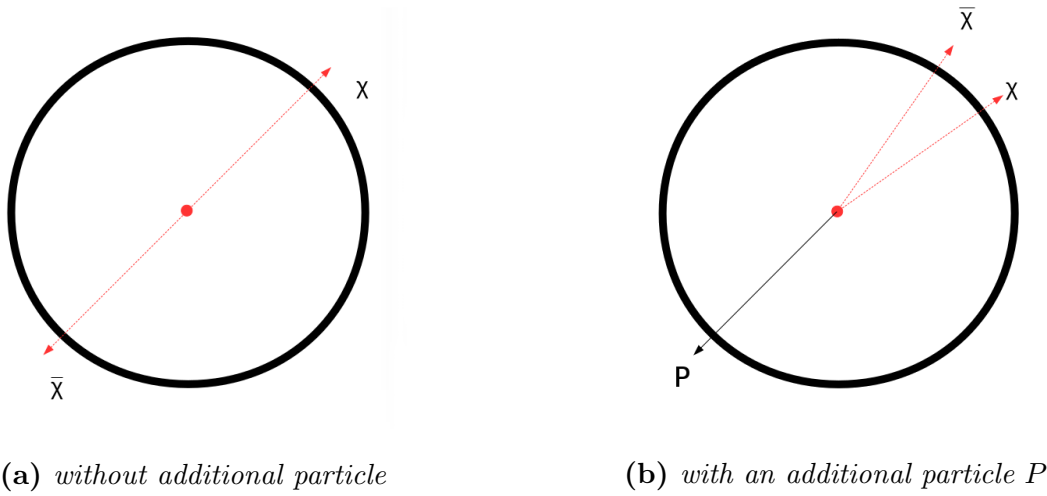


Figure 3.7: Schematic view of the transverse plane of the ATLAS detector. In (a) dark matter is produced without any additional particle. The momenta of the dark matter particles balance, leaving no detectable trace in the detector. (b) shows dark matter production in association with a Standard Model particle, which balances the dark matter transverse momenta. This results in missing transverse energy E_T^{miss} .

spectrum (figure 3.6a). This kind of signature has been searched for in the past, with the most recent results coming from ATLAS [96, 98] and CMS [99].

The second approach is the direct production of dark matter in association with another Standard Model particle. This is commonly referred to as a $MET^2 + X$ search [2, 3]. The dark matter candidate is not expected to interact with the detector material, as it only interacts weakly with baryonic matter. Therefore, it does not leave a trace in the detector which could be used to select such an event (see figure 3.7a). This is true unless there is a Standard Model particle in the final state, which the dark matter can recoil against (see figure 3.7b). In this case there is an energy imbalance in the otherwise balanced transverse plane of the detector, as the Standard Model particle deposits its energy on one side of the detector, whereas the dark matter still evades detection. This imbalance is called missing transverse energy and can be selected. The additional Standard Model particle is usually produced via initial state radiation (ISR), but depending on the model, it can also be produced via mixing with the mediator coupling to the dark matter [97]. The production of the Standard Model particle via ISR favors quarks and gluons, due to the larger coupling strength of α_s over the electroweak couplings.

Choosing the Standard Model particle for a possible search signature trades high statistics for lower backgrounds. The leptonic decays of the electroweak vector bosons allow for a high background suppression, since leptons are easily identified and thus provide a very clean event selection. However, the branching ratio for an initial state radiation gluon is much higher than for an electroweak vector boson which is why for many models this channel remains the signal of choice.

² Other common abbreviations are Missing E_T , or E_T^{miss} .

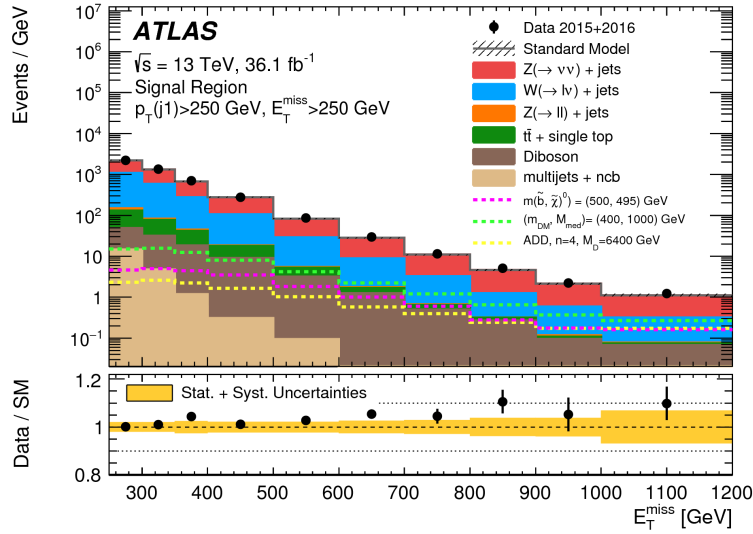


Figure 3.8: Monojet search signal region with new physics models [82]. Show are the measured data compared to the Standard Model prediction. The size of the Standard Model contributions is constrained via a global fit with several control regions. Possible beyond the Standard Model contributions are added as dashed lines. The lower panel shows the ratio between data and Monte Carlo simulation including statistical and systematic uncertainties.

The Classical MET + Jet Search

Many new physics models predict final states with large missing E_T and jets, which is why the conventional search approach, the so called *monojet search*, is introduced here. It is based on the ATLAS results published in [82].

The event selection exploits the final state topology as introduced above, which is a single high p_T leading jet (> 150 GeV) and no leptons (e or μ) in the final state. Furthermore, the momentum imbalance in the transverse plane is exploited by requiring missing transverse energy of at least 250 GeV. The latter also drives the selection at trigger level as at HLT level at least 90 GeV of E_T^{miss} is required. This trigger is fully efficient in the signal region such that no events are lost due to the HLT E_T^{miss} resolution.

At tree level only a single Standard Model process produces the same signature, which is the decay of a Z boson to two neutrinos ($Z \rightarrow \nu\bar{\nu}$). However, the limited acceptance of the detector, as well as inefficiencies in the reconstruction of particles lead to several other backgrounds that need to be accounted for. These are mainly W bosons decaying leptonically, as well as top-antitop and single top production and di-boson production. All these backgrounds can decay leptonically via a W boson, which produces missing transverse energy and, if the lepton is not reconstructed, are therefore reconstructed in the signal region. Lastly multijet events with mismeasured jets can lead to a transverse momentum imbalances large enough to be mistaken as a signal event. This happens very rarely, however, the high cross section of multijet events at the LHC causes it to be a considerable background.

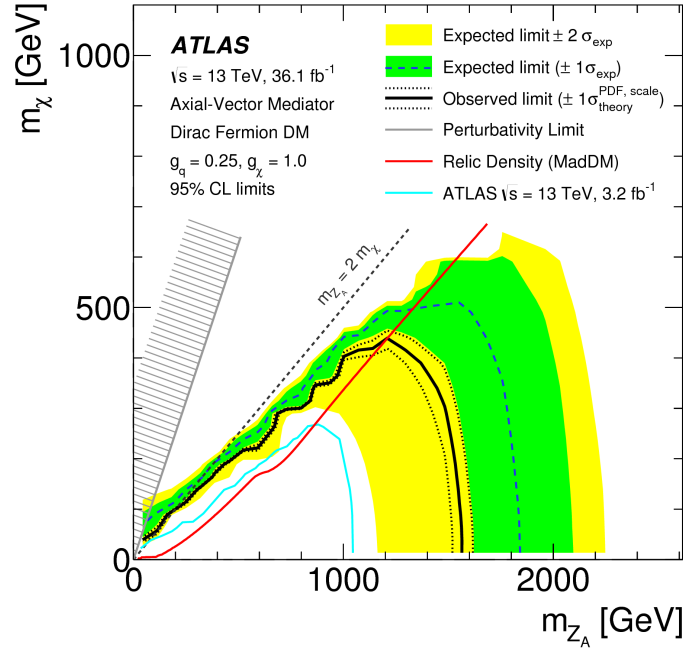


Figure 3.9: Monojet search limit plot for a simplified model with an axial-vector mediator [82]. Shown are expected and observed exclusion limits at 95% CL in the m_{χ} - m_{Z_A} plane. The parameters $g_q = 0.25$ and $g_{\chi} = 1.0$ are fixed. Additional limits are shown excluding the parameter space producing a relic density abundance inconsistent with the WMAP measurements [100] and where perturbative unitarity is violated ($m_{\chi} > \sqrt{\pi/2}m_{Z_A}$ [101]).

Typically the backgrounds in the signal region are estimated via control regions in which their contribution is most significant and their Standard Model cross section can be constrained. The result is then extrapolated to the signal region via a transfer function or by simultaneously fitting the different regions.

The measured data is compared to the predicted Standard Model contribution in the signal region, as illustrated in figure 3.8. Deviations from this comparison hint to physics beyond the Standard Model. Additional models are generated (dashed lines) as possible additions to the measured spectrum.

If no significant deviations are found, models which were expected to give a sizable contribution can be excluded. This is usually done by selecting a few models of interest and scanning their parameter space. In the example of a simplified model with an axial-vector mediator as shown in figure 3.9, the model has 4 parameters, where two of them are fixed and the other two are scanned. This means that a grid of combinations of in this case m_{χ} and m_{Z_A} has to be produced and for every point in this grid signal events have to be simulated, including the detector simulation. Afterwards, the simulated models are excluded at a calculated confidence level (CL). With the extrapolation between the generated grid points contour lines of an exclusion at usually 95% CL are drawn (see figure 3.9).

3.5 Limitations in Current Interpretations

As shown in the above example of a MET + jet search, in the absence of new physics the results obtained in an analysis are used to constrain models which have predicted a signal in the respective phase space. In this case only a very limited amount of models can be constrained. This is because in the conventional approach of a search, the respective models are generated and have to be propagated through a detector simulation in order to compare them to the recorded data. Also the generated grid points in the scanned parameter space have to be optimized in order to reduce computing time. The limited time and resources lead to only a selection of models being constrained.

After the work is published everyone could use the results to constrain additional models. However, the detailed detector simulation used in such an analysis within the ATLAS collaboration is not publicly available. Therefore, new models need to be simulated with an inferior parametrized detector simulation. The results are therefore not as accurate, which results in larger uncertainties and less stringent limits.

A new search approach was developed and published in 2016 in which the data was fully corrected for detector effects [4]. This greatly simplifies constraining an arbitrary number of new models even after the data has been published and therefore increases the longevity of the search results. This will become especially important, when the amount of additional data delivered by the LHC will not increase by orders of magnitude anymore and repeating previous analyses to make use of the additional data becomes less and less practicable.

Correcting the data for detector effects, also referred to as unfolding, eliminates the need for a detector simulation in subsequent limit settings and therefore the need for parametrized detector simulations. The size of the correction depends on the process which is unfolded, since reconstruction efficiencies and resolutions depend of the event topology. In Standard Model measurements, where the contributing processes are well known and simulated, unfolding has been used extensively in the past. In searches on the other hand new difficulties are introduced which have to be addressed.

By definition in a search it is unknown what new physics might be in the data. Therefore, the detector effects on the new physics contributions can not be included when determining the detector corrections. Only the Standard Model contributions can be considered. It has to be ensured, usually by testing various probable models, that new physics contributions do not significantly alter the detector response. This was performed in the first iteration of the detector-corrected search presented in [4] and the first unfolded search results were published in 2016.

A further improvement to this approach is to use an unfolding technique which is able to incorporate new physics into its detector response without having to simulate it. Therefore it would be less dependent on the Monte Carlo simulations used to define the response initially. A technique which is capable of doing this is presented on the following chapter and applying this technique to a dark matter search is the focus of this work.

Chapter 4

Unfolding in Searches

The search presented in this work corrects its measured observables for detector effects and this chapter introduces the concept of *unfolding* in this context (section 4.1). Additional challenges, which arise when unfolding searches for physics beyond the Standard Model, are highlighted and a method called *Iterative Dynamically Stabilized* (IDS) unfolding is introduced in section 4.2, which was developed to address these challenges.

The data analyzed in this work is recorded using the ATLAS detector and reconstruction algorithms as introduced in section 2.3 interpret the signals to infer particle types and their four-momenta in each collision. The particles are therefore measured at the so-called *reconstruction-level*. The theoretical predictions on the other hand are formulated in a quantum field theory, as introduced in sections 3.1 and 3.2. The particles in the final state are therefore always calculated at the so-called *parton-level*. When parton showering and hadronization models are added, the predictions can be extended to the so-called *particle-level*. The parton-level can be regarded as the theoretical product of a collision, while the particle-level is the particle content of the final state accessible at the timescales and distances of current detector technology.

The reconstruction-level is therefore by construction different from the theory prediction it is compared to, as the detector introduces inefficiencies as well as acceptance effects. Inefficiencies mean that some particles may not be reconstructed, as they may not have left a clear signature for the reconstruction algorithms to interpret. Acceptance effects are due to the fact that the detector is not fully instrumented in 4π solid angle. One gap being the beam-line which has to enter and leave the detector, another being the tracking system which is only present at pseudorapidities $|\eta| \leq 2.4$. Furthermore, the energy resolution of the detector is finite, meaning that a particle might be reconstructed at an energy slightly different from its particle-level energy.

In order to assess the validity of a theory it has to be compared to the measurement at the same level and there are two ways to approach this:

1. Run a detector simulation on the theory predictions and compare to the measurement at reconstruction-level.
2. Correct the measurement for detector effects and compare to theory at particle-level.

The first approach is straight forward within a given collaboration, as they have a very precise detector simulation of their experiment at hand. For ATLAS the simulation framework is based on the Monte Carlo based GEANT4 toolkit [102]. It allows for very precise estimates of the Standard Model expectations and has been validated extensively as a framework [103, 104] and the modeling of various Standard Model processes has been investigated [105, 106, 107]. In searches the theory model of interest is also propagated through the full detector simulation which allows to set limits at the reconstruction-level, as introduced in section 3.4.

However, after a search is published only the reconstruction-level distributions are available to the public and reinterpreting those can be difficult. An analysis outside of the ATLAS collaboration has to rely on parametrized detectors simulations like DELPHES [108] to account for the detector effects. These tools will provide less precise estimates resulting in additional uncertainties and hence less stringent limits on a given theory.

The alternative to this procedure is to use the second approach where the measurement is corrected for detector effects using the most precise detector simulation available. This technique is referred to as *unfolding*. It increases the longevity of the physics results and makes it more useful to people outside the respective collaborations.

4.1 Mathematical Formulation

Mathematically, the detector can be regarded as an operation D applied to an event x which yields a measured event y

$$y = Dx. \quad (4.1)$$

This operation D is stochastic and on an event by event basis one can not predict its outcome. It is only possible to make statistical predictions. For an observable at particle-level one can thus obtain a probability density $\rho(r, t)$ for the observable at reconstruction-level. This allows to predict the probability of the reconstructed value r to lie in the interval $[a, b]$ for a given particle-level value t

$$P(r \in [a, b]|t) = \int_a^b \rho(r, t) dr. \quad (4.2)$$

In practice one uses binned histograms at particle-level and reconstruction-level such that the observables always fall into a particular bin t_j and r_i , respectively. This translates into the conditional probability $P(r_i|t_j)$, which is obtained from Monte Carlo simulations where the event information before and after detector simulation is known. One can thus fill the migration matrix A with its elements A_{ij} counting the events in the i^{th} reconstruction-level bin and the j^{th} particle-level bin such that

$$P_{ij} := P(r_i|t_j) = \frac{A_{ij}}{\sum_{k=0}^{N_r} A_{kj}}, \quad (4.3)$$

where N_r is the number of bins at reconstruction-level and $\sum_{k=0}^{N_r} A_{kj}$ is the total number of reconstructed events corresponding to particle-level bin j . In this thesis, the observables at particle-level and reconstruction-level are one-dimensional with identical binning $N_t = N_r$, however, it is straight forward to generalize this to multidimensional observables of different binning [109].

Equation 4.3 can be understood as the *folding matrix* as it allows to calculate the expected number of reconstructed events ($n(r_i)$) in bin i from a corresponding particle-level distribution

$$n(r_i) = \sum_{k=0}^{N_t} P(r_i|t_k)n(t_k), \quad (4.4)$$

where $n(t_k)$ is the number of events at particle-level in bin k .

Using the inverse $P_{ij}^{-1} = \tilde{P}_{ij}$ of P_{ij} as the unfolding matrix can lead to large and unphysical fluctuations in the unfolded distribution when small fluctuations in the measured distribution are present. Also if A is singular, the inverse simply does not exist. Details and how to avoid this by the use of regularized unfolding techniques are described in [110]. In this work the inverse of the folding matrix is therefore obtained using Bayes theorem [111]

$$\tilde{P}_{ij} := P(t_j|r_i) = \frac{P(r_i|t_j)P(t_j)}{P(r_i)} = \frac{P(r_i|t_j)P(t_j)}{\sum_{k=0}^{N_t} P(r_i|t_k)P(t_k)}, \quad (4.5)$$

where the last equality uses equation 4.4 normalized to the total number of events. The inverse now relies entirely on the folding matrix and the *prior* knowledge $P(t_j)$ about the probability distribution at particle-level. This prior knowledge also comes from Monte Carlo simulation and reduces equation (4.5) to

$$\tilde{P}_{ij} := P(t_j|r_i) = \frac{A_{ij}}{\sum_{k=0}^{N_t} A_{ik}}, \quad (4.6)$$

which is expected from equation 4.3 when normalizing the event count within one reconstruction-level bin.

So far the unfolding matrix considers events which are generated in one bin of one distribution and reconstructed in another bin of another distribution¹. In reality this is not always the case as the observable of interest is always constructed in a very specific phase space, tailored to the analysis at hand. This means that certain selections and cuts are applied before the event is classified into its respective bin. These cuts, as well as limited detector acceptance and efficiency, can cause an event to be rejected entirely and three cases need to be distinguished.

¹ Technically the distributions can be of entirely different observables at particle-level and reconstruction-level, as a relation between arbitrary observables and bins can be constructed in a Monte Carlo simulation. However, in strongly differing definitions one would rely entirely on the simulation to describe and extrapolate the physics sufficiently, which is better to be avoided.

1. The event passes reconstruction-level selection, but does not pass particle-level selection.
2. The event passes both reconstruction-level and particle-level selection.
3. The event does not pass reconstruction-level selection, but passes particle-level selection.

The first case is considered a *Fake*, as according to the particle-level selection it was falsely reconstructed. The second case refers to the events that fill the migration matrix which maps the bins at particle-level to the bins at reconstruction-level. In the case of identical observable and binning this matrix will be the unity matrix, unless there are *resolution* effects it accounts for. The last event type is called a *Miss* as according to the particle-level selection it should have been reconstructed but was not. Fakes, misses and migrations together represent the detector *response* and account for all possible corrections due to the detector.

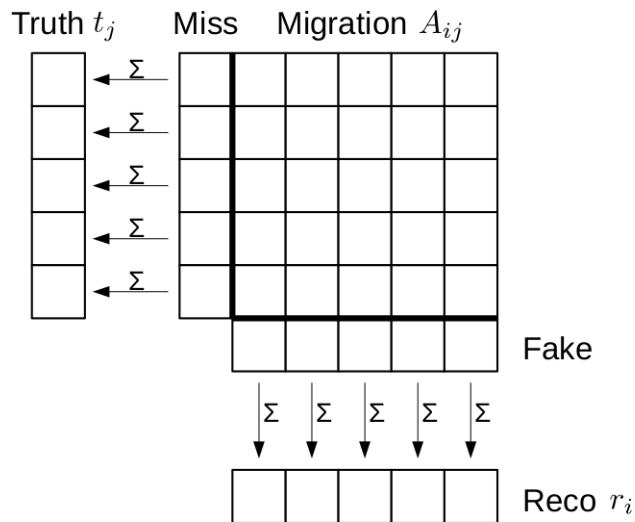


Figure 4.1: Schematic view of reconstruction-level and particle-level events. Events that are present both at reconstruction-level and particle-level fill the migration matrix A_{ij} . Events that are only reconstructed are considered Fake. Events that are only present at particle-level are considered a Miss. The projection of the migration matrix on the particle-level (reconstruction-level) axis added with the missed (fake) events sum to the total number of particle-level t_j (reconstruction-level r_i) events [112].

A visual representation of how fakes and misses can be added as an additional bin to the migration matrix is shown in figure 4.1. It is straight forward to unfold a Monte Carlo generated reconstruction-level distribution by applying this $(N_r + 1 \times N_t + 1)$ -matrix to it, as in Monte Carlo simulation one can easily extend the distribution by a bin for missed events. In recorded data this is not possible and the correction for missed events is done

via an efficiency correction instead, while the migrations matrix has dimension $N_r \times N_t + 1$ only:

$$S_j = \frac{\sum_{k=0}^{N_r} A_{kj}}{n(t_j)}. \quad (4.7)$$

This factor is commonly referred to as *stability correction*.

Likewise, the correction for fake events, also named *purity correction*, can be done via an acceptance

$$P_i = \frac{\sum_{k=0}^{N_t} A_{ik}}{n(r_i)} \quad (4.8)$$

leaving an $(N_r \times N_t)$ -matrix for the migrations.

In the simplest case referred to as *bin-by-bin unfolding* it is assumed that the migrations due to resolution effects are small and can be neglected. This reduces the folding matrix P_{ij} to an identity-matrix, leaving only the stability and purity correction. Since these two corrections are bin-wise correction factors, the bin-by-bin unfolding can be understood as a diagonal matrix with

$$\tilde{P}_{ij} = \begin{cases} \frac{n(t_j)}{n(r_i)} & i = j \\ 0 & i \neq j \end{cases}. \quad (4.9)$$

4.2 Iterative Dynamically Stabilized Unfolding

Known Standard Model processes can be unfolded following the above prescription, when good detector simulation is available. In this case the detector effects can be modeled in simulations for the contributing process and the derived corrections can be applied directly to the measured distribution. In searches this is not the case as the contributing processes are by definition unknown. The detector response may therefore be modified by the presence of new physics and this has to be disproven before unfolding a search is acceptable. The following method allows to unfold a search without the need of proving this, since it incorporates new physics contributions into its particle-level model if new structures are observed at reconstruction-level.

The unfolding method used in this analysis is called Iterative Dynamically Stabilized (IDS) unfolding [113, 114]. It is structured in three steps. In the first step a bin-wise purity correction as described in equation 4.8 is applied, which corrects for events from outside the fiducial phase space² that are reconstructed in the signal region³. This is followed by an iterative migration step, correcting for resolution effects, which is detailed later. Finally,

² The fiducial phase space is a series of geometric and kinematic cuts at particle-level, defined to increase the signal sensitivity.

³ The signal region is the implementation of the fiducial phase space at reconstruction-level and is therefore based on reconstructed objects with all measurement errors.

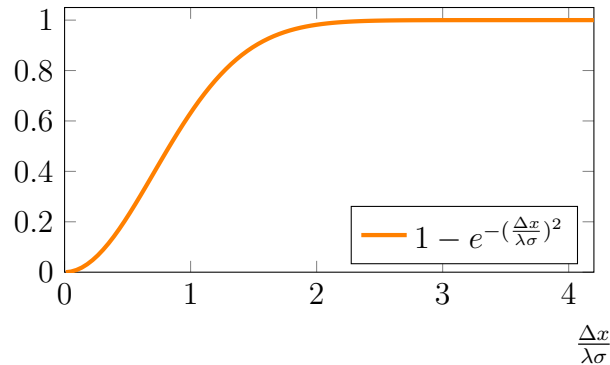


Figure 4.2: The regularization function $f(\Delta x, \lambda, \sigma) = 1 - e^{-(\frac{\Delta x}{\lambda\sigma})^2}$ used in the IDS algorithm.

the stability correction described in equation 4.7 is applied to account for events that are inside the fiducial phase space, but are not reconstructed.

While the purity and stability corrections are straight forward to apply, the IDS method aims at improving the resolution correction in several ways:

1. Improving the normalization of the Monte Carlo simulation with respect to data
2. Taking into account large uncertainties due to background subtraction
3. Recovering new structures in data, which are not present in the Monte Carlo simulation modeling

A central component of the algorithm is a regularization function, which is used in several places. It provides a measure for the significance of a deviation and translates this into a number between 0 and 1. The function needs to be smooth and monotonous and $f(\Delta x, \lambda, \sigma) = 1 - e^{-(\frac{\Delta x}{\lambda\sigma})^2}$ was chosen in this work, which is depicted in figure 4.2. Δx is the absolute size of the deviation in a bin for example between Monte Carlo simulation and measured data. σ is the uncertainty on this deviation and λ serves as a regularization parameter. The choice of this parameter can vary for the different steps where the regularization function is applied. This allows to change what is considered a statistical fluctuation or a real deviation.

Normalizing the Monte Carlo simulation with respect to data corrects the Monte Carlo simulation for potential normalization biases. This is desired when only differences between data and reconstruction-level simulation (i.e. known and unknown structures) are unfolded (see below), as it allows to specifically treat unknown structures as done by the IDS algorithm. At the reconstruction-level this can be done by taking the ratio of the total number of events in data and in the Monte Carlo simulation as a normalization factor. Likewise, the IDS algorithm needs to normalize the Monte Carlo simulation particle-level distributions to the unfolded spectrum, which can be done with the ratio of the sum over

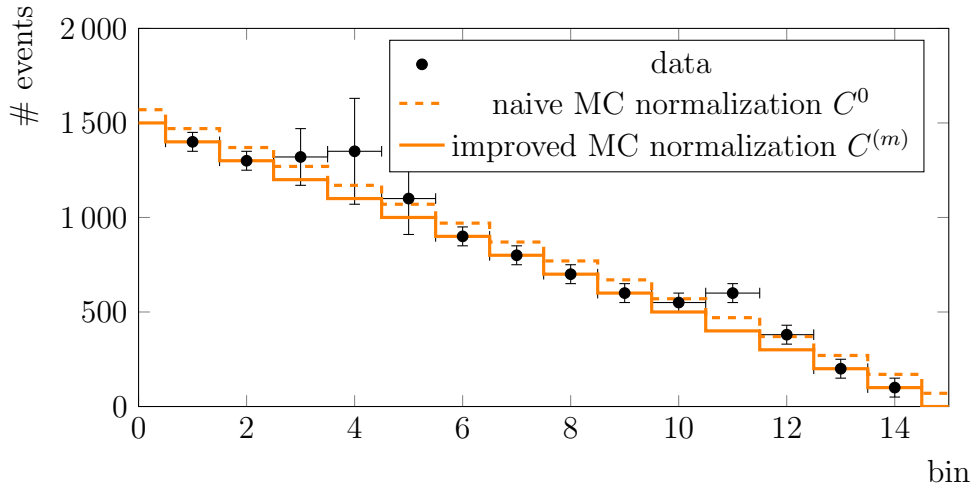


Figure 4.3: Normalization procedure in the IDS algorithm. The resonant structure in data around bin 11, as well as the fluctuations around bin 4 result in a wrong normalization of the Monte Carlo simulation. The normalization is iteratively improved by excluding insignificant excesses as well as not-modeled structures.

these two spectra

$$C^{(0)} = \frac{\sum_{N_r} n(d_i)}{\sum_{N_r} n(r_i^{mc})} = \frac{\sum_{N_t} n(u_i)}{\sum_{N_t} n(t_i^{mc})}, \quad (4.10)$$

where $n(d_i)$ is the number of data events and $n(u_i)$ the number of unfolded events in bin i . Furthermore, $n(r_i^{mc})$ and $n(t_i^{mc})$ are the number of reconstruction-level events and the number of particle-level events in bin i predicted by the Monte Carlo simulation. However, a significant amount of events that were not simulated (like a resonant structure) or large statistical fluctuations (e.g. due to background subtraction) can lead to an offset in otherwise well modeled bins. Therefore the IDS algorithm iteratively improves this normalization by disregarding those events in the data distribution and recalculating the normalization. A visualization of the two effects is given in figure 4.3. The regularization function determines whether a discrepancy between the naive normalization and data is significant. It assures that there is a smooth transition between disregarding a difference entirely and not at all, allowing for a convergence of the normalization procedure. The improved normalization $C^{(m)}$ enhances the ability to differentiate between known and unknown structures which can then be treated accordingly in the unfolding process.

The most important feature of IDS unfolding is its ability to retain structures in data that are not modeled in the Monte Carlo simulation and unfold them correctly to particle-level. In a search it has to be assured that potential new physics is not only identified at reconstruction-level, but is also retained when unfolding to particle-level.

This is done by the iterative structure of the algorithm. After a first unfolding step using

the unfolding matrix \tilde{P}_{kj} as described in equation 4.5 an unfolded spectrum is obtained:

$$n(u_j) = C^{(m)} \cdot n(t_j) + n(bu_j) + \sum_{k=0}^{N_r} f(|\Delta d_k|, \sigma, \lambda_U) \cdot \Delta d_k \cdot \tilde{P}_{kj} + (1 - f(|\Delta d_k|, \sigma, \lambda_U)) \cdot \Delta d_k \cdot \delta_{jk}, \quad (4.11)$$

where

$$\Delta d_k := n(d_k) - n(bd_k) - C^{(m)} \cdot n(r_k) \quad (4.12)$$

and $n(bu_j)$ and $n(bd_k)$ are the number of events coming from fluctuations in the unfolded and data distribution, respectively. Both are estimated in a separate step and in the case of identical binning $n(bu_j) = n(bd_j)$. Cases when $n(r_k) = 0$ or $n(d_k) - n(bd_k) \leq 0$ are detailed in [113].

From equation 4.12 one can see that if the Monte Carlo simulation describes the data perfectly (after the normalization procedure described above) and $n(bd_k) = 0$ then $\Delta d_k = 0$. From equation 4.11 it follows that the unfolded spectrum corresponds exactly to the (normalized) particle-level distribution from Monte Carlo simulation t_j . If not, the unfolding matrix \tilde{P}_{kj} is applied to the remaining difference Δd_k on reconstruction-level and the result is partially (depending on the significance of Δd_k according to the regularization function f) added to the Monte Carlo simulation particle-level spectrum. The remaining fraction $(1-f)$ is added to the particle-level spectrum without applying the unfolding matrix. This assures that only significant deviations are migrated.

In the case of $f(|\Delta d_k|, \sigma, \lambda_U) = 1$ this is equivalent to Bayesian unfolding [109], where the unfolding matrix \tilde{P}_{kj} is applied directly to data

$$n(u_j) = C^{(m)} \cdot n(t_j) + \sum_{k=0}^{N_r} n(d_k) \cdot \tilde{P}_{kj} - C^{(m)} \cdot \underbrace{\sum_{k=0}^{N_r} n(r_k) \cdot \tilde{P}_{kj}}_{n(t_j)} = \sum_{k=0}^{N_r} n(d_k) \cdot \tilde{P}_{kj}. \quad (4.13)$$

The first unfolded result can now be compared to the Monte Carlo simulation particle-level distribution. Any deviations which are statistically non-significant are now classified as a statistical fluctuation and are therefore absorbed into the background term:

$$bd'_j = bu'_j = (1 - f(|\Delta u_j|, \sigma u_j, \lambda_S)) \cdot \Delta u_j, \quad (4.14)$$

where

$$\Delta u_j := n(u_j) - C^{(m)} \cdot n(t_j). \quad (4.15)$$

The size of the absorption is determined by the regularization function.

Finally, the first unfolded result also provides a better estimate for the distribution of events that should have passed the particle-level selections. Hence the migration matrix A_{ij} is updated:

$$A'_{ij} = A_{ij} + f(|\Delta u_j|, \sigma, \lambda_M) \cdot \frac{1}{C^{(m)}} \cdot \Delta u_j \cdot P_{ij}. \quad (4.16)$$

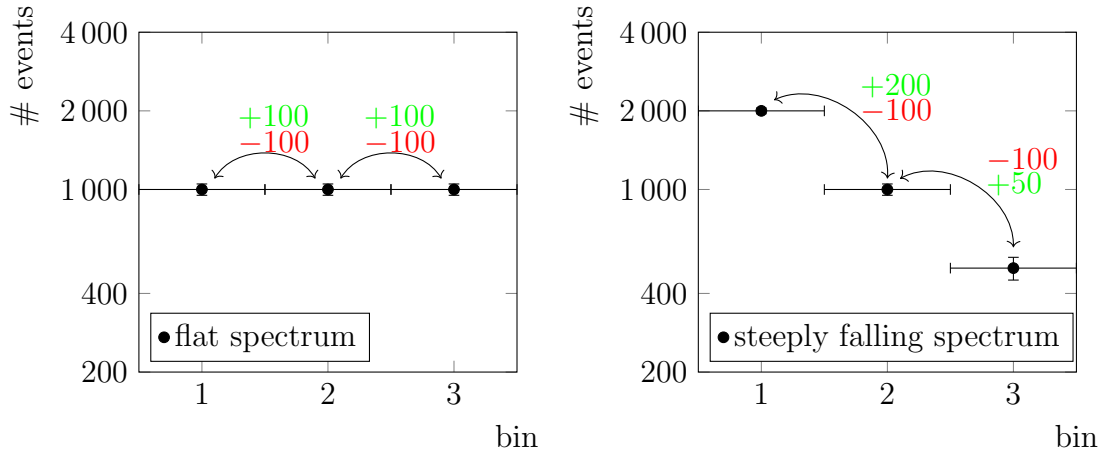


Figure 4.4: *Bin-to-bin migrations in a flat (steeply falling) spectrum, assuming 10% migrations at the edges of the bins. In a flat spectrum the number of events migrating in an out of a particular bin, balance, while in a steeply falling spectrum there is a net-migration towards higher bins.*

It can be shown (see appendix A) that in the case of $f(|\Delta u_k|, \sigma, \lambda_M) = 1$ this is equivalent to using the unfolded distribution⁴ as derived from equation 4.11 as the updated prior in equation 4.5. The IDS method, however, only corrects its matrix if there are significant deviations, which is again determined by the regularization function. It is to be noted that this updated migration matrix A'_{ij} only modifies the unfolding matrix \tilde{P}_{ij} . The folding matrix P_{ij} is assumed to be known exactly and is not modified. According to equation 4.5 this means that implicitly the prior knowledge about the particle-level distribution is updated.

The application of the unfolding matrix according to equation 4.11 and the update of the estimate of the fluctuations and the migration matrix is iteratively repeated. The regularization function thereby causes the modifications to the migration matrix and background term to vanish when the unfolded distribution converges to the true result and any additional iteration will not change the result anymore.

By iteratively updating the particle-level model in the unfolding matrix, potential new physics in the data is incorporated in the unfolding method and therefore unfolded correctly to particle-level. The advantage compared to bin-by-bin unfolding is most obvious when migrations from one bin to another become relevant as they are neglected entirely in bin-by-bin unfolding (see equation 4.9).

Migrations between reconstruction-level and particle-level bins of the same observable happen either due to a wrong scaling between the two (e.g. systematic underestimation of the observable at reconstruction-level) or because of large resolution effects. The former is small as it is mitigated by the calibration procedure, which is subject of the performance

⁴ The stability correction is not yet applied, so it is not the final unfolded distribution, but rather the data corrected for purity and resolution.

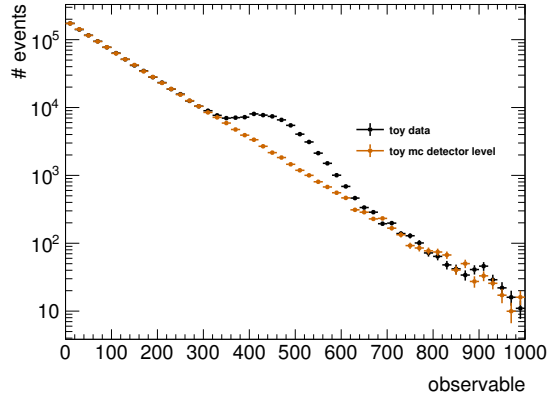


Figure 4.5: *Toy model simulating a steeply falling distribution. An additional Gaussian structure, which is not modeled by the toy Monte Carlo simulation, is added to the toy data distribution.*

groups within the collaboration. The latter is usually mitigated by choosing proper bin sizes, which reduces the amount of bin-to-bin migrations. However, there will always be migrations at the edges of a bin, which can not be avoided.

In a steeply falling spectrum, this results in larger migrations to higher bins than to lower bins, resulting in a change of the spectrum. Figure 4.4 illustrates how in a steeply falling spectrum the distribution changes if 10% of the events migrate to neighbouring bins, while a flat distribution remains constant.

In the presence of new physics these migrations become larger, which is not modeled by the Monte Carlo simulation, but needs to be accounted for in the unfolding method to obtain a consistent result.

The following example shows an exponentially falling distribution which is modeled by a toy simulation. Each entry at particle-level is smeared by a Gaussian centred at 1 with a width of 10%, simulating the resolution of the observable at reconstruction-level. Together they fill the migration matrix A_{ij} . In this example no purity and stability corrections are considered. A data distribution is modeled according to the same distribution with a Gaussian structure added to it. Both are depicted in figure 4.5.

The toy data is unfolded to particle-level using bin-by-bin unfolding as well as the IDS algorithm introduced above. As shown in figure 4.6, the bin-by-bin unfolding does not completely recover the additional feature in the toy data distribution, while the IDS method does. This is because the bin migrations are not treated explicitly in the bin-by-bin method, but are implicitly included in equation 4.9. The additional structure in the above example, however, results in larger bin counts and therefore larger migrations, than what was modeled in the simulation the bin-by-bin unfolding was derived from. The IDS unfolding on the other hand started from the same incomplete simulation, but incorporated the new structure into its particle-level description.

Although the above example uses large migrations and a large potential signal, it clearly motivates the use of a more sophisticated unfolding method.

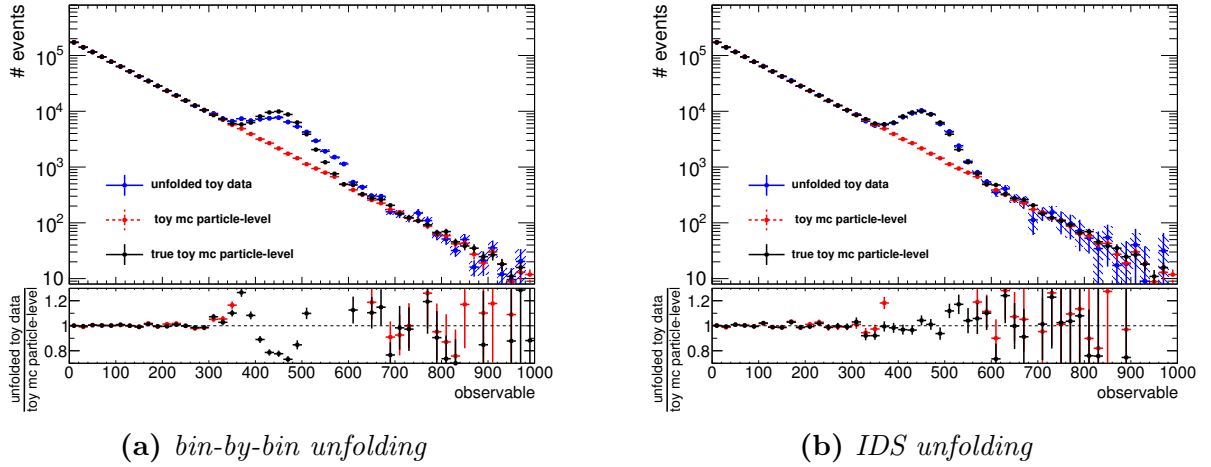


Figure 4.6: Toy data unfolded using (a) bin-by-bin and (b) IDS algorithm. The new structure is well recovered by the IDS algorithm, while the bin-by-bin algorithm does not.

Parameters

In the context of this thesis new physics is not expected to look like a bump as used in the previous example, but rather like an additional tail in a steeply falling distribution.

In order to optimize the parameters of the IDS algorithm, a toy model is constructed which simulates an exponentially falling distribution. This time, an additional acceptance of 95% is defined for events at particle-level, as well as an efficiency of 98% for reconstructed events. This ensures that the purity and stability corrections are non-trivial. As before, an event at particle-level is smeared by a Gaussian centred at 1 with a width of 10%. The new physics contribution, which is not modeled by this toy Monte Carlo simulation but is present in the toy data, is an additional exponential distribution, starting at 450 in this arbitrary observable.

The estimation of the parameters used for the IDS algorithm follows the recommendations given in [113]. First, a maximum of 20 iterations is defined. When testing different sized new physics contributions it was shown that in extreme cases the algorithm may take many iterations to reach convergence with the underlying particle-level distribution. Furthermore, choosing a large number of iterations when only very few are necessary has no disadvantage in case of IDS unfolding. This is because once the algorithm has converged any additional iteration will not modify the result anymore.

The parameter λ_N responsible for the regularization of the normalization procedure is chosen to be 0.5. In a scan of this parameter, no large dependence was found as the additional signal is not very significant, hence does not disturb the normalization procedure. In order to still be sensitive to any mismodeling the parameter is chosen rather low.

According to the recommendations λ_L , which regularizes the migrations in the first unfolding step, is chosen to be large (5). This is in order not to migrate large statistical fluctuations which might be present in the data, before they can be identified according to equation 4.14.

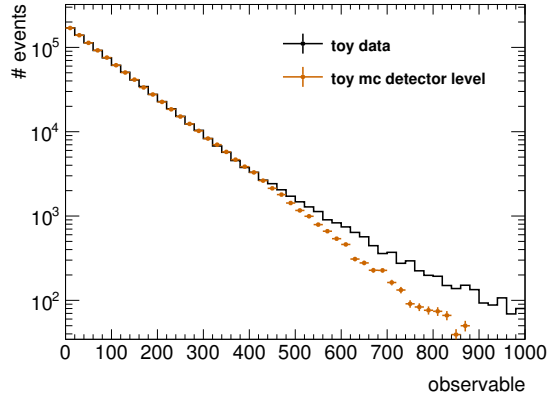


Figure 4.7: *Toy model simulating a steeply falling distribution. An additional exponential structure, which is not modeled by the toy Monte Carlo simulation, is added to the toy data distribution.*

The remaining parameters regularizing the migrations in the subsequent unfolding steps λ_U , the size of the modification of the migration matrix λ_M and the definition of what is considered a statistical fluctuation due to background subtraction λ_S , are determined via a scan. In order to evaluate the performance of the unfolding, a χ^2 between the unfolded distribution and the true toy Monte Carlo simulation distribution at particle-level is calculated. The probability for the given χ^2 is plotted as a function of λ_U and λ_M for various values of λ_S (see appendix B). For intermediate values of λ_U the agreement with the true distribution deteriorates, allowing only small or very large values of λ_U . The dependence on λ_S is found to be small which is why a moderate regularization of $\lambda_S = 1$ is chosen, as depicted in figure 4.8.

For large values of λ_U and λ_M a good χ^2 probability is obtained. However, it is found that this is due to enlarged uncertainties. This can be explained by the low correction per iteration because of the high regularization parameter. More iterations are necessary until the unfolding converges, which results in more iterations in which the uncertainties need to be propagated. It is found that low values for λ_U and λ_M should be used. In order to retain some regularization, values of 0.2 for both parameters are chosen.

Uncertainties

As for any measurement the correct treatment of the uncertainties in the unfolding is crucial. While for bin-by-bin unfolding the propagation of uncertainties is straight forward, Bayesian methods are more involved. Each iteration in the resolution correction introduces correlations between the bins, which have to be treated carefully when propagating their uncertainties. This is especially complex when iterating several times. In this case analytical solutions become too involved to be feasible.

In this work, the data as well as the Monte Carlo simulation are bootstrapped [115]

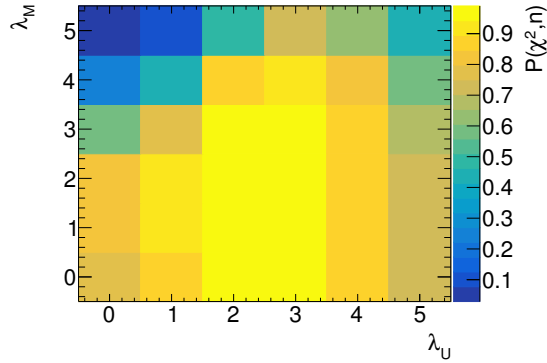


Figure 4.8: Parameter scan of $\lambda_U \in [0, 5]$ and $\lambda_M \in [0, 5]$. λ_S is fixed to 1. The z-axis displays the χ^2 probability when comparing the unfolded distribution to the true toy Monte Carlo simulation at particle-level. For intermediate values of λ_U this agreement becomes worse. High values of λ_U result in a good χ^2 probability, because of enlarged uncertainties in the unfolded distribution. Low values of λ_U and λ_M are preferred.

in order to estimate the uncertainties on the unfolded distribution. For each event n_{rep} numbers are drawn from a Poisson distribution $P(1)$ with a mean of 1: $(x_1, x_2, \dots, x_{n_{rep}})$. An event counted in particle-level bin t_j and reconstruction-level bin r_i is now filled $x_0 = 1$ times in the respective histogram (called nominal histogram) and $x_1, x_2, \dots, x_{n_{rep}}$ times in the n_{rep} replicas of the same histogram. This generates a set of n_{rep} distributions each of which can be unfolded. From this set of unfolded distributions one can now estimate the mean and variance for each bin i .

$$\langle u_i \rangle = \frac{1}{n_{rep}} \sum_{k=1}^{n_{rep}} u_i^k \quad (4.17)$$

$$\sigma_i^2 = \frac{1}{n_{rep}} \sum_{k=1}^{n_{rep}} (u_i^k - \langle u_i \rangle)^2 \quad (4.18)$$

as well as the correlations between bins

$$\rho_{ij} = \frac{V_{ij}}{\sigma_i \sigma_j} \quad (4.19)$$

$$\text{with } V_{ij} = \langle u_i u_j \rangle - \langle u_i \rangle \langle u_j \rangle \quad (4.20)$$

where V_{ij} is referred to as the covariance matrix with $V_{ii} = \sigma_i^2$. This allows for a reliable uncertainty estimation for very complex observables as well as to keep track of the correlations between the unfolded bins.

When unfolding the replicas of the data distribution, the nominal replica of the Monte Carlo simulation defining the detector response is used. This way the statistical uncertainty of only data is propagated to the unfolded result. In addition, the nominal data

distribution is unfolded with all replicas of the detector response, which then accounts for the uncertainty on the unfolded distribution due to limited statistics of the Monte Carlo simulation. Both uncertainties are added in quadrature. Further uncertainties on the unfolding technique are discussed in section 6.3.

Another advantage of the bootstrapping technique is that the Poissonian random numbers which populate the replica histograms are seeded by a unique number, namely the run- and event-number. This means that a given event will always be replicated across the bootstrap replicas in the same way. When applying a systematic variation to the Monte Carlo simulation, in order to account for systematic uncertainties, the nominal distribution and its variation are highly correlated. The identical random seed, however, ensures that this correlation is retained in the bootstrap replicas. Dividing the systematically varied distribution by the nominal distribution for each replica takes these correlation into account. This results in a smaller uncertainty on the systematic uncertainty (see appendix E).

Likewise, in the case of a combination of multiple measurements with overlapping signal regions, the overlapping events will remain correlated via the bootstrap replicas, allowing to derive a correlation matrix between measurements. Taking these correlations into account, again, allows for smaller uncertainties and hence a better combined result.

Chapter 5

MET + Jet Reconstruction-level Analysis

There is compelling evidence that dark matter exists. However, this evidence is based entirely on astrophysical observation and all attempts to prove its existence in a laboratory environment have not succeeded. Assuming the dark matter is made of particles and is within the kinematic reach of the LHC it might be produced from the energy released in its particle collisions. This would provide an excellent environment for discovery as well as the study of its fundamental properties. This chapter introduces the search strategy (section 5.1), object- and event-level selections (section 5.3 and 5.4) and reconstruction-level results (section 5.7) of the dark matter search performed in this thesis. It is largely based on [4] which this work aims to extend. Furthermore, the analyzed data and Monte Carlo simulations are discussed in section 5.2. Backgrounds and Uncertainties are discussed in section 5.5 and 5.6, respectively.

5.1 Search Strategy

Missing transverse energy E_T^{miss} , which is the energy imbalance in the transverse plane of the detector, is one of the most promising signatures to search for dark matter. Usually this imbalance should be close to zero, as in a head-on collision there is no initial momentum in the transverse directions and due to momentum conservation there should not be any in the final state. However, dark matter and neutrinos are not expected to interact with the detector material, hence leaving no measurable energy. Constructing the energy balance of all visible particles thus demonstrates of the transverse energy of the invisible particles.

This requires the existence of at least one visible Standard Model particle in the final state and this search targets hadronic jets, originating from fragmented gluons or quarks.

Two different signatures aiming at different production mechanisms of dark matter are chosen.

1. ≥ 1 **jet**: the monojet signature, where dark matter is produced via some unknown interaction with quarks and recoils against an initial state radiation jet (figure 5.1a)

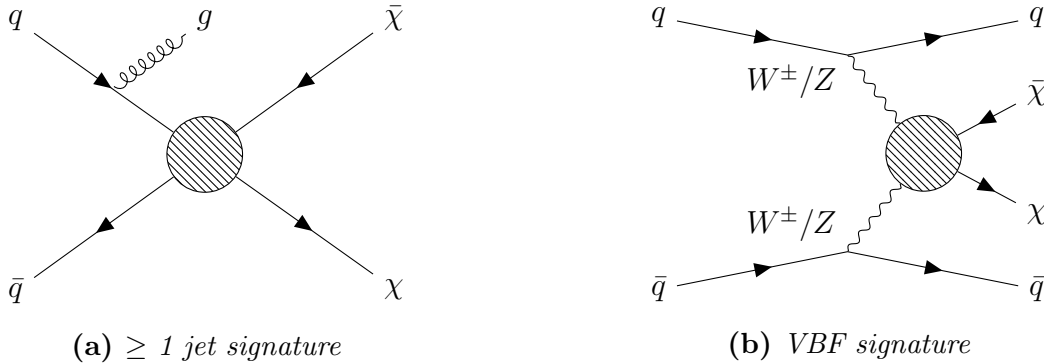


Figure 5.1: Possible Feynman diagrams of the two signatures studied in this work. (a) shows the production of dark matter in association with an initial state gluon. (b) shows the production of dark matter via vector boson fusion.

2. **VBF:** the vector boson fusion signature, where the dark matter is produced through a yet unknown coupling to the electroweak vector bosons which are radiated off when two quarks scatter off each other (figure 5.1b)

Possible Feynman diagrams for both signatures are illustrated in figure 5.1. The first signature is the monojet signature which profits from the strong coupling of the gluon to the initial state quark¹. Therefore the process has a high branching ratio and provides a large statistics dataset in which to search for deviations coming from physics *beyond the Standard Model* (BSM). It is characterized by a single high energy jet in the detector without any other particles present. Furthermore, the dark matter produces large amounts of missing transverse momentum, which balances the p_T of the jet.

Models with weakly interacting dark matter, however, would have a much lower cross section than any QCD process, making it almost impossible to detect in a monojet signature. Therefore, a second signature is added in which the weak production of dark matter is enhanced. The vector boson fusion signature is characterized by two quarks, which scatter off each other at low angles. In the final state this manifests itself as two forward jets in opposite hemispheres of the detector. In the scattering, the two quarks both radiate off an electroweak vector boson, which fuse to produce other particles, potentially dark matter. This will again result in copious amounts of missing transverse energy. The additional signature extends the sensitivity of this search by looking at a larger spectrum of final states in which a given model could manifest itself, as well as specifically targeting new models. As this search aims at improving the longevity of the measured results, being as inclusive as possible and covering a wider variety of models is crucial.

One final state in the Standard Model is indistinguishable from dark matter production. This is the production of a Z boson which decays to two neutrinos ($Z \rightarrow \nu\bar{\nu}$, see figure 5.2). Neutrinos only interact with other matter via the weak force, meaning, like dark matter, they do not leave any visible trace in the detector. Since this background is irreducible it

¹ Similar diagrams with $gg \rightarrow \chi\chi$ and $gq \rightarrow \chi\chi$ exist.

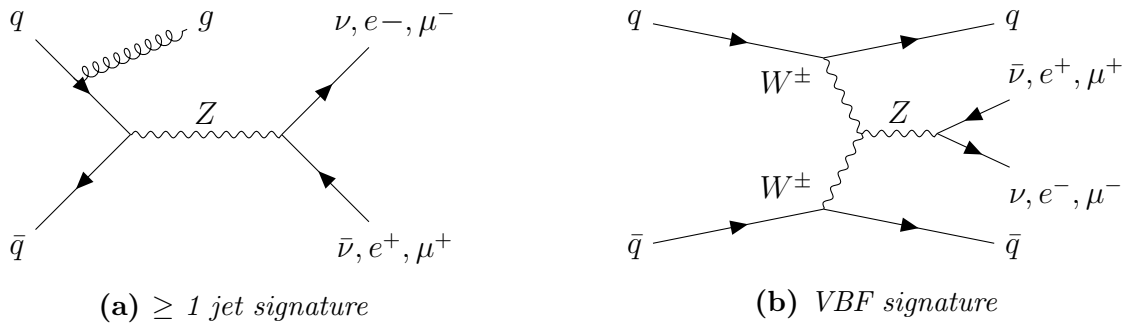


Figure 5.2: Feynman diagrams of the production of a Z boson decaying to either neutrinos $\nu\bar{\nu}$ or charged leptons e^+e^- , $\mu^+\mu^-$ for both the (a) ≥ 1 jet and (b) VBF signature.

is added to the signal definition, ultimately making this search a measurement of the cross section of $Z \rightarrow \nu\bar{\nu}$ and looking for any deviation from the Standard Model prediction.

Furthermore, the decay of the Z boson into a pair of charged leptons differs from its decay to neutrinos only in the mass and electric charge of the fermions. As illustrated in figure 5.2 the Feynman diagrams of both decays look identical². This is why the $Z \rightarrow e^+e^-$ and $Z \rightarrow \mu^+\mu^-$ decays can be selected in almost identical signatures as $Z \rightarrow \nu\bar{\nu}$, all targeting the decay of a Z boson in association with a jet (≥ 1 jet signature) and in a VBF topology, and thereby they serve as control regions to the signal selection.

The cross section of both the signal region and the control regions are measured differentially. This makes maximal use of the available information, as also the shape information of the observables is retained. In the ≥ 1 jet region the cross section is measured in bins of the missing transverse energy E_T^{miss} , same as in the VBF region. This is because physics beyond the Standard Model decaying to dark matter would produce additional events with missing energy, making this observable ideal for dark matter detection. Also the E_T^{miss} spectrum tends to be harder, because of the higher energy scale of the interaction and the large mediator mass present in many models beyond the Standard Model. This results in an increased sensitivity in the large E_T^{miss} bins.

Furthermore, in the VBF region the cross section is measured in bins of the invariant dijet mass m_{jj} and the signed angle between the two leading jets $\Delta\phi_{jj}^{sgn}$. VBF processes generally have a harder m_{jj} spectrum than the QCD production of two forward jets, yielding and increased sensitivity at high m_{jj} values. The signed angle is defined as the azimuthal angle $\Delta\phi$ between the two leading jets, which is an observable sensitive to CP-even and CP-odd models [116]. In this work the two jets are furthermore ordered in rapidity such that the sign of the angle is unambiguously defined. This retains the information about the amount of CP-even and CP-odd contributions, should both be present in the new theory [117]. These observables are therefore complementary in increasing the sensitivity to different BSM models.

Furthermore, the differential distributions are unfolded to particle-level using the IDS

² The prediction of their cross section differs by roughly a factor of 6.

unfolding technique described in section 4.2. This increases the longevity of the results, as it allows for a much simpler reinterpretation of the data. Additionally, it avoids the use of parametrized detector simulations which are inferior to the detector simulation available within the ATLAS collaboration.

Finally, the unfolded distributions are combined in the ratio R_{miss} of the fiducial cross sections of $E_T^{miss} + jets$ and the fiducial cross section of $Z \rightarrow l^+l^- + jets$

$$R_{miss} = \frac{\sigma(E_T^{miss} + jets)}{\sigma(Z \rightarrow l^+l^- + jets)}. \quad (5.1)$$

Many of the experimental uncertainties like energy scale uncertainties and resolution uncertainties are correlated between the numerator and the denominator. Since the two processes in the numerator and the denominator are so similar, they are furthermore expected to be of similar size and the uncertainty on the ratio is thus expected to be small. Mismodeling of the physics processes in the Monte Carlo simulation, originating from the same source, will affect the numerator and denominator in a similar way and will thus be mitigated in the formation of the ratio.

5.2 Datasets and Frameworks

Recorded Data

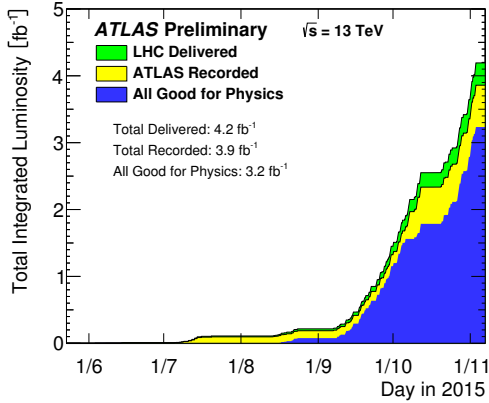
The dataset analyzed in this work corresponds to 36.2 fb^{-1} of proton-proton collisions recorded by the ATLAS experiment in 2015 and 2016 at a center-of-mass energy of 13 TeV. This corresponds to $\sim 92\%$ of the recorded data [118]. The inefficiencies are explained by the so-called warm-start of the pixel and tracking detectors, where preamplifiers and high voltage supply are only switched on once the LHC delivers a stable beam. Furthermore, during data taking some of the detector sub-systems may go into a degraded state which results in incomplete or corrupted events. This is monitored and the system is recovered, however, the corrupted events are excluded from the analyses via so-called *Good-Run Lists*. The recorded integrated luminosity over time in the years 2015 and 2016 are displayed in figure 5.3.

Uncertainties on the integrated luminosity are derived from the calibration of the luminosity scale using x - y beam-separation scans, employing a method similar to the one described in [119]. Furthermore, the calibration uses the LUCID-2 detector for the baseline luminosity measurements [120]³.

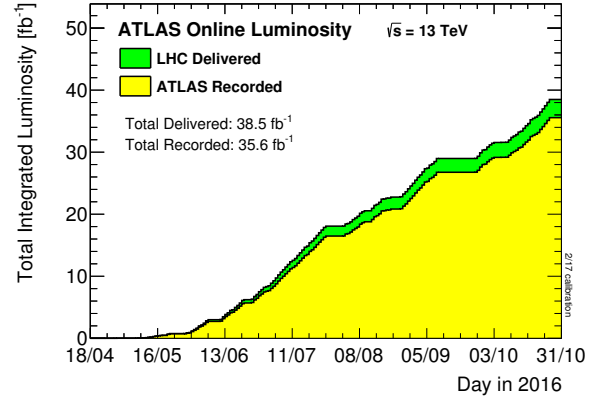
The pileup conditions during the 2015 and 2016 data taking is summarized in figure 5.4. It shows the delivered luminosity of the LHC as a function of the mean number of interactions per bunch crossing. The latter indicates the pileup conditions and is calculated from the instantaneous per bunch luminosity as

$$\mu = L_{\text{bunch}} \cdot \sigma_{\text{inel}} / f_r \quad (5.2)$$

³ The formulation is taken and modified from [121] as proposed by ATLAS luminosity working group.



(a) 2015



(b) 2016

Figure 5.3: Cumulative luminosity as a function of time delivered to ATLAS (green), recorded by ATLAS (yellow), and certified to be good quality data (blue) during stable beams [17].

where L_{bunch} is the instantaneous per bunch luminosity, σ_{inel} is the inelastic cross section which is taken to be 80 mb at a center of mass energy of 13 TeV, and f_r is the LHC revolution frequency [17]. The average number of interactions per crossing was 13.7 in 2015 and 24.9 in 2016, which adds up to an average of 23.7 interactions per bunch crossing over the whole run period.

Monte Carlo Simulation

The simulated data used in the background subtraction as well as the definition of the detector response are obtained using the ATLAS simulation framework [122]. It is generally divided into three steps, the event generation, the detector simulation and the simulated digitization of the analog pulses in the detector into voltages and currents. The output of these simulations contains the same information as recorded data would, allowing for an identical treatment in subsequent analysis steps.

In the event generation the matrix element (ME) of the process of interest is calculated up to a certain order. Usually the calculations are at leading order (LO) with next to leading order (NLO) or even higher contributions for certain parts of the calculation. This matrix element is furthermore convoluted with a parton density function (PDF). The parton density function can not be calculated from first principles, but has to be modeled and tuned to match the existing data. They are provided by several dedicated groups and the PDF sets most commonly used are NNPDF [123], CT14 [124] and MMHT14 [125]. In the event generation also the underlying event is calculated, which is the remaining low energy fragments from the proton that interact aside from the hard scatter.

Following the ME calculation a parton showering model is employed. This is usually an angular- [126] or p_T -ordered [127] emission of secondary particles due to bremsstrahlung

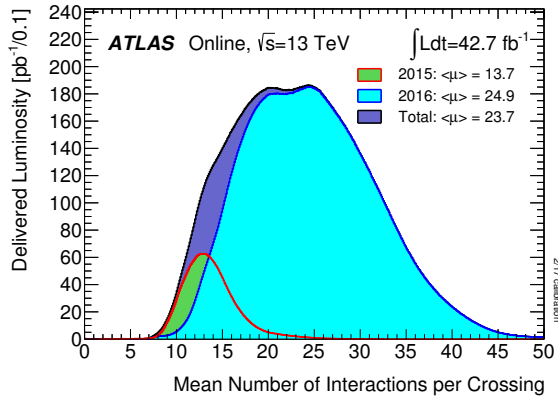


Figure 5.4: Mean number of interactions per bunch crossing for the 2015 and 2016 data taking period. All data delivered to ATLAS during stable beam is shown [17].

or gluon splitting. Usually this is split into initial state radiation (ISR) and final state radiation (FSR). This has to be treated carefully as the radiation of an additional parton is a higher order correction to the ME and might therefore be double counted, if not treated accordingly. To avoid this a match and merge method like CKKW [128, 129], MLM [130] or FxFx NLO [131] merging is employed. Furthermore, multiparton interactions are treated as in the dense environment right after the collision the particles might interact with each other more than once.

The parton showering is evolved in time and produces particles of a few GeV, where perturbative QCD no longer holds. Therefore, hadronization models are employed which form colorless objects from all quarks and gluons which were produced. Common models employed are the cluster model [132] and the string model [127].

Furthermore, the simulated events are overlaid with additional pileup interactions. These are soft QCD events simulated with Pythia 8 [127] using the A2 set of tuned parameters [133] and the MSTW2008LO [134] PDF set [135].

The final particle content of the event is propagated through a GEANT4 based simulation [102] of the ATLAS detector, which simulates the scatterings and energy depositions inside the detector material. The resulting energy deposits (hits) in the detector are then digitized and the detector noise is added. Additionally, the hits in the detector are converted into a bytestream identical to the readout of the detector [122]. The simulation can finally be treated identically to the recorded data and the reconstruction algorithms introduced in section 2.3 identify the physics objects produced in the (simulated) collisions.

Throughout this process, the truth information about the event that was generated is retained. Thus, the Monte Carlo simulation provide the particle- and reconstruction-level event description simultaneously. This is crucial, as it allows to retrieve the simulated detector response.

The full list of simulated Monte Carlo samples together with a detailed tune of the event generation and their cross sections and filter efficiencies can be found in appendix D.

Reweighting of Monte Carlo Simulations

Events in a Monte Carlo simulation are generated with an event weight. This is because only a limited number of events can be generated and all points in the phase space of interest need to be populated. Instead of generating the events according to their probability distribution, they are generated flat, or in slices of certain observables which ensures a uniform population of all distributions. Finally, the events are weighted such that they match their actual probability distribution.

The Monte Carlo simulation (MC16a) is generated with a preliminary pileup profile, which is the expected pileup distribution for 2015 and 2016 data at the time of production. During data taking this may change and the simulation has to be corrected accordingly. The events are therefore reweighted to match the pileup profile of the recorded data [136].

It may occur that a Sherpa generated event has a very large weight. While this is mathematically correct, in a sample with limited statistics, like the Monte Carlo simulation at hand, this can lead to unphysical features in the distributions. Therefore, events with an event weight larger than 100 are rejected, with no impact on the observables in the simulation [137].

Trigger scale factors are applied in the signal region targeting the selection of Z bosons decaying to neutrinos. This is to correct for differences in the trigger efficiency between data and Monte Carlo simulation (see section 5.4).

Known differences in the selection efficiency of leptons between data and Monte Carlo simulation are corrected for by the use of event based scale factors. These scale factors are designed to correct for various effects (reconstruction, identification, isolation, track-to-vertex-association, etc) and their multiplication results in an overall factor calculated per reconstructed lepton.

Pre-Processing

With a total size of ~ 1.4 petabyte for the entire recorded dataset (2015 and 2016) and an additional ~ 250 TB for all necessary simulated datasets, the data is too large to handle efficiently. Since this search targets a monojet signature with large missing transverse energy and a VBF signature with at least two high- p_T jets in the forward direction a *derivation* of the dataset is produced, reducing the total size to < 60 TB. This is achieved by requiring a leading jet with $p_T > 100$ GeV, or by requiring the two leading jets with a $p_T > 40$ GeV and an invariant dijet mass of $m_{jj} > 150$ GeV. Furthermore, only events are selected that pass a list of E_T^{miss} -, single electron-, single muon- or single photon- triggers.

Afterwards, the data is processed further to minimize CPU time when it is analyzed. This is done by a custom made *skim*, which further reduces the amount of information

stored per file to a minimum and handles many of the necessary calibrations. This includes additional restrictions on the triggers, since for this analysis only E_T^{miss} and single electron triggers are necessary. Events not triggered by any of them are rejected. Furthermore, all particles are calibrated to the latest calibration provided by the ATLAS collaboration. The calibrated particles are then used to calculate and calibrate the missing transverse energy in the events. Throughout these calculations, the necessary systematic variations are propagated.

5.3 Particle-level Object and Event Selection

Object Selection

The event and object selections at particle-level define the fiducial phase space targeted by this analysis. It defines the phase space the recorded data will be unfolded to and thereby the selection any analysis has to apply to compare directly to the results of this work. The selections are chosen to be as similar as possible to the reconstruction-level selections in order to minimize the extrapolation in the unfolding process.

Electrons are selected by requiring a $p_T > 7$ GeV and $|\eta| < 2.47$, excluding also the crack region at the end of the electromagnetic barrel $1.37 < |\eta| < 1.52$. Furthermore, dressed electrons are required, meaning that within a cone of $\Delta R < 0.1$ the four-momenta of all photons are added to the electron four-momentum.

Muons are selected in a similar way, by requiring a $p_T > 7$ GeV and $|\eta| < 2.5$. Also here dressed muons are used, adding the four-momenta of photons within a cone of $\Delta R < 0.1$ to the four-momentum of the muon (appendix C motivates the low- p_T choice).

Taus are required to decay hadronically, as leptonic decays will be included in the electron and muon selections. They are required to have a $p_T > 20$ GeV and $|\eta| < 2.47$ also excluding the crack region at $1.37 < |\eta| < 1.52$. Furthermore, they are required to be produced promptly and not be coming from a subsequent decay, like from a mesonic or baryonic decay. Only the visible component of p_T and η are considered, excluding possible neutrinos in the decay. This again aims to have a definition close to the one at reconstruction-level.

Jets are reconstructed using the anti- k_T algorithm with a radius parameter of 0.4. At particle-level the algorithm clusters the four-momenta of particles which were produced in the showering and hadronization process of the partons. They are required to have a $p_T > 30$ GeV and a rapidity $|y| < 4.4$.

An overlap removal is employed to ensure similar minimal distances between particles, like it is done at reconstruction-level. For this purpose jets are removed which are within a

cone of $\Delta R < 0.2$ around an electron, followed by a removal of electrons which are within a cone of $\Delta R < 0.4$ around a jet. Furthermore, jets that fall into a cone of $\Delta R < 0.2$ around a muon are removed, followed by the removal of muons which are within a cone of $\Delta R < 0.4$ around a jet. Finally, jets are removed which are within a cone of $\Delta R < 0.2$ around a tau.

The missing transverse energy at particle-level E_T^{inv} is defined as the sum of all invisible particles in the event. Invisible here means particles which do not interact with the detector and hence can not be reconstructed. As the only Standard Model particle with this property is the neutrino, this is the sum of all neutrinos in the event for Standard Model processes.

The missing transverse energy in the signal region is the Z boson p_T , except for additional low- p_T neutrinos. Since the analysis aims at measuring a ratio between the signature $E_T^{miss} + jets$ in the numerator with the main Standard Model contribution being $Z \rightarrow \nu\bar{\nu} + jets$ and the signature $Z \rightarrow l^+l^- + jets$ in the denominator, it is reasonable to define the E_T^{inv} for the denominator such that they can follow the same selection.

For the $Z \rightarrow l^+l^- + jets$ signature the invisible transverse energy E_T^{inv} is therefore defined as the sum of all neutrinos in the event plus the two leptons coming from the decay of the Z boson. This way the definition of E_T^{inv} is identical in the signal and control regions, both targeting the Z boson p_T plus low- p_T neutrinos. Only the selection of the leptons, which is restricted by p_T and $|\eta|$ requirements, causes some differences in the selected phase space.

Event Selection

The event selection is motivated by the enhancement of the signal over the possible background contributions, as well as the ATLAS detector acceptance and trigger requirements. The selections are summarized in table 5.1.

The most crucial requirement is $E_T^{inv} > 200$ GeV to select events with a large invisible contribution, as would be expected from dark matter production. Additionally, no leptons are expected in the final state of the signal region, so all events with a lepton, according to the above selection, are vetoed. In the control regions this holds for additional leptons aside from the two opposite charged, same flavor leptons coming from the Z decay.

An angular distance of $\Delta\phi > 0.4$ between the first four leading jets and the ϕ direction of the missing transverse momentum is required, to mitigate QCD background with large E_T^{inv} due to mismeasured jets.

In the ≥ 1 jet signature the leading jet is expected to largely balance the Z boson momentum, which is the main contribution to the size of E_T^{inv} . Therefore, a large leading jet $p_T > 120$ GeV in the central part of the detector $|\eta| < 2.4$ is expected.

The VBF signature has at least two jets which scatter off each other at low angles, thereby each radiating off an electroweak vector boson that subsequently fuse. This motivates the selection of two jets with a large angular separation and moderate p_T . Again, the jets balance the outgoing Z boson p_T , which is why their momenta are chosen smaller than in the ≥ 1 jet signature. However, at least one large p_T jet helps in suppressing QCD

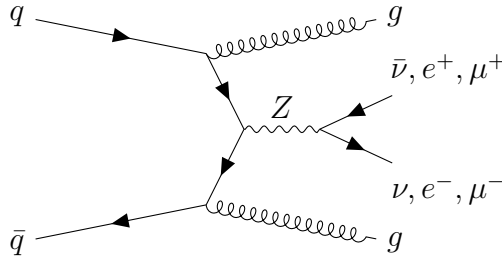


Figure 5.5: Feynman diagram of the production of a Z boson decaying to either neutrinos $\nu\bar{\nu}$ or charged leptons e^+e^- , $\mu^+\mu^-$ for the QCD production of a Z boson is association with two jets.

backgrounds. For this reason asymmetric cuts of 80 GeV and 50 GeV are chosen. The large angular separation could be achieved by requiring a certain $\Delta\eta$. In this analysis, however, a large invariant dijet mass $m_{jj} > 200$ GeV is required. Which is equivalent due to the relation

$$m_{jj} = 2 \cdot p_T^{jet1} p_T^{jet2} \cdot (\cosh(\eta^{jet1} - \eta^{jet2}) - \cos(\phi^{jet1} - \phi^{jet2})). \quad (5.3)$$

The central jet veto is motivated by the missing color connection of the outgoing quarks. A similar diagram to figure 5.2b exists, where the Z boson is produced by quarks (see figure 5.5). In this case the outgoing jets are color connected, leading to additional jets in the gap between them. This is not expected without the color connection and therefore a veto on additional jets in the rapidity gap between the two leading jets is employed.

As introduced above, these selections apply equivalently to the signal and control regions, as the E_T^{inv} is defined accordingly. Additional selections are only necessary for the selection of the two same flavor, opposite charge leptons coming from the Z boson decay.

The leading lepton p_T is required to be larger than 80 GeV, which is less than half the (approximate) Z boson p_T due to the E_T^{inv} cut, but large enough to suppress non leptonic backgrounds. As the processes in the denominator are statistically limit the measurement, the second leading lepton p_T is chosen to be as low as 7 GeV in order not to reduce statistics further. To assure that the leptons are indeed coming from a Z decay, two same flavor, oppositely charged leptons are required. Furthermore, their combined invariant mass m_{ll} is required to be within a 50 GeV window around the Z mass.

5.4 Reconstruction-level Object and Event Selection

Object Selection

The object selection provides an unambiguous definition for the physics objects used in the analysis. As a basis it uses the objects as they are reconstructed by the reconstruction algorithms introduced in section 2.3. However, certain energy deposits may satisfy multiple reconstruction algorithms. Therefore a well-defined object definition is necessary.

Table 5.1: Fiducial phase space cuts listed for the signature $E_T^{miss} + \text{jets}$ in the numerator and the signature $Z \rightarrow l^+l^- + \text{jets}$ in the denominator of the ratio R_{miss} .

Numerator and Denominator	≥ 1 jet	VBF
E_T^{inv} (Additional) lepton veto		> 200 GeV
Jet $ y $		< 4.4
Jet p_T		> 30 GeV
$\Delta\phi_{jet, E_T^{inv}}$		> 0.4 , for the four leading jets with $p_T > 30$ GeV
Leading jet p_T	> 120 GeV	> 80 GeV
Subleading jet p_T	-	> 50 GeV
Leading jet η	< 2.4	-
m_{jj}	-	> 200 GeV
Central-jet veto	-	No jets with $p_T > 30$ GeV and $y_{j1} < y < y_{j2}$
Denominator only		≥ 1 jet and VBF
Leading lepton p_T		> 80 GeV
Subleading lepton p_T		> 7 GeV
Lepton η		e (μ) with $\eta < 2.47$ (2.5)
m_{ll}		66 – 116 GeV

Electrons are required to satisfy the *medium operating point* of a likelihood discriminant. The discriminant combines information from the tracking system and electromagnetic calorimeter into a likelihood function to distinguish electrons from jets and photons. The medium operating point corresponds to a selection efficiency of 88% for prompt electrons of $E_T = 40$ GeV [138]. Furthermore, the electrons are required to be isolated, to distinguish between prompt and non-prompt electrons. A combination of calorimeter based and track based isolation is used, which both quantify the activity around the main energy deposition. The *Gradient isolation operation point* is applied, which has a total selection efficiency of prompt leptons of 90 (99)% at electron energies of $p_T = 25$ (60) GeV [138]. The electron clusters are required to have good quality, meaning that none of the front-end-boards or heavy-voltage supplies malfunctioned. A $p_T > 7$ GeV and $|\eta| < 2.47$ requirement selects the same kinematics as at particle-level, excluding also the crack region at $1.37 < |\eta| < 1.52$. Finally, so-called *track-to-vertex-association* (TTVA) cuts are employed, making sure the origin of the electron is the hard scatter vertex in the interaction. The impact parameters z_0 and d_0 define the distance (of the point of closest approach) of the track to the interaction vertex in the longitudinal and transverse direction respectively. Cuts on $|z_0 \sin(\theta)| < 0.5$ mm and $|d_0|/\sigma(d_0) < 5$ are employed.

Muons are required to satisfy a *loose operation point* designed to maximize the reconstruction efficiency. By default it uses all four muon types (see section 2.3), restricting

calorimeter-tagged and segment-tagged muons to the $|\eta| < 0.1$ region, and combined and extrapolated muons are accepted in $|\eta| < 2.5$ and $2.5 < |\eta| < 2.7$, respectively, requiring a minimal amount of hits in the monitored drift tube layers [39]. In a subsequent step muons are restricted to $p_T > 7$ GeV and $|\eta| < 2.5$ and required to be either segment-tagged or combined muons. They are also required to be isolated, following the *LooseTrackOnly isolation*. It defines a track based isolation variable which quantifies the p_T sum of tracks around the muon track within a specified radius. The cut value on this variable is chosen such that a muon selection efficiency of 99% is reached [39]. Furthermore, track-to-vertex-association cuts are applied to restrict the muons to the hard scatter vertex. $|z_0 \sin(\theta)| < 0.5$ mm and $|d_0|/\sigma(d_0) < 3$ are required.

Leptonically decaying taus are not reconstructed, as they will be included in the reconstructed electrons and muons. The hadronic tau selection uses a boosted decision tree (BDT) to discriminate taus from quark- or gluon-initiated jets. Both 1- and 3-prong decays are reconstructed, which reach a selection efficiency of 85% and 75%, respectively, for the *loose operation point* used in this work [139]. The BDT thereby combines variables about the shower shape in the calorimeters, the p_T of the τ -candidate defined in various ways (p_T^{LC} , p_T^{TPF} , p_T^{interp}) and several event based variables like the number of tracks (for a complete list, see [140]). The τ -candidates are required to have $p_T > 20$ GeV and $|\eta| < 2.47$ excluding the crack region at $1.37 < |\eta| < 1.52$. Furthermore, a dedicated overlap removal with electrons is applied, rejecting 1-prong τ -candidates within a radius of $\Delta R = 0.4$ around an electron.

Jets are required to pass a p_T threshold of 30 GeV and have rapidity $|y| < 4.4$. Furthermore, a discriminant called *jet-vertex-tagger* (JVT) is introduced, which aims at suppressing reconstructed jets coming from pileup [141]. It is constructed as a two-dimensional likelihood of two variables (R_{pT} and corrJVT), which use the fraction of tracks coming from the primary vertex to decide if the origin of the jets was the hard interaction vertex. The *medium operation point* is used, corresponding to a selection efficiency of 92% for jets with $|\eta| < 2.4$. In the forward region at $|\eta| > 2.5$, where no tracking information is available, the so-called *forward JVT* (fJVT) is applied. It reduces stochastic pileup jets, which are jets reconstructed from multiple pileup vertices, using timing and shape information. Additionally, it reduces pileup jets reconstructed from single pileup vertices using topological information. The *tight operation point* is used, which reaches selection efficiencies of 79.9% (94.6%) for jets with $p_T = 20 - 30(40 - 50)$ GeV, thereby reducing pileup jets by $> 50\%$ [142].

The identification of leptons is in most cases more reliable than the identification of a jet, as the latter clusters energy depositions without taking into account additional information, like the shapes or tracks. Therefore, an overlap removal is applied, which favors the reconstructed leptons over jets. It removes jets within a $\Delta R < 0.2$ around a muon and muons within a $\Delta R < 0.4$ around the remaining jets. The latter aims at removing non-prompt muons, which is also targeted by the isolation requirement. The remaining

correction from the overlap removal is therefore expected to be small. Furthermore, jets are removed which are within $\Delta R < 0.2$ around an electron and electrons within $\Delta R < 0.4$ around the remaining jets. The same argument as for the muon case applies here as well. Lastly, jets are removed which are within $\Delta R < 0.2$ around a hadronic τ -candidate. An additional lepton-lepton overlap removal is employed, favoring muons, followed by electron and finally τ -candidates. Electrons are removed if they share a common track with muons, while τ -candidates are removed if they are within $\Delta R < 0.2$ around muons or electrons.

The missing transverse energy is defined as the negative sum of all visible particles, which is equivalent to the particle-level definition. It is computed by adding the four vectors of all particle trajectories or energy depositions and adding their components in the transverse x and y direction

$$E_{x(y)}^{miss} = -E_{x(y)}^{\mu} - E_{x(y)}^e - E_{x(y)}^{\tau} - E_{x(y)}^{\gamma} - E_{x(y)}^{\text{jet}} - E_{x(y)}^{\text{soft}}. \quad (5.4)$$

All tracks and energy depositions are assigned either to one of the physics objects (e , μ , τ , γ , jet) or, if no physics object is found nearby, to the soft term $E_{x(y)}^{\text{soft}}$. This way all contributions are added with the correct energy calibration. This requires that the physics objects, which the tracks and clusters are assigned to, are defined in an unambiguous way. The leptons are thus selected according to the definitions introduced in this chapter. Jets are defined as all objects coming from the jet reconstruction algorithms without any additional selection, such that a more inclusive assignment of tracks and clusters to the physics objects is possible. Only the JVT and fJVT selection is applied to exclude jets from pileup vertices. In the case of overlapping signals a preferred order is followed, where muons are favored over electrons, followed by τ -candidates and jets and finally the soft term [143].

In the case of an overlapping jet with a muon a special treatment is employed. Jets are rejected if they are likely to come from pileup or a catastrophic muon energy loss. They are not rejected entirely if they have a very low number of tracks and a low track p_T compared to the muon. In this case it is assumed that the jet was produced from bremsstrahlung of the muon. Therefore, the jet momentum is corrected to the electromagnetic scale and is included in the E_T^{miss} calculation [143].

Similarly, in the case of an electron overlapping with a jet, the energy of the jet is partially retained. All energy contributions coming from the electron are subtracted from the jet and if the remaining jet- p_T at the electromagnetic scale is still significant (larger than 20 GeV), it is included in the E_T^{miss} calculation.

The calculation of missing transverse energy via the four-vectors of all components allows to infer its magnitude, but also its ϕ^{miss} direction in the transverse plane [143].

The E_T^{miss} calculation furthermore allows to treat certain particles as if they were invisible to the detector. This means that leptons coming from the Z boson decay in the control regions can be treated in the same way as the neutrinos are treated for the signal region: as missing energy. Rather than subtracting the leptons from the real missing energy in an event, this assures that the treatment of overlapping signals is consistent and double counting of energy depositions is avoided.

Event Selection

Reconstructed events are required to pass a Good-Run List as introduced in section 5.2 in order to exclude partially reconstructed or corrupted events. Furthermore, requirements on the data quality are employed. Events are excluded if any errors from the tile- or liquid argon calorimeters are reported. Also no errors must be reported from SCT or due to incomplete events from a TTC restart. Finally, events are vetoed which contain jets likely to come from non-collision background. This may be beam induced background or a cosmic ray shower overlapping with the collision event. Additional sources of energy might significantly deteriorate the E_T^{miss} reconstruction, therefore the event is rejected entirely if any jet is likely to come from non-collisional background. This is facilitated by a set of *loose* selection criteria applied to all jets, or a *tight* set of selections applied to the leading jet (for details see [144]).

A primary vertex must be reconstructed, which requires at least 2 reconstructed tracks associated to it, as well as several quality and position requirements on the associated tracks (for details see [145]). The vertex from the hard interaction is then defined to be the one with the highest $\sum_i p_{T,i}^2$ of the tracks i associated to it.

At least one trigger element in a set of triggers has to be passed. The list of triggers is selected according to the targeted signature. For the signal region targeting new physics and the decay of a Z boson to two neutrinos, the lowest unprescaled E_T^{miss} trigger in every run period is selected. The same holds for the control region targeting Z bosons decaying to a pair of muons. This is possible because muons are invisible to the HLT missing energy triggers and can therefore be treated as invisible particles. The control region for Z bosons decaying to a pair of electrons is triggered by a set of unprescaled single electron triggers. Details about the trigger selections and efficiencies are found in section 5.4.

The event selection to single out the processes of interest follows table 5.1. Defining the particle-level and reconstruction-level as similar as possible reduces the amount of physics extrapolation in the unfolding procedure. This extrapolation would have to be modeled by the Monte Carlo simulation in addition to the detector induced effects.

The missing transverse momentum is required to be greater than 200 GeV in the signal and control regions. Here the advantage of defining the charged leptons from the Z boson decay as invisible becomes obvious, as no separate selection needs to be applied.

No leptons are allowed in the event. In the signal region any selected lepton thus vetoes the event. In the two-lepton control regions any additional lepton, aside from the two leptons from the Z boson decay, rejects the event.

In order to suppress the large QCD background, giving rise to multijet final states, a $\Delta\phi > 0.4$ between the ϕ direction of the missing transverse energy and the first four leading jets is required. These multijet final states should be largely suppressed by the requirement of large missing transverse momentum. However, mismeasurements of single jets may result in large missing transverse momenta and the large cross section of this process at a hadron collider makes this a sizable contribution. If the missing transverse momentum is caused by a mismeasured jet it will also point into the direction of the mismeasured jet. Therefore a minimal $\Delta\phi$ between E_T^{miss} and jets suppresses this contribution (referred to as jet- E_T^{miss} veto).

In the ≥ 1 jet signature a leading jet with $p_T > 120$ GeV in the central part of the detector $|\eta| < 2.4$ is required. This is motivated by the recoil of the jet against the Z boson, which will largely balance the missing transverse momentum from the decay products.

In the VBF signature two high energy, forward jets are expected. Therefore p_T cuts of 80 GeV and 50 GeV for the leading and subleading jet, respectively, are required. The jets are forced to point in forward direction by requiring a large invariant mass of the leading dijet system, as introduced in equation 5.3. Finally, a central jet veto is employed, which suppresses events with additional jets in the rapidity gap between the two leading jets. This suppresses the QCD production of a Z boson coming from the diagram depicted in figure 5.5, where the color connection between the two leading jets results in additional QCD activity between them.

Additionally, for the two control regions two same flavor, opposite sign leptons (e, μ) are required. The invariant mass of the dilepton system is furthermore required to be within 50 GeV of the Z boson mass ($66 < m_{ll} < 116$). The leading leptons must have a transverse momentum larger than 80 GeV.

Trigger Selection and Efficiency

Triggering the events of interest is crucial for an analysis performed at ATLAS. The signatures of interest need to be defined before the data is taken, as non-triggered data is irretrievably lost (see section 2.2).

This analysis targets large amounts of missing energy which is why trigger items with E_T^{miss} are defined. As the energy resolution at trigger-level is not as good as in the offline analysis (not all calibrations are feasible at HLT), the trigger threshold needs to be below the thresholds applied in the analysis. However, very low thresholds would occupy too much bandwidth in the readout system. Therefore very low thresholds are prescaled, meaning not every event that satisfies the trigger condition is written out. This reduces statistics in exchange for a smaller bandwidth. Which trigger is prescaled and by how much depends on the run conditions and may change over the course of a data taking period.

In this analysis the lowest unprescaled trigger is chosen in every run period. Assuring the highest possible statistics with the lowest available threshold. The missing E_T triggers are defined as follows:

- 2015 all periods: HLT_xe70_mht,
- 2016 periods A-D3: HLT_xe90_mht_L1XE50,
- 2016 periods D4-L: HLT_xe110_mht_L1XE50,

triggering events at 70 GeV in 2015, and 90 GeV and 110 GeV in different periods of 2016 [146]. In all cases the HLT trigger is seeded by events passing the Level-1 trigger with missing transverse energy above 50 GeV and E_T^{miss} is calculated from jets only, but including a correction for the soft term. These triggers apply for the signal region as well as the two-muon control region. This is because the HLT missing energy algorithms do not

use muon information and they are thus treated as invisible. A two-muon decay therefore has the same signature as a two-neutrino decay.

The control region targeting Z boson decays to electrons is triggered using single electron triggers. A logical OR of all lowest unprescaled triggers is used. In 2015 these are

- HLT_e24_lhmedium_L1EM20VH,
- HLT_e60_lhmedium,
- HLT_e120_lhloose,

and in 2016

- HLT_e24_lhtight_nod0_ivarloose,
- HLT_e24_lhmedium_nod0_L1EM20VH,
- HLT_e26_lhtight_nod0_ivarloose,
- HLT_e60_lhmedium_nod0,
- HLT_e60_lhmedium,
- HLT_e140_lhloose_nod0,
- HLT_e300_etcut,

where HLT_e24_lhtight_nod0_ivarloose is used in periods A-D3 and HLT_e24_lhmedium_nod0_L1EM20VH is necessary in order to recover the full statistics due to an autoprescale error in period A. HLT_e26_lhtight_nod0_ivarloose is used starting in period D4, while all others are applied throughout the year 2016 [147]. The triggers use a likelihood discriminant for the electron identification, paired with thresholds between 24 GeV and 300 GeV, depending on the applied working point of this discriminant.

In the following the trigger efficiencies of events in the signal and control regions are investigated. For this purpose all selections according to section 5.4 are applied, except for the trigger and the requirement of missing transverse momentum greater 200 GeV.

All events are counted in bins of the missing transverse momentum, before and after applying the trigger strategy detailed above. The ratio between the two defines the trigger efficiency as a function of the calibrated (offline) missing transverse momentum introduced in this chapter.

Figure 5.6 shows the resulting trigger efficiencies in the signal region. The two control regions can be found in appendix F. In 2015 the trigger efficiency in data is greater than 99% in the signal region (i.e. for $E_T^{miss} > 200$ GeV) (figure 5.6a), while in 2016 the efficiency is greater 97% (figure 5.6b). In the Monte Carlo simulation (MC) the trigger efficiency is greater than 99% in the signal region for the triggers applied in 2015 (figure 5.6c) and 2016 (figure 5.6d).

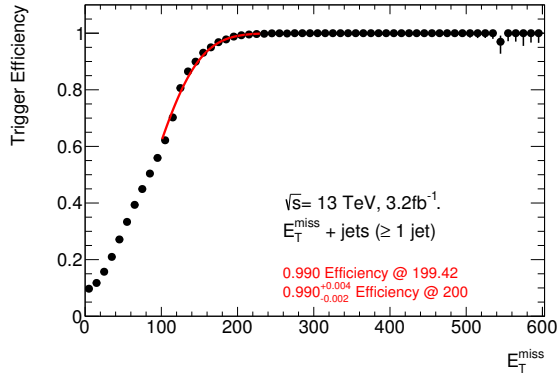
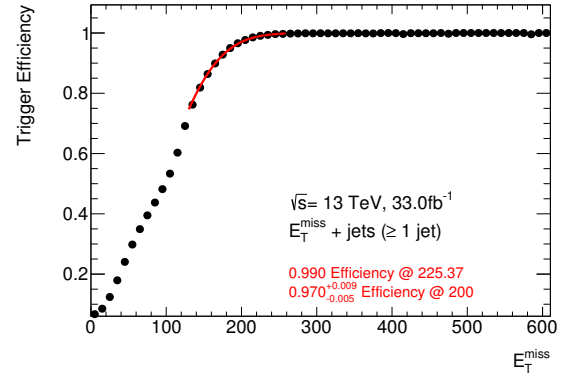
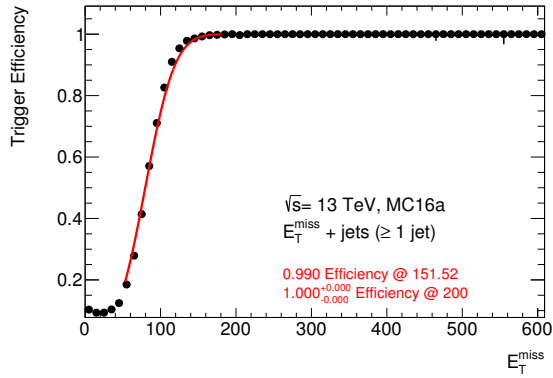
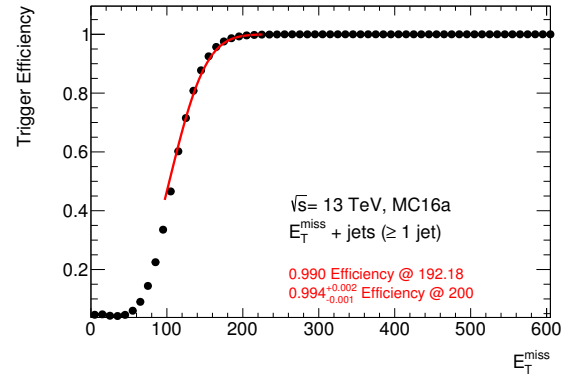
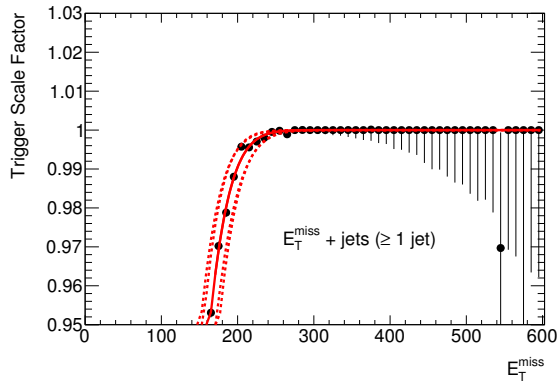
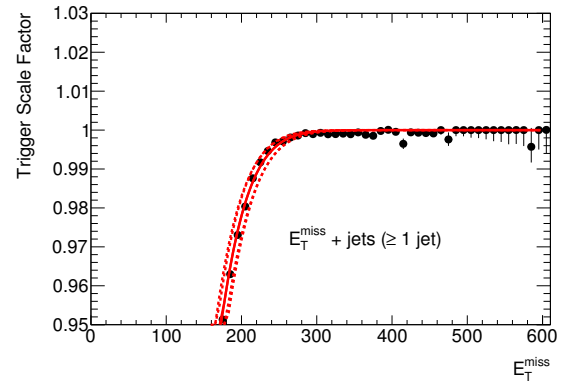
(a) *trigger turn-on in 2015 data*(b) *trigger turn-on in 2016 data*(c) *trigger turn-on MC: 2015 triggers*(d) *trigger turn-on MC: 2016 triggers*(e) *scale factors for 2015 trigger simulation*(f) *scale factors for 2016 trigger simulation*

Figure 5.6: Trigger turn on curves for the trigger strategies applied in 2015 and 2016, for data (top row), Monte Carlo simulation (middle row) and the ratio of both resulting in the correction factor applied to the Monte Carlo simulation (bottom row).

Table 5.2: *The trigger efficiency as a function of E_T^{miss} for data is divided by the same trigger efficiency for the Monte Carlo simulation. The resulting plot is fitted, using an error function with two parameters p_1 and p_2 to determine the correction factors applied to the Monte Carlo simulation. The parameters p_1 and p_2 as they are returned from the fit are displayed.*

parameter	p_1	p_2
2015	77 ± 12	52 ± 5
2016	52 ± 8	74 ± 3

The ratio between the trigger efficiencies of data and Monte Carlo simulation serves as a correction (scale factor) applied to the Monte Carlo simulation. As illustrated in figure 5.6e and 5.6f the scale factors near the E_T^{miss} threshold of 200 GeV are of the order of 1% and 2% for the triggers applied in 2015 and 2016 respectively.

A fit is performed using the error function

$$0.5 \cdot \left[1 + \text{Erf} \left(\frac{x - p_1}{\sqrt{2p_2^2}} \right) \right] \quad (5.5)$$

the parameters p_1 and p_2 as estimated by the fit are given in table 5.2. The fitted errorfunction is shown in figures 5.6e and 5.6f together with its uncertainties. The dashed uncertainty lines correspond to the fit function with the parameters varied up and down one at a time, by one standard deviation.

For the two control regions the trigger efficiencies for the trigger selection in 2015 and 2016 are greater than 99% in all bins of E_T^{miss} . This holds for data as well as the Monte Carlo simulation. The resulting trigger scale factors are all statistically compatible with unity, which is why no trigger scale factors are applied in the control regions.

5.5 Backgrounds

Background estimates are taken from the Monte Carlo simulations of the various contributing Standard Model processes. The full list of simulated Monte Carlo samples can be found in appendix D.

The QCD multijet background contributing to the signal region is estimated using a data-driven technique, since the multijet in Monte Carlo simulations is rather imprecise in this phase space. QCD multijets are largely suppressed by the requirement of large missing transverse momentum, since there is no real E_T^{miss} in the event. However, mismeasured jets can result in an imbalance in the transverse plane which is reconstructed as missing transverse energy. Most of this background is further suppressed by requiring a large azimuthal angle $\Delta\phi$ between the missing transverse energy and the first four leading jets, however, the large cross section of multijet events still makes it a sizable background.

In order to estimate this background the jet smearing technique described in [4] is used. A set of well-measured dijet events which are required to have almost no missing transverse momentum is selected, which serve as seed events. The jets from these events are smeared according to the jet energy resolution. By applying a random jet smearing 1000 times to the seed events, a large pseudo data set is generated which contains events with large quantities of missing transverse energy. For the correct normalization a control region is defined which resembles the signal region with only the jet- E_T^{miss} veto being inverted. This multijet enriched control region is selected in data and other contributing backgrounds are subtracted using Monte Carlo simulation. What remains is the dijet spectrum in the multijet enriched control region. For each bin in the observable of interest a transfer factor is now derived by selecting the signal region and multijet enriched control region in the “smeared” pseudo-dataset. The ratio of the two defines a transfer function between the two regions and can be used to obtain a multijet estimate in the signal region [148].

Additionally, non-collision backgrounds (NCB) might have an effect on the signal region. These are signals recorded by the detector, not coming from particle collisions, but which are supplemental signals from cosmic particles, detector noise or beam-backgrounds. These signals are expected to be low in energy, which is why an effect is only expected in the low E_T^{miss} region of the ≥ 1 jet signature. NCB is largely suppressed by the jet quality requirements, such that only small contributions are expected. The requirement of at least two jets in the VBF signature, suppresses events recorded due to NCBs.

The low E_T^{miss} region was investigated for clear signatures of NCB and a slight increase of events with the leading jet at the end of the tracker at $\eta = 2.5$ and $\phi = 0, \pi$ is observed. The latter is a distinct signature for non-collision background [149]. The fact that it originates mainly from regions outside the tracker, indicates that electrons might be identified as jets and the jets are not tagged as NCB by the rejection cuts. More details on the NCB study are found in appendix G. For a proper determination of the non-collision backgrounds further investigations are necessary. Since the effect is expected to be small it is ignored in this work.

5.6 Uncertainties

Measuring the binned distribution of an observable corresponds to performing a counting experiment in every bin. Thus, for measured data each bin follows a Poissonian distribution with an uncertainty of $\sigma \approx \sqrt{n_{obs}}$. As introduced above, the Monte Carlo simulation does not simulate each event according to the underlying distributions, but rather flat or in slices of a given observable and reweights the simulated events to the corresponding cross section. This way low statistics bins can be populated more efficiently and computation time is minimized. In addition, the Monte Carlo simulation is reweighting for pileup and scale factors to correct for known disagreements between data and Monte Carlo simulation. Furthermore, it is scaled to the corresponding integrated luminosity. The uncertainty is thus assumed to be Gaussian distributed, which for simulation is a good approximation

according to the central limit theorem, as all bins are well populated.

As indicated in section 4.2, the statistical uncertainties can also be determined via bootstrapping. In this work 5000 replicas of each event are filled into the replica-histograms and the uncertainty is determined according to equation 4.18. Here, too, the uncertainty is thus assumed to follow a Gaussian distribution. In the unfolded distribution bin-to-bin migrations introduce correlations, which affect the statistical uncertainties on individual bins. The bootstrapped histograms provide a distribution of bin counts for each bin according to their probability density, allowing for an exact description of the uncertainty on the unfolded results.

Experimental Systematic Uncertainties

Calibrating the observed final state particles to the correct energy scale is crucial, especially when calculating complex observables like the missing transverse momentum E_T^{miss} . From the methods and measurements used to calculate the calibrations (see Section 2.3), uncertainties are derived and are propagated as nuisance parameters. This allows to vary the calibrations within their uncertainties and to study the effect on the result. The uncertainties on the energy scales and resolutions of all physics objects are propagated, by recalibrating all objects within their uncertainties and repeating the measurement. The calibration is varied by one standard deviation ($+1\sigma$ and -1σ) of a nuisance parameter and one physics object (jets, electrons, muons, taus) at a time (rows 1-7 of table 5.3). The relative shifts of the final distributions with respect to the nominal distribution is taken as an uncertainty. For the jet energy resolution uncertainty applied in this work and the E_T^{miss} soft term resolution, which also comes with an uncertainty (rows 8-9 of table 5.3), only the $+1\sigma$ variation is provided. The down-variation is approximated by symmetrizing the up-variation. Initially each nuisance parameter corresponds to a specific parameter or object which is varied in the uncertainty estimation. However, in order to reduce computation times, the uncertainties are also provided in combined subsets of the initial nuisance parameters. In the combination the least correlated variables are iteratively combined by adding their uncertainties in quadrature. Thereby the meaning of the nuisance parameters is lost, as well as some correlation information [150]. Using all nuisance parameters in conjunction with the computationally intensive bootstrapping is not feasible for this work. Thus, the conservative uncertainty due to the reduced set of nuisance parameter is accepted.

When estimating the systematic uncertainty on the results due to each of the nuisance parameters, the bootstrap method is exploited to obtain a realistic uncertainty on the systematic shift. The systematically varied distribution is highly correlated to the nominal one. Using the bootstrap replicas and dividing the systematically varied distribution by the nominal one replica-by-replica takes these correlations into account. The mean value of the replicas of the divided histograms provides the systematic uncertainty for each bin and the root-mean-square, provides the uncertainty thereof. Due to the respected correlations the latter provides a better estimate, than the one obtained from error propagation of only two divided histograms (see appendix E).

Table 5.3: *Experimental systematic variations and their corresponding nuisance parameters.*

Systematic variation	nuisance parameter
jet energy scale	JET_EtaIntercalibration_NonClosure_highE
	JET_EtaIntercalibration_NonClosure_negEta
	JET_EtaIntercalibration_NonClosure_posEta
	JET_Flavor_Response
	JET_GroupedNP_1
	JET_GroupedNP_2
jet energy resolution	JET_GroupedNP_3
	JET_RelativeNonClosure_MC16
	JET_JER_DataVsMC
	JET_JER_EffectiveNP_1
	JET_JER_EffectiveNP_2
	JET_JER_EffectiveNP_3
	JET_JER_EffectiveNP_4
JET_JER_EffectiveNP_5	
electron energy scale	JET_JER_EffectiveNP_6
	JET_JER_EffectiveNP_7restTerm
electron energy resolution	EG_SCALE_ALL
muon energy scale	EG_RESOLUTION_ALL
	MUON_SCALE
	MUON_SAGITTA_RHO
muon track resolution	MUON_SAGITTA_RESBIAS
	MUON_ID
tau energy scale	MUON_MS
	TAUS_TRUEHADTAU_SME_TES_DETECTOR
	TAUS_TRUEHADTAU_SME_TES_INSITU
E_T^{miss} soft term scale	TAUS_TRUEHADTAU_SME_TES_MODEL
	MET_SoftTrk_Scale
E_T^{miss} soft term resolution	MET_SoftTrk_ResoPara
	MET_SoftTrk_ResoPerp
electron reconstruction efficiency	EL_EFF_Reco_TOTAL_1NPCOR_PLUS_UNCOR
electron identification efficiency	EL_EFF_ID_TOTAL_1NPCOR_PLUS_UNCOR
muon reconstruction efficiency	MUON_EFF_RECO_STAT
	MUON_EFF_RECO_SYS
	MUON_EFF_RECO_STAT_LOWPT
	MUON_EFF_RECO_SYS_LOWPT
muon isolation efficiency	MUON_EFF_ISO_STAT
	MUON_EFF_ISO_SYS
muon track-to-vertex-association efficiency	MUON_EFF_TTVA_STAT
	MUON_EFF_TTVA_SYS
trigger scale factors	TRIG_SF_P1
	TRIG_SF_P2
pileup reweighting	PRW_DATASF

Additionally to the calibration of the physics objects, the. In addition to the uncertainties on the energy scales and resolutions, uncertainties arise from selection efficiency mismodeling for leptons. The operation points for the lepton selection are provided with so-called scale factors, which account for these known differences (estimated in dedicated measurements [39, 151, 138]). These scale factors are modifications to the event weight (per lepton) and have an uncertainty which has to be propagated to the final result. As before the scale factors are varied within their uncertainty and the measurement is repeated (rows 10-14 of table 5.3).

Additional uncertainties come from the pileup reweighting, as well as the scale factors introduced in section 5.4. Both modify the event weight and thereby reweight the final distributions to better model the measured data. Again varying this reweighting or the parameters thereof (in case of the trigger scale factors) yields an uncertainty on the final result (rows 15-16 of table 5.3).

Theoretical Systematic Uncertainties

The simulation of the Standard Model as well as new physics models is done using fixed-order perturbation theory. Higher-order terms are neglected which introduces an uncertainty on the calculated cross section. To quantify the effect of possible higher order corrections the QCD renormalization and factorization scales (see section 3.1) are varied up and down by a factor of 2 (first row of table 5.4). As for the experimental uncertainties the measurement is repeated and the shift with respect to the nominal variation is taken as an uncertainty. The envelope of the 7-point scale variations are taken as a systematic uncertainty on the final result.

The parton density functions (PDF) used to parametrize the contributions to different initial state partons are determined by dedicated groups, which fit measured data for the most probable composition of the proton. The PDF sets are provided with n error sets accounting for different free parameters in the fit and measurement uncertainties of the fitted data. For the NNPDF30_nnlo_as_0118 PDF set there are $n = 101$ variations [123] (second row of table 5.4). The total uncertainty on the PDF set is determined by the Standard deviation of all PDF variations:

$$\delta^{\text{PDF}}\sigma = \sqrt{\frac{1}{n-1} \sum_{k=1}^n (\sigma^{(k)} - \langle\sigma\rangle)^2} \quad (5.6)$$

with

$$\langle\sigma\rangle = \frac{1}{n} \sum_{k=1}^n \sigma^{(k)} \quad (5.7)$$

Furthermore, the value of the strong coupling α_S is determined via dedicated measurements and extrapolated to the relevant energy scale via the renormalization group equation. As the former yields experimental uncertainties on α_S and the latter is only calculated up to

Table 5.4: *Theoretical systematic variations and their corresponding nuisance parameters.*

Systematic variation	nuisance parameter
renormalization and factorization scale variation	MUR0.5_MUF0.5_PDF261000
	MUR0.5_MUF1_PDF261000
	MUR1_MUF0.5_PDF261000
	MUR1_MUF1_PDF261000
	MUR1_MUF2_PDF261000
	MUR2_MUF1_PDF261000
	MUR2_MUF2_PDF261000
nuisance parameter variation of default pdf set	MUR1_MUF1_PDF261001 ... MUR1_MUF1_PDF261100
variation of α_s	MUR1_MUF1_PDF269000 MUR1_MUF1_PDF270000
variation of pdf set	MUR1_MUF1_PDF13000 MUR1_MUF1_PDF25300

a certain order, this uncertainty has to be propagated to the calculated cross section. It is calculated by using PDF fits with different values of α_s and repeating the analysis (third row of table 5.4). The uncertainty on α_s is then determined by

$$\delta^{\alpha_s} \sigma = \frac{\sigma(\alpha_s = 0.119) - \sigma(\alpha_s = 0.117)}{2} \quad (5.8)$$

In accordance with [152] the PDF uncertainties as well as the uncertainties on α_s are combined by adding equation 5.8 and 5.6 in quadrature.

$$\delta^{\text{PDF}+\alpha_s} \sigma = \sqrt{(\delta^{\text{PDF}} \sigma)^2 + (\delta^{\alpha_s} \sigma)^2} \quad (5.9)$$

Finally, two other PDF sets (CT14nn1o [124] and MMHT2014nn1o68c1 [125]) apart from the nominal are used (last row of table 5.4). The shift with respect to the nominal PDF set is taken as uncertainty and added in quadrature to the other systematics.

Smoothing of Systematic Uncertainties

Additionally, a smoothing procedure is applied to the systematic uncertainties to minimize large fluctuations due to statistical limitations of the measurement. The bins of each spectrum of systematic uncertainties are iteratively combined until their Gaussian significance is larger than two standard deviations. The improved uncertainty estimate due to the bootstrapping technique provides the uncertainties used in this calculation. Finally, a Gaussian kernel smoothing obtains the values in the original binning [150].

5.7 Reconstruction-level Results

ATLAS data recorded in 2015 and 2016 is analyzed with a total integrated luminosity of 36.2 fb^{-1} . The analysis selection is applied and the observables are compared to their reconstruction-level prediction as generated by the Standard Model Monte Carlo simulation. The multijet background is estimated using a data-driven technique as described in section 5.5.

In the following the observables of interest in the signal and control regions of the ≥ 1 jet and vector boson fusion selection are displayed. The agreement between data and Monte Carlo simulation is generally good and the experimental and theoretical uncertainties cover all observed deviations. Displayed in figures 5.7-5.9 are the experimental uncertainties (derived as described in section 5.6) added in quadrature to the statistical uncertainties. The uncertainties listed in table 5.3 are assumed to be uncorrelated, hence they are added in quadrature for each bin. Furthermore, the theoretical uncertainties on the Monte Carlo predictions are displayed. They are calculated bin wise, according to the descriptions in section 5.6.

In the E_T^{miss} distribution of the ≥ 1 jet signal region (see figure 5.7a) an agreement at the level of 5% between data and the Monte Carlo prediction is observed and better agreement in the control regions (figures 5.8a and 5.9a). The first bin in the signal region has an increased disagreement of about 10%, which is most probably caused by non-collision background. The added statistical- and experimental systematic uncertainties are found to be between 13% (low E_T^{miss}) and 24% (high E_T^{miss}). The largest systematic uncertainty contribution originates from the jet energy scale and jet energy resolution uncertainties, with a combined uncertainty of $\sim 5\%$. All other systematic uncertainties contribute with less than 1%. Uncertainties in the control regions behave comparably, with additional uncertainties originating mostly from the lepton efficiencies. In both the two-electron and two-muon control regions these contribute with uncertainties of the order of 5% and 1-3%, respectively. The total systematic uncertainties range between 12% and 25% with the largest contribution being caused by the renormalization scale variations. These uncertainties are consistent between the signal and control regions.

The E_T^{miss} distribution in the VBF signal region shows a flat disagreement between data and Monte Carlo simulation of about 10% (figure 5.7b). Similar differences are observed in both control regions (figures 5.8b and 5.9b). The uncertainties are comparable to the ones observed in the ≥ 1 jet signature.

The m_{jj} distribution of the VBF signal regions shows a significant shape difference going from an underestimation of the Monte Carlo simulation of about 10% in the low m_{jj} bins, to an overestimate of about 20% in the high m_{jj} tail, above 1.5 TeV (figure 5.7c). This behavior is expected due to known modeling issues of the Sherpa simulation [153] and is also present in the two-muon control region (figure 5.9c). The two-electron control region (figure 5.8c) shows a similar behavior until 1.5 TeV. However, above 1.5 TeV no overestimation of the Monte Carlo simulation is observed, but the ratio between data and simulation fluctuates high, statistically compatible with one. The experimental uncertainties are comparable to the ones observed in the E_T^{miss} distributions. The theo-

retical uncertainties are slightly larger, ranging between 15% and 30%, thus, covering all observed deviations.

The $\Delta\phi_{jj}^{sng}$ distribution of the VBF signal regions is modeled well for large absolute values of $\Delta\phi_{jj}^{sng}$, with a considerable underestimation of the simulation of $\sim 15\%$ when $\Delta\phi_{jj}^{sng}$ tends towards zero (figure 5.8d). The same behavior is observed in the control regions, where only the bin at zero is compatible with one and deviates by 5% in the two-electron and two-muon control region, respectively (figures 5.8d and 5.8d). As in the m_{jj} distribution this mismodeling has been observed before in the Sherpa simulations [153] and is covered entirely by the theoretical uncertainties.

The ratio R_{miss} (see equation 8.11) between the signal region and the per-bin-average of the two control regions is displayed in figure 5.10. The observed ratio is found to be compatible with its reconstruction-level prediction. The outliers in the first bin of the E_T^{miss} distribution and the central bin in the $\Delta\phi_{jj}^{sng}$ distribution both deviate by roughly two standard deviations. The trend in the m_{jj} distribution is caused by the different behavior of data and Monte Carlo simulation in the high m_{jj} range of the two-electron control region, compared to the signal and two-muon control region. However, all data points are still compatible with their prediction within less than two standard deviations.

The size of the uncertainties is comparable between the signal region and the per-bin-average of the two control regions, in all observables. The theoretical uncertainties thus cancel each other to $\sim 1\%$ precision across all bins of the E_T^{miss} distributions. Similar behavior is observed for the jet energy scale and resolution uncertainties, where the uncertainties cancel down to a percent level, except for the highest E_T^{miss} bins ($\sim 4\%$). The largest experimental uncertainty of the order of 2.5% - 3.5% originates from the lepton efficiencies. In the high E_T^{miss} - and m_{jj} region, the ratio measurement is statistically limited, with statistical uncertainties of $> 20\%$. This is driven by the denominator, where the total number of observed events is about a factor of 20 smaller than in the numerator. Combining the two control regions doubles the statistics, nevertheless, it remains the limiting factor.

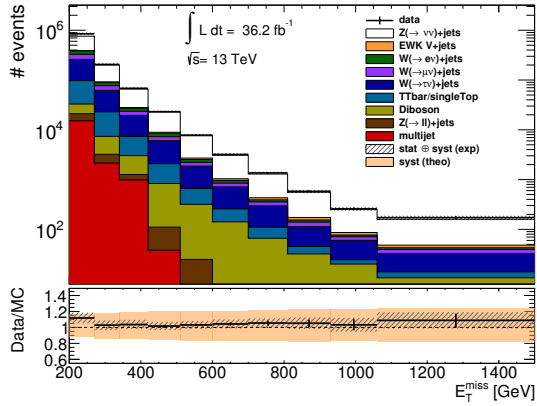
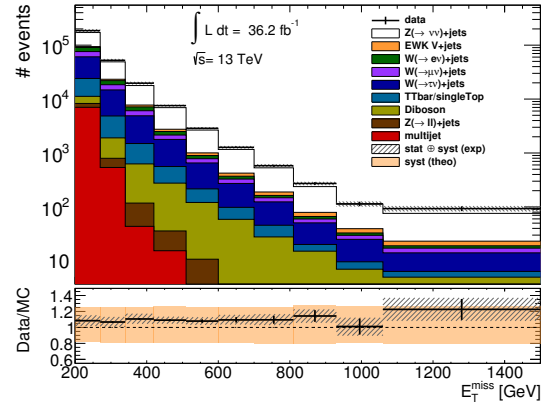
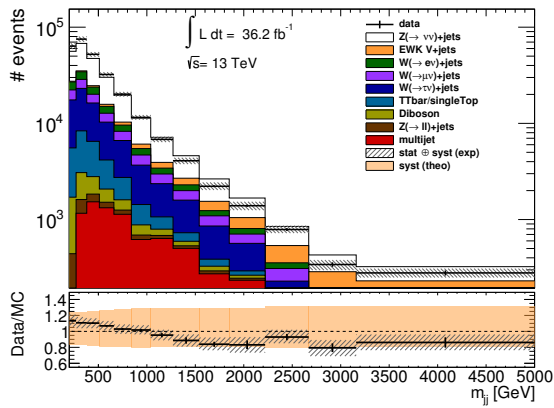
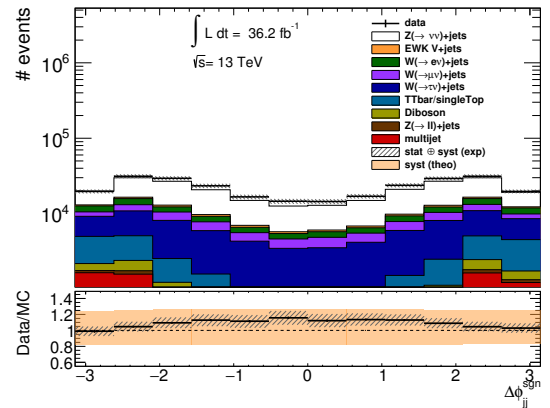
(a) E_T^{miss} in ≥ 1 jet phase space(b) E_T^{miss} in VBF phase space(c) m_{jj} in VBF phase space(d) $\Delta\phi_{jj}^{\text{sgn}}$ in VBF phase space

Figure 5.7: Agreement of data and Monte Carlo simulation for zero-lepton signal region. Theoretical systematic uncertainties are displayed only in the ratio panel.

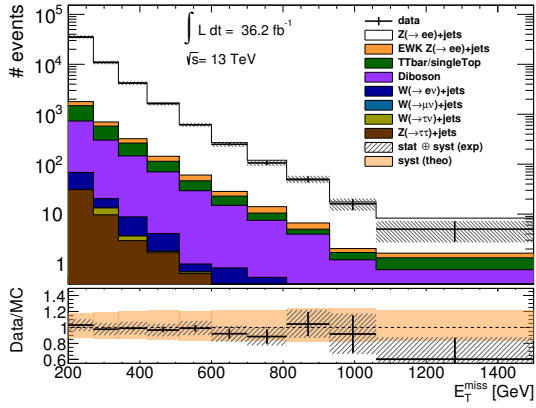
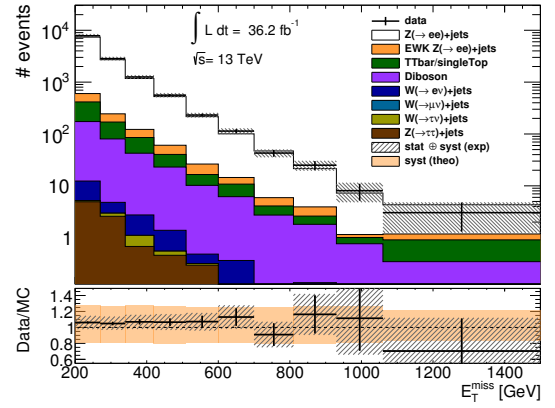
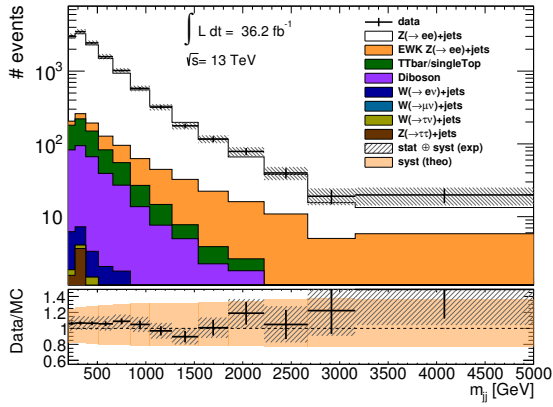
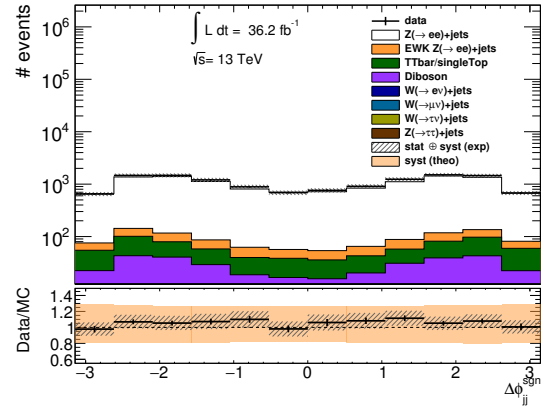
(a) E_T^{miss} in ≥ 1 jet phase space(b) E_T^{miss} in VBF phase space(c) m_{jj} in VBF phase space(d) $\Delta\phi_{jj}^{sgn}$ in VBF phase space

Figure 5.8: Agreement of data and Monte Carlo simulation for two-electron control region. Theoretical systematic uncertainties are displayed only in the ratio panel.

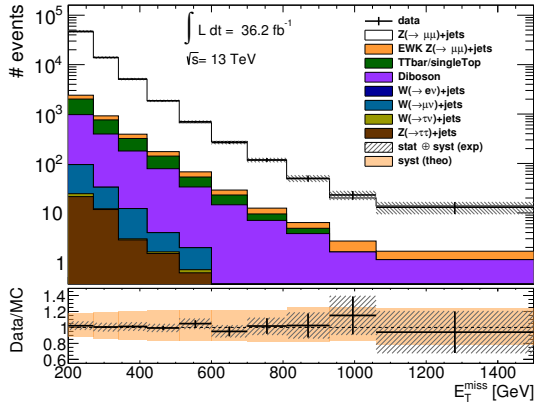
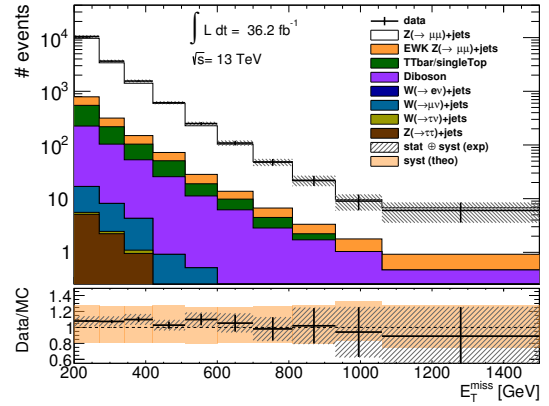
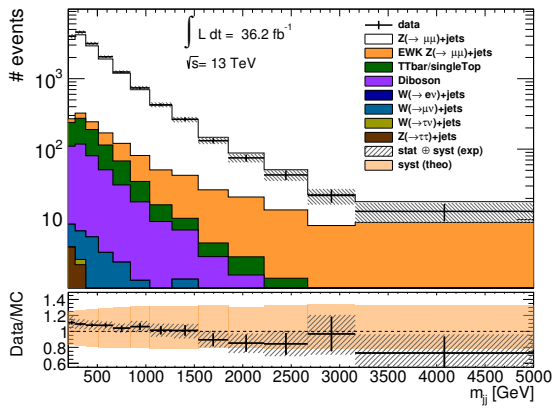
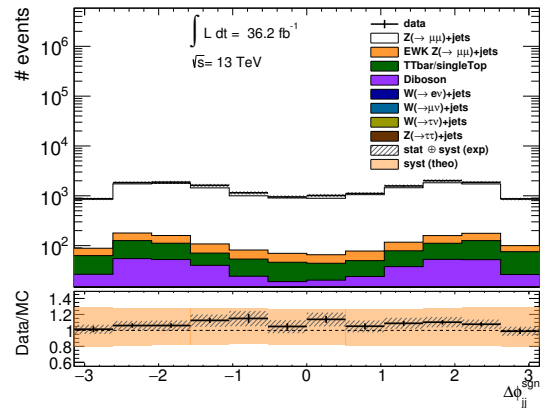
(a) E_T^{miss} in ≥ 1 jet phase space(b) E_T^{miss} in VBF phase space(c) m_{jj} in VBF phase space(d) $\Delta\phi_{jj}^{sgn}$ in VBF phase space

Figure 5.9: Agreement of data and Monte Carlo simulation for two-muon control region. Theoretical systematic uncertainties are displayed only in the ratio panel.

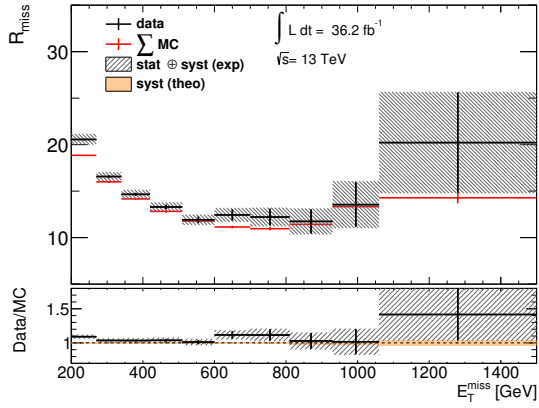
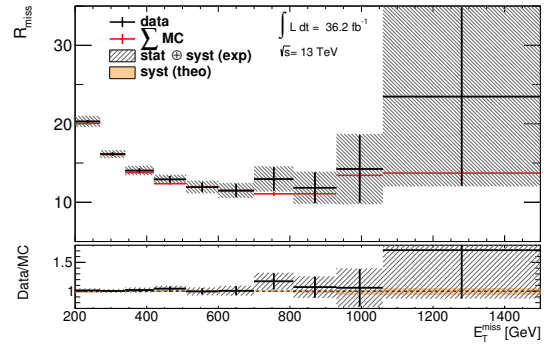
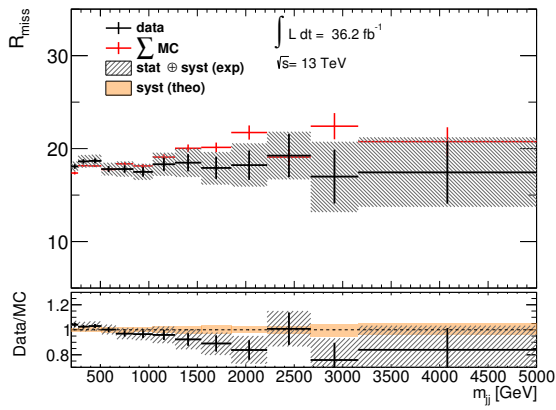
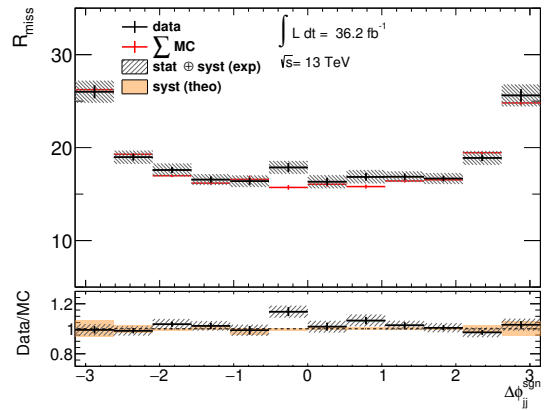
(a) E_T^{miss} in ≥ 1 jet phase space(b) E_T^{miss} in VBF phase space(c) m_{jj} in VBF phase space(d) $\Delta\phi_{jj}^{sgn}$ in VBF phase space

Figure 5.10: Agreement of ratios R_{miss} between data and Monte Carlo simulation. Theoretical systematic uncertainties are displayed only in the ratio panel.

Chapter 6

Correcting for Detector Effects

The reconstruction-level results presented in the previous chapter are unfolded to particle-level, in order to be able to compare the results directly to possible BSM models. This chapter introduces the unfolding strategy applied in this search. First, the optimized binning, which is already used at reconstruction-level is motivated in section 6.1. Afterwards, the investigation of two different possible approaches for the unfolding strategy are presented (section 6.2). The unfolded distributions are presented in section 6.3.

In order to correct the measured distributions for detector effects the unfolding method introduced in section 4.2 is employed. The particle-level and reconstruction-level event selection introduced in section 5.3 and 5.4 ensure a kinematically similar selection. The only difference apart from the calibrated energy of the objects are measurement-related cuts, like the data quality cuts and the rejection of non-collision background jets. This minimizes the extrapolation performed by the unfolding method and mostly detector effect are corrected for.

The measured observables have a finite resolution causing events to migrate from one reconstructed bin into another particle-level bin. The size of this resolution depends on the observable. As introduced in chapter 4 the unfolding can generally be split into three different corrections: purity correction, resolution effects and stability correction. In the resolution correction the migrations are treated and the uncertainties and correlations are accounted for. However, in order to reduce the amount of migrations due to the resolution correction, the bin width can be optimized.

6.1 Binning Optimization for Observables

Optimizing the bin width needs to balance two effects. On the one hand the migrations in the unfolding need to be minimized, which can be achieved by choosing very large bins. On the other hand as much of the shape information of the observable as possible needs to be retained, requiring as small bins as possible.

If the bin size is chosen at the size of the resolution about 60% of the events will migrate to the neighboring bin and about 13% will even migrate to next-to-neighboring bins. On the other hand, if the bin is four times as wide as the resolution of the observable an event falling perfectly into the middle of a bin will migrate to neighboring bins in only 5%

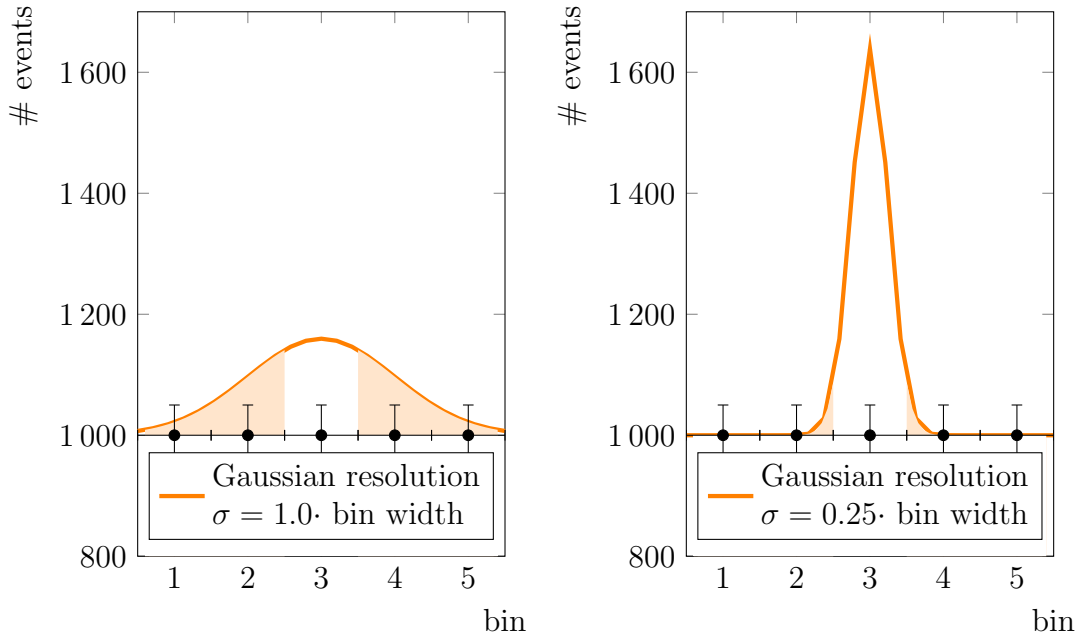


Figure 6.1: *Illustration of events migrating from one bin to another due to the finite detector resolution. (left) If the bin width is chosen at the size of the resolution $\sim 60\%$ of these events migrate, $\sim 13\%$ even to next-to-neighboring bins. (right) If the bin width is chosen to be four times the resolution of the observable $\sim 5\%$ of the events in the middle of the bin migrate to neighboring bins.*

of the cases (assuming a Gaussian distribution for the resolution). Both these cases are illustrated in figure 6.1.

In this work the migrations are treated by the unfolding algorithm, so all migrations are accounted for. However, events with large uncertainties, introduced in the background subtraction, which are iteratively moved from one bin to another can propagate these uncertainties and create large correlations between bins. Furthermore, a possible mismodeling of the detector will be propagated, hence increasing a potential bias. The migration of events with large uncertainties is suppressed by the IDS algorithm (see section 4.2), however, reducing this from the beginning is desirable. A bin width of twice the resolution is chosen. This way about 31% of the events will migrate to neighboring bins, however, only a negligible amount of 2.7% to next-to-neighboring bins, suppressing correlations between multiple bins.

Another constraint is that the binning has to be identical for the same observable in all control regions as well as the signal region. This is because a ratio of the unfolded distributions is measured and the binning has to match in the division. Therefore the bin width is dictated by the region with the worst resolution for a particular bin. In order to achieve this the main contribution to the signal region and each control region is studied. These are the QCD production of Z bosons decaying to two neutrinos, to two electrons and to two muons, respectively.

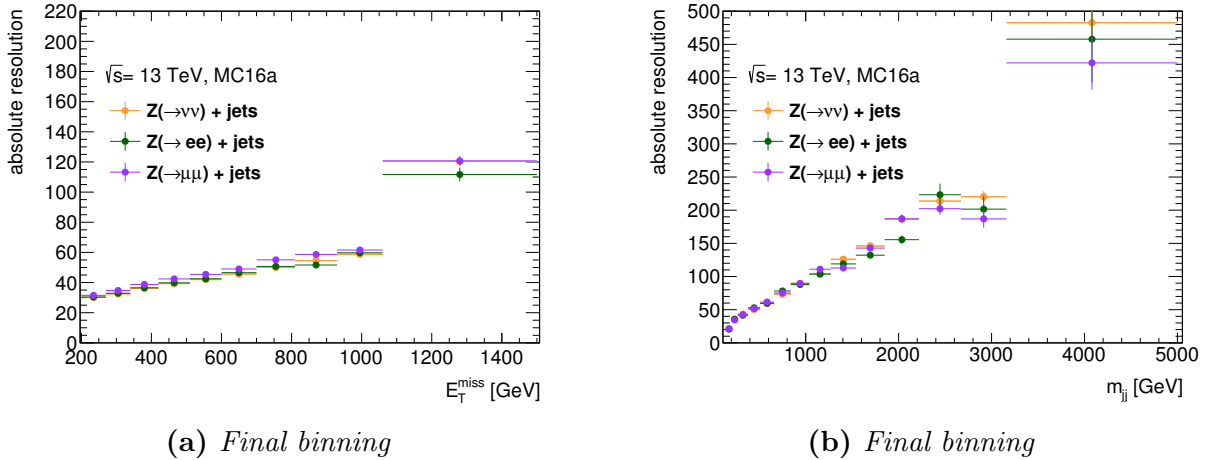


Figure 6.2: Absolute resolutions of (a) E_T^{miss} and (b) m_{jj} in bins of the reconstructed E_T^{miss} and m_{jj} respectively. Shown are the optimal binning for each channel after synchronizing the bin edges among the regions.

Starting with the E_T^{miss} observable the resolution is obtained from Monte Carlo simulation by analyzing the particle-level spectrum in a given E_T^{miss} -range. The root-mean-square (RMS) is used as the observable's resolution, rather than fitting a Gaussian and using its standard deviation, due to large tails in the distribution.

An iterative procedure is used to obtain the optimal binning for each of the three leading processes in the signal and control regions. Here the bin edges are always rounded to the next largest 10 GeV value. Afterwards, the bin edges between the processes are synchronized in a conservative way, meaning the largest bin size of all three processes is kept (details on the procedure are found in appendix H). An additional constraint requires a minimal amount of expected event per bin. This is to avoid empty bins and to ensure that the migrations are not statistically significant¹. An optimum of at least six events was determined.

Above 1.5 TeV there are less than 1 event expected in the E_T^{miss} distributions of the two control regions, which is why the last bin is cut off there. Likewise, the m_{jj} spectrum is cut off at 5 TeV. Figure 6.2 shows the absolute resolution within the optimized binning after synchronizing the bin edges between the signal and control regions, for both the E_T^{miss} and m_{jj} distribution. This includes the constraints on the minimal bin count and also excludes the underflow bin at 150-200 GeV (see below). The absolute resolutions of the individual channels and the corresponding relative resolutions can be found in appendix H.

For the unfolding one additional bin below the nominal cut values of 200 GeV in E_T^{miss} and m_{jj} is retained and filled when constructing the detector response. This way migrations

¹ Another technical issue is that the bootstrap replicas require a minimal amount of events per bin, since a replica may otherwise be left with only a single negative entry in the migration matrix. This would be unphysical and can be avoided with a minimal amount of events per bin, which reduces the probability for such a scenario.

into and out of the fiducial phase space are taken into account. The final phase space cuts are applied afterwards.

Only the E_T^{miss} and m_{jj} observables are optimized. The remaining measured observable $\Delta\phi_{jj}^{sgn}$ is expected to be comparably flat, which is why migration asymmetries as in a steeply falling spectrum (see figure 4.4) are not an issue. Furthermore, it is designed to differentiate between CP even and CP odd operators contributing to the coupling of the two vector bosons, which can be detected by a very coarse binning already. An equidistant binning of 12 bins in $[-\pi, \pi]$ is chosen, to avoid a finer, memory intensive binning.

6.2 Unfolding Strategies

Two possible unfolding strategies are considered in this work.

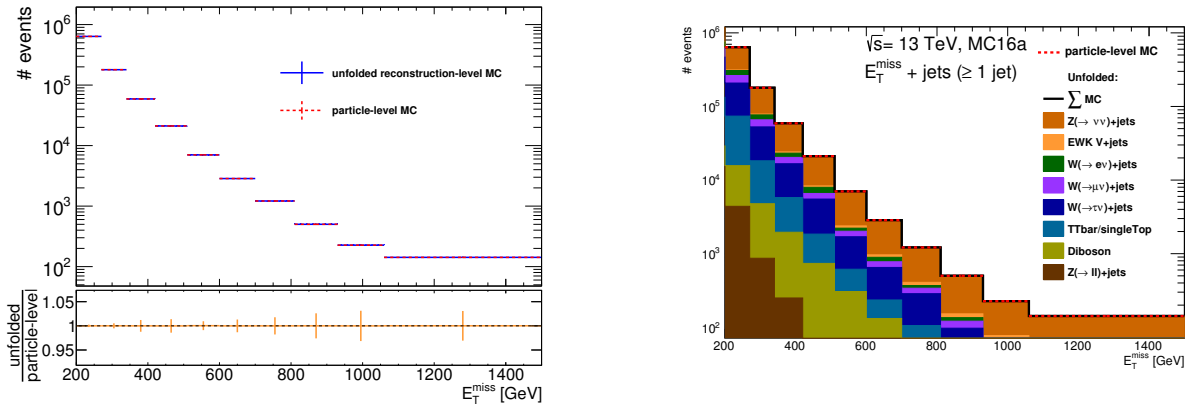
The first approach is to unfold the data without subtracting any backgrounds, but the entire topological selection, hence referred to as *topology unfolding*. In this work the signal region corresponds to the $E_T^{miss} + jets$ signature. Therefore, Z bosons decaying to neutrinos as well as W bosons with out-of-acceptance leptons are selected along with other minor backgrounds. In the unfolding, the detector response of the process under consideration is used, as it is expected to best describe the relation between particle- and reconstruction-level. Thus, in the topology unfolding strategy the response of the summed Standard Model contributions is used. Potential new physics contributions in the data need to be taken care of by the unfolding method as demonstrated in chapter 4. Backgrounds like multijets which do not contain any real E_T^{miss} and are therefore only reconstructed as fake events are subtracted before (this is equivalent to a larger purity correction). In the following studies the multijet background is therefore excluded.

In the second approach all but the most dominant Standard Model contribution are subtracted from the data. What remains is the Standard Model process of $Z \rightarrow \nu\bar{\nu} + jets$ in the signal region, plus potential new physics contributions. In this scenario the detector response is consequently taken from the Monte Carlo simulation of that process. An advantage of this strategy is, that data-driven background estimates can be used, reducing the Monte Carlo simulation and thus the theory dependence.

Both of the strategies mentioned above can be applied in a completely analogous way to the two control regions, in which a $Z \rightarrow l^+l^- + jets$ topology is selected.

Topology unfolding

The detector response used in the unfolding method has to describe the event selection probabilities at particle- and reconstruction level as good as possible. Different processes have different event topologies in the signal region, leading to varying efficiencies and acceptances of the produced particles, which modify the event selection probability. In the presented signal region an event with a leptonically decaying W will only pass the particle-level selection, if the lepton is out of the detector acceptance. This forward topology is very different from a Z boson decaying to neutrinos, which will decay mostly in the central part



(a) Unfolded sum of Monte Carlo simulations closes with particle-level expectation

(b) Stacked unfolded contributions (colored) close with particle-level expectation

Figure 6.3: Topology unfolding applied to all Standard Model contributions in the ≥ 1 jet signal region. The detector response is retrieved from the sum of the same set of Monte Carlo simulations. (a) Unfolding the E_T^{miss} distribution of the sum of Monte Carlo simulations shows perfect closure with the particle-level prediction. (b) Equivalently every simulated contribution is unfolded separately and the (stacked) sum of them closes also with the particle-level expectation.

of the detector, due to the high E_T^{miss} requirement. At reconstruction-level this may lead to a modified resolution of reconstructed variables like the E_T^{miss} . In the case of topology unfolding the idea is to unfold the data as it is measured, without subtracting any of the Standard Model backgrounds. This requires the detector response for all possible processes in the selection. Naturally the sum of all contributing Standard Model processes scaled to the integrated luminosity of the data are used. In the following this is referred to as the *topology response*.

Using the reconstruction-level prediction of the Monte Carlo simulation as a proxy for data, it can be shown that this detector response perfectly recovers the corresponding particle-level prediction, as shown in figure 6.3a. As the unfolded Monte Carlo simulation is simply the sum of its Standard Model contributions, this is equivalent to unfolding each contribution separately using the above mentioned topology response. When adding these unfolded contributions back together the particle-level prediction is recovered, as illustrated in figure 6.3b.

Mathematically, the closure demonstrated in figure 6.3a is expected, since the detector response is defined to map from exactly this reconstruction-level distribution to this exact particle-level distribution.

Biases due to the Purity/Stability Corrections

When unfolding each Monte Carlo simulation contribution separately the use of the topology response is not expected to achieve this closure. This is because the event selection

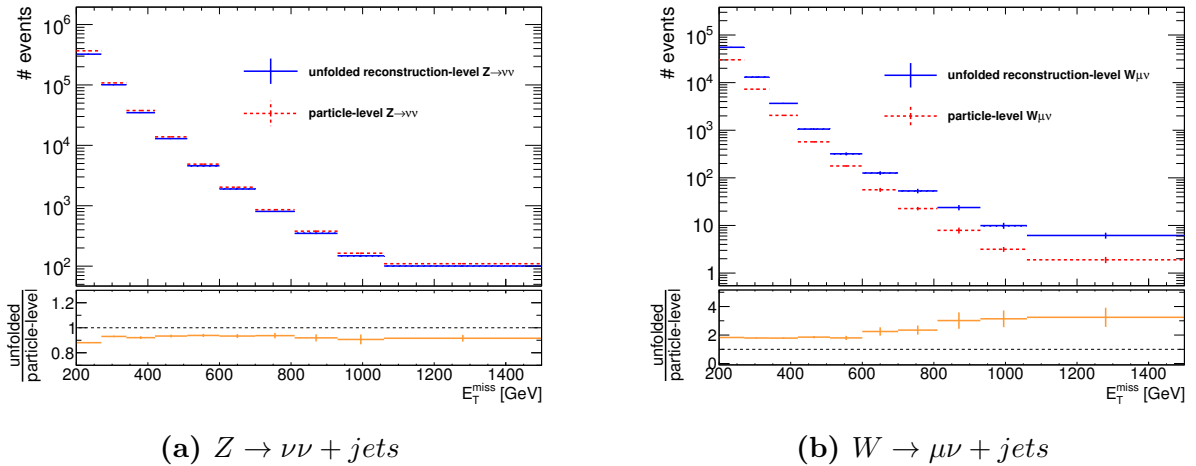


Figure 6.4: Topology unfolded Monte Carlo simulation processes contributing to the ≥ 1 jet signal region. Unfolding the E_T^{miss} distribution of the (a) $Z \rightarrow \nu\nu + jets$ and (b) $W \rightarrow \mu\nu + jets$ component shows a non-closure with the particle-level prediction.

efficiencies are not specific to this single process, as demanded above, but rather an average of all contributing Standard Model processes.

Figure 6.4 illustrates the bias on two of the topology-unfolded components to the signal region. The main Standard Model contribution $Z \rightarrow \nu\nu + jets$ deviates by 5%-10% from its particle-level prediction, while the $W \rightarrow \mu\nu + jets$ process deviates by 200%-300%. Figure 6.3b, however, shows that the biases of all individual processes, weighted with their fractional contribution, balance exactly in the result, where all unfolded processes are added together.

The biases are explained by the topology (averaged) detector response of all Monte Carlo simulation contributions used here. In the following the purity and stability corrections, which are applied in the unfolding using the topology response, are compared to the actual purity and stability of the different Standard Model processes. The corrections of the topology response are in most cases found to be very different from what is necessary according to the response of the individual processes.

Figure 6.5a shows the matching efficiency of particle-level events, which are selected in the ≥ 1 jet signal region, to their corresponding reconstruction-level selection. The efficiency is plotted as a function of E_T^{miss} . Any deviation from one means that events which are in the signal region at particle-level are missed at reconstruction-level and therefore need to be corrected for in the stability correction². Figure 6.5b shows the equivalent matching efficiency for reconstruction-level events. A deviation from one corresponds to faked events, which are reconstructed even though they are outside the fiducial phase space. This is corrected for in the purity correction.

A clear difference between the matching efficiencies of particle-level and reconstruction-

² Plotted in figure 6.5a is 1/stability correction since the stability correction maps from the resolution corrected data to particle-level and not vice versa as in the plot.

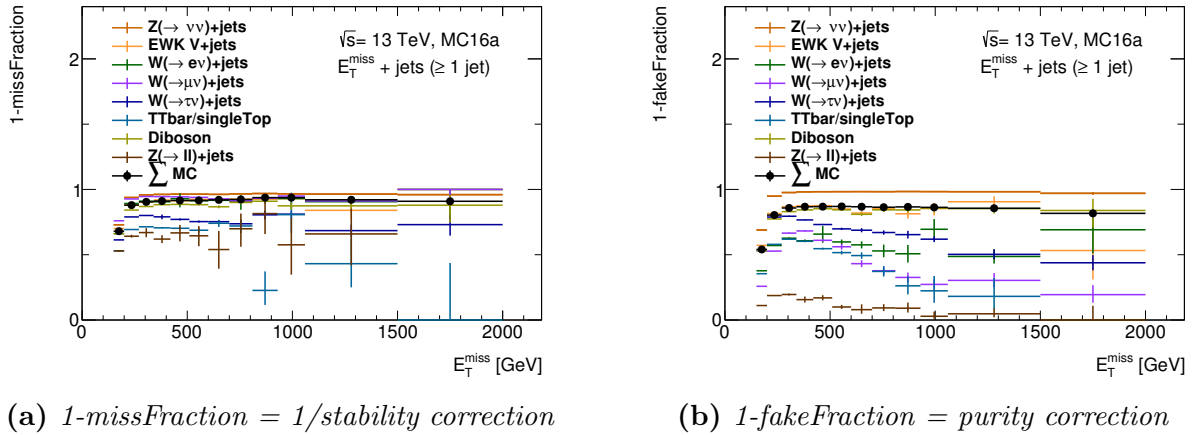
(a) $1\text{-missFraction} = 1/\text{stability correction}$ (b) $1\text{-fakeFraction} = \text{purity correction}$

Figure 6.5: Matching efficiencies for particle-level and reconstruction-level events to their respective reconstruction-level and particle-level counterpart. The efficiencies are plotted in the ≥ 1 jet signal region as a function of E_T^{miss} . The matching efficiencies are directly related to the stability and purity correction applied in IDS unfolding.

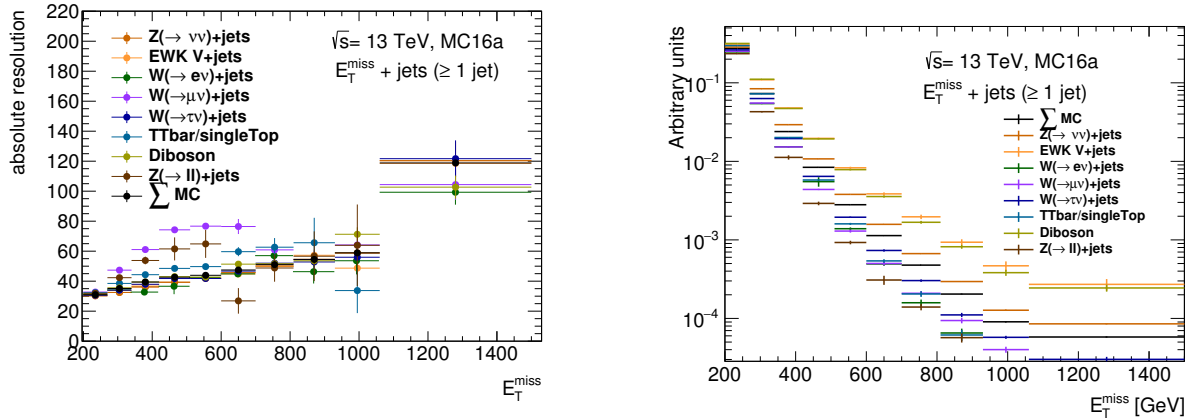
level events can be observed for the individual processes. The stability correction is rather similar for the individual processes, where mostly events including τ -particles are missed. This happens because hadronically decaying taus which are outside the p_T - or η -acceptance are misidentified as jets at reconstruction-level. These jets often point into the same direction as the missing transverse energy, as they decay in association with a neutrino and the jet- E_T^{miss} veto thus rejects the event. Additional misses come from the lepton veto, which rejects the event, when the τ is reconstructed within the acceptance of the detector.

The larger difference between the processes is found in the purity correction. Here events including out-of-acceptance muons are affected by the E_T^{miss} cut, since at reconstruction-level these muons will leave no detectable trace in the detector, hence contributing to the E_T^{miss} calculation³. At particle-level the muons are not added to the E_T^{inv} term, so events with only small amounts of E_T^{inv} may pass the reconstruction-level selection.

The largest effect, however, comes from the lepton identification efficiencies. Events which are vetoed at particle-level because of a lepton within the fiducial phase space are selected at reconstruction-level because the lepton is not reconstructed. This reconstruction efficiency drops as a function of E_T^{miss} , especially because the decay products become more collimated, resulting in a decreased efficiency of passing the isolation criterion.

The stability and purity corrections are non-iterative bin-wise correction factors on the distribution of interest. Large deviations as seen in figure 6.5b will therefore have an immediate effect on the unfolded spectrum. Especially leptonic processes are scaled very differently with the averaged purity correction than they are supposed to be, resulting in large biases with respect to their particle-level prediction. The different sizes of the

³ Out-of-acceptance electrons will be reconstructed as jets and are therefore accounted for with the wrong energy when the object is considered for the E_T^{miss} calculation.



(a) E_T^{miss} resolution per Standard Model process

(b) E_T^{miss} shapes per Standard Model process

Figure 6.6: E_T^{miss} resolution and shape per Standard Model process contributing to the ≥ 1 jet signal region. The resolutions are similar across the different processes, except for muonic processes, whereas the shapes deviate significantly.

stability and purity correction are thus the main contribution to the biases seen in figure 6.4.

Biases due to the Resolution Correction

The resolution correction is iterative and hence does not simply scale with the fractional contribution of the respective process. This means that when the migration matrix of the topology response, instead of the individual process is used in the resolution correction, this matrix is iteratively updated to best describe the unfolded process. These updates to the migration matrix might have a large effect and even bias the overall result when they are employed in the artificial example of unfolding the Monte Carlo simulation.

The bin-to-bin migrations in the resolution correction are a convolution of the resolution of the observable and its underlying shape. The E_T^{miss} resolution per Standard Model processes together with the E_T^{miss} distribution normalized to unity are displayed in figure 6.6. The resolution of processes including muons significantly deviate from the other processes (see figure 6.6a) since out-of-acceptance muons add to the missing transverse momentum at reconstruction-level, but not at particle level. The other processes are quite similar in their resolution, with only the top-anti-top and single-top processes deviating slightly. This is because here the E_T^{miss} is not necessarily coming from a single boson, as is the case for the other backgrounds, but is topologically more complex, resulting in a slightly larger resolution. The shapes on the other hand are quite different, since the high E_T^{miss} region is populated by events in the central part of the detector, whereas many of the events coming from backgrounds with leptons will be in the forward region, where the lepton is not identified. The leptonic backgrounds therefore preferably populate the lower E_T^{miss} region, resulting in a softer spectrum.

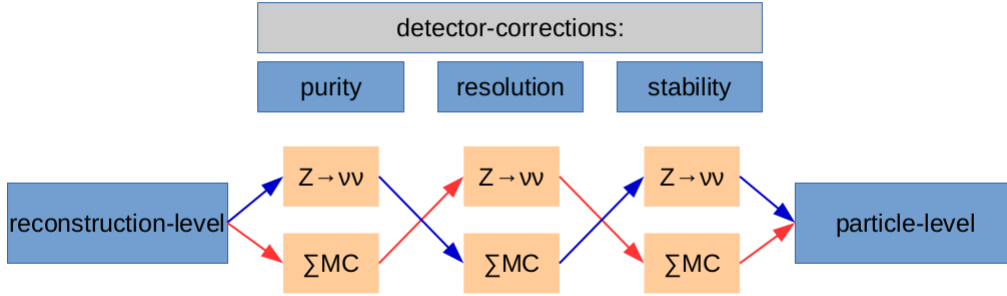


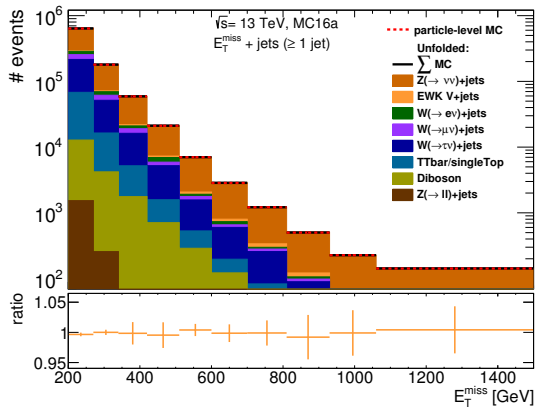
Figure 6.7: Illustration of the different unfolding scheme to test for a potential resolution correction bias. Blue: The purity and stability correction come from the simulation of the individual process (here $Z \rightarrow \nu\nu$) and the resolution correction come from the topology response. Red: The purity and stability correction come from the topology response and the resolution correction come from the individual process.

Different steps of the unfolding procedure are varied in the following, to illustrate the effect of the resolution correction. In the example of unfolding the $Z \rightarrow \nu\nu + jets$ component, the purity and stability correction can either come from the $Z \rightarrow \nu\nu$ or the topology response. Likewise, the migration matrix, used in the resolution correction, can be retrieved from either of the two responses. Mixing the responses, as illustrated in figure 6.7, in both cases yields a test, sensitive to the iterative updates to the migration matrix.

The first test is to unfold each Standard Model process individually, applying the purity and stability correction of the respective process. This corresponds to the blue path in figure 6.7, replacing $Z \rightarrow \nu\nu$ with the individual processes. This correction will by definition be correct. Only in the resolution correction the (“wrong”) migration matrix of the topology response is applied. When applying this unfolding scheme and adding the unfolded contributions back together it shows that the overall effect on the result is very small (see figure 6.8a). However, as was the case for the full topology unfolding it can be shown that each unfolded process individually shows a deviation from its particle-level prediction of up to 20% for $Z \rightarrow ll + jet$ and 40% for $W \rightarrow \mu\nu + jet$: see figure 6.8b. These are the processes which showed the largest resolution differences according to figure 6.6a. All individual processes unfolded with this unfolding scheme are found in appendix I. This effect is considerably smaller than the effect of the purity correction, however, it is a significant shift.

In the above case the migration matrix is not suitable to be applied to the individual process since it is an average of all Standard Model contributions. However, the migration matrix applied might also not be ideal because it is applied to a distribution, significantly different from what it was defined for.

Therefore, in the second test each Standard Model contribution is unfolded using the



(a) Stacked unfolded processes

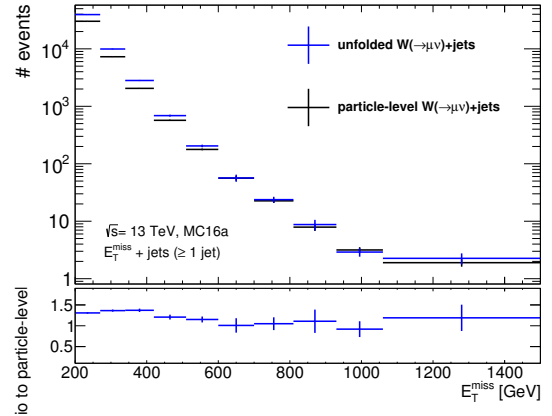
(b) Unfolded $W(\rightarrow \mu\nu) + jets$ versus particle-level expectation

Figure 6.8: (a) Overall bias between the sum of the individually unfolded Monte Carlo simulation processes versus the unfolded sum of Monte Carlo simulations. (b) Unfolded single component: $W(\rightarrow \mu\nu) + jets$ versus particle-level expectation. In the unfolding the purity and stability correction from the individual processes are used, while the resolution correction uses the migration matrix from the topology response.

purity and stability correction of the topology response, while the (“correct”) migration matrix of the individual process is used for the resolution correction, as illustrated by the red path in figure 6.7. For each process, a resolution correction is thus applied to a purity-corrected spectrum, with a shape, different from what it would have been if the (“correct”) purity correction from the individual process was applied. Again this unfolding scheme is applied to all individual processes and the unfolded components are added back together. After one iteration of the unfolding algorithm one can see that even though the correct migration matrix was used for every processes, the summed unfolded distributions do not recover the particle-level prediction (see figure 6.9a). This is exactly because the spectrum that is unfolded is not what the migration matrix in the resolution correction was defined for. After 20 iterations, however, the migration matrices are modified sufficiently by the IDS algorithm, that the expected spectrum is mostly recovered (see figure 6.9b). The first bin, however, still deviates by $\sim 4\%$. All individual unfolded processes are also displayed in appendix I.

The latter example shows that the resolution correction can have a crucial impact on the unfolded result. If the resolution correction is applied to a spectrum of unexpected shape even the iterative IDS algorithm might not fully recover the true particle-level spectrum. The biases on the unfolded components might not balance each other and an overall bias on the result follows. In case of topology unfolding the migration matrix of the topology response is defined neither for the individual process corrected by the true purity correction, nor the averaged purity correction. A bias on the final result thus can not be excluded.

Furthermore, comparing the $Z \rightarrow ll + jets$ contribution in figure 6.8 and 6.9b one

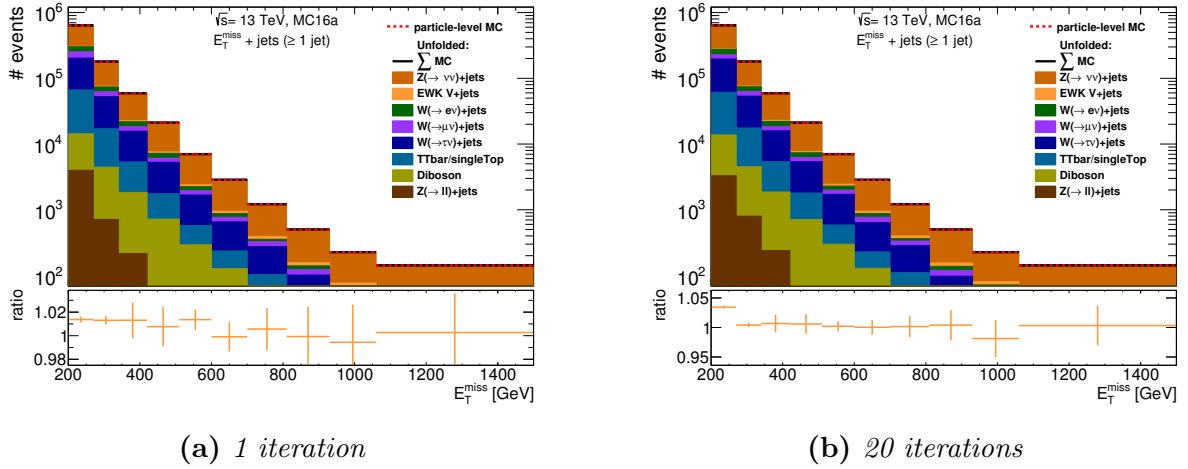


Figure 6.9: Overall bias between the sum of the individually unfolded Monte Carlo simulation processes versus the unfolded sum of Monte Carlo simulations. In the unfolding the purity and stability correction from the topology response are used, while the resolution correction uses the migration matrix from the individual processes.

can see that using the topology response in any of the unfolding steps leads to differences in the unfolded spectra of the individual components. These effects mostly balance each other, such that the Standard Model expectation is recovered to good approximation. This is because most of the corrections are linear operations, like the bin-by-bin scaling in the purity and stability correction or the matrix multiplication in the resolution correction. These balance each other when they are weighted with the respective fiducial cross section, such that the result remains the same. However, non-linearities in the IDS algorithm result in some deviations as seen in figure 6.9. This is especially true when the exact composition of the unfolded distribution is not known, as is the case in measured data.

Since it is already clear from section 5.7 that the Monte Carlo simulation does not agree perfectly with the measured data, there are biases in the unfolded distribution, which need to be accounted for. Consistently determining an uncertainty on this, however, is a major challenge and the added uncertainty will deteriorate the results.

Unfolding with Background Subtraction

When the subdominant backgrounds are subtracted from the measured data, most of the considerations for topology unfolding do not apply. In simulation it is trivial to subtract all but the leading $Z \rightarrow \nu\nu + jets$ Standard Model contribution and the detector response can be simulated using the Monte Carlo simulation of this remaining process. Unfolding the reconstruction-level prediction to particle-level, by-construction retrieves the particle-level expectation, as illustrated in figure 6.10 and there is no ambiguity which other process is to be used for the unfolding. This means that there is no additional uncertainty on the unfolded distributions because of potential biases in the procedure.

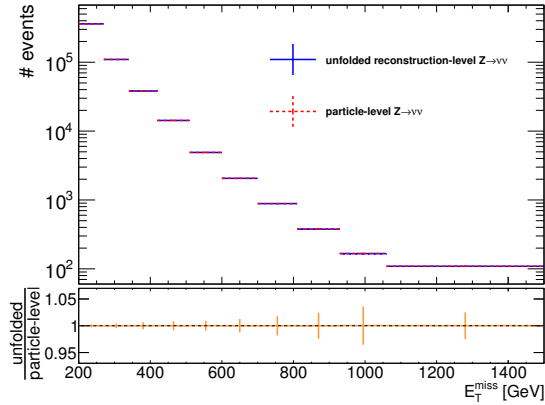


Figure 6.10: *Unfolding closure in unfolding with background subtraction. Subtracting all subdominant backgrounds leaves only the $Z \rightarrow \nu\nu + jets$ process from which also the detector response is retrieved. Unfolding the reconstruction-level prediction to particle-level retrieves the particle-level expectation.*

The corrections which are applied to the data distribution are all very small. As illustrated in figure 6.5 the purity and stability corrections are both at the level of 5% with a turn-on in the underflow bin from 150-200 GeV in E_T^{miss} . The resolution correction introduces correlations between the E_T^{miss} bins of the order of 20% (see figure 6.11a), however, the net-migrations are almost negligible as illustrated in figure 6.11b. The latter figure shows the reconstruction-level expectation of the $Z \rightarrow \nu\nu + jets$ process corrected for purity as well its particle-level expectation corrected by the inverse of the stability correction. The ratio of the two shows an overall correction factor (disregarding correlations) to each bin which is close to 1 for the entire spectrum. This is explained by a slight skew of the resolution in each E_T^{miss} bin, which results in fractionally larger migrations to lower E_T^{miss} bins than to higher ones. This counteracts the effect of the steeply falling distribution.

The small corrections in the unfolding with background subtraction originates from the fact that the particle- and reconstruction-level phase spaces are very similar and that the detector does not introduce large corrections to the measured spectrum. Larger corrections as present in topology unfolding rely more on the Monte Carlo simulation to model this difference. The correction factors for the E_T^{miss} distribution in the ≥ 1 jet signal region as they would be applied in a bin-by-bin unfolding are displayed in the following figure 6.12.

It shows that the extrapolation from reconstruction- to particle-level is larger in topology unfolding than in the unfolding with background subtraction. This is mainly because by including the leptonic W backgrounds, the topology response has to account for inefficiencies in the lepton reconstruction. The modeling of leptons can be neglected entirely in the unfolding procedure in the case of background subtraction.

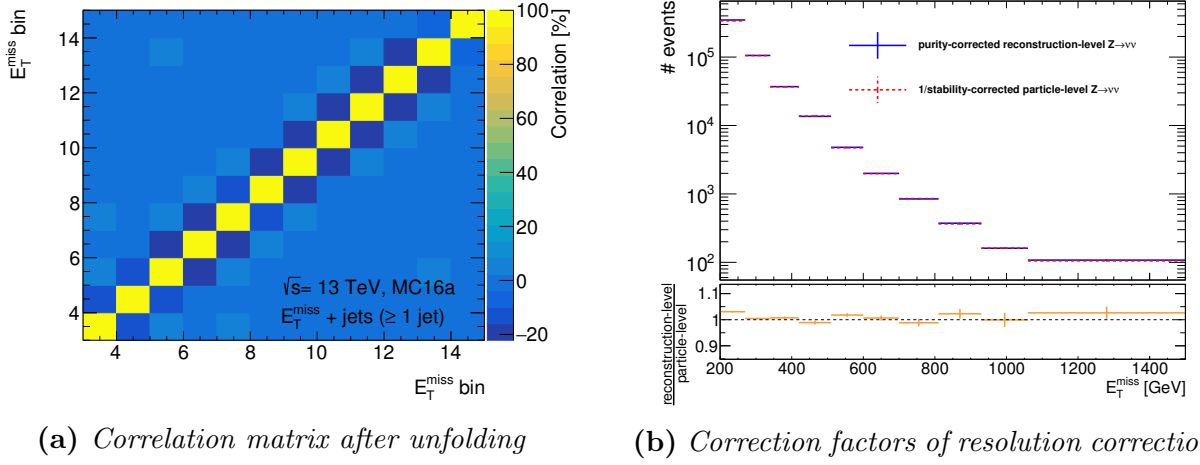


Figure 6.11: (a) Correlations between bins of the E_T^{miss} distribution in the ≥ 1 jet signal region introduced by the unfolding procedure. Neighboring bins show a correlation of the order of 20%. (b) Ratio between the purity-corrected reconstruction-level distribution and the 1/stability-corrected particle-level distribution. This estimates the resolution correction per bin. The net-migrations to other bins are found to be close to one.

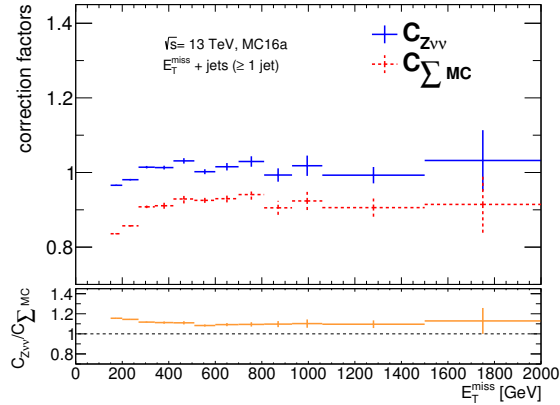


Figure 6.12: Correction factors for the E_T^{miss} distribution in the ≥ 1 jet signal region as they would be applied by a bin-by-bin unfolding. When unfolding with background subtraction the corrections $C_{Z\nu}$ are close to 1 for the entire spectrum, while in topology unfolding $C_{\Sigma MC}$ they are at the order of 10% smaller.

Conclusion and Decision

Topology unfolding is a method which allows to unfold measured spectra to particle-level without the need of background subtraction. Furthermore, this reduces the effect of theory uncertainties on the final results, as the uncertainties on the individual backgrounds are not propagated in the background subtraction.

However, the theory uncertainties can not be fully cancelled from the final results as they still affect the topology response, which is used to unfold the data to particle-level. This can not be avoided and the unfolding will always rely on the Monte Carlo simulation modeling via the definition of the detector response and thereby induce theory uncertainties.

In the presented analysis, the topology unfolding, furthermore, has to model additional leptonic backgrounds, which are present in the signal regions. These background have very different acceptances and efficiencies than the signal and thereby they introduce large purity and stability corrections into the topology response. These differences lead to large biases in the unfolded individual Monte Carlo simulation processes which contribute to the signal region. Even though these biases cancel in the artificial example of unfolding the Monte Carlo simulation, this will not be the case when the exact composition of the data is unknown. It was shown that applying the topology response in any of the 3 detector-correction steps will lead to biases in the individual unfolded distributions and might therefore lead to biases in the unfolded result. An additional uncertainty has to be introduced in order to account for these biases, however, estimating this uncertainty is very challenging. The iterative unfolding technique, which partially recovers mismodeling when using a wrong detector response adds to the complexity of these uncertainties.

Furthermore, the overall corrections which are applied in the unfolding with background subtraction are much smaller, indicating a smaller dependence on the Monte Carlo simulation.

Another consideration is that the ratio measurement performed in this analysis relies on the fact that the numerator and denominator are essentially the same process, as the Z boson can either decay to neutrinos or charged leptons. In case of topology unfolding this ratio would include additional processes including W bosons and top-anti-top or single top production. The experimental and theoretical uncertainties on such processes are not as similar anymore which would result in a reduced mitigation of these uncertainties in the final ratio measurement.

For these reasons in the following the subdominant backgrounds are subtracted from data and the unfolding is done using the detector response as simulated for the leading Z boson production process.

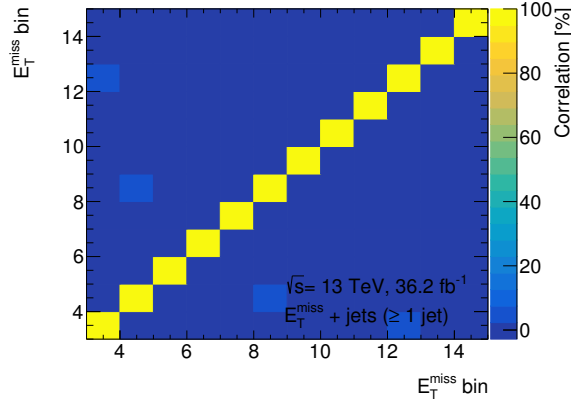


Figure 6.13: Correlations between bins in the background subtracted data-distribution of E_T^{miss} . The event selection is the signal region in the ≥ 1 jet signature. 5000 bootstrap replicas are used for the data distribution to keep the correlations due to the finite amount of replicas small. Correlations are smaller than 2.5% for most of the bins.

6.3 Detector Corrected Measurement

The measured data is unfolded to particle-level, after all subdominant backgrounds are subtracted. The detector response is obtained from the Monte Carlo simulation of the leading Standard Model process in the selection. Potential additional contributions are taken care of by the IDS algorithm. In the following the derivation of the statistical and systematic uncertainties is detailed and the unfolded results are presented.

The histograms used in the unfolding process are produced with 5000 bootstrap replicas to ensure that no artificial correlations due to the finite amount of replicas are introduced between bins. Figure 6.13 shows the correlations (according to equation 4.20) of the background subtracted data for the E_T^{miss} distribution in the ≥ 1 jet signature. The correlations between bins are smaller than 2.5% for all bins except for 2 outliers with 2.6% and 3.0%. Correlations in the other observables are found to be of similar size.

The nominal data replica unfolded with the nominal detector response yields the unfolded data spectrum. The statistical uncertainty on this result is determined via the bootstrap replicas in the following way: All background-subtracted data replicas are unfolded using the nominal replica of the detector response. The standard deviation of all unfolded replicas represent the statistical uncertainty on the unfolded result, due to the limited data statistics. Furthermore, the statistical uncertainty of the Monte Carlo simulation is taken into account, by using all replicas of the detector response to unfold the nominal data distribution (both covariance matrices are found in appendix J). The two uncertainties are added in quadrature for a total statistical uncertainty on the unfolded data⁴.

⁴ It was checked that it is equivalent to unfolding each data replica with a different replica of the detector response, which is easier to technically merge both statistical uncertainties into one (bootstrapped-) histogram.

In the unfolding procedure events are migrated from one bin to another resulting in correlations between the bins up to 40%. These correlations are determined from the bootstrap replicas using equation 4.20. Furthermore, the bootstrap histograms allow to determine the correlations between different observables of interest. This is because every event is seeded with the run- and event-numbers, which means that an event being reconstructed in several of the observables will be distributed among the histogram replicas in an identical way. Following the notation in section 4.2 the degree of correlation between two bins of any distribution can therefore be retrieved via

$$\rho_{ij} = \frac{1}{n_{rep}\sigma_i\sigma_j} \sum_{k=1}^{n_{rep}} (u_i^k - \bar{u}_i^k)(u_j^k - \bar{u}_j^k). \quad (6.1)$$

The obtained correlation matrix between all bins of all observables can be found in appendix J. Accounting for the statistical correlations between bins of all observables allows to take these into account, for example when limits on new physics models are derived.

Systematic uncertainties are propagated to the final result by varying one nuisance parameter from the list of experimental and theoretical uncertainties (see section 5.6) at a time and repeating the unfolding. In the systematically varied unfolding procedure the varied reconstruction-level predictions of all backgrounds are used in the background subtraction. Likewise, the varied $Z \rightarrow \nu\bar{\nu} + jets$ Monte Carlo simulation provides the detector response which is used in the unfolding procedure in the signal region. The unfolded results, using systematically varied backgrounds and responses, divided by the nominal unfolded results yield the systematic uncertainty for each bin. Due to the CPU and memory intensive calculation of the bootstrap replicas, the varied backgrounds as well as the varied detector responses are generated without bootstrapping. This omits the statistical uncertainty of the Monte Carlo simulations on the uncertainty of the systematic variation. This is acceptable, since statistics in simulation are generally better than in data and the uncertainty is thus subdominant. Furthermore, this merely yield a better estimate of the uncertainty on the systematic uncertainty, which is used in the smoothing procedure.

The experimental systematic uncertainties added in quadrature to the statistical uncertainties are displayed in figures 6.14-6.16 as hashed bands. Furthermore, the theoretical uncertainties on the unfolded data as detailed above are displayed in the ratio panels as an orange band (around one for visibility).

Figures 6.14-6.16 show the background subtracted data unfolded to particle-level for the four observables of interest. In the signal region this is compared to the particle-level prediction of $Z \rightarrow \nu\bar{\nu} + jets$, while the two-electron and two-muon control regions compare to the particle-level prediction of $Z \rightarrow e^+e^- + jets$ and $Z \rightarrow \mu^+\mu^- + jets$, respectively.

The agreement in the E_T^{miss} distribution of the ≥ 1 jet signal region (see figure 6.14a) is good, with an almost flat ratio between data and Monte Carlo simulation at the level of 6%. The first bin agrees well with the particle-level prediction, indicating that data events migrated out of the fiducial phase space, into the low E_T^{miss} region, when the IDS algorithm updated its prior, taking into account the additional observed events. Similar

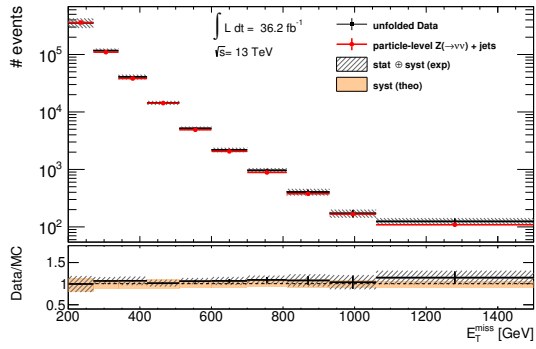
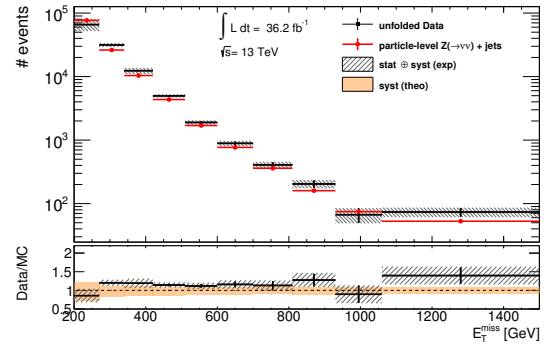
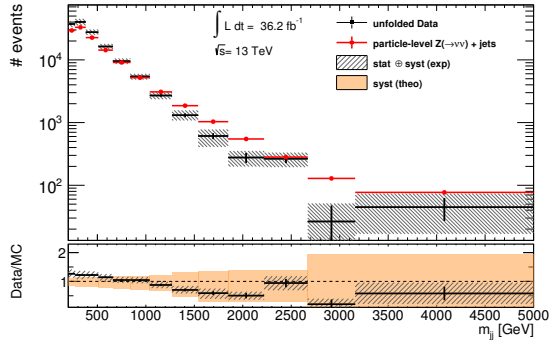
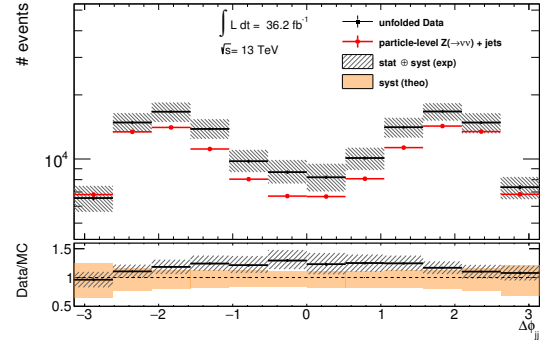
(a) E_T^{miss} in ≥ 1 jet phase space(b) E_T^{miss} in VBF phase space(c) m_{jj} in VBF phase space(d) $\Delta\phi_{jj}^{sgn}$ in VBF phase space

Figure 6.14: Agreement of background subtracted data unfolded to particle-level and particle-level Monte Carlo simulation in the zero-lepton signal region. Theoretical systematic uncertainties are displayed only in the ratio panel.

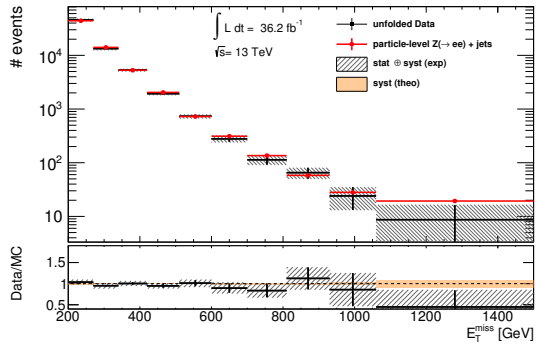
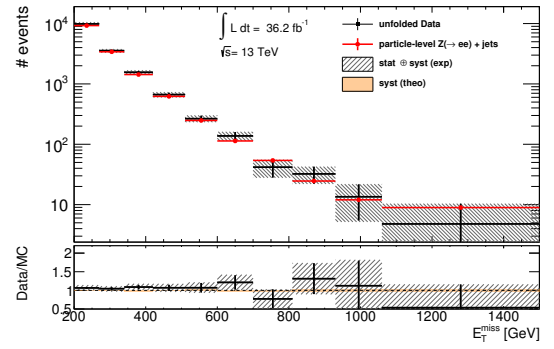
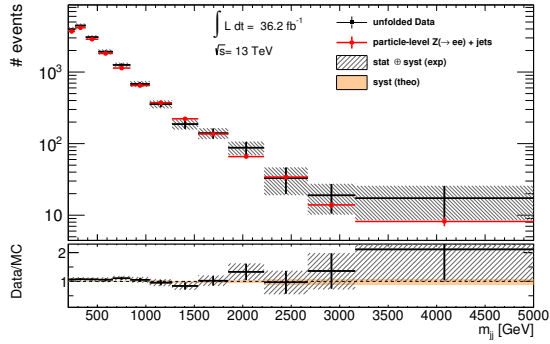
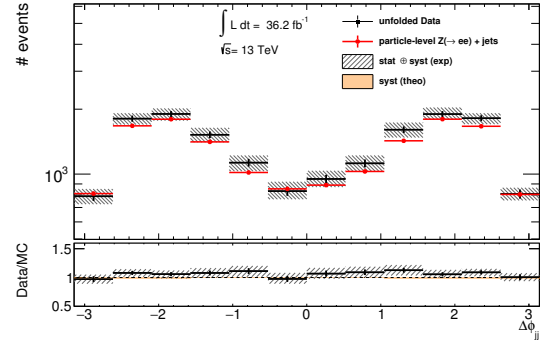
(a) E_T^{miss} in ≥ 1 jet phase space(b) E_T^{miss} in VBF phase space(c) m_{jj} in VBF phase space(d) $\Delta\phi_{jj}^{sgn}$ in VBF phase space

Figure 6.15: Agreement of background subtracted data unfolded to particle-level and particle-level Monte Carlo simulation in the two-electron control region. Theoretical systematic uncertainties are displayed only in the ratio panel.

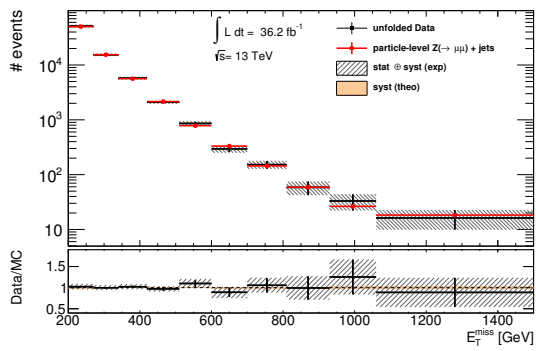
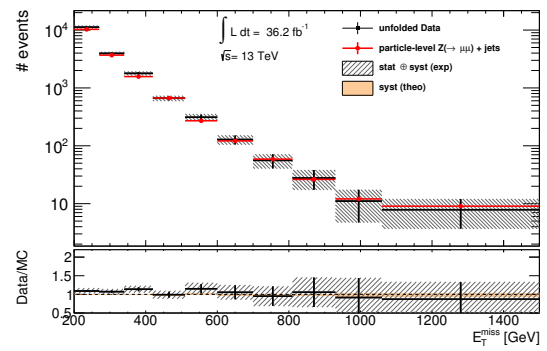
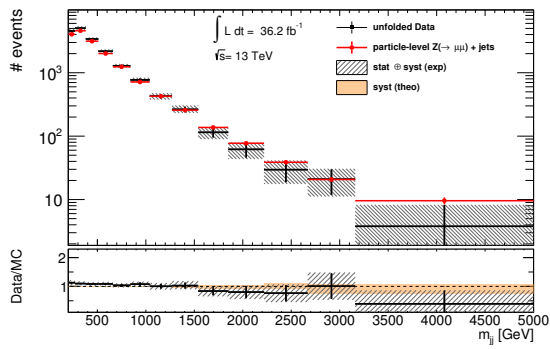
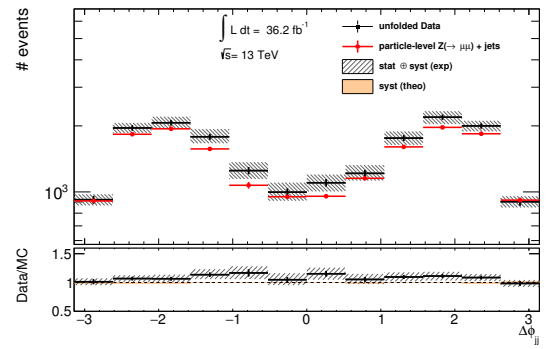
(a) E_T^{miss} in ≥ 1 jet phase space(b) E_T^{miss} in VBF phase space(c) m_{jj} in VBF phase space(d) $\Delta\phi_{jj}^{sgn}$ in VBF phase space

Figure 6.16: Agreement of background subtracted data unfolded to particle-level and particle-level Monte Carlo simulation in the two-muon control region. Theoretical systematic uncertainties are displayed only in the ratio panel.

to the reconstruction-level results, the control regions (figures 6.15a and 6.16a) show better agreement, with the ratio of unfolded data and particle-level Monte Carlo simulation fluctuating around one. The deviations in the signal region are covered by the statistical (systematic) uncertainties ranging between 0.5% (20%) in the low E_T^{miss} region and 15% (5%) in the high E_T^{miss} region.

Similar agreement is observed in the E_T^{miss} distribution of the VBF signature, where an almost flat disagreement of 15%-20% between data and simulation is observed in the signal region (figure 6.14b). As in the ≥ 1 jet signal region the first bin obtained a large correction, due to events migrating to the low E_T^{miss} region. The agreement in the control regions is better with a data-simulation disagreement at the level of 5%-10% covered entirely by the statistical uncertainty (figures 6.15b and 6.16b). The uncertainties in the signal region are of similar size as in the ≥ 1 jet signature, such that unfolded data and Monte Carlo prediction are compatible with each other.

The m_{jj} distribution of the VBF signature shows a similar behavior as at reconstruction-level (figure 6.14c). A shape difference between data and Monte Carlo simulation can be observed, with a difference of +25% in the first bin and -50% around 2 TeV. The relative shape difference increased with respect to the reconstruction-level results, due to the background subtraction, which keeps the absolute difference between data and Monte Carlo simulation constant. In the signal region this effect is more pronounced than in the control regions, since the background processes make up about 50% of the measured data in the signal region, while in the control region only about 5% of the measured events are considered background. The data-to-Monte Carlo simulation agreement in the control regions is thus similar to the one at reconstruction-level, between +10% and -20% (figures 6.15c and 6.16c). The theoretical systematic uncertainties in the signal region range from 15% in the low m_{jj} region to 95% in the highest m_{jj} bin, thus, covering all deviation from the Monte Carlo prediction. The smaller uncertainties in the control regions also cover all observed deviations.

The same effect is observed in the $\Delta\phi_{jj}^{sng}$ distribution of the VBF signature. The large background subtraction in the signal region increases the relative difference between data and simulation, resulting in an increased disagreement at particle-level (figure 6.14d) of the order of 30% when $\Delta\phi_{jj}^{sng}$ approaches zero. The agreement improves for larger absolute values of $\Delta\phi_{jj}^{sng}$. This trend is not as pronounced in the control regions (figures 6.15d and 6.16d) where the background subtraction has a smaller effect. Here the ratio between data and simulation is statistically compatible with one. Again the systematic uncertainties in the signal region cover all deviation within less than two standard deviations.

The overall trends agree between signal and control regions, but partially vary by their magnitude, mostly because of the reinforcing effect of the background subtraction. Therefore, when constructing the ratio R_{miss} between the signal region and the per-bin-average of the control regions, a remaining mismodeling is observed. The ratio at particle-level is displayed in figure 6.17. The E_T^{miss} distributions in the ≥ 1 jet and VBF signature, show an increase in data of 5%-15%, as expected from the larger disagreement in the signal region. The first bin, where many events in the signal region migrated into the low E_T^{miss} region is lower than the prediction. Furthermore, the increased disagreements in the signal

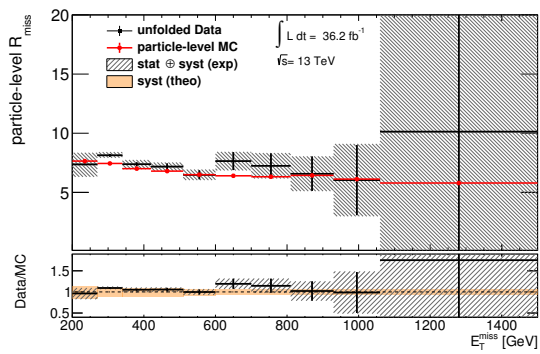
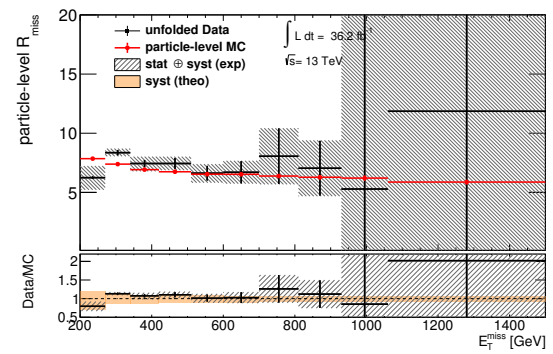
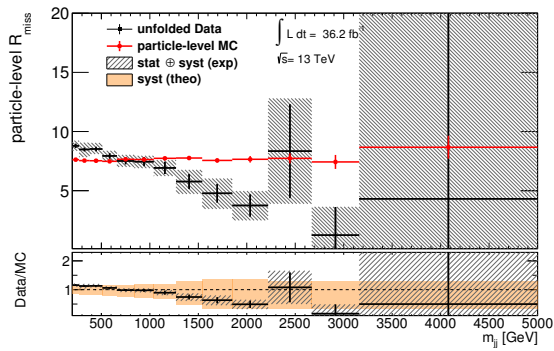
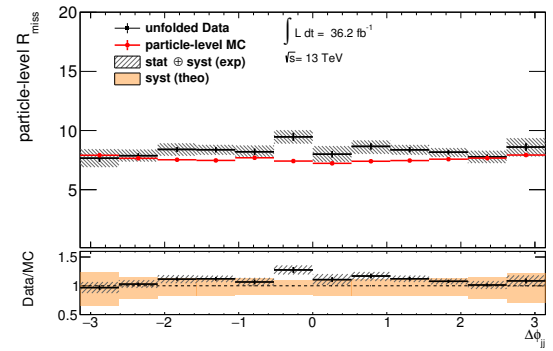
(a) E_T^{miss} in ≥ 1 jet phase space(b) E_T^{miss} in VBF phase space(c) m_{jj} in VBF phase space(d) $\Delta\phi_{jj}^{sgn}$ in VBF phase space

Figure 6.17: Agreement of ratios R_{miss} between unfolded data and particle-level Monte Carlo simulation. Theoretical systematic uncertainties are displayed only in the ratio panel.

Table 6.1: *Experimental and theoretical systematic uncertainties and statistical uncertainty on the ratio R_{miss} . Displayed are the uncertainties on the first bin of E_T^{miss} in the ≥ 1 jet signature, the first bin and the bin at 3 TeV of m_{jj} and the central bin greater than zero of $\Delta\phi_{jj}^{sng}$ in the VBF signature.*

Ratio R_{miss}	E_T^{miss}	low m_{jj}	high m_{jj}	$\Delta\phi_{jj}^{sng}$
expected	7.6	7.6	7.7	7.2
observed	7.4	8.8	3.7	8.0
Systematic uncertainty source	E_T^{miss} [%]	low m_{jj} [%]	high m_{jj} [%]	$\Delta\phi_{jj}^{sng}$ [%]
Jet energy resolution and scale	+13, -14	+4.3, -4.1	+24, -23	+7.7, -7.2
E_T^{miss} soft term	+2.9, -3.0	+1.1, -1.0	+5.5, -4.7	+1.1, -0.8
Lepton efficiencies (combined)	+0.8, -0.8	+0.9, -0.9	+2.0, -2.3	+0.9, -1.0
Trigger scale factors	+1.1, -1.2	+0.2, -0.1	+0.6, -0.5	+0.1, -0.1
Pileup reweighting	+0.7, -1.0	+0.1, -0.2	+2.0, -1.6	+0.0, -0.2
Scale uncertainties (μ_R, μ_F)	+13, -17	+11, -15	+28, -66	+11, -17
PDF and α_S	+1.1, -1.2	+1.1, -0.8	+11, -8	+1.0, -1.6
Total systematic uncertainty	+19, -22	+12, -16	+39, -71	+14, -19
Statistical uncertainty	0.8	2.5	32	4.2
Total uncertainty	+19, -22	+12, -16	+50, -78	+14, -19

region is clearly visible in the ratios of the m_{jj} and $\Delta\phi_{jj}^{sng}$ distributions, where trends due to the Sherpa mismodeling are largest. Disagreements between +10% and -50% are observed in the m_{jj} distribution as well as up to 30% in $\Delta\phi_{jj}^{sng}$. The uncertainties are very different between the signal and control regions, also driven by the different impact of the background subtraction, such that they do not cancel as at reconstruction-level. The uncertainties as given in table 6.1 are driven by the uncertainties coming from the signal region and cover all deviations observed in the ratio distributions.

Table 6.1 shows the increased systematic uncertainties, which are dominated by the scale uncertainties of the Monte Carlo simulation, followed by the jet energy scale and resolution uncertainties. The statistical uncertainties are subdominant. The simulation comes with large theoretical uncertainties, which are propagated to the result in the background subtraction. Without further constraints the use of the Monte Carlo simulation to derive the background estimates, limits this search. The agreement as well as the uncertainties are expected to improve, when data-driven background estimates are used.

Chapter 7

Interpretation

The unfolded distributions presented in the previous chapter constrain new physics models, since none of the deviations from the Standard Model prediction are found to be significant. The results are thus used to derive limits on two possible models beyond the Standard Model. Limits on a simplified model of dark matter are derived in section 7.1 and the invisible branching fraction of the Standard Model Higgs boson is constrained in section 7.2. In the following the methodology to derive such limits is described.

Since a theory can never be proven, but only falsified, models are constrained by excluding certain parameters. If a particular set of parameters would lead to a signal, which contributes to the measurement significantly enough that it would be seen in the data, but no excess is observed, the model (set of parameters) can be excluded. As neither observation nor expectation are known with infinite precision, possible excesses may be due to fluctuations and a notion of significance needs to be defined.

The CL_s method [154, 155] is a procedure used to derive a *confidence limit* to exclude a certain model. It developed from frequentist exclusion limits on model parameters, which provide intervals that cover the parameters with a given probability. These frequentist limits, however, allow to exclude models, which the experiment is not sensitive to [156]. The CL_s method thus penalizes the frequentist limits by also considering the exclusion limits under the background-only hypothesis. If the sensitivity to distinguish the two is low, a large penalty is applied to avoid false exclusions.

The Likelihood

In order to derive a confidence limit, the observed quantity is compared to its expectation. The latter is usually given in terms of a probability density and a probability can be determined, whether the observed value could have originated from a fluctuation of the expectation, or is incompatible with the expectation. In this work the event counts in different bins of different observables are measured, each of which can be considered as independent counting experiments. The observed quantity in each bin i is thus n_{obs}^i , while its expectation is given by n_{exp}^i . The probability of a counting experiment is usually given

by a Poisson distribution and (omitting the bin index)

$$P(n_{obs}|n_{exp}) = \frac{(n_{exp})^{n_{obs}}}{n_{obs}!} \exp(-n_{exp}) \quad (7.1)$$

returns the probability for the observation. Since the Monte Carlo simulation estimates, after being rescaled for various effects, are not expected to follow Poissonian statistics anymore, the bootstrapping method [115] was introduced. A distribution of n_{exp}^i is thus obtained from the bootstrap replicas, which can be normalized and used as its probability density. In this work, however, the probability density is approximated by a Gaussian distribution in order to reduce computation times. The root-mean-square $\sigma_{n_{exp}}^i$ and mean value $\langle n_{exp}^i \rangle$ (n_{exp}^i for brevity) of the bootstrap replicas are used to define the probability density (omitting the bin index)

$$G(n_{obs}|n_{exp}, \sigma_{n_{exp}}) = \frac{1}{2\pi\sigma_{n_{exp}}^2} \exp\left(\frac{-(n_{obs} - n_{exp})^2}{2\sigma_{n_{exp}}^2}\right). \quad (7.2)$$

Experimental and theoretical uncertainties are introduced via nuisance parameters $\vec{\theta}$. Since both uncertainties can be understood as modifications to the expected event yield, they are introduced as

$$\hat{n}_{exp}^i(\vec{\theta}) = n_{exp}^i + \sum_k \sigma_{\theta_k}^i \theta_k, \quad (7.3)$$

where n_{exp}^i is the expected event yield when all nuisance parameter take their nominal values (0) and $\sigma_{\theta_k}^i$ is the absolute uncertainty on the event yield in bin i due to nuisance parameter θ_k . Since the systematic uncertainties are described by Gaussian uncertainties around their most probably value, the nuisance parameters θ_k are constrained by a Gaussian distribution centered at zero with a width of one $G(\theta_k|0, 1)$. A one sigma variation of the nuisance parameter thus modifies the event yields by the Gaussian width of the uncertainty: $\sigma_{\theta_k}^i$. The combined probability of all measured bins, given an expected event yield, taking into account their nuisance parameters, is thus given by

$$\mathcal{L}(\vec{n}_{obs}|\vec{n}_{exp}, \vec{\theta}) = \prod_i G(n_{obs}^i|\hat{n}_{exp}^i(\vec{\theta}), \sigma_{n_{exp}}^i) \prod_l G(\theta_l|0, 1). \quad (7.4)$$

Modifying the nuisance parameters θ_k in favor for a better agreement of n_{obs}^i and \hat{n}_{exp}^i thus penalizes the likelihood due to the Gaussian distribution of the nuisance parameter. A multidimensional optimization has to be performed, to obtain the maximum likelihood estimated of \vec{n}_{exp} .

Limits on a particular model are usually parametrized in terms of a *signal strength* μ . This means that the number of expected events is a sum of the expected Standard Model contribution b_{exp}^i and the expected signal contribution s_{exp}^i , scaled by the signal strength.

The impact of experimental and theoretical uncertainties are derived separately for each of them

$$\hat{n}_{exp}^i(\mu, \vec{\theta}) = b_{exp}^i + \mu \cdot s_{exp}^i + \sum_k (\sigma_{\theta_k}^{b^i} + \mu \cdot \sigma_{\theta_k}^{s^i}) \theta_k, \quad (7.5)$$

where $\sigma_{\theta_k}^{s^i}$ and $\sigma_{\theta_k}^{b^i}$ are the impacts of the uncertainties in bin i due to nuisance parameter θ_k on the signal yield and background yield, respectively.

So far only statistical uncertainties on n_{exp}^i were considered, while the statistical uncertainty on n_{obs}^i and possible new signals were omitted. After unfolding the observed events in each bin are no longer statistically independent, but correlated as shown in figure 8.19 of appendix J. This means that the multiplication of independent Gaussian probability densities as done in equation 7.4 is no longer valid. Instead, the likelihood is generalized to a multivariate Gaussian distribution defined as (omitting normalization)

$$\mathcal{L}(\vec{n}_{obs}|\mu, \vec{\theta}) \propto \exp\left(\left(\vec{n}_{obs} - \vec{\hat{n}}_{exp}(\mu, \vec{\theta})\right)^T V^{-1} \left(\vec{n}_{obs} - \vec{\hat{n}}_{exp}(\mu, \vec{\theta})\right)\right) \prod_l G(\theta_l|0, 1) \quad (7.6)$$

where V^{-1} is the inverse of the covariance matrix, which accounts for the statistical uncertainties of n_{obs} as well as \hat{n}_{exp} by adding the statistical uncertainties of signal and backgrounds in quadrature to the diagonal elements of the covariance matrix of n_{obs} :

$$V_{ij} = V_{ij}^{n_{obs}} + \delta_{ij}(\sigma_{n_{exp}}^{b^i} + \mu \cdot \sigma_{n_{exp}}^{s^i}). \quad (7.7)$$

For technical reasons, $\sigma_{n_{exp}}^{s^i}$ is omitted in the later minimization. Due to its small size compared to the other uncertainties the uncertainty is negligible.

Hypothesis Testing

In order to test the measured data against different model hypotheses a *test statistic* is defined. This test statistic allows to summarize the measured data-vector into a single quantity. Furthermore, it is defined such that the probability density of the test statistics is distributed differently for the different models under test. For a maximal separation power between models, the most powerful test statistic is the ratio of the likelihoods of the two hypotheses under test, according to the Neyman Pearson Lemma [157]. The test statistic defined for this work is q_μ , which is a modification of the *profile likelihood ratio* λ_μ . It uses the likelihood introduced in equation 7.6:

$$q_\mu = \begin{cases} -2 \ln \lambda_\mu & \text{if } \mu \leq \mu' \leq 0 \\ 0 & \text{else} \end{cases}, \quad (7.8)$$

$$\lambda_\mu = \frac{\mathcal{L}(\vec{n}_{obs}|\mu, \vec{\theta}^*)}{\mathcal{L}(\vec{n}_{obs}|\mu', \vec{\theta}')}, \quad (7.9)$$

where μ' and $\vec{\theta}'$ are the parameters of the global maximum of the likelihood, while $\vec{\theta}^*$ maximizes the likelihood for a given parameter μ . According to the Neyman Pearson Lemma it thus separates optimally between the model with signal strength μ under test and the model with the best fit value μ' . Defining q_μ in this way, furthermore, allows to minimize a sum of the parabolas, which were the arguments in the exponential functions of the Gaussian distributions in 7.6. This is computationally advantageous over maximizing a product of exponentials. The restriction on μ' assures that no negative signal contributions are allowed and that the limits are computed one-sided. This means fluctuations in data, resulting in a higher global μ' than the μ under test, can not lead to the rejection of the model.

The test statistic takes exactly one value q_μ^{obs} for the measured data, given a specific model and parameter μ . In order to reject the model or not based on this observation, the probability distribution $f(q_\mu|\mu)$ of the test statistic q_μ for the model under test must be known in order to determine the p -value p_{s+b} . This p -value is defined as the probability to obtain the observed value q_μ^{obs} or larger, simply due to a statistical fluctuation within its expectation:

$$p_{s+b} = \int_{q_\mu^{obs}}^{\infty} f(q_\mu|\mu) dq_\mu \equiv CL_{s+b}. \quad (7.10)$$

The value of p_{s+b} defines the confidence in the model with signal strength μ under the signal-plus-background hypothesis. Conventionally a limit $\alpha = 0.05$ is defined, such that models are rejected at 95% confidence level if $p_{s+b} < \alpha$.

The probability density $f(q_\mu|\mu)$ can be generated using pseudo experiments. Poissonian random numbers for n_{obs}^i are drawn as well as random values for the nuisance parameters, after the latter were fit to their most probably values. For a specific value of μ a distribution of q_μ can thus be obtained [158]. This method, however, is computationally too expensive, due to the many measured bins and nuisance parameters used in this analysis and an *asymptotic approximation* based on theorems by Wilks and Wald [159, 160] is employed. In this approximation, the profile likelihood is approximated as

$$-2 \ln \lambda_\mu \approx \frac{(\mu - \mu')^2}{\sigma_\mu^2} \quad (7.11)$$

and consequently $f(q_\mu|\mu)$ is given analytically with only the standard deviation σ_μ left to be defined [161]. It can be shown that an artificial dataset called *Asimov dataset* exists¹, which can be used to approximate μ' and σ_μ . In the presented case it is given by the expected event yields, when all nuisance parameters are set to their expected value, under the background-only hypothesis. Scanning μ and calculating q_μ with this dataset yields μ' and σ_μ , which then define $f(q_\mu|\mu)$ [161]. This procedure has to be performed only once, in contrast to the many pseudo experiments, which are otherwise necessary. Given this

¹ The existence is not strictly proven, but in binned analyses, like the one presented, an Asimov dataset can typically be found [161].

approximation the p -value under the signal-plus-background hypothesis can be computed according to equation 7.10. The value $1 - p_{s+b}$ yields the exclusion probability of the frequentist limits.

As mentioned at the beginning of this chapter, frequentist limits allow to reject models, even when the measurement is not sensitive to distinguish between background-only and signal-plus-background. The CL_s method solves this issue by also considering the p -value under the background-only hypothesis, setting $\mu = 0$. The final p -value, which is no longer a p -value in the frequentist sense, is thus defined as

$$p_s = \frac{p_{s+b}}{1 - p_b} \equiv \frac{CL_{s+b}}{CL_b} \equiv CL_s \quad (7.12)$$

using

$$1 - p_b = \int_{q_\mu^{obs}}^{\infty} f(q_\mu|0) dq_\mu. \quad (7.13)$$

When the sensitivity of an experiment is very high, the probability densities $f(q_\mu|\mu)$ and $f(q_\mu|0)$ are well separated such that $p_b \rightarrow 0$. In this case the CL_s limit approaches its frequentist limit. In the worst case of no sensitivity the distributions can not be distinguished such that $p_{s+b} = 1 - p_b$ and thus $p_s = 1$, which allows no exclusion. By definition the CL_s limit therefore *overcovers* the true value.

Exclusion limits are presented for each model as CL_s limits. In addition to the *observed limits*, which use q_μ^{obs} as the lower integration limit in equations 7.10 and 7.13, the *expected limits* are cited. The latter are computed under the assumption that no additional signal is present, thus setting n_{obs}^i to its Standard Model expectation b_{exp}^i . This corresponds exactly to the Asimov dataset introduced above and q_μ^{obs} is consequently replaced by the median of $f(q_\mu|0)$: q_μ^A . The exclusion limits are computed for this value in the p -value calculations in a completely analogous way. The $\pm 1\sigma$ and $\pm 2\sigma$ uncertainty bands are furthermore calculated from the respective quantiles around the median q_μ^A .

7.1 Simplified S-Channel Mediator Model

The results presented in section 6.3 are translated into exclusion limits on a simplified model of dark matter [162]. The model introduces a WIMP dark matter candidate and an axial-vector boson, mediating between the Standard Model and the dark sector. As introduced in section 3.2, the spin-1 mediator couples to pairs of Standard Model fermions, as well as pairs of dark matter particles, which produces final states like the ones targeted in the presented search. Events are generated at NLO precision using Powheg-Box v2 [163]. The NNPDF30nnlo PDF set [123] is used such that PDF related uncertainties can be directly correlated with the Standard Model processes. The parton showering is performed using Pythia 8 [127] with the A14 [133] tune. The event generation is performed within the software frameworks provided by the ATLAS collaboration [122].

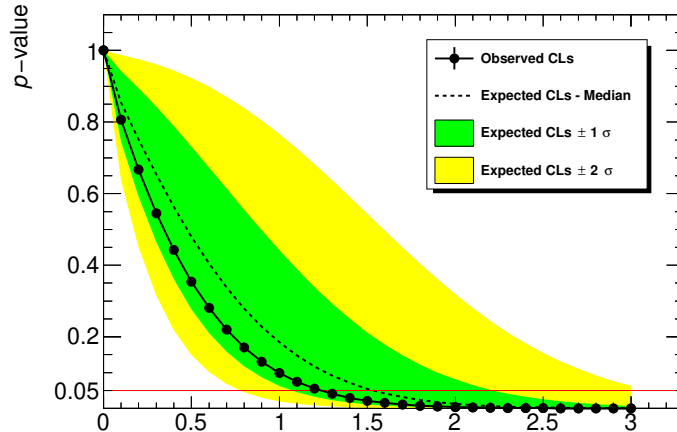


Figure 7.1: Construction of the expected and observed CL_s limits on μ . p -values according to the CL_s method are calculated for a simplified model with dark matter mass $m_\chi = 250$ GeV and mediator mass $m_A = 1500$ GeV [162]. The coupling of the axial-vector mediator to quarks is set to $g_q = 0.25$ and the coupling to dark matter is set to $g_\chi = 1.0$. Uncertainties on the expected limit are indicated by the $\pm 1\sigma$ and $\pm 2\sigma$ bands.

The coupling of the axial-vector mediator to quarks is set to $g_q = 0.25$, while the coupling to the dark matter candidate is set to $g_\chi = 1$, as recommended by the ATLAS CMS Dark Matter Forum [83]. A grid of mass points is generated in the mediator versus dark matter candidate mass plane ($m_A - m_\chi$). For each of these grid points a set of 10 000 events is generated.

The generated events are further analyzed using a Rivet [164] routine², written to apply the particle-level selections presented in section 5.3. The Rivet analysis yields particle-level distributions of the relevant observables, such that expected event yields per bin can be extracted for the generated models.

The observed data, the Standard Model expectation and the BSM prediction are combined in the likelihood of equation 7.6. Nuisance parameters are introduced for each of the systematic sources listed in table 5.4. To reduce computation times and ensure convergence of the minimization, the PDF variations are combined into a single nuisance parameter, with an uncertainty as calculated in equation 5.6. Similarly, experimental uncertainties are added one nuisance parameter at a time as listed in table 5.3. Uncertainties contributing insignificantly to the overall systematic uncertainty are neglected. These are the scale and resolution uncertainties on electrons, muons and taus, as well as the pileup reweighting uncertainty.

The BSM signal expectation is extracted from the generated events, for each of the models generated in the $m_\chi - m_A$ plane and a scan of the signal strength $\mu \in [0, 3]$ in steps of 0.1. Using the test statistic of equation 7.8, the expected and observed CL_s limits as

² The Rivet routine was taken from [4] and modified to fit the exact fiducial selections of this work.

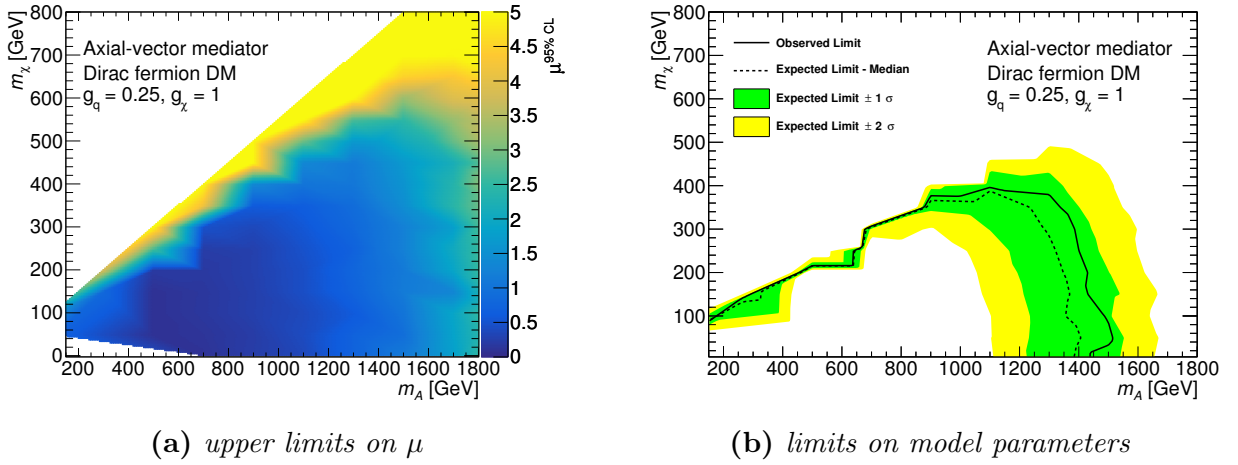


Figure 7.2: Upper limits on μ and expected and observed exclusion limits in the $m_\chi - m_A$ mass plane for a simplified dark matter model [162]. The coupling of the axial-vector mediator to quarks is set to $g_q = 0.25$ and the coupling to dark matter is set to $g_\chi = 1.0$. (a) Upper limits at 95% confidence level on the signal strength μ , calculated for a grid of dark matter and mediator masses. Signal strengths between the generated grid points are interpolated. (b) Exclusion limits on m_χ and m_A : Mass points below the $\mu = 1$ line are excluded by this measurement. Uncertainties on the expected limits are indicated by the $\pm 1\sigma$ and $\pm 2\sigma$ bands.

presented in equation 7.12 are calculated. Figure 7.1 displays an example for $m_\chi = 250$ GeV and $m_A = 1500$ GeV.

The red line in figure 7.1 indicates a p -value of 0.05, meaning that values below this line are excluded at 95% confidence level. The intersection of the observed limits with 0.05 thus defines the *upper limit* on μ to be 1.2. The model under test can therefore not be excluded by this measurement, since the signal strength would be required to be larger than one. The same considerations apply for the expected limit in the absence of a signal, indicated by the black dashed line and its uncertainty bands.

Observed and expected upper limits on μ are thus derived in the $m_\chi - m_A$ plane and displayed in figure 7.2. Limits between the generated mass points are interpolated using Delaunay Triangulation and linear barycentric interpolation. The contour line, where $\mu = 1$ in this interpolated mass plane, indicates the edge of the mass points, which the data excludes at 95% confidence level. All mass points below this line are thus excluded. The contours are calculated for the observed and expected limits as well as the uncertainty band at $\pm 1\sigma$ and $\pm 2\sigma$.

Mediator masses up to 1.4 TeV are expected to be excluded, as well as dark matter particle masses up to 390 GeV. The observed limits are slightly higher, excluding mediator masses up to 1.5 TeV and dark matter particle masses up to 400 GeV. This improves on the previously observed (expected) results obtained in [4] by $\sim 20\%$ ($\sim 30\%$).

Most of this sensitivity comes from the E_T^{miss} distribution of the ≥ 1 jet signature. As

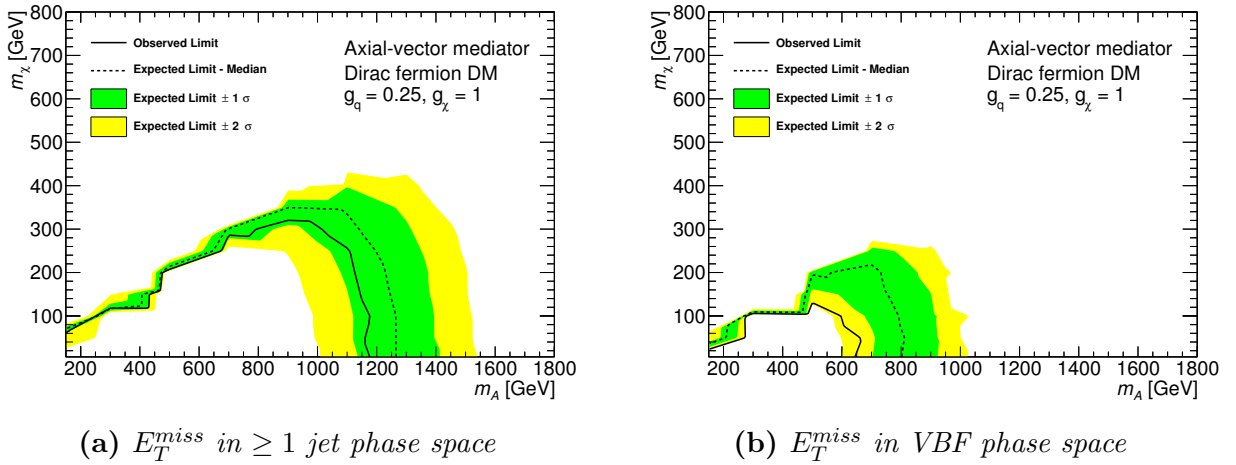


Figure 7.3: Expected and observed exclusion limits in the $m_\chi - m_A$ mass plane for a simplified dark matter model [162]. The coupling of the axial-vector mediator to quarks is set to $g_q = 0.25$ and the coupling to dark matter is set to $g_\chi = 1.0$. Mass points below the $\mu = 1$ line are excluded by this measurement. Uncertainties on the expected limits are indicated by the $\pm 1\sigma$ and $\pm 2\sigma$ bands. (a) Exclusion limits calculated by only considering the measurement of the E_T^{miss} distribution of the ≥ 1 jet signature. (b) Exclusion limits calculated by only considering the measurement of the E_T^{miss} distribution of the VBF signature.

illustrated in figure 7.3a the expected limits derived by considering only this distribution are about 10% weaker than the limits from the combination of all signatures. However, additional sensitivity is added by the E_T^{miss} distribution of the VBF phase space. The two distributions are highly correlated, as shown in appendix J, but the latter adds significantly to the achieved limits. The m_{jj} and $\Delta\phi_{jj}^{sgn}$ distributions are not sensitive to this particular model. However, when including the two distributions in the limit setting, the underfluctuation of data in the m_{jj} distribution affects the minimization of the likelihood and thus the impact of the nuisance parameters. The most probable Monte Carlo prediction is thus increased, such that an overall underfluctuation of data is observed. This causes the observed limits to be stronger than the expected limits.

7.2 Invisible Higgs Decays

Events are generated to set limits on invisible Higgs decays. The cross sections and uncertainties for the Standard Model Higgs boson production are taken from reference [165]. $H \rightarrow ZZ \rightarrow \nu\bar{\nu}\nu\bar{\nu}$ events are generated using Powheg-Box v1 [166, 167, 168] with the NNPDF30nnlo PDF set [123] and parton showering, using Pythia 8 [127]. The branching fraction of the Higgs boson decaying invisibly is set to 100%, but smaller branching fractions are obtained by scaling the event yield accordingly. The events are finally propagated through a Rivet routine, in order to apply the selections described in section 5.3. From

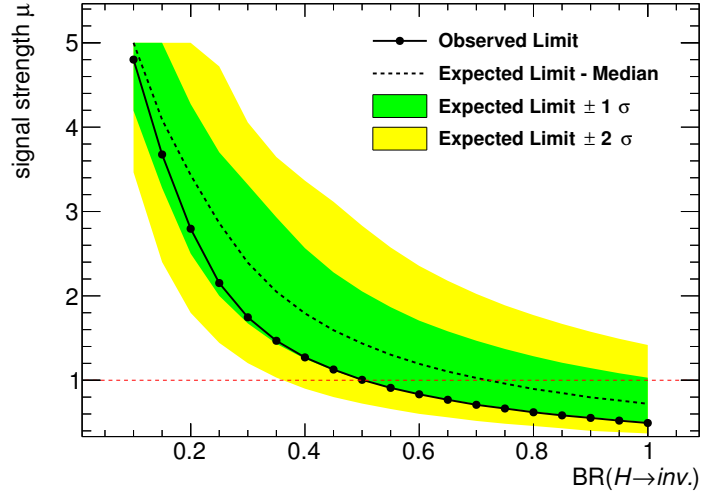


Figure 7.4: Limits on the branching fraction of the Standard Model Higgs boson decaying invisibly.

the distributions obtained by applying the Rivet routing, the expected event yields per bin are extracted and combined with the Standard Model expectation and observed events. Limits are derived on the invisible branching fraction of the Higgs boson.

Branching fractions between 0.1 and 1 are considered in steps of 0.05. For each branching fraction the CL_s limits according to equation 7.12 are calculated, as a function of the signal strength parameter μ . The observed and expected upper limits on μ are extracted and displayed in figure 7.4, together with the $\pm 1\sigma$ and $\pm 2\sigma$ uncertainty bands. Branching fractions can be excluded if the signal strength is smaller than one as indicated by the red dashed line.

According to figure 7.4 branching fractions larger than 0.7 were expected to be excluded by this measurement in the absence of a signal. The observed exclusion limit is found to be at a branching fraction of 0.5. The increased sensitivity is driven by the overestimation of the Monte Carlo simulation in the tail of the m_{jj} distribution. The latter is the variable most sensitive to invisible Higgs decays, since large contributions at high m_{jj} are expected. The down fluctuation of data allows to identify possible new physics contributions more easily, hence better limits than the expectation are observed.

The most recent dedicated ATLAS search [169] for invisibly decaying Higgs bosons, optimized for the Higgs mass at 125 GeV finds observed (expected) exclusion limits at 95% confidence level of 0.37 (0.28).

Discussion

The derived limits demonstrate that a limit setting procedure based on the unfolded distributions yields reasonable constraints on new physics models. Even though a background subtraction based on the Monte Carlo simulation is suboptimal, the observed (expected) limits derived on a simplified dark matter model improved on the previous detector-corrected measurement [4] by $\sim 20\%$ ($\sim 30\%$). The use of data-driven background estimation techniques is expected to yield even stronger limits, especially on the invisible branching fraction of the Higgs boson. The latter suffered from the Sherpa mismodelling of the m_{jj} distribution, which is expected provide largest sensitivity to this signature. A better background estimate with reduced uncertainties is thus expected to strongly improve the obtained limits.

All the tools used to set limits as described in this chapter are publicly available, allowing more new physics models to be constrained in later studies. No detector simulation is necessary, instead events can be generated with any event generator and analyzed using for example a Rivet analysis. The resulting contributions to the measured distributions can be translated into limits on the proposed model, allowing to constrain a variety of models in a simple and straightforward way.

Chapter 8

Conclusion and Outlook

There is compelling evidence from astrophysical observations for the existence of dark matter. So far, all these observations are based on the gravitational force exerted by the dark matter. Interactions with baryonic matter via any of the other fundamental forces have yet to be proven.

The presented analysis searches for dark matter signatures using 36.2 fb^{-1} of proton-proton collisions at $\sqrt{s} = 13 \text{ TeV}$, delivered by the LHC and recorded by the ATLAS detector. The cross sections of two different topological selections are measured differentially, in four observables. The first topology aims at mono-jet signatures which are expected from the production of dark matter recoiling against an initial state radiation jet. The second topology enhances the sensitivity to the electroweak production of dark matter by selecting a vector boson fusion signature. It therefore enhances the sensitivity of the search and, furthermore, allows to constrain a wider range of models. Two control regions are defined which target Z bosons decaying to two electrons or two muons, respectively. The results are presented as a ratio of cross sections of the signal and the combined control regions.

In conventional search approaches, only a few models can be tested against the data, due to the computationally intensive detector simulations. In this work the measured data is instead corrected for detector effects, allowing to compare the results to new physics models at the particle-level. The unfolding method, employed in this work, carefully takes new physics structures into account, that are not included in the description of the detector response.

Two different unfolding strategies are investigated in the context of the work. The first one unfolds the entire selected topology, meaning that no background subtraction is necessary. The second one subtracts all but the most dominant Standard Model processes contributing to the measured spectra, before unfolding the remaining data. The topology unfolding is found to introduce biases in the results and the background subtraction method is consequently used to obtain the final results.

CL_s limits are derived on a simplified model with mediator couplings fixed to $g_q = 0.25$ and $g_\chi = 1.0$. Observed (expected) upper limits at 95% confidence level are found to exclude axial-vector mediator masses of up to 1.5 (1.4) TeV and dark matter masses of 400 (390) GeV. Furthermore, limits on the invisible branching fraction of the Standard Model Higgs boson are derived at 95% CL. Branching fractions larger than 0.5 (0.7) are observed (expected) to be excluded.

In order to significantly improve this analysis the background estimates taken from Monte Carlo simulation are required to be replaced by data-driven techniques. Furthermore, the considered control regions statistically limit the derived limits. Additional control regions with photons, jets or leptonically decaying W bosons in association with jets, provide larger cross sections and, thus, smaller statistical uncertainties. This is expected to significantly improve the sensitivity of this search.

Appendix

A Equivalence of IDS and Bayesian Unfolding

Update Unfolding Matrix

According to equation 4.3 the folding matrix is related to the migration matrix via

$$A_{ij} = n(t_j) \cdot P_{ij} \quad (8.1)$$

this uses the particle-level distribution obtained from Monte Carlo simulation t_j . In the case of an unfolded distribution the latter can be replaced by $n(u_j)$, which is coming from data and is therefore implicitly normalized by $C^{(m)}$. This is reverted

$$A'_{ij} = \frac{1}{C^{(m)}} \cdot n(u_j) \cdot P_{ij} \quad (8.2)$$

and adding 0 leads to

$$A'_{ij} = \frac{1}{C^{(m)}} \cdot n(u_j) \cdot P_{ij} + n(t_j) \cdot P_{ij} - n(t_j) \cdot P_{ij} \quad (8.3)$$

$$= n(t_j) \cdot P_{ij} + [n(u_j) - C^{(m)} \cdot n(t_j)] \cdot \frac{1}{C^{(m)}} \cdot P_{ij} \quad (8.4)$$

$$= n(t_j) \cdot P_{ij} + \Delta u_j \cdot \frac{1}{C^{(m)}} \cdot P_{ij} \quad (8.5)$$

$$= A_{ij} + \Delta u_j \cdot \frac{1}{C^{(m)}} \cdot P_{ij}, \quad (8.6)$$

which is the formula used to modify the migration matrix in IDS unfolding method using $f(|\Delta d_k|, \sigma, \lambda) = 1$. From this A'_{ij} , a temporary folding matrix can be deduced

$$P'_{ij} = \frac{A'_{ij}}{n(u_j)} = \frac{A'_{ij}}{\sum_{k=0}^{N_r} A'_{kj}}. \quad (8.7)$$

Using Bayes theorem as in equation 4.5, with the unfolded distribution u_j as truth prior, this leads to an updated unfolding matrix

$$\tilde{P}'_{ij} = \frac{A'_{ij}}{\sum_{k=0}^{N_t} A'_{ik}}. \quad (8.8)$$

In the IDS algorithm equation 8.7 and the application of Bayes theorem are implicit and equation 8.8 can directly be applied.

B Parameter Estimation for the IDS Method

Parameter Scan of λ_U and λ_M

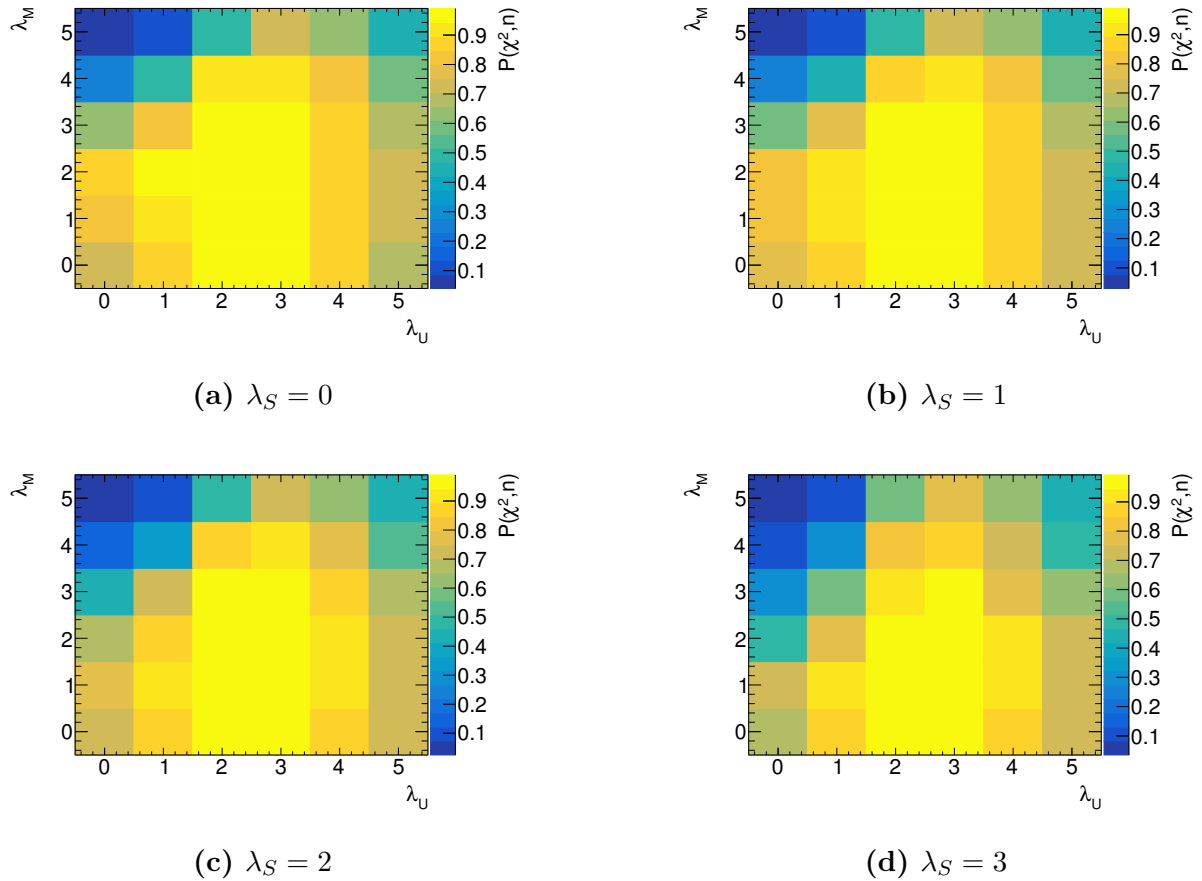


Figure 8.1: Parameter scan of $\lambda_U \in [0, 5]$ and $\lambda_M \in [0, 5]$ for various values of λ_S (a)-(d).

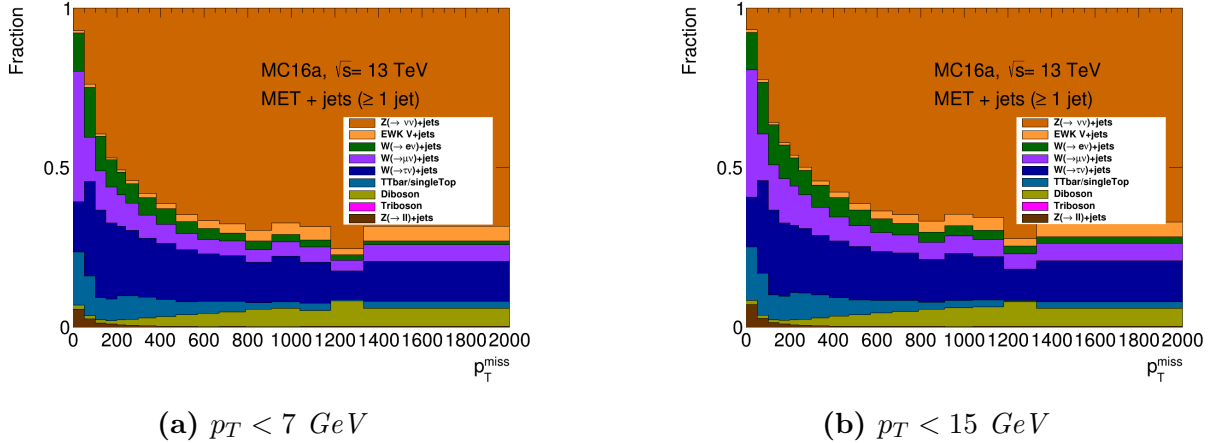


Figure 8.2: Relative Contribution for different cut values of the minimal lepton p_T .

C Choice of Lepton p_T Cut

The p_T dependence of the signal significance in the ≥ 1 jet phase space was studied, to decide between a lepton p_T -cut of 15 GeV or 7 GeV.

The signal region is defined as in table 5.1, only the lepton selection is varied by changing the lepton p_T threshold between the two values. Figure 8.2 shows the relative contributions of the signal ($Z \rightarrow \nu\bar{\nu} + \text{jets}$) and the most dominant background contributions in the signal region. The relative contributions and resulting significance

$$s = \frac{n_{sig}}{\sqrt{n_{bkg}}} \quad (8.9)$$

per bin are shown in the following tables for the selection with $p_T < 7$ GeV in table 8.1 and for $p_T < 15$ GeV in table 8.2.

It is shown that the signal fraction is larger in the case of a lower lepton p_T threshold. This is explained, by the higher suppression factor for leptonic backgrounds like $W \rightarrow l\nu$. A lower threshold increases the fiducial acceptance of the leptons and thereby increases the suppression due to the leptonic veto.

A global improvement of the significance from 715 to 779 for $E_T^{miss} > 200$ GeV and from 1040 to 1140 for $E_T^{miss} > 150$ GeV is found. In both cases this corresponds to an improvement of $\sim 10\%$.

Table 8.1: Relative contribution and significance for lepton $p_T < 7$ GeV

bin	150-	200-	240-	300-	380-	470-	570-	670-	790-	910-	1040-	1180-
$Z \rightarrow \nu\nu$	46.9	50.6	54.0	58.0	61.2	64.8	66.6	67.6	69.6	67.3	68.5	75.4
$W \rightarrow e\nu$	8.46	7.01	6.07	5.52	4.92	3.75	3.33	2.49	2.62	2.23	2.21	1.66
$W \rightarrow \mu\nu$	11.3	9.91	8.54	7.20	5.92	5.06	4.56	4.53	4.00	4.51	4.73	3.41
$W \rightarrow \tau\nu$	23.8	21.7	20.5	18.5	17.6	16.3	14.9	14.4	12.7	14.3	12.9	8.85
Significance	842	521	439	308	189	122	74.1	49.8	31.9	19.5	13.0	9.89

Table 8.2: *Relative contribution and significance for lepton $p_T < 15$ GeV*

bin	150-	200-	240-	300-	380-	470-	570-	670-	790-	910-	1040-	1180-
$Z \rightarrow \nu\nu$	42.2	46.1	49.8	54.1	57.7	61.2	63.5	64.7	66.7	64.6	65.6	72.2
$W \rightarrow e\nu$	10.6	8.87	7.73	6.88	6.11	4.91	4.29	3.51	3.15	3.11	2.81	2.41
$W \rightarrow \mu\nu$	13.9	12.2	10.5	8.89	7.45	6.58	5.94	5.73	5.29	5.55	5.35	4.75
$W \rightarrow \tau\nu$	23.0	21.2	20.3	18.6	17.8	16.7	15.3	14.9	13.5	14.7	13.5	9.84
Significance	767	477	404	285	176	114	69.4	46.7	29.9	18.4	12.2	9.12

D Monte Carlo Simulation Samples used for the Analysis

The following descriptions are standardized descriptions provided by the ATLAS collaboration. They were obtained from [170], to describe the Monte Carlo simulation used in this work.

Events containing W or Z bosons with associated jets are simulated using the Sherpa 2.2.1 [132] event generator. Matrix elements are calculated for up to 2 partons at NLO and 4 partons at LO using Comix [171] and OpenLoops [172] and merged with the Sherpa parton shower [173] according to the ME+PS@NLO prescription [174]. The NNPDF30nnlo PDF set [123] is used in conjunction with dedicated parton shower tuning developed by the Sherpa authors. The W/Z + jets events are normalized with the NNLO cross sections (see k-Factors below).

For the generation of ttbar events, Powheg-Box v2 [175, 176, 163] is used with the CT10 PDF set [177] in the matrix element calculations. Electroweak t-channel, s-channel and Wt-channel single top-quark events are generated with Powheg-Box v1. This event generator uses the four-flavor scheme for the NLO matrix element calculations together with the fixed four-flavor PDF set CT10f4. For all top processes, top-quark spin correlations are preserved (for t-channel, top quarks are decayed using MadSpin [178]). The parton shower, hadronization, and the underlying event are simulated using Pythia 6.428 [179] with the CTEQ6L1 PDF set [180] and the corresponding Perugia 2012 set of tuned parameters (P2012) [181]. The top mass is set to 172.5 GeV. The EvtGen 1.2.0 program [182] is used for the properties of b- and c-hadron decays.

The renormalization and factorization scales are set to:

- t-channel: $4 \cdot \sqrt{m(b)^2 + p_T(b)^2}$ - b denotes the spectator b-quark
- s-channel: $m(\text{top})$
- Wt : $m(\text{top})$
- ttbar : $\sqrt{m(t)^2 + p_T(t)^2}$

Diboson processes with one of the bosons decaying hadronically and the other leptonically are simulated with the Sherpa 2.2.1 event generator [132]. They are calculated for up to 1 additional parton at NLO and up to 3 additional partons at LO using Comix [171] and OpenLoops [172], and merged with the Sherpa parton shower [173] according to the ME+PS@NLO prescription [174]. The NNPDF30nnlo PDF set [123] is used in conjunction with dedicated parton shower tuning developed by the Sherpa authors. The event generator cross sections are used in this case (already at NLO). Diboson processes with 4 charged leptons, 3 charged leptons + 1 neutrino or 2 charged leptons and 2 neutrinos are simulated with the Sherpa 2.2.2 event generator [132]. Matrix elements contain all diagrams with four electroweak vertices. They are calculated for up to 1 partons at NLO and up to 3 partons at LO using Comix [171] and OpenLoops [172], and merged with the Sherpa parton shower [173] according to the ME+PS@NLO prescription [174]. The NNPDF3.0nnlo PDF set [123] is used in conjunction with dedicated parton shower tuning developed by the Sherpa authors. The event generator cross sections are used in this case (already at NLO). Multiple overlaid proton-proton collisions are simulated with the soft QCD processes of Pythia 8.186 [183] using the A2 set of tuned parameters [133] and the MSTW2008LO [134] PDF set [135].

Table 8.3: *EWKVjj Sherpa 2.2.1 Monte Carlo simulation samples with production cross section times branching ratio, K-factors and filter efficiencies.*

Sample ID	Sample	$\sigma \times \text{BR}$ [pb]	K-factor	Filter eff.
308092	EWKVjj_Sh221_Zee2jets	0.6315	1.0	1.0
308093	EWKVjj_Sh221_Zmm2jets	0.6353	1.0	1.0
308094	EWKVjj_Sh221_Ztautau2jets	0.6334	1.0	1.0
308095	EWKVjj_Sh221_Znu2jets	2.9327	1.0	1.0
308096	EWKVjj_Sh221_Wenu2jets	6.803	1.0	1.0
308097	EWKVjj_Sh221_Wmunu2jets	6.8008	1.0	1.0
308098	EWKVjj_Sh221_Wtaunu2jets	6.7983	1.0	1.0

Table 8.4: $Z \rightarrow \nu\nu$ Sherpa 2.2.1 Monte Carlo simulation samples with production cross section times branching ratio, K -factors and filter efficiencies.

Sample ID	Sample	$\sigma \times \text{BR}$ [pb]	K-factor	Filter eff.
364142	Znunu_MAXHTPTV0_70_CVetoBVeto	10706	0.9728	0.8211
364143	Znunu_MAXHTPTV0_70_CFilterBVeto	10705	0.9728	0.1119
364144	Znunu_MAXHTPTV0_70_BFilter	10705	0.9728	0.0674
364145	Znunu_MAXHTPTV70_140_CVetoBVeto	607.65	0.9728	0.6903
364146	Znunu_MAXHTPTV70_140_CFilterBVeto	607.59	0.9728	0.1896
364147	Znunu_MAXHTPTV70_140_BFilter	607.97	0.9728	0.1196
364148	Znunu_MAXHTPTV140_280_CVetoBVeto	222.33	0.9728	0.6170
364149	Znunu_MAXHTPTV140_280_CFilterBVeto	222.31	0.9728	0.2337
364150	Znunu_MAXHTPTV140_280_BFilter	222.38	0.9728	0.1581
364151	Znunu_MAXHTPTV280_500_CVetoBVeto	47.423	0.9728	0.5613
364152	Znunu_MAXHTPTV280_500_CFilterBVeto	47.401	0.9728	0.2650
364153	Znunu_MAXHTPTV280_500_BFilter	47.421	0.9728	0.1805
364154	Znunu_MAXHTPTV500_1000	9.9101	0.9728	1.0
364155	Znunu_MAXHTPTV1000_E_CMS	0.818	0.9728	1.0

Table 8.5: $Z \rightarrow ee$ Sherpa 2.2.1 Monte Carlo simulation samples with production cross section times branching ratio, K -factors and filter efficiencies.

Sample ID	Sample	$\sigma \times \text{BR}$ [pb]	K-factor	Filter eff.
364114	Zee_MAXHTPTV0_70_CVetoBVeto	1981.6	0.9751	0.8213
364115	Zee_MAXHTPTV0_70_CFilterBVeto	1981.5	0.9751	0.1139
364116	Zee_MAXHTPTV0_70_BFilter	1982	0.9751	0.0658
364117	Zee_MAXHTPTV70_140_CVetoBVeto	110.65	0.9751	0.6942
364118	Zee_MAXHTPTV70_140_CFilterBVeto	110.5	0.9751	0.1886
364119	Zee_MAXHTPTV70_140_BFilter	110.46	0.9751	0.1183
364120	Zee_MAXHTPTV140_280_CVetoBVeto	40.679	0.9751	0.6162
364121	Zee_MAXHTPTV140_280_CFilterBVeto	40.671	0.9751	0.2329
364122	Zee_MAXHTPTV140_280_BFilter	40.674	0.9751	0.1533
364123	Zee_MAXHTPTV280_500_CVetoBVeto	8.6701	0.9751	0.5674
364124	Zee_MAXHTPTV280_500_CFilterBVeto	8.6668	0.9751	0.2662
364125	Zee_MAXHTPTV280_500_BFilter	8.6812	0.9751	0.1765
364126	Zee_MAXHTPTV500_1000	1.8092	0.9751	1.0
364127	Zee_MAXHTPTV1000_E_CMS	0.1488	0.9751	1.0

Table 8.6: $Z \rightarrow \mu\mu$ Sherpa 2.2.1 Monte Carlo simulation samples with production cross section times branching ratio, K-factors and filter efficiencies.

Sample ID	Sample	$\sigma \times \text{BR}$ [pb]	K-factor	Filter eff.
364100	Zmumu_MAXHTPTV0_70_CVetoBVeto	1982.4	0.9751	0.8218
364101	Zmumu_MAXHTPTV0_70_CFilterBVeto	1982.1	0.9751	0.1136
364102	Zmumu_MAXHTPTV0_70_BFilter	1981.5	0.9751	0.0658
364103	Zmumu_MAXHTPTV70_140_CVetoBVeto	109.13	0.9751	0.6895
364104	Zmumu_MAXHTPTV70_140_CFilterBVeto	108.81	0.9751	0.1970
364105	Zmumu_MAXHTPTV70_140_BFilter	108.98	0.9751	0.1177
364106	Zmumu_MAXHTPTV140_280_CVetoBVeto	39.873	0.9751	0.6028
364107	Zmumu_MAXHTPTV140_280_CFilterBVeto	39.86	0.9751	0.2353
364108	Zmumu_MAXHTPTV140_280_BFilter	39.891	0.9751	0.1562
364109	Zmumu_MAXHTPTV280_500_CVetoBVeto	8.5256	0.9751	0.5602
364110	Zmumu_MAXHTPTV280_500_CFilterBVeto	8.5259	0.9751	0.2664
364111	Zmumu_MAXHTPTV280_500_BFilter	8.5273	0.9751	0.1766
364112	Zmumu_MAXHTPTV500_1000	1.7871	0.9751	1.0
364113	Zmumu_MAXHTPTV1000_E_CMS	0.1476	0.9751	1.0

Table 8.7: $Z \rightarrow \tau\tau$ Sherpa 2.2.1 Monte Carlo simulation samples with production cross section times branching ratio, K-factors and filter efficiencies.

Sample ID	Sample	$\sigma \times \text{BR}$ [pb]	K-factor	Filter eff.
364128	Ztautau_MAXHTPTV0_70_CVetoBVeto	1981.7	0.9751	0.8345
364129	Ztautau_MAXHTPTV0_70_CFilterBVeto	1981.7	0.9751	0.1096
364130	Ztautau_MAXHTPTV0_70_BFilter	1982.1	0.9751	0.0658
364131	Ztautau_MAXHTPTV70_140_CVetoBVeto	110.61	0.9751	0.6927
364132	Ztautau_MAXHTPTV70_140_CFilterBVeto	110.56	0.9751	0.1902
364133	Ztautau_MAXHTPTV70_140_BFilter	110.66	0.9751	0.1109
364134	Ztautau_MAXHTPTV140_280_CVetoBVeto	40.771	0.9751	0.6181
364135	Ztautau_MAXHTPTV140_280_CFilterBVeto	40.716	0.9751	0.2343
364136	Ztautau_MAXHTPTV140_280_BFilter	40.746	0.9751	0.1553
364137	Ztautau_MAXHTPTV280_500_CVetoBVeto	8.6639	0.9751	0.5634
364138	Ztautau_MAXHTPTV280_500_CFilterBVeto	8.676	0.9751	0.2643
364139	Ztautau_MAXHTPTV280_500_BFilter	8.6795	0.9751	0.1763
364140	Ztautau_MAXHTPTV500_1000	1.8078	0.9751	1.0
364141	Ztautau_MAXHTPTV1000_E_CMS	0.1483	0.9751	1.0

Table 8.8: $W \rightarrow e\nu$ Sherpa 2.2.1 Monte Carlo simulation samples with production cross section times branching ratio, K -factors and filter efficiencies.

Sample ID	Sample	$\sigma \times \text{BR}$ [pb]	K-factor	Filter eff.
364170	Wenu_MAXHTPTV0.70_CVetoBVeto	19153	0.9702	0.8247
364171	Wenu_MAXHTPTV0.70_CFilterBVeto	19145	0.9702	0.1309
364172	Wenu_MAXHTPTV0.70_BFilter	19138	0.9702	0.0448
364173	Wenu_MAXHTPTV70.140_CVetoBVeto	944.98	0.9702	0.6748
364174	Wenu_MAXHTPTV70.140_CFilterBVeto	945.74	0.9702	0.2441
364175	Wenu_MAXHTPTV70.140_BFilter	945.75	0.9702	0.1034
364176	Wenu_MAXHTPTV140.280_CVetoBVeto	339.67	0.9702	0.5988
364177	Wenu_MAXHTPTV140.280_CFilterBVeto	339.87	0.9702	0.2888
364178	Wenu_MAXHTPTV140.280_BFilter	339.64	0.9702	0.1090
364179	Wenu_MAXHTPTV280.500_CVetoBVeto	72.074	0.9702	0.5483
364180	Wenu_MAXHTPTV280.500_CFilterBVeto	72.105	0.9702	0.3197
364181	Wenu_MAXHTPTV280.500_BFilter	72.091	0.9702	0.1371
364182	Wenu_MAXHTPTV500.1000	15.047	0.9702	1.0
364183	Wenu_MAXHTPTV1000_E_CMS	1.2344	0.9702	1.0

Table 8.9: $W \rightarrow \mu\nu$ Sherpa 2.2.1 Monte Carlo simulation samples with production cross section times branching ratio, K -factors and filter efficiencies.

Sample ID	Sample	$\sigma \times \text{BR}$ [pb]	K-factor	Filter eff.
364156	Wmunu_MAXHTPTV0.70_CVetoBVeto	19149	0.9702	0.8245
364157	Wmunu_MAXHTPTV0.70_CFilterBVeto	19142	0.9702	0.1309
364158	Wmunu_MAXHTPTV0.70_BFilter	19138	0.9702	0.0446
364159	Wmunu_MAXHTPTV70.140_CVetoBVeto	945.52	0.9702	0.6743
364160	Wmunu_MAXHTPTV70.140_CFilterBVeto	945.38	0.9702	0.2435
364161	Wmunu_MAXHTPTV70.140_BFilter	944.34	0.9702	0.0837
364162	Wmunu_MAXHTPTV140.280_CVetoBVeto	339.71	0.9702	0.6020
364163	Wmunu_MAXHTPTV140.280_CFilterBVeto	339.88	0.9702	0.2925
364164	Wmunu_MAXHTPTV140.280_BFilter	339.64	0.9702	0.1103
364165	Wmunu_MAXHTPTV280.500_CVetoBVeto	72.079	0.9702	0.5477
364166	Wmunu_MAXHTPTV280.500_CFilterBVeto	72.1	0.9702	0.3202
364167	Wmunu_MAXHTPTV280.500_BFilter	72.058	0.9702	0.1254
364168	Wmunu_MAXHTPTV500.1000	15.006	0.9702	1.0
364169	Wmunu_MAXHTPTV1000_E_CMS	1.2348	0.9702	1.0

Table 8.10: $W \rightarrow \tau\nu$ Sherpa 2.2.1 Monte Carlo simulation samples with production cross section times branching ratio, K -factors and filter efficiencies.

Sample ID	Sample	$\sigma \times \text{BR}$ [pb]	K-factor	Filter eff.
364184	Wtaunu_MAXHTPTV0.70_CVetoBVeto	19155	0.9702	0.8246
364185	Wtaunu_MAXHTPTV0.70_CFilterBVeto	19149	0.9702	0.1315
364186	Wtaunu_MAXHTPTV0.70_BFilter	19144	0.9702	0.0451
364187	Wtaunu_MAXHTPTV70.140_CVetoBVeto	945.02	0.9702	0.6756
364188	Wtaunu_MAXHTPTV70.140_CFilterBVeto	946.23	0.9702	0.2425
364189	Wtaunu_MAXHTPTV70.140_BFilter	945.71	0.9702	0.1039
364190	Wtaunu_MAXHTPTV140.280_CVetoBVeto	339.66	0.9702	0.5988
364191	Wtaunu_MAXHTPTV140.280_CFilterBVeto	339.74	0.9702	0.2874
364192	Wtaunu_MAXHTPTV140.280_BFilter	339.31	0.9702	0.1058
364193	Wtaunu_MAXHTPTV280.500_CVetoBVeto	72.075	0.9702	0.5700
364194	Wtaunu_MAXHTPTV280.500_CFilterBVeto	71.984	0.9702	0.3187
364195	Wtaunu_MAXHTPTV280.500_BFilter	71.945	0.9702	0.1360
364196	Wtaunu_MAXHTPTV500.1000	15.052	0.9702	1.0
364197	Wtaunu_MAXHTPTV1000_E_CMS	1.2341	0.9702	1.0

Table 8.11: $TTbar$ and $SingleTop$ Monte Carlo simulation samples with production cross section times branching ratio, K -factors and filter efficiencies.

Sample ID	Sample	$\sigma \times \text{BR}$ [pb]	K-factor	Filter eff.
410470	ttbar_hdamp258p75_nonall had	729.77	1.1398	0.5438
410644	singletop_schan_lept_top	2.0267	1.0170	1.0
410645	singletop_schan_lept_antitop	1.2674	1.0167	1.0
410646	Wt_DR_inclusive_top	37.936	0.9450	1.0
410647	Wt_DR_inclusive_antitop	37.905	0.9457	1.0
410658	tchan_BW50_lept_top	36.996	1.0	1.0
410659	tchan_BW50_lept_antitop	22.175	1.0	1.0

Table 8.12: *Diboson Sherpa 2.2.1 Monte Carlo simulation samples with production cross section times branching ratio, K-factors and filter efficiencies.*

Sample ID	Sample	$\sigma \times \text{BR}$ [pb]	K-factor	Filter eff.
363355	Sherpa_221_NNP30NNLO_ZqqZvv	15.567	1.0	0.2798
363356	Sherpa_221_NNP30NNLO_ZqqZll	15.561	1.0	0.1409
363357	Sherpa_221_NNP30NNLO_WqqZvv	6.7908	1.0	1.0
363358	Sherpa_221_NNP30NNLO_WqqZll	3.4332	1.0	1.0
363359	Sherpa_221_NNP30NNLO_WpqqWmlv	24.710	1.0	1.0
363360	Sherpa_221_NNP30NNLO_WplvWmqq	24.728	1.0	1.0
363489	Sherpa_221_NNP30NNLO_WlvZqq	11.418	1.0	1.0
363494	Sherpa_221_NNP30NNLO_vvvv	0.6033	1.0	1.0
364250	Sherpa_222_NNP30NNLO_llll	1.2519	1.0	1.0
364253	Sherpa_222_NNP30NNLO_lllv	4.5786	1.0	1.0
364254	Sherpa_222_NNP30NNLO_llvv	12.500	1.0	1.0
364255	Sherpa_222_NNP30NNLO_lvvv	3.2350	1.0	1.0

Table 8.13: *Triboson Sherpa 2.2.2 Monte Carlo simulation samples with production cross section times branching ratio, K-factors and filter efficiencies.*

Sample ID	Sample	$\sigma \times \text{BR}$ [pb]	K-factor	Filter eff.
364242	Sherpa_222_NNP30NNLO_WWW_3l3v	7.1979e-03	1.0	1.0
364243	Sherpa_222_NNP30NNLO_WWZ_4l2v	1.7966e-03	1.0	1.0
364244	Sherpa_222_NNP30NNLO_WWZ_2l4v	3.5467e-03	1.0	1.0
364245	Sherpa_222_NNP30NNLO_WZZ_5l1v	1.8807e-04	1.0	1.0
364246	Sherpa_222_NNP30NNLO_WZZ_3l3v	1.6680e-03	1.0	0.4463
364247	Sherpa_222_NNP30NNLO_ZZZ_6l0v	1.4508e-05	1.0	1.0
364248	Sherpa_222_NNP30NNLO_ZZZ_4l2v	3.8533e-04	1.0	0.2245
364249	Sherpa_222_NNP30NNLO_ZZZ_2l4v	3.8545e-04	1.0	0.4447

E Bootstrapped Uncertainties in Systematic Variations

When systematically varying one of the nuisance parameters of the analysis (see table 5.3) the spectrum of the final observable will vary to a certain degree, since the object selection or calibration changed. The relative change in each bin

$$R = \frac{r_i^{\text{varied}}}{r_i^{\text{nominal}}} \quad (8.10)$$

of the distribution is taken as a systematic uncertainty due to this nuisance parameter.

When estimating the statistical error on the systematic uncertainty one could use normal error propagation, using the statistical error of the numerator and denominator. However, this does not respect the correlations between the two distribution.

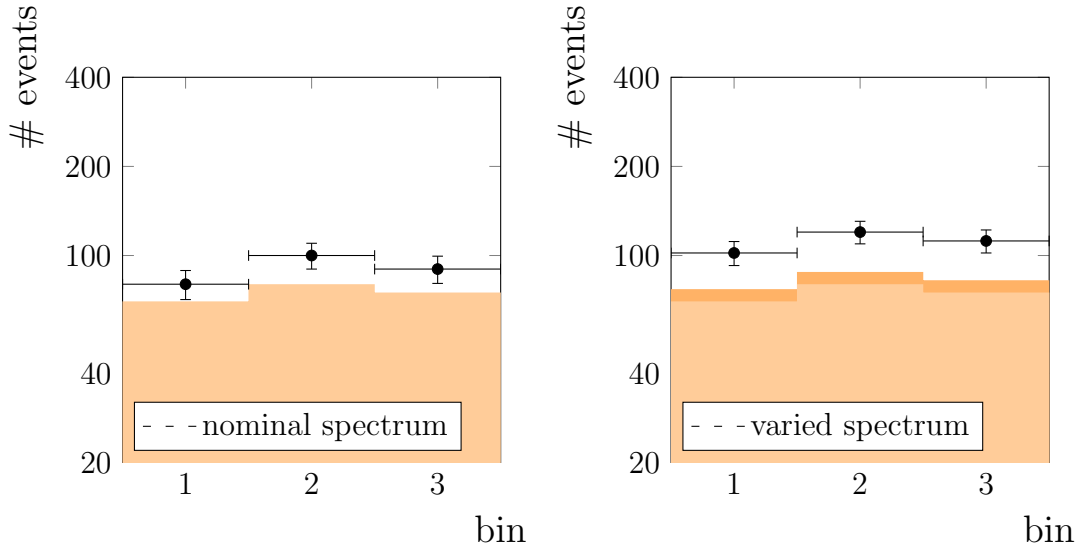


Figure 8.3: Systematic variation indicating an up-shift in the bin content of $\sim 10\%$ (black points). The events that are identical between the nominal and the varied distribution (light orange) are shifted exactly by 10% (dark orange) whereas additional events which migrated in/out have an additional effect (changing whitespace between orange bars and black points).

Looking at a particular bin r_i , in the varied distribution many of the events will remain in the same bin as they were in the nominal distribution (light orange in figure 8.3). These events may modify the spectrum due to the systematic shift (e.g. modified event weight due to lepton efficiency scale factors, dark orange in figure 8.3), however, they are reconstructed in the same bin. Only a few events will have migrated out to other bins or in from neighboring bins (changing whitespace between orange bars and black points in figure 8.3), thereby modifying the spectrum due to their systematic shift (as above)

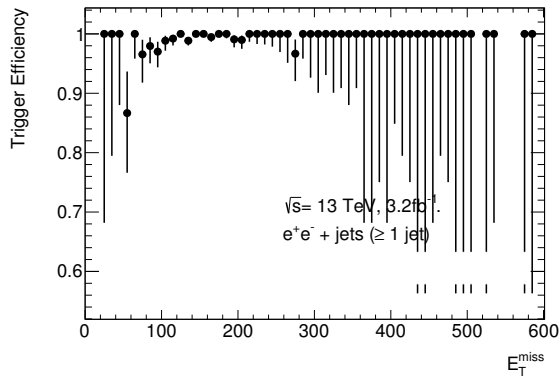
and their presence in a different bin. Keeping track of the correlations between bins without bootstrapping is in principle possible, but tedious. However, without taking the correlations into account and using normal error propagation, some information is lost.

This challenge is solved by the bootstrapping approach. Each event in the bootstrap replicas is initialized with an individual random seed, which is always the same. This means that a particular event will distribute to the bootstrap replicas in the same way for the nominal and varied distributions. Calculating the ratio between the varied and the nominal distribution of all bootstrap replicas means that the shift due to the identical events in a bin is thus exactly the same in all bootstrap replicas. If no migrations from one bin to another were present, the uncertainty on the shift would therefore be 0, as it is present in all replicas in an identical way. However, some events are different between the nominal and varied bin content and the shift is therefore not the same in all replicas. The spread of the shift over all replicas is the uncertainty on the systematic variation. The large fraction of identical events, which are respected with the bootstrap method, however, result in a more realistic uncertainty estimate.

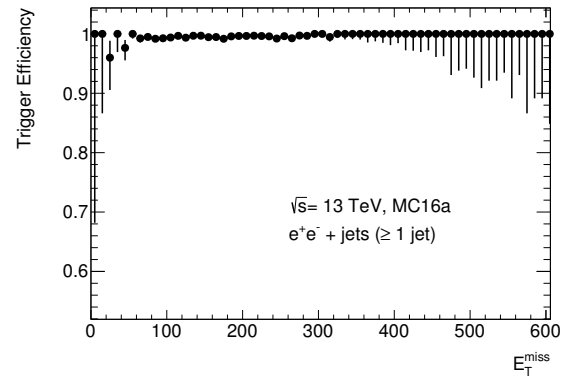
Hypothetically, if no events are reconstructed in the same bin before and after a systematic variation, the uncertainty from Gaussian error propagation is recovered, as the replicas would be completely uncorrelated. In the case of 100% of the events being in the same bin before and after the variation, an uncertainty on the systematic variation of 0 could be assigned.

F Trigger Efficiency for $Z \rightarrow ee$ and $Z \rightarrow \mu\mu$ Selection

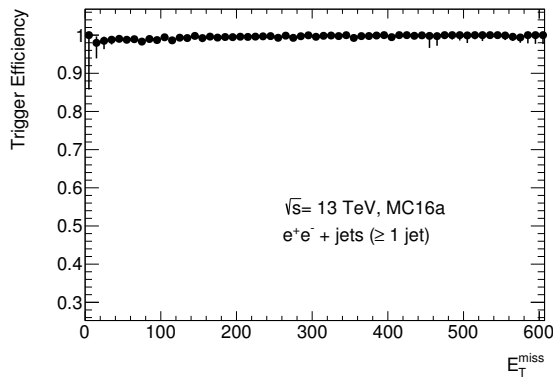
Shown in figures 8.4 and 8.5 are the trigger efficiencies for the control regions targeting the Z boson decay to two electron and two muons, respectively. Both trigger strategies are more than 99% efficient in their respective control region. This is true for data recorded in 2015 and 2016 as well as for the Monte Carlo simulation. The resulting scale factors are compatible with one, such that no scale factors to correct for data to Monte Carlo simulation disagreements are applied in the analysis.



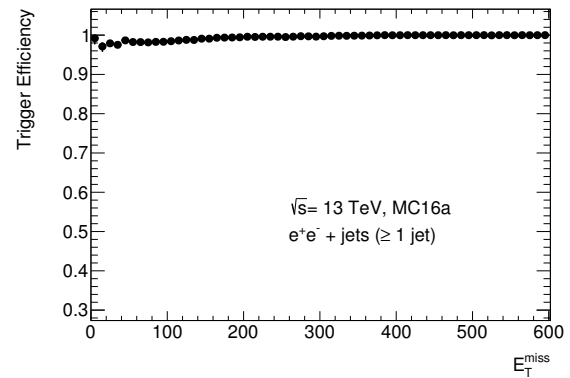
(a) trigger turn-on in 2015 data



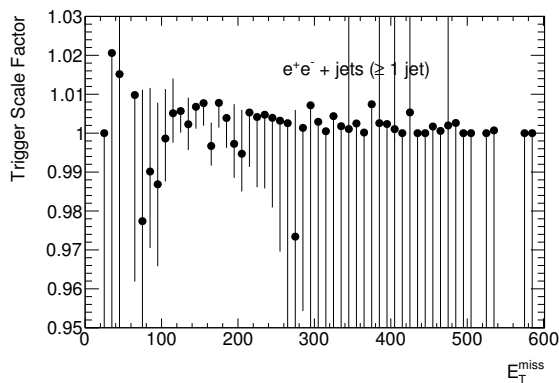
(b) trigger turn-on in 2016 data



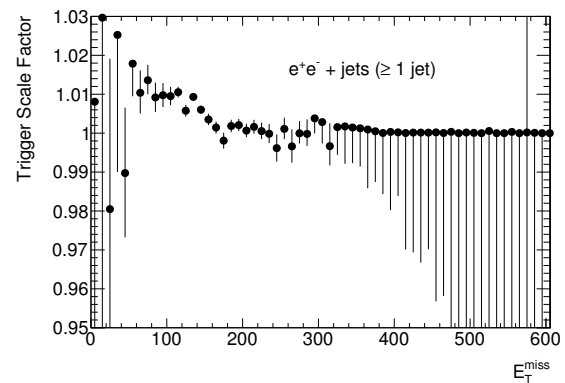
(c) trigger turn-on MC: 2015 triggers



(d) trigger turn-on MC: 2016 triggers

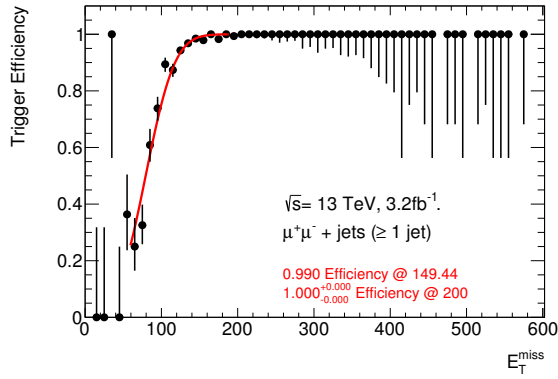


(e) scale factors for 2015 trigger simulation

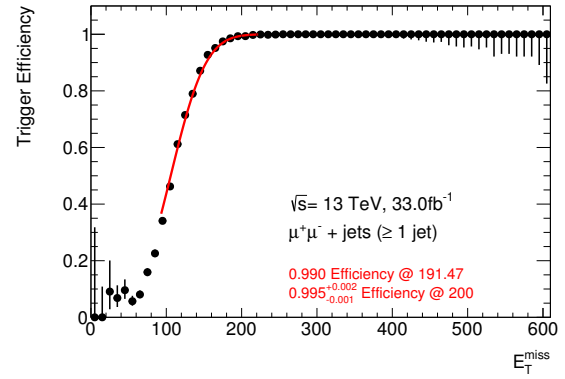


(f) scale factors for 2016 trigger simulation

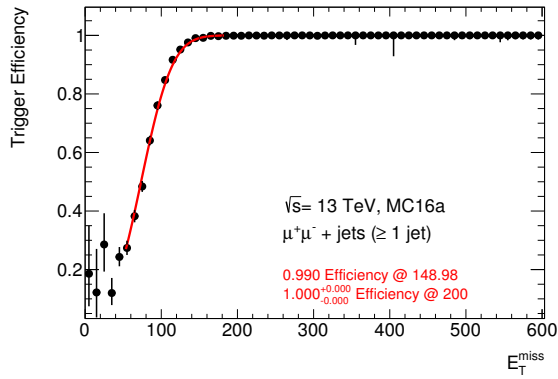
Figure 8.4: Trigger turn-on curves (a-b) in data and (c-d) in Monte Carlo simulation and (e-f) corresponding scale factors in (left) 2015 and (right) 2016.



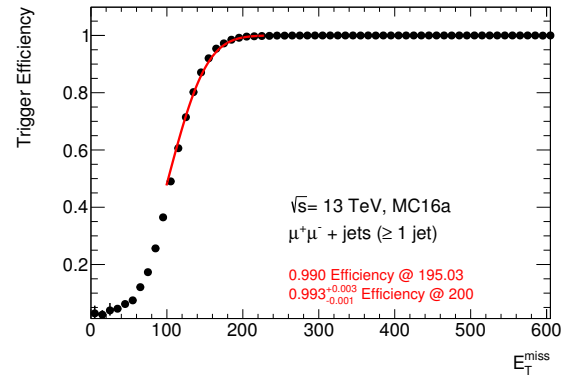
(a) trigger turn-on in 2015 data



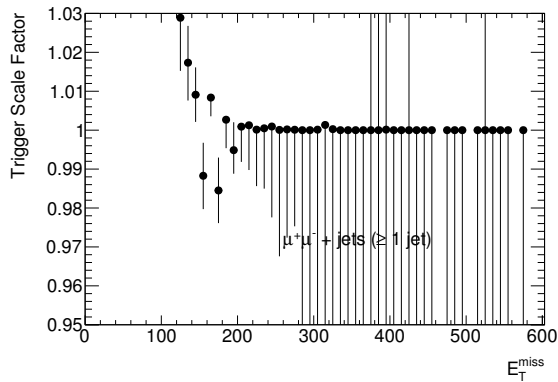
(b) trigger turn-on in 2016 data



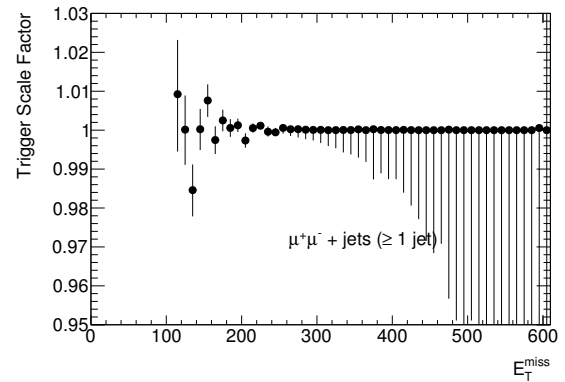
(c) trigger turn-on MC: 2015 triggers



(d) trigger turn-on MC: 2016 triggers



(e) scale factors for 2015 trigger simulation



(f) scale factors for 2016 trigger simulation

Figure 8.5: Trigger turn-on curves (a-b) in data and (c-d) in Monte Carlo simulation and (e-f) corresponding scale factors in (left) 2015 and (right) 2016.

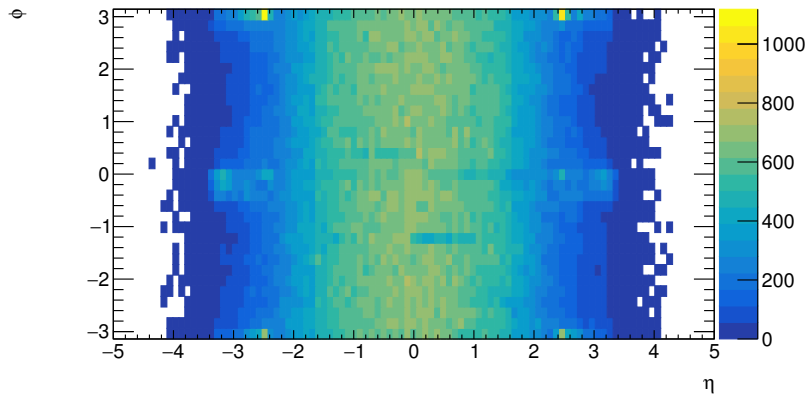


Figure 8.6: η - ϕ map of the leading jet in the ≥ 1 jet phase space. Excesses of jets are found at $\phi \sim 0$ and $\phi \sim \pi$ outside the tracker coverage, at $|\eta| > 2.5$.

G Non-Collision Background in the Signal Region

Non-collision background (NCB) are signals recorded by the detector, which do not come from particle collisions, but are supplemental signals from cosmic particles, detector noise or beam-backgrounds. It is found, that there is a contribution of beam background remaining in the signal region, which is faking jets. Fake jets due to non-collision background are suppressed by the jet cleaning cuts introduced in section 5.4. However, a significant amount is found to remain at low missing transverse energies in the ≥ 1 jet signal region.

Fake jets from beam induced backgrounds are identified as excesses in the ϕ distribution of the jets [149], which is observed in the signal region of the ≥ 1 jet selection, as depicted in figure 8.8 (figure shows $200 \text{ GeV} < E_T^{miss} < 270 \text{ GeV}$ slice). Here excesses of jets are found at $\phi \sim 0$ and $\phi \sim \pi$ outside the tracker coverage, at $|\eta| > 2.5$.

Furthermore, non-collision backgrounds can be identified as belated signals in the detector, since they do not originate from bunch crossings, which are timed precisely. Displayed in figure 8.7a is the timing of jets faked by beam-background, compared to nominal collision jets, as it is expected from beam-backgrounds [184]. Additionally the observed events as a function of ϕ and the timing in nano-seconds are shown in figure 8.7b. Mistimed jets are present with a similar timing profile, tending towards early signals at negative timing values, as is expected from beam-background. The jets are found in the ϕ region where excesses of jets are observed.

Furthermore, it is found that these fake jets deposit a significant amount of energy in the electromagnetic calorimeter and have a very narrow width in the ϕ direction. Both of these properties hint to electrons, which are misidentified as jets. Electrons are identified very efficiently, as long as they are within the tracking acceptance. This is no longer the case at $|\eta| > 2.5$, thus, they are more easily misidentified as jets.

These events can partially be rejected by applying cuts on the jets, applying the following logic:

- Events are rejected if any jet within $|\phi| < 0.5$ or $|\phi| > 2.5$, and $|\eta| > 2.5$ is timed at

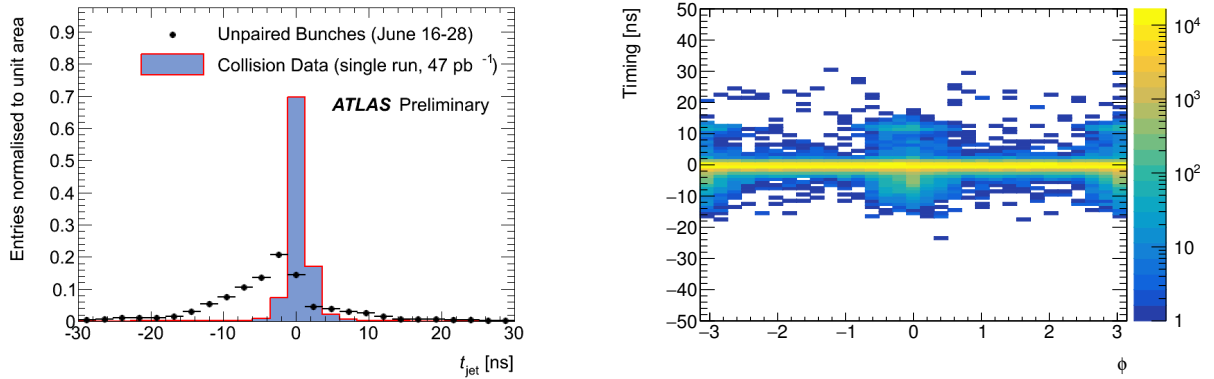
(a) *Expected beam-background timing [184]*(b) *observed beam-background timing*

Figure 8.7: *Faked jets due to non-collision backgrounds (a) compared to jet coming from the bunch crossings (separate study taken from [184]). (b) Number of jets measured as function of ϕ and timing. Excesses towards early (negative timing values) signals are identified as jets coming from beam background.*

$$t > 4\text{ns} \text{ or } t < -2\text{ns}.$$

- Events are rejected if the leading jet is timed at $t > 4\text{ns}$ or $t < -2\text{ns}$.
- Events are rejected if the leading jet is within $|\phi| < 0.5$ or $|\phi| > 2.5$, and $|\eta| > 2.5$, and has an electromagnetic fraction larger than 95% or a width in the ϕ direction smaller than 0.005.

It is found that jets are efficiently reduced in the targeted region and the ϕ distribution approaches a flat behavior, as would be expected without NCB.

The effect on the E_T^{miss} distribution of the ≥ 1 signal region is found to be $\sim 3\%$ in the 200-270GeV bin and $< 1\%$ in all other bins. The effect on the distribution of the VBF signal region is found to be negligible. More detailed studies are ongoing in order to deduce a background estimate or a correction for this effect.

H Binning Optimization for Observables

Introduced in this section are the iterative procedure and supplementary plots to the binning optimization of the E_T^{miss} and m_{jj} observables.

Starting with the E_T^{miss} observable, a two dimensional map of all events in the respective signal/control region is constructed, counting all events reconstructed in bin r_i and coming from particle-level bin t_j . At this point the histogram is binned very finely in steps of 1 GeV (see figure 8.9a).

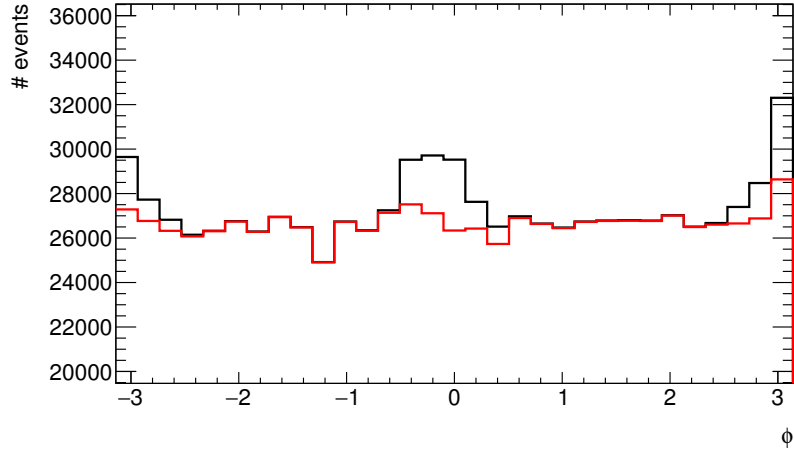
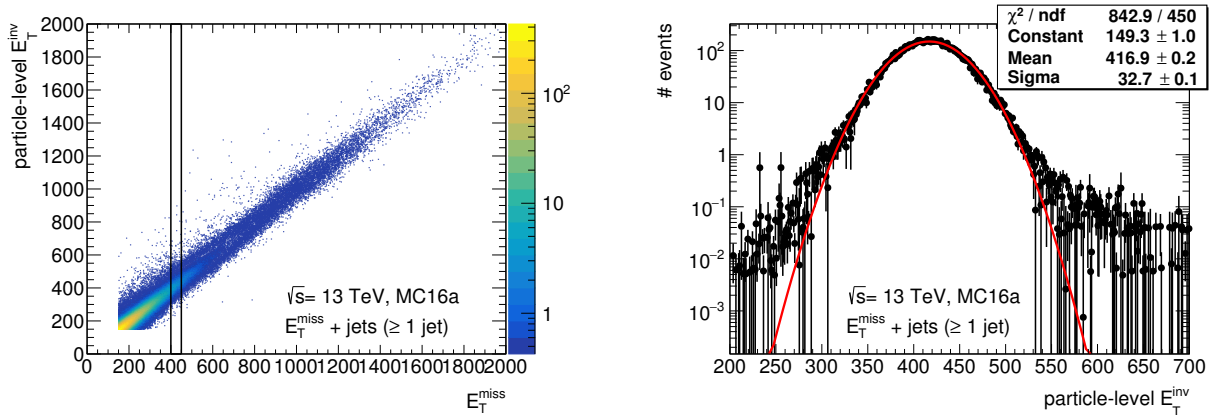


Figure 8.8: Number of events as a function of ϕ in the $[200, 270]$ GeV E_T^{miss} bin in the ≥ 1 jet region, before (black) and after (red) the addition NCB rejection cuts.

For a given range of reconstructed E_T^{miss} the resolution can be determined by looking at the distribution of the particle-level E_T^{inv} in that bin¹. Figure 8.9b illustrates the distribution of particle-level E_T^{inv} in the range of $400 \text{ GeV} < E_T^{miss} < 450 \text{ GeV}$, as marked in figure 8.9a. The resolution as given by a Gaussian fit to the distribution is 32.7 GeV. Large tails of the distribution cause a slight underestimation of the resolution, which is why in the following the root-mean-square (RMS) is used instead of a fit to the distribution.



(a) E_T^{miss} versus particle-level E_T^{inv} in 1 GeV binning

(b) particle-level E_T^{inv} distribution in the range $400 \text{ GeV} < E_T^{miss} < 450 \text{ GeV}$

Figure 8.9: A resolution estimate in a given interval of E_T^{miss} is estimated by analyzing the distribution of E_T^{inv} in that interval. A Gaussian fit underestimates the tails of this distribution, motivating the use of the RMS for the resolution.

¹ E_T^{inv} at particle-level is the transverse energy of all invisible particles, which is the equivalent of E_T^{miss} at reconstruction-level.

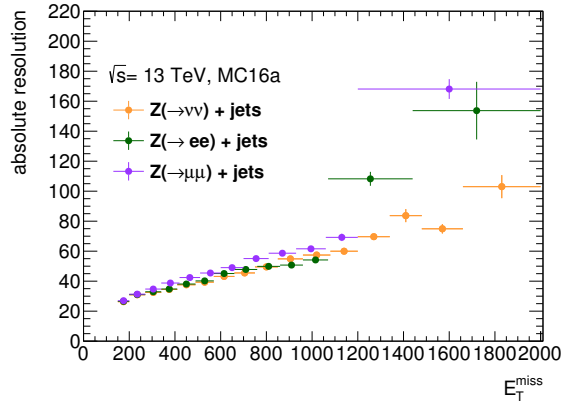


Figure 8.10: Absolute resolutions of E_T^{miss} in bins of the reconstructed E_T^{miss} . Shown are the optimal binning for each channel individually before synchronizing the bin edges.

To obtain a bin size as close as possible to twice the resolution for all bins, an iterative approach is implemented. The bins from figure 8.9a are added one by one from small to large values of E_T^{miss} , until the resolution within this (growing) bin is smaller than twice the bin size. Afterwards it is rounded to the next largest 10 GeV value. The upper edge then defines the lower edge for the next bin where the process is repeated.

This is done for all three signal and control regions with the respective Z decay, resulting in an optimal binning for each channel. The absolute resolution for each region within this optimized binning is illustrated in figure 8.10 (relative resolutions are shown in 8.11a).

In order to synchronize the bin edges, all edges between the three channels are compared. The first deviating bin edge, again going from small to large values of the observable, is fixed to the largest upper bin edge for all channels. Afterwards the bin edges for the remaining bins are re-optimized according to the above prescription, before the next synchronized upper edge is determined.

Figure 6.2a in the main body of the text shows the optimized E_T^{miss} binning for the three regions after the bins are synchronized (relative resolutions are shown in figure 8.11b).

The same procedure as described for the E_T^{miss} observable is employed for m_{jj} . The respective plots and the final binning are summarized below. Figure 8.12 shows the reconstruction-level vs particle-level m_{jj} distribution used to optimize the binning. Figure 8.13 shows the optimized binning of the m_{jj} observable for the three regions before synchronizing the bin edges, while figure 6.2b shows the absolute resolution after the synchronization. The relative resolutions in both cases are furthermore shown in figure 8.14.

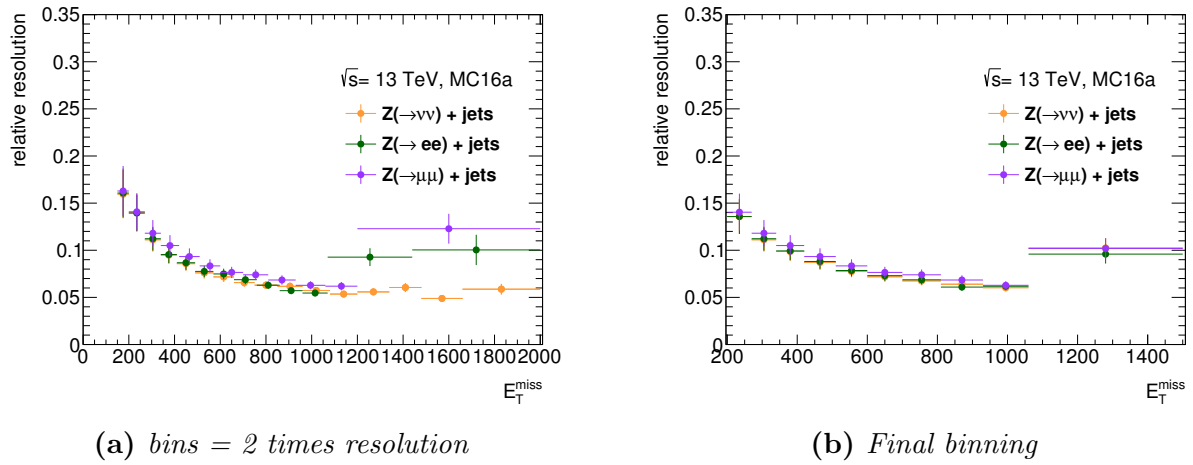


Figure 8.11: Relative resolutions of E_T^{miss} in bins of the reconstructed E_T^{miss} . Shown are the optimal binning for each channel individually before (a) and after (b) synchronizing the bin edges.

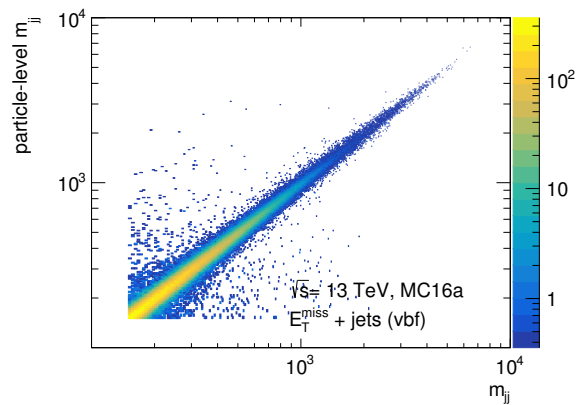


Figure 8.12: m_{jj} versus particle-level m_{jj} in 5 GeV binning

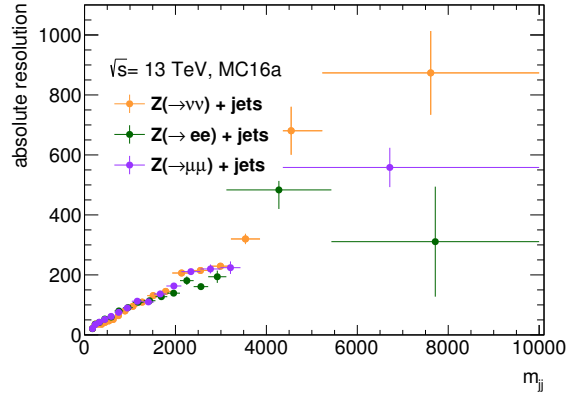
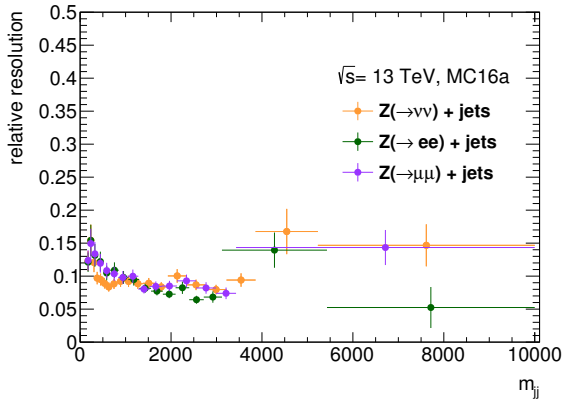
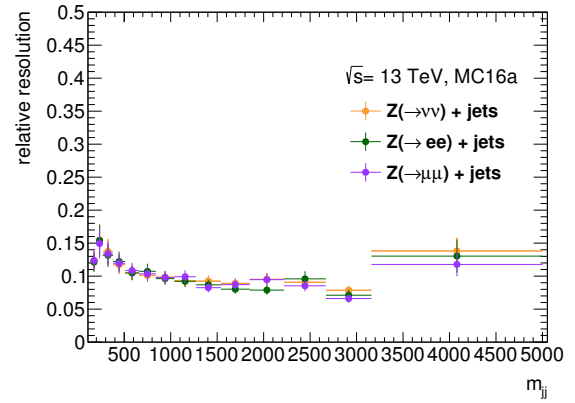


Figure 8.13: Absolute resolutions of m_{jj} in bins of the reconstructed m_{jj} . Shown are the optimal binning for each channel individually before synchronizing the bin edges.



(a) bins = 2 times resolution



(b) Final binning

Figure 8.14: Relative resolutions of m_{jj} in bins of the reconstructed m_{jj} . Shown are the optimal binning for each channel individually before (a) and after (b) synchronizing the bin edges.

I Variations of Process versus Topology Detector Responses

Shown in figures 8.15 and 8.16 are the different Monte Carlo simulation processes contributing to the ≥ 1 jet signal region. Each of the processes is unfolded and compared to its particle-level expectation. In the unfolding the four possible combinations are tested in which purity and stability correction are coming from either the topology response or the individual process, and the resolution correction is coming from either of the two as well.

Using all corrections coming from the individual process by construction recovers the particle-level expectation (green), whereas using all corrections coming from the topology response recovers the biases seen in figure 6.4 (yellow).

Choosing only the resolution correction from the topology response, while the stability and purity correction are coming from the simulation of the individual process, shows the bias due to the different migration matrices (blue).

Using the stability and purity correction from the topology response and taking the migration matrix from the individual process is more difficult to interpret. The purity correction results in modified spectrum different from what the migration matrix of the individual process is build from. Hence the IDS algorithm will modify the migration matrix in order to recover this mismodeling. Furthermore, the bias introduced by the stability and purity correction, as seen in topology-response-only unfolding is also visible here (red).

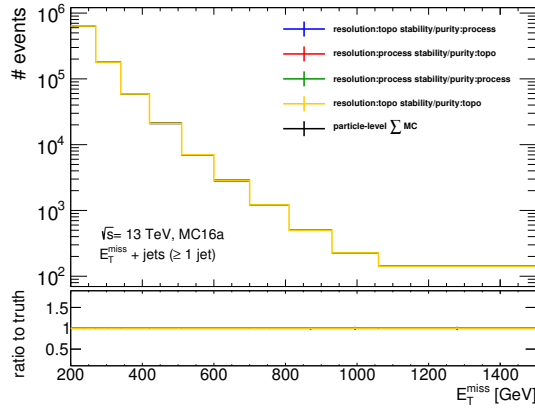
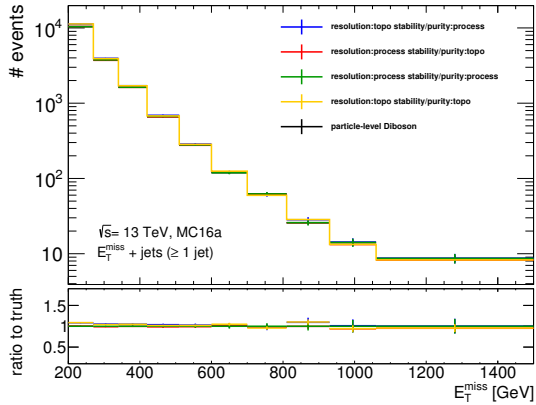
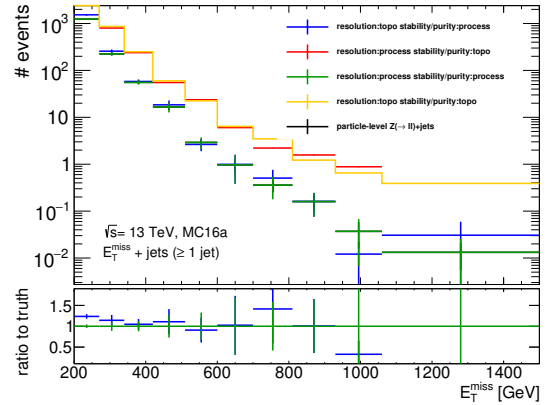
(a) $\sum MC$ (b) *DiBoson*(c) $Z \rightarrow ll + jets$

Figure 8.15: Biases in the unfolding as function of E_T^{miss} with respect to the particle-level expectation of the individual processes contributing to the ≥ 1 jet signal region. The input to the unfolding is varied to use the stability-, purity- and resolution correction from either the topology response or the individual process.

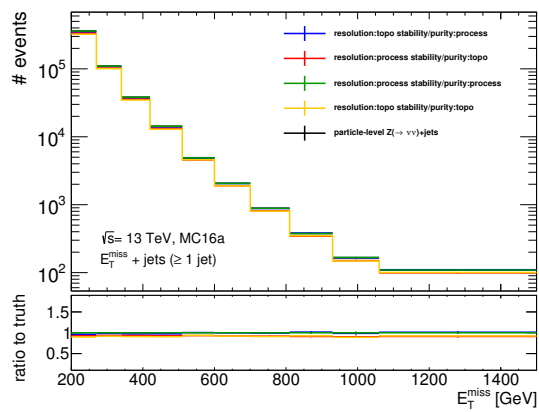
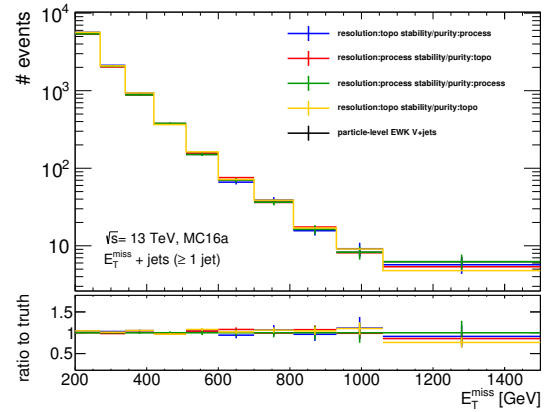
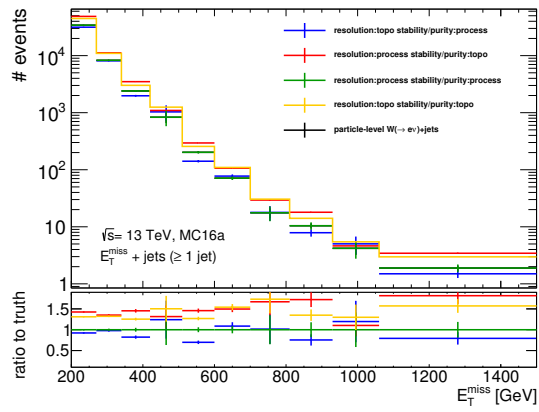
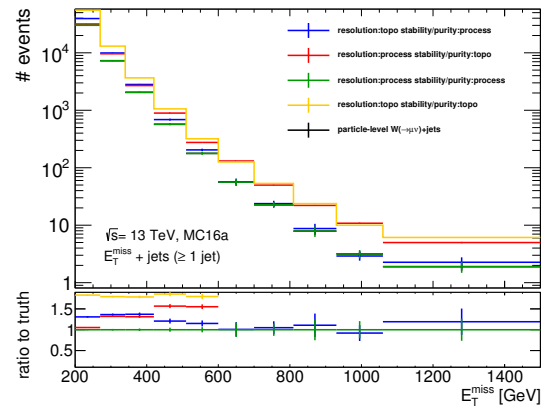
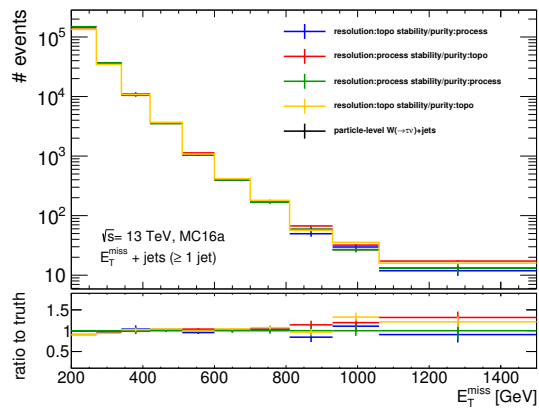
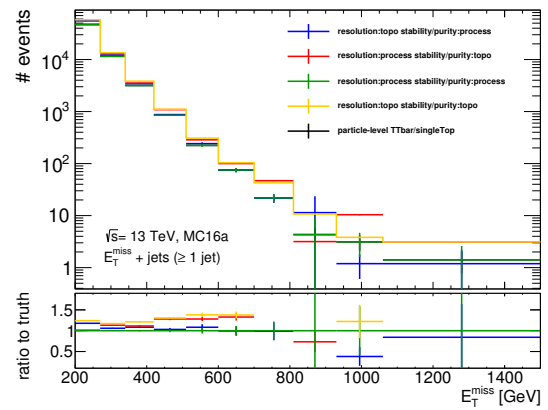

 (a) $Z \rightarrow \nu\bar{\nu} + jets$

 (b) $EWK V + jets$

 (c) $W \rightarrow e\nu + jets$

 (d) $W \rightarrow \mu\nu + jets$

 (e) $W \rightarrow \tau\nu + jets$

 (f) $TT\bar{t}/singleTop$

Figure 8.16: Biases in the unfolding as function of E_T^{miss} with respect to the particle-level expectation of the individual processes contributing to the ≥ 1 jet signal region. The input to the unfolding is varied to use the stability-, purity- and resolution correction from either the topology response or the individual process.

J Covariances and Correlations after Unfolding

The unfolding procedure introduces correlations between the measured bins, due to the migration of events from one bin to another. Therefore, after the unfolding the statistical uncertainties on the respective bins are also correlated. This is represented in the covariance matrices displayed below.

The covariance matrices show the uncertainty on the E_T^{miss} bins in the signal region of the ≥ 1 jet signature after taking into account the statistical uncertainty on the data and the Monte Carlo simulation respectively. The uncertainty coming from the limited statistics of the background subtracted data is obtained by unfolding 5000 bootstrap replicas (see section 4.2) of the data distribution with the nominal detector response from Monte Carlo simulation (see figure 8.17). The uncertainty on the Monte Carlo simulation is obtained by unfolding the background subtracted data distribution with 5000 bootstrap replicas of the detector response (see figure 8.18).

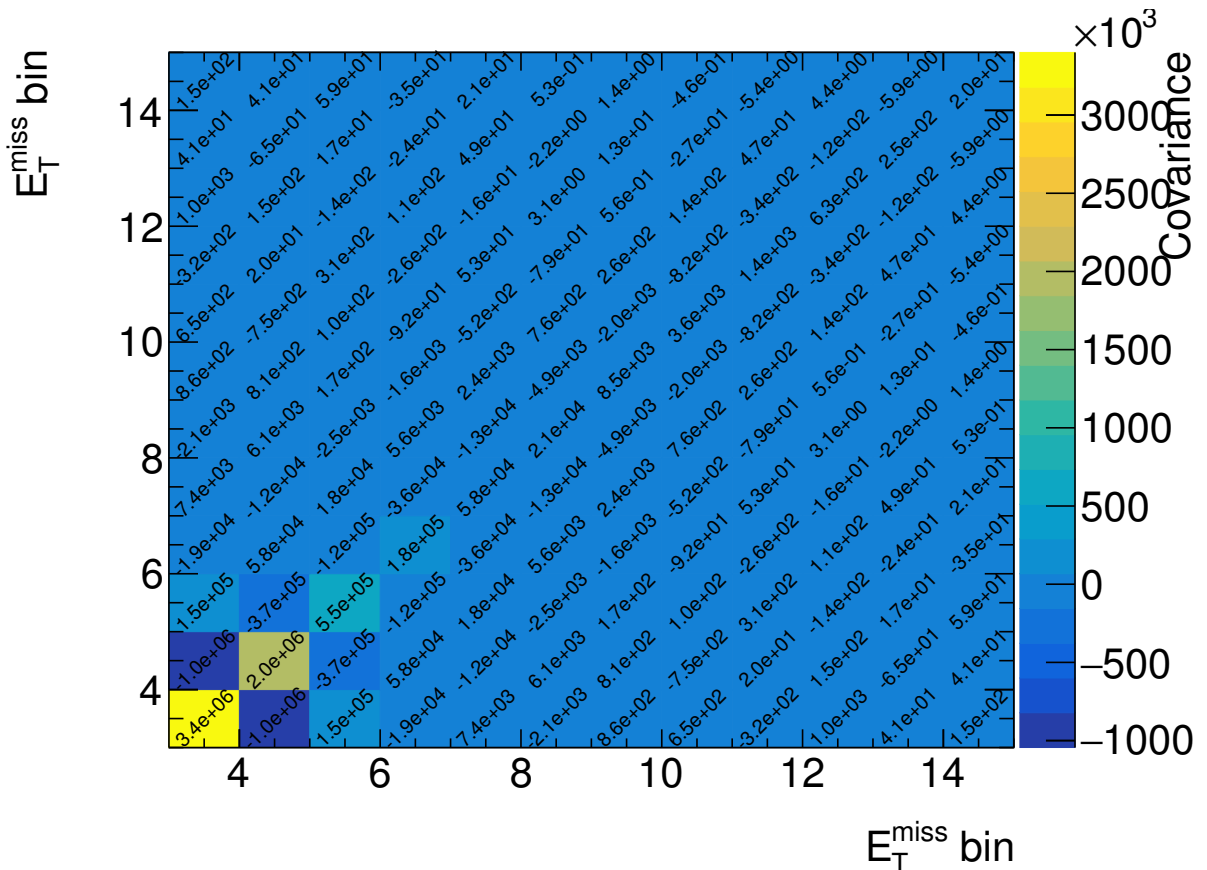


Figure 8.17: Covariance matrix of the unfolded E_T^{miss} distribution in the signal region of the ≥ 1 jet signature due to limited data statistics.

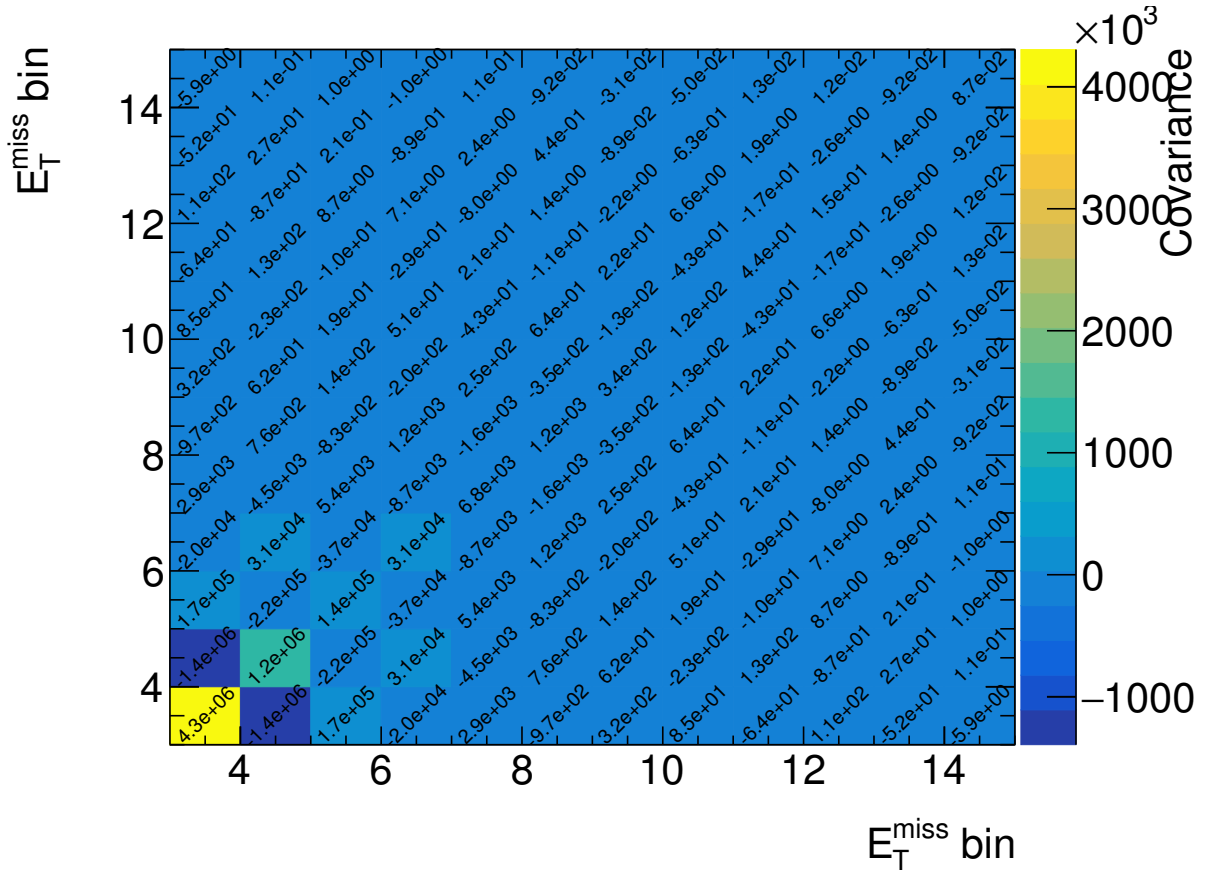


Figure 8.18: Covariance matrix of the unfolded E_T^{miss} distribution in the signal region of the ≥ 1 jet signature due to limited Monte Carlo statistics.

The uncertainties are added in quadrature by the equivalent procedure of unfolding the 5000 data distributions using 5000 response replicas.

Furthermore, the correlations between the different observables are determined via the bootstrap replicas. The correlations between all bins of the four observables of interest in the signal region is displayed below. It is found that the E_T^{miss} distributions of the ≥ 1 jet and the VBF signature are highly correlated, whereas all others mostly show correlations with neighboring bins.

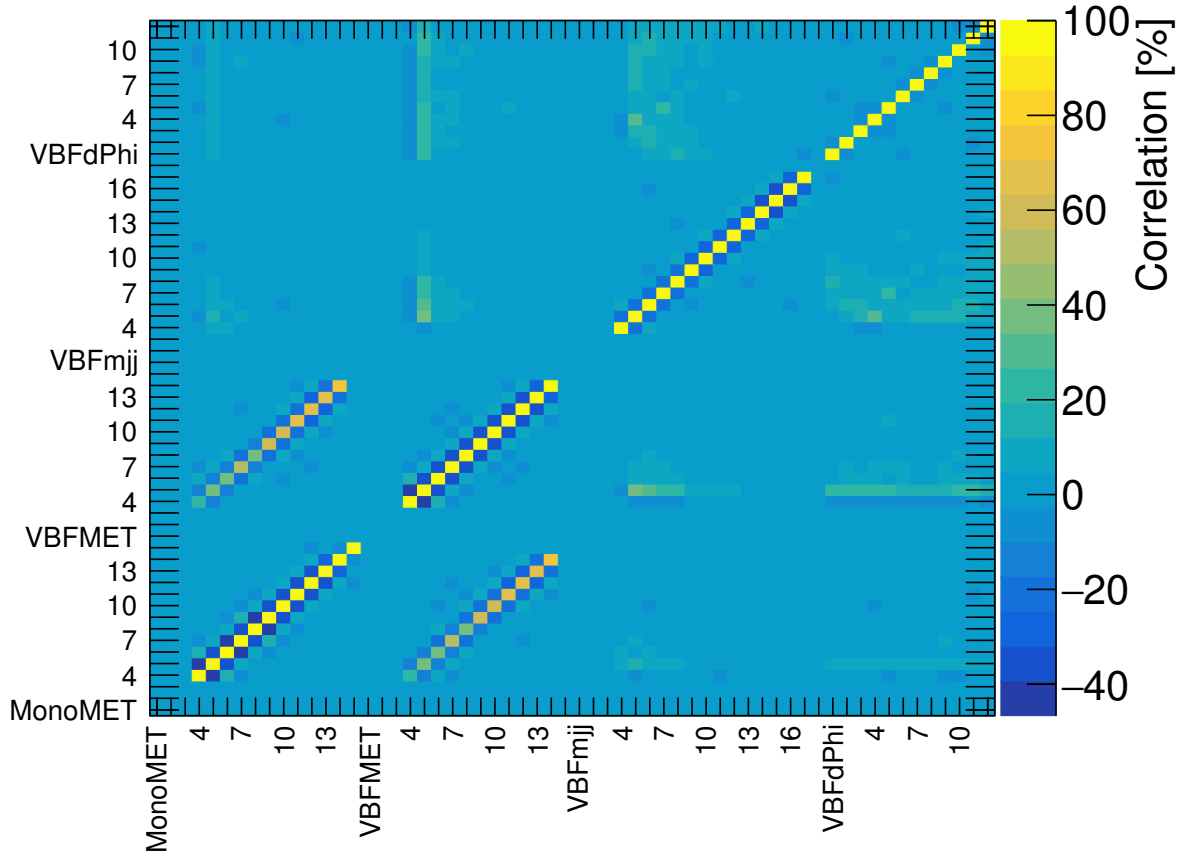


Figure 8.19: Correlation matrix of the bins of all observables of interest in the signal region. Large correlations between the E_T^{miss} distributions of the ≥ 1 jet and the VBF signature are observed.

K Likelihood Combination of $Z \rightarrow ee$ and $Z \rightarrow \mu\mu$ for 2016 Paper

In the published paper “Measurement of detector-corrected observables sensitive to the anomalous production of events with jets and large missing transverse momentum in pp -collisions at $\sqrt{s} = 13$ TeV using the ATLAS detector” [4] two control regions targeting leptonically decaying Z bosons are measured. In order to construct a ratio

$$R_{miss} = \frac{\sigma(E_T^{miss} + jets)}{\sigma(Z \rightarrow l^+l^- + jets)}. \quad (8.11)$$

between the signal region and the two control regions, a statistical combination of the latter was required. In the paper a combination using the best linear unbiased estimate (BLUE) method [185] is employed. To check the validity of these results a maximum likelihood (ML) estimation technique is performed in addition. This served as a cross check for the

results obtained by BLUE.

In a ML estimation the set of parameters is searched, which maximizes the probability for the measured data. In the presented case, the parameters of interest are the number of expected events in each bin of the measured distributions n_{exp}^i for a Z boson decaying to two leptons $Z \rightarrow ll$. Measured data was obtained for the Z boson decay to two electrons $n_{obs,ee}^i$ as well as to two muons $n_{obs,\mu\mu}^i$. The uncertainties are assumed to follow Gaussian statistics, as the data was unfolded to particle-level, which introduces correlations between the bins, such that the uncertainties no longer follow Poissonian statistics. The probability for a measurement, given a certain expectation value is thus defined by

$$G(n_{obs}|n_{exp}, \sigma_{n_{obs}}) = \frac{1}{2\pi\sigma_{n_{obs}}^2} \exp\left(\frac{-(n_{obs} - n_{exp})^2}{2\sigma_{n_{obs}}^2}\right). \quad (8.12)$$

where $\sigma_{n_{obs}}$ is the statistical uncertainty on the measurement of n_{obs} . The likelihood for a single bin is the product of the probability densities of the two measurements, given that they should both have the same expectation value:

$$\mathcal{L}(n_{obs,ee}, n_{obs,\mu\mu}|n_{exp}) = G(n_{obs,ee}|n_{exp}, \sigma_{n_{obs,ee}}) \cdot G(n_{obs,\mu\mu}|n_{exp}, \sigma_{n_{obs,\mu\mu}}). \quad (8.13)$$

Systematic uncertainties on the measurement are introduced via nuisance parameters $\vec{\theta}$. Since an uncertainty can be understood as a possible modification to the observed event yield, they are introduced as

$$\hat{n}_{obs}^i(\vec{\theta}) = n_{obs}^i + \sum_k \sigma_{\theta_k}^i \theta_k, \quad (8.14)$$

where n_{obs}^i is the number of observed events when all nuisance parameters are set to 0 and $\sigma_{\theta_k}^i$ is the absolute uncertainty on the event yield in bin i due to nuisance parameter θ_k . The systematic uncertainties are described by Gaussian uncertainties around their most probably value, so that the nuisance parameters θ_k are constrained by a Gaussian distribution centered at zero with a width of one $G(\theta_k|0, 1)$. A one sigma variation of the nuisance parameter thus modifies the event yields by the Gaussian width of the uncertainty: $\sigma_{\theta_k}^i$.

The Gaussian constraints are multiplied to the Likelihood. Correlated uncertainties like the jet energy scale and resolution are constrained by the same nuisance parameter, whereas individual uncertainties like the electron and muon efficiency uncertainties are constrained by different nuisance parameters.

The likelihood for the combination of the two channels is therefore given by

$$\begin{aligned} \mathcal{L}(\vec{\hat{n}}_{obs,ee}, \vec{\hat{n}}_{obs,\mu\mu}|\vec{n}_{exp}, \vec{\theta}) &= \prod_i G(\hat{n}_{obs,ee}^i(\vec{\theta})|n_{exp}^i, \sigma_{n_{obs,ee}}^i) \cdot G(\hat{n}_{obs,\mu\mu}^i(\vec{\theta})|n_{exp}^i, \sigma_{n_{obs,\mu\mu}}^i) \\ &\times \prod_k^{N_{corr}} G(\theta_k|0, 1) \prod_l^{2N_{uncorr}} G(\theta_l|0, 1). \end{aligned} \quad (8.15)$$

The negative natural logarithm of this likelihood is minimized, in order to find the most probably values for n_{exp}^i as well as the nuisance parameters θ_k and the obtained results are checked against the estimates obtained by BLUE.

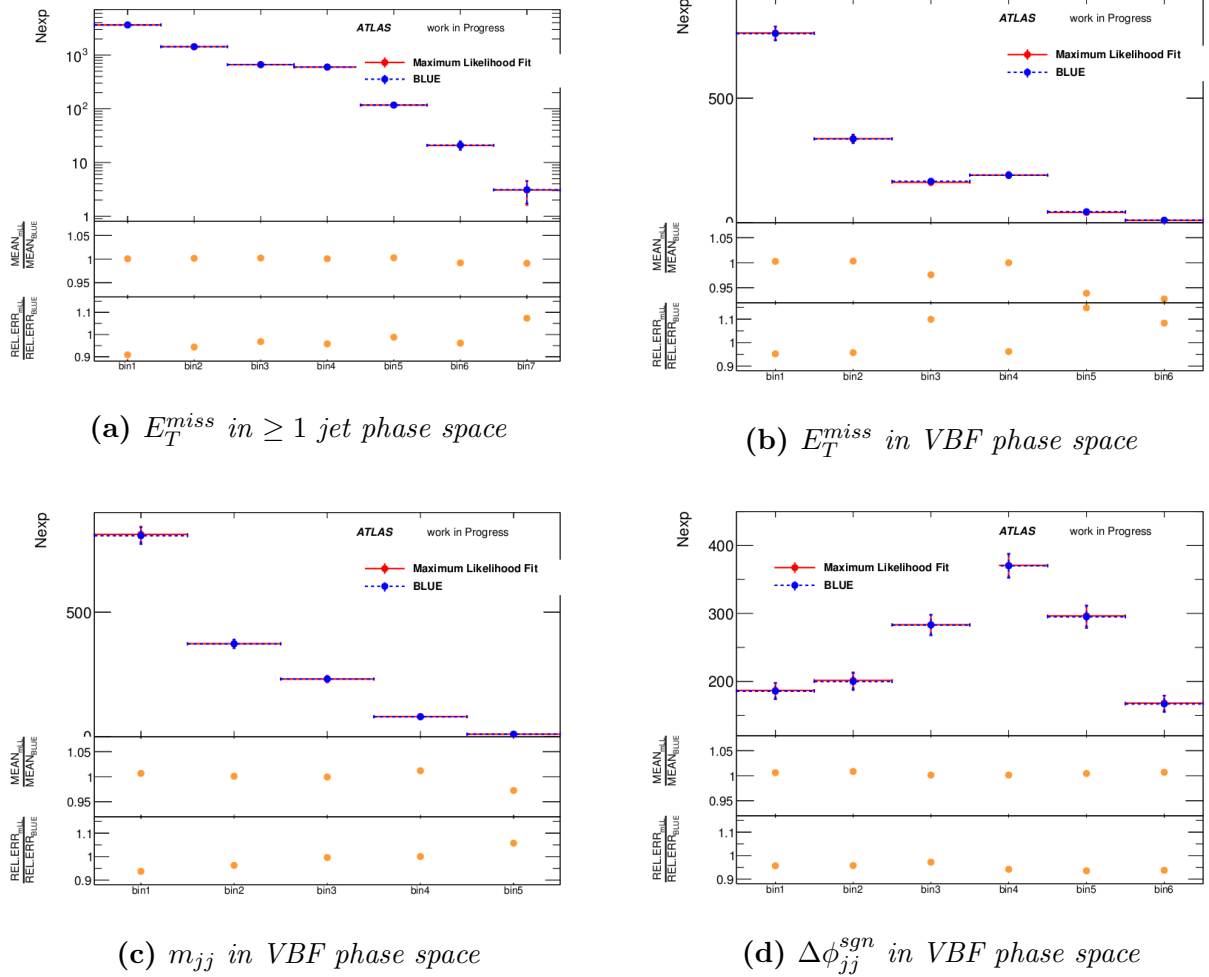


Figure 8.20: Agreement between the best linear unbiased estimator and the maximum likelihood estimate of the two control regions.

As illustrated in figure 8.20 the estimates of the BLUE and the ML method are in agreement with each other. Small deviations of up to 7% are found in bins with a very low event yield, where the assumption of Gaussian uncertainties no longer holds. The uncertainties are in agreement at the level of less than 10% between the two methods. Since the cross check was designed to get a coarse estimate of the validity of the results obtained by BLUE, no further investigations were conducted.

Bibliography

- [1] P. A. R. Ade et al. “Planck 2015 results. XIII. Cosmological parameters”. In: *Astron. Astrophys.* 594 (2016), A13. DOI: 10.1051/0004-6361/201525830. arXiv: 1502.01589 [astro-ph.CO].
- [2] Morad Aaboud et al. “Constraints on mediator-based dark matter and scalar dark energy models using $\sqrt{s} = 13$ TeV pp collision data collected by the ATLAS detector”. In: (2019). arXiv: 1903.01400 [hep-ex].
- [3] *CMS Exotics Public Results*. <https://twiki.cern.ch/twiki/bin/view/CMSPublic/PhysicsResultsEX0>. Accessed: 2019-04-30.
- [4] Morad Aaboud et al. “Measurement of detector-corrected observables sensitive to the anomalous production of events with jets and large missing transverse momentum in pp collisions at $\sqrt{s} = 13$ TeV using the ATLAS detector”. In: *Eur. Phys. J. C* 77.11 (2017), p. 765. DOI: 10.1140/epjc/s10052-017-5315-6. arXiv: 1707.03263 [hep-ex].
- [5] Lyndon Evans and Philip Bryant. “LHC Machine”. In: *Journal of Instrumentation* 3.08 (Aug. 2008), S08001–S08001. DOI: 10.1088/1748-0221/3/08/s08001. URL: <https://doi.org/10.1088/1748-0221/3/08/s08001>.
- [6] G. Aad et al. “The ATLAS Experiment at the CERN Large Hadron Collider”. In: *JINST* 3 (2008), S08003. DOI: 10.1088/1748-0221/3/08/S08003.
- [7] Oliver Sim Brüning et al. *LHC Design Report*. Vol. 1. CERN Yellow Reports: Monographs. Geneva: CERN, 2004. URL: <http://cds.cern.ch/record/782076>.
- [8] *Guinness World Records*. <http://www.guinnessworldrecords.de>. Accessed: 2018-12-28.
- [9] Georges Aad et al. “Observation of a new particle in the search for the Standard Model Higgs boson with the ATLAS detector at the LHC”. In: *Phys. Lett.* B716 (2012), pp. 1–29. DOI: 10.1016/j.physletb.2012.08.020. arXiv: 1207.7214 [hep-ex].
- [10] Serguei Chatrchyan et al. “Observation of a new boson at a mass of 125 GeV with the CMS experiment at the LHC”. In: *Phys. Lett.* B716 (2012), pp. 30–61. DOI: 10.1016/j.physletb.2012.08.021. arXiv: 1207.7235 [hep-ex].
- [11] M. Jacob, ed. *Proceedings, ECFA-CERN Workshop on large hadron collider in the LEP tunnel*. 1984. DOI: 10.5170/CERN-1984-010-V-1, 10.5170/CERN-1984-010-V-2.

- [12] Christiane Lefèvre. “The CERN accelerator complex. Complexe des accélérateurs du CERN”. Dec. 2008. URL: <https://cds.cern.ch/record/1260465>.
- [13] Michael Benedikt et al. *LHC Design Report*. Vol. 3. CERN Yellow Reports: Monographs. Geneva: CERN, 2004. URL: <http://cds.cern.ch/record/823808>.
- [14] A Beuret et al. “The LHC Lead Injector Chain”. In: LHC-Project-Report-776. CERN-LHC-Project-Report-776 (Aug. 2004). revised version submitted on 2004-09-23 14:33:06, 4 p. URL: <https://cds.cern.ch/record/792709>.
- [15] Thomas Sven Pettersson and P. Lefèvre. “The Large Hadron Collider: Conceptual design”. In: (1995).
- [16] Werner Herr and B Muratori. “Concept of luminosity”. In: (2006). URL: <https://cds.cern.ch/record/941318>.
- [17] *Luminosity summary plots*. Accessed: 2019-02-22. URL: <https://twiki.cern.ch/twiki/bin/view/AtlasPublic/LuminosityPublicResultsRun2>.
- [18] *Jet Calibration and Systematic Uncertainties for Jets Reconstructed in the ATLAS Detector at $\sqrt{s} = 13$ TeV*. Tech. rep. ATL-PHYS-PUB-2015-015. Geneva: CERN, July 2015. URL: <http://cds.cern.ch/record/2037613>.
- [19] Joao Pequeno. “Computer generated image of the whole ATLAS detector”. Mar. 2008. URL: <https://cds.cern.ch/record/1095924>.
- [20] C. Berger. *Elementarteilchenphysik: Von den Grundlagen zu den modernen Experimenten*. Springer-Lehrbuch. Springer Berlin Heidelberg, 2014, p. 528. ISBN: 9783642417535. DOI: 10.1007/978-3-642-41753-5".
- [21] G. Aad et al. “The ATLAS Inner Detector commissioning and calibration”. In: *Eur. Phys. J. C* 70 (2010), pp. 787–821. DOI: 10.1140/epjc/s10052-010-1366-7. arXiv: 1004.5293 [physics.ins-det].
- [22] M. Aharrouche et al. “Energy Linearity and Resolution of the ATLAS Electromagnetic Barrel Calorimeter in an Electron Test-Beam”. In: *Nucl. Instrum. Methods Phys. Res., A* 568.physics/0608012 (Aug. 2006), 601–623. 48 p. URL: <https://cds.cern.ch/record/976098>.
- [23] Bernard Aubert et al. “Performance of the ATLAS electromagnetic calorimeter end-cap module 0”. In: *Nucl. Instrum. Meth.* A500 (2003), pp. 178–201. DOI: 10.1016/S0168-9002(03)00344-9.
- [24] T Davidek and the Atlas Tilecal system. “ATLAS Tile Calorimeter performance for single particles in beam tests”. In: *Journal of Physics: Conference Series* 160 (Apr. 2009), p. 012057. DOI: 10.1088/1742-6596/160/1/012057. URL: <https://doi.org/10.1088%2F1742-6596%2F160%2F1%2F012057>.
- [25] B Dowler et al. “Performance of the ATLAS hadronic end-cap calorimeter in beam tests”. In: *Nucl. Instrum. Meth.* A482 (2002), pp. 94–124. DOI: 10.1016/S0168-9002(01)01338-9.

-
- [26] J. P. Archambault et al. “Energy calibration of the ATLAS liquid argon forward calorimeter”. In: *JINST* 3 (2008), P02002. DOI: 10.1088/1748-0221/3/02/P02002.
- [27] Morad Aaboud et al. “Performance of the ATLAS Trigger System in 2015”. In: *Eur. Phys. J. C* 77.5 (2017), p. 317. DOI: 10.1140/epjc/s10052-017-4852-3. arXiv: 1611.09661 [hep-ex].
- [28] R. Achenbach et al. “The ATLAS level-1 calorimeter trigger”. In: *JINST* 3 (2008), P03001. DOI: 10.1088/1748-0221/3/03/P03001.
- [29] Georges Aad et al. “Performance of the ATLAS Trigger System in 2010”. In: *Eur. Phys. J. C* 72 (2012), p. 1849. DOI: 10.1140/epjc/s10052-011-1849-1. arXiv: 1110.1530 [hep-ex].
- [30] M Shochet et al. *Fast TracKer (FTK) Technical Design Report*. Tech. rep. CERN-LHCC-2013-007. ATLAS-TDR-021. ATLAS Fast Tracker Technical Design Report. June 2013. URL: <https://cds.cern.ch/record/1552953>.
- [31] *Particle ID at ATLAS*. http://stanford.edu/group/stanford_atlas/4Particle%20Collision%20and%20Detection. Accessed: 2019-04-07.
- [32] M. Aaboud et al. “Performance of the ATLAS Track Reconstruction Algorithms in Dense Environments in LHC Run 2”. In: *Eur. Phys. J. C* 77.10 (2017), p. 673. DOI: 10.1140/epjc/s10052-017-5225-7. arXiv: 1704.07983 [hep-ex].
- [33] R. Fruhwirth. “Application of Kalman filtering to track and vertex fitting”. In: *Nucl. Instrum. Meth.* A262 (1987), pp. 444–450. DOI: 10.1016/0168-9002(87)90887-4.
- [34] *Performance of the ATLAS Silicon Pattern Recognition Algorithm in Data and Simulation at $\sqrt{s} = 7$ TeV*. Tech. rep. ATLAS-CONF-2010-072. Geneva: CERN, July 2010. URL: <http://cds.cern.ch/record/1281363>.
- [35] “Performance of the ATLAS Inner Detector Track and Vertex Reconstruction in the High Pile-Up LHC Environment”. In: (2012).
- [36] W Lampl et al. *Calorimeter Clustering Algorithms: Description and Performance*. Tech. rep. ATL-LARG-PUB-2008-002. ATL-COM-LARG-2008-003. Geneva: CERN, Apr. 2008. URL: <https://cds.cern.ch/record/1099735>.
- [37] Morad Aaboud et al. “Electron reconstruction and identification in the ATLAS experiment using the 2015 and 2016 LHC proton-proton collision data at $\sqrt{s} = 13$ TeV”. In: *Submitted to: Eur. Phys. J.* (2019). arXiv: 1902.04655 [physics.ins-det].
- [38] Morad Aaboud et al. “Electron and photon energy calibration with the ATLAS detector using 2015-2016 LHC proton-proton collision data”. In: *JINST* 14.03 (2019), P03017. DOI: 10.1088/1748-0221/14/03/P03017. arXiv: 1812.03848 [hep-ex].
- [39] Georges Aad et al. “Muon reconstruction performance of the ATLAS detector in proton-proton collision data at $\sqrt{s} = 13$ TeV”. In: *Eur. Phys. J. C* 76.5 (2016), p. 292. DOI: 10.1140/epjc/s10052-016-4120-y. arXiv: 1603.05598 [hep-ex].

- [40] Georges Aad et al. “Topological cell clustering in the ATLAS calorimeters and its performance in LHC Run 1”. In: *Eur. Phys. J. C* 77 (2017), p. 490. DOI: 10.1140/epjc/s10052-017-5004-5. arXiv: 1603.02934 [hep-ex].
- [41] Matteo Cacciari, Gavin P. Salam, and Gregory Soyez. “The anti- k_t jet clustering algorithm”. In: *JHEP* 04 (2008), p. 063. DOI: 10.1088/1126-6708/2008/04/063. arXiv: 0802.1189 [hep-ph].
- [42] Stephen D. Ellis and Davison E. Soper. “Successive combination jet algorithm for hadron collisions”. In: *Phys. Rev. D* 48 (1993), pp. 3160–3166. DOI: 10.1103/PhysRevD.48.3160. arXiv: hep-ph/9305266 [hep-ph].
- [43] Yuri L. Dokshitzer et al. “Better jet clustering algorithms”. In: *JHEP* 08 (1997), p. 001. DOI: 10.1088/1126-6708/1997/08/001. arXiv: hep-ph/9707323 [hep-ph].
- [44] M. Wobisch and T. Wengler. “Hadronization corrections to jet cross-sections in deep inelastic scattering”. In: *Monte Carlo generators for HERA physics. Proceedings, Workshop, Hamburg, Germany, 1998-1999*. 1998, pp. 270–279. arXiv: hep-ph/9907280 [hep-ph].
- [45] M. Aaboud et al. “Jet energy scale measurements and their systematic uncertainties in proton-proton collisions at $\sqrt{s} = 13$ TeV with the ATLAS detector”. In: *Phys. Rev. D* 96.7 (2017), p. 072002. DOI: 10.1103/PhysRevD.96.072002. arXiv: 1703.09665 [hep-ex].
- [46] Georges Aad et al. “Jet energy measurement with the ATLAS detector in proton-proton collisions at $\sqrt{s} = 7$ TeV”. In: *Eur. Phys. J. C* 73.3 (2013), p. 2304. DOI: 10.1140/epjc/s10052-013-2304-2. arXiv: 1112.6426 [hep-ex].
- [47] M. Tanabashi et al. “Review of Particle Physics”. In: *Phys. Rev. D* 98 (3 Aug. 2018), p. 030001. DOI: 10.1103/PhysRevD.98.030001. URL: <https://link.aps.org/doi/10.1103/PhysRevD.98.030001>.
- [48] *Reconstruction, Energy Calibration, and Identification of Hadronically Decaying Tau Leptons in the ATLAS Experiment for Run-2 of the LHC*. Tech. rep. ATL-PHYS-PUB-2015-045. Geneva: CERN, Nov. 2015. URL: <http://cds.cern.ch/record/2064383>.
- [49] H. Poincaré. “Sur la dynamique de l’électron”. In: *Rendiconti del Circolo matematico di Palermo, Vol. 21, pp. 129-176* 21 (Jan. 1906), pp. 129–176. DOI: 10.1007/BF03013466.
- [50] E. Noether. “Invarianten beliebiger Differentialausdrücke.” German. In: *Nachr. Ges. Wiss. Göttingen, Math.-Phys. Kl.* 1918 (1918), pp. 37–44.
- [51] Andrew Purcell. “Go on a particle quest at the first CERN webfest. Le premier webfest du CERN se lance à la conquête des particules”. In: BUL-NA-2012-269. 35/2012 (Aug. 2012), p. 10. URL: <https://cds.cern.ch/record/1473657>.

-
- [52] Sean M. Carroll. *Spacetime and geometry: An introduction to general relativity*. 2004. ISBN: 0805387323, 9780805387322. URL: <http://www.slac.stanford.edu/spires/find/books/www?cl=QC6:C37:2004>.
- [53] David J Griffiths. *Introduction to elementary particles; 2nd rev. version*. Physics textbook. New York, NY: Wiley, 2008. URL: <https://cds.cern.ch/record/111880>.
- [54] Bo Andersson. “The Lund model”. In: *Camb. Monogr. Part. Phys. Nucl. Phys. Cosmol.* 7 (1997), pp. 1–471.
- [55] G. Marchesini et al. “HERWIG: A Monte Carlo event generator for simulating hadron emission reactions with interfering gluons. Version 5.1 - April 1991”. In: *Comput. Phys. Commun.* 67 (1992), pp. 465–508. DOI: 10.1016/0010-4655(92)90055-4.
- [56] Nicola Cabibbo. “Unitary Symmetry and Leptonic Decays”. In: *Phys. Rev. Lett.* 10 (1963). [,648(1963)], pp. 531–533. DOI: 10.1103/PhysRevLett.10.531.
- [57] Makoto Kobayashi and Toshihide Maskawa. “CP Violation in the Renormalizable Theory of Weak Interaction”. In: *Prog. Theor. Phys.* 49 (1973), pp. 652–657. DOI: 10.1143/PTP.49.652.
- [58] V. N. Gribov and L. N. Lipatov. “Deep inelastic e p scattering in perturbation theory”. In: *Sov. J. Nucl. Phys.* 15 (1972). [Yad. Fiz.15,781(1972)], pp. 438–450.
- [59] L. N. Lipatov. “The parton model and perturbation theory”. In: *Sov. J. Nucl. Phys.* 20 (1975). [Yad. Fiz.20,181(1974)], pp. 94–102.
- [60] Guido Altarelli and G. Parisi. “Asymptotic Freedom in Parton Language”. In: *Nucl. Phys.* B126 (1977), pp. 298–318. DOI: 10.1016/0550-3213(77)90384-4.
- [61] Yuri L. Dokshitzer. “Calculation of the Structure Functions for Deep Inelastic Scattering and e+ e- Annihilation by Perturbation Theory in Quantum Chromodynamics.” In: *Sov. Phys. JETP* 46 (1977). [Zh. Eksp. Teor. Fiz.73,1216(1977)], pp. 641–653.
- [62] Gustavo Burdman. “New solutions to the hierarchy problem”. In: *Braz. J. Phys.* 37 (2007), pp. 506–513. DOI: 10.1590/S0103-97332007000400006. arXiv: hep-ph/0703194 [hep-ph].
- [63] B. Pontecorvo. “Inverse beta processes and nonconservation of lepton charge”. In: *Sov. Phys. JETP* 7 (1958). [Zh. Eksp. Teor. Fiz.34,247(1957)], pp. 172–173.
- [64] Ziro Maki, Masami Nakagawa, and Shoichi Sakata. “Remarks on the unified model of elementary particles”. In: *Prog. Theor. Phys.* 28 (1962). [,34(1962)], pp. 870–880. DOI: 10.1143/PTP.28.870.
- [65] Steen Hannestad. “Neutrino physics from precision cosmology”. In: *Prog. Part. Nucl. Phys.* 65 (2010), pp. 185–208. DOI: 10.1016/j.pnpnp.2010.07.001. arXiv: 1007.0658 [hep-ph].

- [66] V. C. Rubin, Jr. Ford W. K., and N. Thonnard. “Extended rotation curves of high-luminosity spiral galaxies”. In: *Astrophysical Journal* 225 (1978), pp. 107–111. URL: <https://cds.cern.ch/record/437297>.
- [67] J H Oort. “The force exerted by the stellar system in the direction perpendicular to the galactic plane and some related problems”. In: *Bull. Astron. Inst. Netherlands* 6 (1932), pp. 249–287. URL: <https://cds.cern.ch/record/436532>.
- [68] F Zwicky. “Die Rotverschiebung von extragalaktischen Nebeln”. In: *Helv. Phys. Acta* 6 (1933), pp. 110–127. URL: <https://cds.cern.ch/record/437297>.
- [69] M. Milgrom. “A Modification of the Newtonian dynamics as a possible alternative to the hidden mass hypothesis”. In: *Astrophys. J.* 270 (1983), pp. 365–370. DOI: 10.1086/161130.
- [70] M. Milgrom. “A modification of the Newtonian dynamics: implications for galaxy systems”. In: *Astrophys. J.* 270 (1983), pp. 384–389. DOI: 10.1086/161132.
- [71] Jacob D. Bekenstein. “Relativistic gravitation theory for the MOND paradigm”. In: *Phys. Rev. D* 70 (2004). [Erratum: *Phys. Rev. D* 71, 069901(2005)], p. 083509. DOI: 10.1103/PhysRevD.70.083509, 10.1103/PhysRevD.71.069901. arXiv: [astro-ph/0403694](https://arxiv.org/abs/astro-ph/0403694) [[astro-ph](https://arxiv.org/abs/astro-ph)].
- [72] Salvatore Capozziello and Mauro Francaviglia. “Extended Theories of Gravity and their Cosmological and Astrophysical Applications”. In: *Gen. Rel. Grav.* 40 (2008), pp. 357–420. DOI: 10.1007/s10714-007-0551-y. arXiv: 0706.1146 [[astro-ph](https://arxiv.org/abs/astro-ph)].
- [73] Salvatore Capozziello and Mariafelicia De Laurentis. “Extended Theories of Gravity”. In: *Phys. Rept.* 509 (2011), pp. 167–321. DOI: 10.1016/j.physrep.2011.09.003. arXiv: 1108.6266 [[gr-qc](https://arxiv.org/abs/gr-qc)].
- [74] Douglas Clowe et al. “A direct empirical proof of the existence of dark matter”. In: *Astrophys. J.* 648 (2006), pp. L109–L113. DOI: 10.1086/508162. arXiv: [astro-ph/0608407](https://arxiv.org/abs/astro-ph/0608407) [[astro-ph](https://arxiv.org/abs/astro-ph)].
- [75] Albert Einstein. “Lens-Like Action of a Star by the Deviation of Light in the Gravitational Field”. In: *Science* 84 (1936), pp. 506–507. DOI: 10.1126/science.84.2188.506.
- [76] Sidney Liebes. “Gravitational Lenses”. In: *Phys. Rev.* 133 (1964), B835–B844. DOI: 10.1103/PhysRev.133.B835.
- [77] Maxim Markevitch et al. “Direct constraints on the dark matter self-interaction cross-section from the merging galaxy cluster 1E0657-56”. In: *Astrophys. J.* 606 (2004), pp. 819–824. DOI: 10.1086/383178. arXiv: [astro-ph/0309303](https://arxiv.org/abs/astro-ph/0309303) [[astro-ph](https://arxiv.org/abs/astro-ph)].
- [78] Savvas Dimopoulos and Howard Georgi. “Softly Broken Supersymmetry and SU(5)”. In: *Nucl. Phys.* B193 (1981), pp. 150–162. DOI: 10.1016/0550-3213(81)90522-8.
- [79] A. Liam Fitzpatrick et al. “The Effective Field Theory of Dark Matter Direct Detection”. In: *JCAP* 1302 (2013), p. 004. DOI: 10.1088/1475-7516/2013/02/004. arXiv: 1203.3542 [[hep-ph](https://arxiv.org/abs/hep-ph)].

-
- [80] Stephen P. Martin. “A Supersymmetry primer”. In: (1997). [Adv. Ser. Direct. High Energy Phys.18,1(1998)], pp. 1–98. DOI: 10.1142/9789812839657_0001, 10.1142/9789814307505_0001. arXiv: hep-ph/9709356 [hep-ph].
- [81] Jalal Abdallah et al. “Simplified Models for Dark Matter Searches at the LHC”. In: *Phys. Dark Univ.* 9-10 (2015), pp. 8–23. DOI: 10.1016/j.dark.2015.08.001. arXiv: 1506.03116 [hep-ph].
- [82] Morad Aaboud et al. “Search for dark matter and other new phenomena in events with an energetic jet and large missing transverse momentum using the ATLAS detector”. In: *JHEP* 01 (2018), p. 126. DOI: 10.1007/JHEP01(2018)126. arXiv: 1711.03301 [hep-ex].
- [83] Daniel Abercrombie et al. “Dark Matter Benchmark Models for Early LHC Run-2 Searches: Report of the ATLAS/CMS Dark Matter Forum”. In: (2015). Ed. by Antonio Boveia et al. arXiv: 1507.00966 [hep-ex].
- [84] S. Dittmaier et al. “Handbook of LHC Higgs Cross Sections: 1. Inclusive Observables”. In: (2011). DOI: 10.5170/CERN-2011-002. arXiv: 1101.0593 [hep-ph].
- [85] S. Dittmaier et al. “Handbook of LHC Higgs Cross Sections: 2. Differential Distributions”. In: (2012). DOI: 10.5170/CERN-2012-002. arXiv: 1201.3084 [hep-ph].
- [86] James M. Cline et al. “Update on scalar singlet dark matter”. In: *Phys. Rev. D* 88 (2013). [Erratum: *Phys. Rev. D* 92, no. 3, 039906 (2015)], p. 055025. DOI: 10.1103/PhysRevD.92.039906, 10.1103/PhysRevD.88.055025. arXiv: 1306.4710 [hep-ph].
- [87] Kim Griest and Howard E. Haber. “Invisible decays of Higgs bosons in supersymmetric models”. In: *Phys. Rev. D* 37 (3 Feb. 1988), pp. 719–728. DOI: 10.1103/PhysRevD.37.719. URL: <https://link.aps.org/doi/10.1103/PhysRevD.37.719>.
- [88] A. Djouadi et al. “SUSY decays of Higgs particles”. In: *Phys. Lett.* B376 (1996), pp. 220–226. DOI: 10.1016/0370-2693(96)00414-5. arXiv: hep-ph/9603368 [hep-ph].
- [89] Anjan S. Joshipura and J. W. F. Valle. “Invisible Higgs decays and neutrino physics”. In: *Nucl. Phys.* B397 (1993), pp. 105–122. DOI: 10.1016/0550-3213(93)90337-0.
- [90] Nima Arkani-Hamed, Savvas Dimopoulos, and G. R. Dvali. “The Hierarchy problem and new dimensions at a millimeter”. In: *Phys. Lett.* B429 (1998), pp. 263–272. DOI: 10.1016/S0370-2693(98)00466-3. arXiv: hep-ph/9803315 [hep-ph].
- [91] Gian F. Giudice, Riccardo Rattazzi, and James D. Wells. “Graviscalars from higher dimensional metrics and curvature Higgs mixing”. In: *Nucl. Phys.* B595 (2001), pp. 250–276. DOI: 10.1016/S0550-3213(00)00686-6. arXiv: hep-ph/0002178 [hep-ph].
- [92] Teresa Marrodán Undagoitia and Ludwig Rauch. “Dark matter direct-detection experiments”. In: *J. Phys.* G43.1 (2016), p. 013001. DOI: 10.1088/0954-3899/43/1/013001. arXiv: 1509.08767 [physics.ins-det].

- [93] Jennifer M. Gaskins. “A review of indirect searches for particle dark matter”. In: *Contemp. Phys.* 57.4 (2016), pp. 496–525. DOI: 10.1080/00107514.2016.1175160. arXiv: 1604.00014 [astro-ph.HE].
- [94] Marc Schumann. “Direct Detection of WIMP Dark Matter: Concepts and Status”. In: (2019). arXiv: 1903.03026 [astro-ph.CO].
- [95] Antonio Boveia and Caterina Doglioni. “Dark Matter Searches at Colliders”. In: *Ann. Rev. Nucl. Part. Sci.* 68 (2018), pp. 429–459. DOI: 10.1146/annurev-nucl-101917-021008. arXiv: 1810.12238 [hep-ex].
- [96] Morad Aaboud et al. “Search for new phenomena in dijet events using 37 fb^{-1} of pp collision data collected at $\sqrt{s} = 13 \text{ TeV}$ with the ATLAS detector”. In: *Phys. Rev. D* 96.5 (2017), p. 052004. DOI: 10.1103/PhysRevD.96.052004. arXiv: 1703.09127 [hep-ex].
- [97] Cristiano Alpigiani. “Searches for Dark Matter in ATLAS”. In: *5th Large Hadron Collider Physics Conference (LHCP 2017) Shanghai, China, May 15-20, 2017*. 2017. arXiv: 1708.09674 [hep-ex].
- [98] M. Aaboud et al. “Search for low-mass dijet resonances using trigger-level jets with the ATLAS detector in pp collisions at $\sqrt{s} = 13 \text{ TeV}$ ”. In: *Phys. Rev. Lett.* 121.8 (2018), p. 081801. DOI: 10.1103/PhysRevLett.121.081801. arXiv: 1804.03496 [hep-ex].
- [99] Albert M Sirunyan et al. “Search for narrow and broad dijet resonances in proton-proton collisions at $\sqrt{s} = 13 \text{ TeV}$ and constraints on dark matter mediators and other new particles”. In: *JHEP* 08 (2018), p. 130. DOI: 10.1007/JHEP08(2018)130. arXiv: 1806.00843 [hep-ex].
- [100] Giorgio Busoni et al. “Recommendations on presenting LHC searches for missing transverse energy signals using simplified s -channel models of dark matter”. In: (2016). Ed. by Antonio Boveia et al. arXiv: 1603.04156 [hep-ex].
- [101] Felix Kahlhoefer et al. “Implications of unitarity and gauge invariance for simplified dark matter models”. In: *JHEP* 02 (2016), p. 016. DOI: 10.1007/JHEP02(2016)016. arXiv: 1510.02110 [hep-ph].
- [102] S. Agostinelli et al. “GEANT4: A Simulation toolkit”. In: *Nucl. Instrum. Meth.* A506 (2003), pp. 250–303. DOI: 10.1016/S0168-9002(03)01368-8.
- [103] D Costanzo et al. *Validation of the GEANT4-Based Full Simulation Program for the ATLAS Detector: An Overview of Performance and Robustness*. Tech. rep. ATL-SOFT-PUB-2005-002. ATL-COM-SOFT-2005-004. CERN-ATL-SOFT-PUB-2005-002. Geneva: CERN, Mar. 2005. URL: <https://cds.cern.ch/record/830149>.
- [104] A Rimoldi et al. *Final Report of the Simulation Optimization Task Force*. Tech. rep. ATL-SOFT-PUB-2008-004. ATL-COM-SOFT-2008-023. Follow up to note ATL-SOFT-PUB-2008-002. Geneva: CERN, Dec. 2009. URL: <https://cds.cern.ch/record/1151298>.

-
- [105] Andrea Knue et al. *Improvements in $t\bar{t}$ modelling using NLO+PS Monte Carlo generators for Run2*. Tech. rep. ATL-COM-PHYS-2018-813. Geneva: CERN, June 2018. URL: <https://cds.cern.ch/record/2624546>.
- [106] *ATLAS simulation of boson plus jets processes in Run 2*. Tech. rep. ATL-PHYS-PUB-2017-006. Geneva: CERN, May 2017. URL: <https://cds.cern.ch/record/2261937>.
- [107] *Multi-Boson Simulation for 13 TeV ATLAS Analyses*. Tech. rep. ATL-PHYS-PUB-2017-005. Geneva: CERN, May 2017. URL: <https://cds.cern.ch/record/2261933>.
- [108] J. de Favereau et al. “DELPHES 3, A modular framework for fast simulation of a generic collider experiment”. In: *JHEP* 02 (2014), p. 057. DOI: 10.1007/JHEP02(2014)057. arXiv: 1307.6346 [hep-ex].
- [109] G. D’Agostini. “A Multidimensional unfolding method based on Bayes’ theorem”. In: *Nucl. Instrum. Meth.* A362 (1995), pp. 487–498. DOI: 10.1016/0168-9002(95)00274-X.
- [110] Olaf Behnke et al., eds. *Data analysis in high energy physics*. Weinheim, Germany: Wiley-VCH, 2013. ISBN: 9783527410583, 9783527653447, 9783527653430. URL: <http://www.wiley-vch.de/publish/dt/books/ISBN3-527-41058-9>.
- [111] T. Bayes. “An essay towards solving a problem in the doctrine of chances”. In: *Phil. Trans. of the Royal Soc. of London* 53 (1763), pp. 370–418.
- [112] Falk Bartels. “Improving the Sensitivity of Dark Matter Searches by Combining Unfolded Experimental Signatures”. Masterarbeit. Universität Heidelberg, Dec. 2017.
- [113] Bogdan Malaescu. “An Iterative, dynamically stabilized method of data unfolding”. In: (2009). arXiv: 0907.3791 [physics.data-an].
- [114] Bogdan Malaescu. “An Iterative, Dynamically Stabilized(IDS) Method of Data Unfolding”. In: *Proceedings, PHYSTAT 2011 Workshop on Statistical Issues Related to Discovery Claims in Search Experiments and Unfolding, CERN, Geneva, Switzerland 17-20 January 2011*. 2011, pp. 271–275. DOI: 10.5170/CERN-2011-006.271. arXiv: 1106.3107 [physics.data-an].
- [115] B. Efron. “Bootstrap Methods: Another Look at the Jackknife”. In: *Ann. Statist.* 7.1 (Jan. 1979), pp. 1–26. DOI: 10.1214/aos/1176344552. URL: <https://doi.org/10.1214/aos/1176344552>.
- [116] Tilman Plehn, David L. Rainwater, and Dieter Zeppenfeld. “Determining the Structure of Higgs Couplings at the LHC”. In: *Phys. Rev. Lett.* 88 (2002), p. 051801. DOI: 10.1103/PhysRevLett.88.051801. arXiv: hep-ph/0105325 [hep-ph].
- [117] V. Hankele et al. “Anomalous Higgs boson couplings in vector boson fusion at the CERN LHC”. In: *Phys. Rev.* D74 (2006), p. 095001. DOI: 10.1103/PhysRevD.74.095001. arXiv: hep-ph/0609075 [hep-ph].

- [118] *Luminosity summary plots*. Accessed: 2019-02-22. URL: <https://twiki.cern.ch/twiki/bin/view/AtlasPublic/RunStatsPublicResults2010>.
- [119] Morad Aaboud et al. “Luminosity determination in pp collisions at $\sqrt{s} = 8$ TeV using the ATLAS detector at the LHC”. In: *Eur. Phys. J. C* 76.12 (2016), p. 653. DOI: 10.1140/epjc/s10052-016-4466-1. arXiv: 1608.03953 [hep-ex].
- [120] G. Avoni et al. “The new LUCID-2 detector for luminosity measurement and monitoring in ATLAS”. In: *JINST* 13.07 (2018), P07017. DOI: 10.1088/1748-0221/13/07/P07017.
- [121] *Luminosity for Physics ATLAS recommendation*. <https://twiki.cern.ch/twiki/bin/view/Atlas/LuminosityForPhysics>. Accessed: 2019-05-01.
- [122] G. Aad et al. “The ATLAS Simulation Infrastructure”. In: *Eur. Phys. J. C* 70 (2010), pp. 823–874. DOI: 10.1140/epjc/s10052-010-1429-9. arXiv: 1005.4568 [physics.ins-det].
- [123] Richard D. Ball et al. “Parton distributions for the LHC Run II”. In: *JHEP* 04 (2015), p. 040. DOI: 10.1007/JHEP04(2015)040. arXiv: 1410.8849 [hep-ph].
- [124] Sayipjamal Dulat et al. “New parton distribution functions from a global analysis of quantum chromodynamics”. In: *Phys. Rev. D* 93.3 (2016), p. 033006. DOI: 10.1103/PhysRevD.93.033006. arXiv: 1506.07443 [hep-ph].
- [125] L. A. Harland-Lang et al. “Parton distributions in the LHC era: MMHT 2014 PDFs”. In: *Eur. Phys. J. C* 75.5 (2015), p. 204. DOI: 10.1140/epjc/s10052-015-3397-6. arXiv: 1412.3989 [hep-ph].
- [126] Torbjörn Sjöstrand. “Status and developments of event generators”. In: *PoS LHCP2016* (2016), p. 007. DOI: 10.22323/1.276.0007. arXiv: 1608.06425 [hep-ph].
- [127] Torbjörn Sjöstrand et al. “An Introduction to PYTHIA 8.2”. In: *Comput. Phys. Commun.* 191 (2015), pp. 159–177. DOI: 10.1016/j.cpc.2015.01.024. arXiv: 1410.3012 [hep-ph].
- [128] Leif Lonnblad. “Correcting the color dipole cascade model with fixed order matrix elements”. In: *JHEP* 05 (2002), p. 046. DOI: 10.1088/1126-6708/2002/05/046. arXiv: hep-ph/0112284 [hep-ph].
- [129] Leif Lonnblad and Stefan Prestel. “Matching Tree-Level Matrix Elements with Interleaved Showers”. In: *JHEP* 03 (2012), p. 019. DOI: 10.1007/JHEP03(2012)019. arXiv: 1109.4829 [hep-ph].
- [130] Michelangelo L. Mangano et al. “Matching matrix elements and shower evolution for top-quark production in hadronic collisions”. In: *JHEP* 01 (2007), p. 013. DOI: 10.1088/1126-6708/2007/01/013. arXiv: hep-ph/0611129 [hep-ph].
- [131] Rikkert Frederix and Stefano Frixione. “Merging meets matching in MC@NLO”. In: *JHEP* 12 (2012), p. 061. DOI: 10.1007/JHEP12(2012)061. arXiv: 1209.6215 [hep-ph].

-
- [132] T. Gleisberg et al. “Event generation with SHERPA 1.1”. In: *JHEP* 02 (2009), p. 007. DOI: 10.1088/1126-6708/2009/02/007. arXiv: 0811.4622 [hep-ph].
- [133] “Summary of ATLAS Pythia 8 tunes”. In: (2012).
- [134] A. D. Martin et al. “Parton distributions for the LHC”. In: *Eur. Phys. J.* C63 (2009), pp. 189–285. DOI: 10.1140/epjc/s10052-009-1072-5. arXiv: 0901.0002 [hep-ph].
- [135] *Luminosity for Physics ATLAS recommendation*. https://twiki.cern.ch/twiki/bin/viewauth/AtlasProtected/ReferenceCONF13TeVMC15#Pile_Up. Accessed: 2019-05-01.
- [136] William Buttinger. *Using Event Weights to account for differences in Instantaneous Luminosity and Trigger Prescale in Monte Carlo and Data*. Tech. rep. ATL-COM-SOFT-2015-119. Geneva: CERN, May 2015. URL: <https://cds.cern.ch/record/2014726>.
- [137] *Luminosity for Physics ATLAS recommendation*. https://twiki.cern.ch/twiki/bin/view/AtlasProtected/BosonJetsFocusGroup#Treating_pathological_high_weigh. Accessed: 2019-05-01.
- [138] ATLAS Collaboration. *Electron reconstruction and identification in the ATLAS experiment using the 2015 and 2016 LHC proton–proton collision data at $\sqrt{s} = 13\text{TeV}$* . Tech. rep. ATL-COM-PHYS-2018-436. Geneva: CERN, Apr. 2018. URL: <https://cds.cern.ch/record/2315291>.
- [139] *Tau Working Point Definition: release/21.2.55*. Accessed: 2019-02-26. URL: <https://gitlab.cern.ch/atlas/athena/blob/release/21.2.55/PhysicsAnalysis/TauID/TauAnalysisTools/doc/README-TauSelectionTool.rst>.
- [140] *Measurement of the tau lepton reconstruction and identification performance in the ATLAS experiment using pp collisions at $\sqrt{s} = 13\text{TeV}$* . Tech. rep. ATLAS-CONF-2017-029. Geneva: CERN, May 2017. URL: <http://cds.cern.ch/record/2261772>.
- [141] *Tagging and suppression of pileup jets with the ATLAS detector*. Tech. rep. ATLAS-CONF-2014-018. Geneva: CERN, May 2014. URL: <https://cds.cern.ch/record/1700870>.
- [142] Ariel Schwartzman, Matthew Henry Klein, and Francesco Rubbo. *Identification and rejection of pileup jets in the forward region with the ATLAS detector*. Tech. rep. ATL-COM-PHYS-2016-710. Geneva: CERN, July 2016. URL: <https://cds.cern.ch/record/2158916>.
- [143] *E_T^{miss} performance in the ATLAS detector using 2015–2016 LHC p-p collisions*. Tech. rep. ATLAS-CONF-2018-023. Geneva: CERN, June 2018. URL: <http://cds.cern.ch/record/2625233>.
- [144] *Selection of jets produced in 13TeV proton-proton collisions with the ATLAS detector*. Tech. rep. ATLAS-CONF-2015-029. Geneva: CERN, July 2015. URL: <https://cds.cern.ch/record/2037702>.

- [145] Morad Aaboud et al. “Reconstruction of primary vertices at the ATLAS experiment in Run 1 proton–proton collisions at the LHC”. In: *Eur. Phys. J. C* 77.5 (2017), p. 332. DOI: 10.1140/epjc/s10052-017-4887-5. arXiv: 1611.10235 [physics.ins-det].
- [146] *TriggerRecommendations MET Triggers*. <https://twiki.cern.ch/twiki/bin/view/Atlas/RecommendedMetTriggers2015>, <https://twiki.cern.ch/twiki/bin/view/Atlas/RecommendedMetTriggers2016>. Accessed: 2019-05-01.
- [147] *TriggerRecommendations Electron Triggers*. <https://twiki.cern.ch/twiki/bin/view/Atlas/TrigEgammaRecommendedTriggers2015>, <https://twiki.cern.ch/twiki/bin/view/Atlas/TrigEgammaRecommendedTriggers2016>. Accessed: 2019-05-01.
- [148] Sebastian Mario Weber. “Title to be announced”. PhD Thesis. Universität Heidelberg, expected 2020.
- [149] “Non-collision backgrounds as measured by the ATLAS detector during the 2010 proton-proton run”. In: (2011).
- [150] Georges Aad et al. “Jet energy measurement and its systematic uncertainty in proton-proton collisions at $\sqrt{s} = 7$ TeV with the ATLAS detector”. In: *Eur. Phys. J. C* 75 (2015), p. 17. DOI: 10.1140/epjc/s10052-014-3190-y. arXiv: 1406.0076 [hep-ex].
- [151] Maurizio De Santis. *Reconstruction efficiency for muons close to jets in Run-2 data with release 21*. Tech. rep. ATL-COM-PHYS-2018-473. Geneva: CERN, May 2018. URL: <https://cds.cern.ch/record/2316076>.
- [152] Jon Butterworth et al. “PDF4LHC recommendations for LHC Run II”. In: *J. Phys. G* 43 (2016), p. 023001. DOI: 10.1088/0954-3899/43/2/023001. arXiv: 1510.03865 [hep-ph].
- [153] Georges Aad et al. “Measurement of the electroweak production of dijets in association with a Z-boson and distributions sensitive to vector boson fusion in proton-proton collisions at $\sqrt{s} = 8$ TeV using the ATLAS detector”. In: *JHEP* 04 (2014), p. 031. DOI: 10.1007/JHEP04(2014)031. arXiv: 1401.7610 [hep-ex].
- [154] Thomas Junk. “Confidence level computation for combining searches with small statistics”. In: *Nucl. Instrum. Meth. A* 434 (1999), pp. 435–443. DOI: 10.1016/S0168-9002(99)00498-2. arXiv: hep-ex/9902006 [hep-ex].
- [155] Alexander L. Read. “Presentation of search results: The CL(s) technique”. In: *J. Phys. G* 28 (2002). [11(2002)], pp. 2693–2704. DOI: 10.1088/0954-3899/28/10/313.
- [156] Eilam Gross. “LHC Statistics for Pedestrians”. In: (2008). URL: <https://cds.cern.ch/record/1099994>.

-
- [157] J. Neyman and E. S. Pearson. “On the Problem of the Most Efficient Tests of Statistical Hypotheses”. In: *Philosophical Transactions of the Royal Society of London Series A* 231 (1933), pp. 289–337. DOI: 10.1098/rsta.1933.0009.
- [158] Bernhard Mistlberger and Falko Dulat. “Limit setting procedures and theoretical uncertainties in Higgs boson searches”. In: (2012). arXiv: 1204.3851 [hep-ph].
- [159] S. S. Wilks. “The Large-Sample Distribution of the Likelihood Ratio for Testing Composite Hypotheses”. In: *Ann. Math. Statist.* 9.1 (Mar. 1938), pp. 60–62. DOI: 10.1214/aoms/1177732360. URL: <https://doi.org/10.1214/aoms/1177732360>.
- [160] Abraham Wald. “An Extension of Wilks’ Method for Setting Tolerance Limits”. In: *Ann. Math. Statist.* 14.1 (Mar. 1943), pp. 45–55. DOI: 10.1214/aoms/1177731491. URL: <https://doi.org/10.1214/aoms/1177731491>.
- [161] Glen Cowan et al. “Asymptotic formulae for likelihood-based tests of new physics”. In: *Eur. Phys. J. C* 71 (2011). [Erratum: *Eur. Phys. J.* C73,2501(2013)], p. 1554. DOI: 10.1140/epjc/s10052-011-1554-0, 10.1140/epjc/s10052-013-2501-z. arXiv: 1007.1727 [physics.data-an].
- [162] Ulrich Haisch, Felix Kahlhoefer, and Emanuele Re. “QCD effects in mono-jet searches for dark matter”. In: *JHEP* 12 (2013), p. 007. DOI: 10.1007/JHEP12(2013)007. arXiv: 1310.4491 [hep-ph].
- [163] Simone Alioli et al. “A general framework for implementing NLO calculations in shower Monte Carlo programs: the POWHEG BOX”. In: *JHEP* 06 (2010), p. 043. DOI: 10.1007/JHEP06(2010)043. arXiv: 1002.2581 [hep-ph].
- [164] Andy Buckley et al. “Rivet user manual”. In: *Comput. Phys. Commun.* 184 (2013), pp. 2803–2819. DOI: 10.1016/j.cpc.2013.05.021. arXiv: 1003.0694 [hep-ph].
- [165] J R Andersen et al. “Handbook of LHC Higgs Cross Sections: 3. Higgs Properties”. In: (2013). Ed. by S Heinemeyer et al. DOI: 10.5170/CERN-2013-004. arXiv: 1307.1347 [hep-ph].
- [166] Simone Alioli et al. “NLO Higgs boson production via gluon fusion matched with shower in POWHEG”. In: *JHEP* 04 (2009), p. 002. DOI: 10.1088/1126-6708/2009/04/002. arXiv: 0812.0578 [hep-ph].
- [167] Paolo Nason and Carlo Oleari. “NLO Higgs boson production via vector-boson fusion matched with shower in POWHEG”. In: *JHEP* 02 (2010), p. 037. DOI: 10.1007/JHEP02(2010)037. arXiv: 0911.5299 [hep-ph].
- [168] E. Bagnaschi et al. “Higgs production via gluon fusion in the POWHEG approach in the SM and in the MSSM”. In: *JHEP* 02 (2012), p. 088. DOI: 10.1007/JHEP02(2012)088. arXiv: 1111.2854 [hep-ph].
- [169] Morad Aaboud et al. “Search for invisible Higgs boson decays in vector boson fusion at $\sqrt{s} = 13$ TeV with the ATLAS detector”. In: (2018). DOI: 10.1016/j.physletb.2019.04.024. arXiv: 1809.06682 [hep-ex].

- [170] *Monte Carlo simulation descriptions*. Accessed: 2019-02-28. URL: <https://twiki.cern.ch/twiki/bin/viewauth/AtlasProtected/ReferenceCONF13TeVMC15>.
- [171] Tanju Gleisberg and Stefan Hoeche. “Comix, a new matrix element generator”. In: *JHEP* 12 (2008), p. 039. DOI: 10.1088/1126-6708/2008/12/039. arXiv: 0808.3674 [hep-ph].
- [172] Fabio Cascioli, Philipp Maierhofer, and Stefano Pozzorini. “Scattering Amplitudes with Open Loops”. In: *Phys. Rev. Lett.* 108 (2012), p. 111601. DOI: 10.1103/PhysRevLett.108.111601. arXiv: 1111.5206 [hep-ph].
- [173] Steffen Schumann and Frank Krauss. “A Parton shower algorithm based on Catani-Seymour dipole factorisation”. In: *JHEP* 03 (2008), p. 038. DOI: 10.1088/1126-6708/2008/03/038. arXiv: 0709.1027 [hep-ph].
- [174] Stefan Hoeche et al. “QCD matrix elements + parton showers: The NLO case”. In: *JHEP* 04 (2013), p. 027. DOI: 10.1007/JHEP04(2013)027. arXiv: 1207.5030 [hep-ph].
- [175] Stefano Frixione, Paolo Nason, and Carlo Oleari. “Matching NLO QCD computations with Parton Shower simulations: the POWHEG method”. In: *JHEP* 11 (2007), p. 070. DOI: 10.1088/1126-6708/2007/11/070. arXiv: 0709.2092 [hep-ph].
- [176] Paolo Nason. “A New method for combining NLO QCD with shower Monte Carlo algorithms”. In: *JHEP* 11 (2004), p. 040. DOI: 10.1088/1126-6708/2004/11/040. arXiv: hep-ph/0409146 [hep-ph].
- [177] Hung-Liang Lai et al. “New parton distributions for collider physics”. In: *Phys. Rev. D* 82 (2010), p. 074024. DOI: 10.1103/PhysRevD.82.074024. arXiv: 1007.2241 [hep-ph].
- [178] Pierre Artoisenet et al. “Automatic spin-entangled decays of heavy resonances in Monte Carlo simulations”. In: *JHEP* 03 (2013), p. 015. DOI: 10.1007/JHEP03(2013)015. arXiv: 1212.3460 [hep-ph].
- [179] Torbjorn Sjöstrand, Stephen Mrenna, and Peter Z. Skands. “PYTHIA 6.4 Physics and Manual”. In: *JHEP* 05 (2006), p. 026. DOI: 10.1088/1126-6708/2006/05/026. arXiv: hep-ph/0603175.
- [180] J. Pumplin et al. “New generation of parton distributions with uncertainties from global QCD analysis”. In: *JHEP* 07 (2002), p. 012. DOI: 10.1088/1126-6708/2002/07/012. arXiv: hep-ph/0201195 [hep-ph].
- [181] Peter Zeiler Skands. “Tuning Monte Carlo Generators: The Perugia Tunes”. In: *Phys. Rev. D* 82 (2010), p. 074018. DOI: 10.1103/PhysRevD.82.074018. arXiv: 1005.3457 [hep-ph].
- [182] D. J. Lange. “The EvtGen particle decay simulation package”. In: *Nucl. Instrum. Meth. A* 462 (2001), p. 152. DOI: 10.1016/S0168-9002(01)00089-4.

- [183] Torbjorn Sjöstrand, Stephen Mrenna, and Peter Z. Skands. “A Brief Introduction to PYTHIA 8.1”. In: *Comput. Phys. Commun.* 178 (2008), p. 852. DOI: 10.1016/j.cpc.2008.01.036. arXiv: 0710.3820 [hep-ph].
- [184] *Non-Collision Background Public Results*. <https://twiki.cern.ch/twiki/bin/view/AtlasPublic/NonCollisionBackgroundPublicResults>. Accessed: 2019-04-23.
- [185] Richard Nisius. “On the combination of correlated estimates of a physics observable”. In: *Eur. Phys. J. C* 74.8 (2014), p. 3004. DOI: 10.1140/epjc/s10052-014-3004-2. arXiv: 1402.4016 [physics.data-an].

Acknowledgements

Finally, I would like to express my gratitude to all the people without whom this thesis would not have been possible.

First, I would like to thank my supervisor Prof. Dr. Hans-Christian Schultz-Coulon for allowing me to pursue my research within the field of particle physics. I am truly grateful to him for the opportunity to work on the forefront of human knowledge, within this great collaboration and with all the wonderful people within his research group. The outstanding support, working conditions and social dynamics within the group are owed to him and he kept me motivated when I needed a push.

Furthermore, I would like to thank Prof. Dr. Klaus Reygers, who kindly agreed to co-review this thesis.

For their incredible amount of feedback, the continuous support and all the great discussions on and off physics topics, I would like to thank Pavel and Monica. Especially when things got stressful you had encouraging words, constructive advice and the bigger picture waiting for me.

Thanks also to Rainer and Martin for getting me started in the group and being there ever after. Working on L1Calo made me appreciate the dedicated work, which is necessary to keep such an enormous experiment going. And even something innocent like a look-up table can turn out to be a painful detail to be understood.

I would also like to thank Chris, Mat, Vas and all the great people from the Unfolded MET+jets group. We had great times at the meetings and I'm glad I got to visit Manchester and London with you guys. You know cutflows are fun...

Special thanks also to my officemates Basti, Fabrizio, Merve, Lars and Sebastian for the great atmosphere in the office and the many discussions leading who knows where. Physicists are always happy when they can discuss - anything - especially when they know they are right...right?

Also my farm team: Sebastian, Pavel and most recently Falk and Lars. I learned tons and tons about the optimization of networks, storage capacity, linux in general and how much I like order. Thanks for the sometimes painful, but fun times and proving that texting - a lot - late in the evenings never remains unnoticed.

Thanks to all the careful proof readers, Pavel, Monica, Rainer, Martin, Jan, Philipp, Martin², Lars, Sebastian and Falk, for finding all the many typos, commas and providing valuable suggestions for reformulations, hopefully making this work better to digest.

The group continues to evolve and people come and go, but the spirit, the solidarity and

² Yes, there are two Martins.

the coffee breaks with wonderful people always stay. Thank you all and especially Manuel and Hanno for their helping hands³, distractions and seemingly infinite good mood.

I would also like to thank my friends. Even when time flies by, with some people things always simply continue where you left off and it feels like home, instantly.

Especially I would like to mention my family: Hinderk, Barbara and Thorsten. For their continuous support, for the great opportunities you provide me with, for the inspiration, the motivation and sometimes just listening, thank you!

Finally, I would like to thank Livia, for being there for me, for believing in me and for supporting me. Thank you for reminding me what life is all about. I am glad I met you!

³ When you should be at home curing your sickness.